Theoretical and numerical analysis of near-field thermophotonic energy harvesters

Julien Legendre

N° d'ordre NNT : 2023ISAL0094

THÈSE de DOCTORAT de l'INSA LYON
Membre de l'Université de Lyon

École Doctorale MEGA (ED 162)
Mécanique, Énergétique, Génie Civil, Acoustique

Spécialité de Doctorat
Thermique et Énergétique

Soutenue publiquement le 22/11/2023 par

Julien Legendre

Theoretical and numerical analysis of near-field thermophotonic energy harvesters

---

Devant le jury composé de

NOM, Prénom	Grade/Qualité	Établissement	Rôle
GOUPIL, Christophe	Professeur	Univ. Paris-Cité	Président
PAPADAKIS, Georgia	Professeure	ICFO	Rapporteure
VAILLON, Rodolphe	Directeur de recherche	CNRS	Rapporteur
CLERC, Raphaël	Professeur	Univ. Jean-Monnet	Examinateur
REVOL, Inès	Chargée de recherche	CNRS	Examinatrice
CHAPUIS, Pierre-Olivier	Chargé de recherche HDR	CNRS	Directeur de thèse
OKSANEN, Jani	Chercheur	Aalto Univ.	Membre invité

INSTITUT NATIONAL DES SCIENCES APPLIQUÉES LYON

Département de la Formation par la Recherche et des Études Doctorales (**FEDORA**)

Bâtiment INSA direction, 1er étage
37, av. J. Capelle
69621 Villeurbanne Cédex
fedora@insa-lyon.fr

Référence : TH1025_LEGENDRE Julien

L'INSA Lyon a mis en place une procédure de contrôle systématique via un outil de détection de similitudes (logiciel Compilatio). Après le dépôt du manuscrit de thèse, celui-ci est analysé par l'outil. Pour tout taux de similarité supérieur à 10%, le manuscrit est vérifié par l'équipe de FEDORA. Il s'agit notamment d'exclure les auto-citations, à condition qu'elles soient correctement référencées avec citation expresse dans le manuscrit.

Par ce document, il est attesté que ce manuscrit, dans la forme communiquée par la personne doctorante à l'INSA Lyon, satisfait aux exigences de l'Etablissement concernant le taux maximal de similitude admissible.

INSA LYON
Campus LyonTech La Doua
20, avenue Albert Einstein - 69621 Villeurbanne cedex - France
Tél. +33 [0]4 72 43 83 83 - Fax +33 [0]4 72 43 85 00
www.insa-lyon.fr

Département FEDORA – INSA Lyon - Ecoles Doctorales

SIGLE	ECOLE DOCTORALE	NOM ET COORDONNEES DU RESPONSABLE
CHIMIE	**CHIMIE DE LYON** **https://www.edchimie-lyon.fr** Sec. : Renée EL MELHEM Bât. Blaise PASCAL, 3e étage secretariat@edchimie-lyon.fr	**M. Stéphane DANIELE** C2P2-CPE LYON-UMR 5265 Bâtiment F308, BP 2077 43 Boulevard du 11 novembre 1918 69616 Villeurbanne **directeur@edchimie-lyon.fr**
E.E.A.	**ÉLECTRONIQUE, ÉLECTROTECHNIQUE, AUTOMATIQUE** **https://edeea.universite-lyon.fr** Sec. : Stéphanie CAUVIN Bâtiment Direction INSA Lyon Tél : 04.72.43.71.70 secretariat.edeea@insa-lyon.fr	**M. Philippe DELACHARTRE** INSA LYON Laboratoire CREATIS Bâtiment Blaise Pascal, 7 avenue Jean Capelle 69621 Villeurbanne CEDEX Tél : 04.72.43.88.63 **philippe.delachartre@insa-lyon.fr**
E2M2	**ÉVOLUTION, ÉCOSYSTÈME, MICROBIOLOGIE, MODÉLISATION** **http://e2m2.universite-lyon.fr** Sec. : Bénédicte LANZA Bât. Atrium, UCB Lyon 1 Tél : 04.72.44.83.62 secretariat.e2m2@univ-lyon1.fr	**Mme Sandrine CHARLES** Université Claude Bernard Lyon 1 UFR Biosciences Bâtiment Mendel 43, boulevard du 11 Novembre 1918 69622 Villeurbanne CEDEX **sandrine.charles@univ-lyon1.fr**
EDISS	**INTERDISCIPLINAIRE SCIENCES-SANTÉ** **http://ediss.universite-lyon.fr** Sec. : Bénédicte LANZA Bât. Atrium, UCB Lyon 1 Tél : 04.72.44.83.62 secretariat.ediss@univ-lyon1.fr	**Mme Sylvie RICARD-BLUM** Institut de Chimie et Biochimie Moléculaires et Supramoléculaires (ICBMS) - UMR 5246 CNRS - Université Lyon 1 Bâtiment Raulin - 2ème étage Nord 43 Boulevard du 11 novembre 1918 69622 Villeurbanne Cedex Tél : +33(0)4 72 44 82 32 **sylvie.ricard-blum@univ-lyon1.fr**
INFOMATHS	**INFORMATIQUE ET MATHÉMATIQUES** **http://edinfomaths.universite-lyon.fr** Sec. : Renée EL MELHEM Bât. Blaise PASCAL, 3e étage Tél : 04.72.43.80.46 infomaths@univ-lyon1.fr	**M. Hamamache KHEDDOUCI** Université Claude Bernard Lyon 1 Bât. Nautibus 43, Boulevard du 11 novembre 1918 69 622 Villeurbanne Cedex France Tél : 04.72.44.83.69 **hamamache.kheddouci@univ-lyon1.fr**
Matériaux	**MATÉRIAUX DE LYON** **http://ed34.universite-lyon.fr** Sec. : Yann DE ORDENANA Tél : 04.72.18.62.44 yann.de-ordenana@ec-lyon.fr	**M. Stéphane BENAYOUN** Ecole Centrale de Lyon Laboratoire LTDS 36 avenue Guy de Collongue 69134 Ecully CEDEX Tél : 04.72.18.64.37 **stephane.benayoun@ec-lyon.fr**
MEGA	**MÉCANIQUE, ÉNERGÉTIQUE, GÉNIE CIVIL, ACOUSTIQUE** **http://edmega.universite-lyon.fr** Sec. : Stéphanie CAUVIN Tél : 04.72.43.71.70 Bâtiment Direction INSA Lyon mega@insa-lyon.fr	**M. Jocelyn BONJOUR** INSA Lyon Laboratoire CETHIL Bâtiment Sadi-Carnot 9, rue de la Physique 69621 Villeurbanne CEDEX **jocelyn.bonjour@insa-lyon.fr**
ScSo	**ScSo*** **https://edsciencessociales.universite-lyon.fr** Sec. : Mélina FAVETON INSA : J.Y. TOUSSAINT Tél : 04.78.69.77.79 melina.faveton@univ-lyon2.fr	**M. Bruno MILLY** Université Lumière Lyon 2 86 Rue Pasteur 69365 Lyon CEDEX 07 **bruno.milly@univ-lyon2.fr**

*ScSo : Histoire, Géographie, Aménagement, Urbanisme, Archéologie, Science politique, Sociologie, Anthropologie

Remerciements

La plupart du temps, lorsque l'on prépare une thèse, on travaille seul - dans mon cas, seul face à mes deux écrans et des brouillons épars. Cependant, la réussite de ces travaux est loin de ne tenir qu'à moi. Je souhaite ici remercier toutes les personnes ayant contribué, de près ou de loin, à cette réussite.

Tout d'abord, l'éternel second auteur de mes travaux, mon directeur de thèse, Pierre-Olivier Chapuis. Je souhaite le remercier de m'avoir permis de participer à ce beau projet de thèse. Également, d'avoir pris le temps d'avoir avec moi de longues et instructives discussions scientifiques, qui permettaient à chaque fois de donner un nouvel éclairage sur mes observations et donnaient forme à des idées parfois chaotiques. Je le remercie également d'avoir su me donner les ficelles du métier de chercheur, que ce soit à propos de la direction de la recherche ou de la communication scientifique.

Je remercie également les membres de mon jury d'avoir accepté d'évaluer mes travaux de thèse. Les échanges que j'ai pu avoir avec chacun d'eux durant ma soutenance ont été très enrichissants. D'abord, merci à Christophe Goupil d'avoir accepté de présider mon jury. Merci également à Georgia Papadakis et Rodolphe Vaillon d'avoir rapporté ma thèse, et d'avoir pris le temps d'examiner en profondeur mon travail ; je souhaite également remercier ici Rodolphe pour les nombreuses discussions que nous avons pu avoir tout au long de ma thèse, au fil de nos rencontres. Merci aussi à Raphaël Clerc et Inès Revol d'avoir accepté le rôle d'examinateur de ma thèse.

Je souhaite remercier tous les membres du projet européen TPX-Power, dont ma thèse faisait partie. Les échanges que j'ai pu avoir avec chacun d'eux m'ont permis d'avoir une compréhension bien plus globale des systèmes étudiés, sur le plan théorique mais aussi expérimental, grâce à la complémentarité des expertises de chacun. Je tiens à remercier particulièrement Jani Oksanen, le coordinateur du projet sans qui tous ces échanges n'auraient pu avoir lieu, ainsi que Pyry Kivisaari, Toufik Sadi et Jasper van Gastel pour les fréquentes discussions que nous avons pu avoir et qui nous ont permis de faire avancer ensemble la modélisation et la compréhension des systèmes thermophotoniques. Merci aussi à Thomas Châtelet, Wissal Sghaier et Mathieu Thomas, les trois autres doctorants du CETHIL embarqués dans cette collaboration internationale ; ma thèse n'aurait pas été la même sans vous au labo !

Je remercie aussi les membres de l'équipe MiNT du laboratoire, qui m'ont tous beaucoup apportés - que ce soit lors de group meetings ou durant les nombreux repas partagés au CNRS. Merci aux membres permanents de l'équipe, Séverine Gomès, Stéphane Lefèvre, Olivier Merchiers et Konstantinos Termentzidis, qui m'ont permis de mieux appréhender le monde de la recherche. Merci également aux doctorants et post-doctorants de l'équipe que j'ai eu l'occasion de rencontrer durant ma thèse : en plus des trois mentionnés précédemment, j'aimerais remercier Carlos Acosta, Paul Desmarchelier, Kyriaki Kontou, Markos Poulos, Sreyash Sarkar, mais également "l'ancien" de l'équipe, Christophe Lucchesi.

Merci également à toutes les personnes des services techniques et de gestion pour leur travail, qui m'ont permis de pouvoir me concentrer sur la recherche. Je remercie notamment Loïc Guilmard et Bertrand Lecareux du service informatique, ainsi que Noura Bouhila, Edwige Buttet, Mériem Dahmani et Brigitte Kregar du service gestion.

J'ai déjà évoqué nombre de doctorants et post-doctorants du laboratoire précédemment, mais

je souhaite ici tous les remercier pour les moments que nous avons pu partager, que ce soit autour d'une boisson chaude, d'une bière ou d'un appareil à raclette. Mention spéciale à Antoine Courouble, Célia Sondaz et Aurore Toulou pour tous les impromptus rendez-vous dans le bureau de ces dernières et pour les belles soirées passées ensemble.

Pour moi, faire une thèse était un moyen de continuer à assouvir ma curiosité scientifique. Cette curiosité ne s'est pas cultivée seule, et je souhaite ici remercier toutes les personnes qui m'ont permis de développer cet esprit scientifique. Je pense notamment à tous les enseignants que j'ai pu avoir au long de ma vie, et également à mes parents, aux autres membres de ma famille et aux amis qui ont su créer et entretenir cette curiosité.

Enfin, je remercie Julie ; nous nous sommes mesurés ensemble à la thèse, à ses joies et à ses difficultés, et avons réussi ensemble à en sortir grandis.

Abstract

Theoretical and numerical analysis of near-field thermophotonic energy harvesters

With 70% of the world's primary energy consumption being lost as heat during conversion, finding ways to make use of this waste heat is a key challenge. One way is to convert it back into useful energy with heat engines, for instance by using solid-state heat engines to directly convert heat into electricity. In this context, the field of near-field thermophotonics has recently attracted increasing interest. In such an engine, a light-emitting diode heated by the waste heat is placed in the immediate vicinity of a photovoltaic cell at room temperature. The radiation emitted by the light-emitting diode, which displays high intensity due to both electroluminescence and near-field effects, allows the photovoltaic cell to generate a significant amount of electrical power even for low heat source temperatures. Although the light-emitting diode consumes some of this electrical power to run, the complete device is still capable of generating substantial electrical power as long as the two components are efficient enough.

In this thesis, we aim to analyse the operation of near-field thermophotonic engines by theoretical and numerical means. To deepen the understanding of thermophotonic devices, the light-to-electricity and electricity-to-light conversions occurring in the light-emitting diode and the photovoltaic cell are first modelled using detailed-balance approaches. This notably allows developing an analytical upper limit for the efficiency at maximum power for both monochromatic and broadband radiation. We study the influence of several key quantities, such as the bandgap energy or the conductance with the thermal reservoirs, and pinpoint the importance of achieving a high quantum efficiency for the device to reach high power output and efficiency. In a second step, the charge transport in semiconductors is simulated thanks to an in-house one-dimensional drift-diffusion solver including thermionic emission and charge carrier tunnelling at interfaces, enabling the investigation of complete structures. The first system considered is composed of AlGaAs and GaAs homostructures, and is found to be capable of generating a maximum power output of the order of 1 $W.cm^{-2}$ for an LED heated at 600 K. By analysing the charge transport in the two components, we highlight the importance of operating in the near field, the increase in quantum efficiency it causes being essential to achieve satisfactory operation. Because accounting for a significant surface recombination rate or including temperature and composition dependencies in the non-radiative recombination coefficients would make this device inoperable, we propose a new architecture based on heterostructures composed of InGaP confinement layers and InGaAs active layers. This allows reducing non-radiative losses and thus mitigates the power drop when the previously mentioned phenomena are included, with a reduction factor of 4 only. While several idealising assumptions still remains, this shall open a path for the design and optimisation of near-field thermophotonic engines.

Keywords: Thermophotonics, Near-field radiation, Solid-state heat engine, Thermodynamics

Étude théorique et numérique de systèmes thermophotoniques en champ proche appliqués à la récupération d'énergie

En moyenne, on estime que 70% de l'énergie primaire consommée mondialement est perdue sous forme de chaleur durant sa conversion : il est donc nécessaire de trouver des moyens de valoriser cette chaleur fatale. L'une d'elles consiste à la convertir en énergie utile à l'aide de machines thermiques, par exemple grâce à des dispositifs électroniques ou photoniques permettant de convertir directement la chaleur en électricité. Dans ce contexte, le concept de conversion thermophotonique en champ proche a récemment émergé. Dans un tel système, une diode électroluminescente chauffée par la chaleur fatale est placée à très faible distance d'une cellule photovoltaïque maintenue à température ambiante. Le rayonnement émis par la diode électroluminescente, qui présente une intensité élevée grâce aux phénomènes d'électroluminescence et d'effet tunnel de photons, permet à la cellule photovoltaïque de produire une quantité importante d'énergie électrique. Malgré la consommation d'une partie de cette énergie par la diode électroluminescente, le système thermophotonique reste capable de générer une puissance électrique conséquente dès lors que les deux composants présentent une efficacité suffisante.

Dans cette thèse, on analyse le fonctionnement de systèmes thermophotoniques en champ proche par des approches théoriques et numériques. Afin d'approfondir la compréhension de tels systèmes, la conversion de rayonnement en électricité (et vice-versa) ayant lieu dans la diode électroluminescente et la cellule photovoltaïque est d'abord modélisée à l'aide d'équations de conservation. Cela permet notamment de développer une expression analytique de la valeur maximale que peut prendre l'efficacité au maximum de puissance dans un système thermophotonique, dans le cas d'un rayonnement monochromatique ou à large spectre. On étudie l'influence de plusieurs paramètres clés, tel que la largeur de la bande interdite ou la conductance avec les réservoirs thermiques ; on remarque notamment l'importance d'atteindre des efficacités quantiques élevées pour rendre la puissance de sortie et l'efficacité compétitives. Dans un second temps, le transport de charges dans les semi-conducteurs est simulé grâce à un code développé en interne résolvant les équations de dérive-diffusion en une dimension et incluant les phénomènes d'émission thermoïonique et d'effet tunnel aux interfaces, permettant l'étude de structures complètes. L'optimisation de systèmes composés d'homostructures permet d'obtenir un dispositif capable de générer une puissance maximale de l'ordre du $W.cm^{-2}$ pour une diode électroluminescente maintenue à 600 K. L'analyse du transport de charge dans les deux composants révèle par ailleurs l'importance du fonctionnement en champ proche, l'augmentation de l'efficacité quantique qu'il induit étant essentiel au bon fonctionnement du système. On propose enfin un dispositif plus robuste, basé sur des hétérostructures composées de couches de confinement en InGaP et de couches actives en InGaAs limitant les pertes non-radiatives. Une telle architecture permet de conserver de bonnes performances même lorsque des pertes non-radiatives auparavant négligées sont ajoutées au modèle, la puissance maximale ne diminuant que d'un facteur 4 lorsque ces pertes sont incluses. Bien que plusieurs hypothèses restent présentes dans les simulations effectuées, ces études ouvrent la voie à la conception et à l'optimisation de systèmes thermophotoniques en champ proche.

Mots-clés: Thermophotonique, Rayonnement en champ proche, Machine thermique à semi-conducteurs, Thermodynamique

Contents

Remerciements iv

Abstract vi

Contents ix

Nomenclature xii

List of Figures xv

List of Tables xix

General introduction 1

I Thermodynamics and detailed-balance analyses of thermophotonic devices down to the nanoscale 5

1 Concepts, key questions and state of the art 7

1.1 What is a thermophotonic device? . . . 7

1.1.1 Thermodynamics and conversion of radiation . . . 7

1.1.2 Basics of optoelectronics . . . 10

1.1.3 Application to photovoltaics and electroluminescent cooling . . . 13

1.1.4 Thermophotonics . . . 14

1.2 Extension to near field . . . 17

1.2.1 Physics of near-field radiation . . . 17

1.2.2 Model for the simulation of near-field radiation . . . 19

1.2.3 Main contributions to the dielectric function . . . 22

1.2.4 Gap distance in near-field thermophotonic engines . . . 26

1.3 State-of-the-art . . . 26

1.3.1 Material for solar photovoltaics and other optoelectronic applications . . . 28

1.3.2 Thermophotovoltaics . . . 29

1.3.3 Electroluminescent cooling and related photonic cooling . . . 30

1.3.4 Thermophotonic heat engine . . . 31

1.3.5 Comparison of the different engines . . . 33

1.4 To sum up . . . 34

2 Far-field performance of ideal thermophotonic engines 35

2.1 Maximum efficiency of luminescent heat engines . . . 35

2.1.1 Luminescent engine with passive emitter: from Landsberg to Carnot . . . 37

2.1.2 Luminescent engine with active emitter: a standard Carnot heat engine . 40

2.2 Efficiency at maximum power of thermophotonic devices . . . 42

2.2.1 Detailed-balance modelling of thermophotonic conversion . . . 43

2.2.2 Monochromatic radiation . . . 46

2.2.3 Above-bandgap radiation . . . 48

2.2.4 Addition of below-bandgap losses . . . 53

2.3 To sum up . . . 54

3 Detailed-balance analysis of GaAs-based devices in the near field 57
3.1 A small discussion on modelling . . . 57
3.1.1 Near-field radiation calculations: phenomenological vs. numerical . . . 57
3.1.2 On non-radiative recombinations and the vagueness of the quantum efficiency definition . . . 58
3.2 Why GaAs-based structures? . . . 60
3.2.1 Required properties for performant thermophotonics . . . 60
3.2.2 Aligning bandgaps for optimal conversion . . . 62
3.3 Performance of an AlGaAs-GaAs device in the near field . . . 63
3.3.1 Power-voltage characteristics . . . 64
3.3.2 Radiation in the near field . . . 69
3.3.3 Efficiency and below-bandgap photons . . . 72
3.4 Beyond the exoreversible limit . . . 76
3.4.1 Introduction . . . 76
3.4.2 Numerical resolution . . . 78
3.4.3 Performance for above-bandgap radiation . . . 81
3.4.4 Impact of below-bandgap photons . . . 83
3.5 To sum up . . . 85

II Physics and design of GaAs-based near-field thermophotonic devices 87

4 Charge transport in semiconductors 89
4.1 Charge carriers in semiconductors . . . 90
4.1.1 Charge distribution at equilibrium . . . 90
4.1.2 Quasi Fermi levels and out-of-equilibrium conditions . . . 91
4.1.3 Sources of non-radiative recombinations . . . 92
4.1.4 Radiative recombinations: radiative vs. electrical framework . . . 94
4.1.5 Joining semiconductors for charge carrier separation . . . 95
4.2 Drift-diffusion modelling . . . 97
4.2.1 The drift-diffusion equations . . . 97
4.2.2 Why using our own drift-diffusion solver? . . . 99
4.2.3 Material properties . . . 100
4.3 To sum up . . . 101

5 Study of AlGaAs-GaAs PIN homostructures 103
5.1 Numerical methods . . . 103
5.1.1 Details on the algorithm . . . 103
5.1.2 Validation of the solver . . . 107
5.2 Study of an optimised structure . . . 108
5.2.1 Description of the structure . . . 108
5.2.2 Radiative heat transfer . . . 110
5.2.3 Maximum power and related efficiency . . . 110
5.2.4 Local charge distribution at maximum power point . . . 115
5.2.5 Fundamental asymmetry between LED and PV operation . . . 117
5.2.6 Impact of non-radiative recombinations . . . 120
5.2.7 Quantum efficiency in the near field . . . 124
5.3 Impact of bandgap misalignment in the case of non-abrupt bandgaps . . . 125

5.3.1 Urbach tails: definition and implementation . . . 125
5.3.2 Influence of Urbach tails on TPX performance . . . 128
5.3.3 Analysis of the resonance modes close to E_g . . . 129
5.4 To sum up . . . 131

6 Extension to heterostructures for efficient charge transport 133
6.1 Physics and modelling of heterojunctions . . . 133
6.1.1 Charge transport at heterojunctions . . . 134
6.1.2 Drift-diffusion solver for heterostructures . . . 139
6.1.3 Numerical stability issues . . . 139
6.1.4 Back to the chemical potential . . . 143
6.1.5 Photon recycling and thoughts on the locality approximation . . . 144
6.1.6 Comparison to SCAPS . . . 146
6.2 Analysis of TPX devices based on AlGaAs/InGaP heterostructures . . . 147
6.2.1 Structure optimisation of AlGaAs/InGaP devices . . . 148
6.2.2 Performance of optimised AlGaAs/InGaP heterostructures . . . 151
6.2.3 Impact of the heterojunction model on TPX performance . . . 152
6.2.4 Charge transport at maximum power point . . . 153
6.3 Towards more realistic and performant TPX devices . . . 156
6.3.1 Temperature and alloy fraction dependency of non-radiative recombination coefficients . . . 156
6.3.2 InGaAs/InGaP heterostructures for robust TPX devices . . . 158
6.4 To sum up . . . 162

Conclusion 167

Appendices 171

A Methodology for near-field radiative heat transfer simulations 173

B Material properties 177

C Modelling the performance of different solid-state heat engines 181

D Additional derivations of the efficiency at maximum power 183

E Detailed numerical methods for 1D drift-diffusion resolution 187

F Supplementary data on 1D charge transport 193

Bibliography 197

Nomenclature

Fundamental constants

Symbol	Signification	Unit
c	Light velocity	$\mathrm{m.s^{-1}}$
e	Elementary charge	C
k_B	Boltzmann constant	$\mathrm{J.K^{-1}}$
m_0	Electron mass	kg
$\hbar$	Reduced Planck constant	J.s

Latin symbols

Symbol	Signification	Unit
A^*	Effective Richardson constant	$\mathrm{A.m^{-2}.K^{-2}}$
B	Radiative recombination coefficient	$\mathrm{m^3.s^{-1}}$
C	Auger recombination coefficient	$\mathrm{m^6.s^{-1}}$
D	Diffusion coefficient	$\mathrm{m^2.s^{-1}}$
d	Gap (or separation) distance	m
E	Energy	J
E_F	Fermi level	J
E_g	Bandgap energy	J
$\mathcal{E}$	Electric field	$\mathrm{V.m^{-1}}$
$\mathcal{F}$	Transmission function	$\mathrm{m^{-2}}$
f_BE	Bose-Einstein distribution	-
G	Generation rate	$\mathrm{m^{-3}}$
G_th	Thermal conductance	$\mathrm{W.m^{-2}.K^{-1}}$
$\bar{\bar{\boldsymbol{G}}}$	Green tensor	$\mathrm{m^{-1}}$ ($\mathcal{E}$) / $\mathrm{m^{-2}}$ ($\mathcal{H}$)
$\mathcal{H}$	Magnetic field	$\mathrm{A.m^{-1}}$
J	Electrical current density	$\mathrm{A.m^{-2}}$
$\mathbf{k}$	Wavevector	$\mathrm{rad.m^{-1}}$
m^*	Carrier effective mass	kg
$N_\mathrm{a/d}$	Acceptor/donor doping level	$\mathrm{m^{-3}}$
$N_\mathrm{c/v}$	Conduction/valence band effective density of states	$\mathrm{m^{-3}}$
$\dot{N}$	Photon flux density	$\mathrm{m^{-2}.s^{-1}}$
n	Electron concentration	$\mathrm{m^{-3}}$
n_i	Intrinsic carrier concentration	$\mathrm{m^{-3}}$
P	Electrical power	$\mathrm{W.m^{-2}}$
p	Hole concentration	$\mathrm{m^{-3}}$
q	Heat flux density	$\mathrm{W.m^{-2}}$
R	Recombination rate	$\mathrm{m^{-3}}$
S	Surface recombination velocity	$\mathrm{m.s^{-1}}$
s	Entropy flux density	$\mathrm{W.m^{-2}.K^{-1}}$
T	Temperature	K
t	Thickness	m
$\mathcal{T}$	Transmission coefficient	-
U	Voltage	V
V	Electrostatic potential	V
w	Weighting factor	-
x, y, z	Cartesian coordinates	m

Greek symbols

Symbol	Signification	Unit
α	Absorptivity	m^{-1}
ε	Dielectric function	-
ζ	Tolerance	NA
η	Efficiency	-
η_C	Carnot efficiency	-
η_{CA}	Curzon-Ahlborn efficiency	-
λ	Wavelength	m
μ	Chemical potential	J
ξ	Correction term for heterostructure	-
ρ, θ, z	Cylindrical coordinates	m (ρ, z)/ rad (θ)
τ	Carrier lifetime	s
Φ	Slotboom variable	-
χ	Electron affinity	J
Ψ	Normalised electrostatic potential	-
$\dot{\Omega}$	Grand potential flux density	$W.m^{-2}$
ω	Angular frequency	$rad.s^{-1}$

Subscripts

Symbol	Signification
X_{abs}	Absorbed
X_c	Cold
X_{el}	Electroluminescent
X_{em}	Emitted
X_h	Hot
X_{in}	Incoming
X_{nonrad}	Non-radiative
X_{oc}	Open-circuit
X_{out}	Outgoing
X_{rad}	Radiative
X_{sc}	Short-circuit

Acronyms

LED light-emitting diode
LIA low-injection approximation
MPP maximum power point
NF near field
PPR power production region
PV photovoltaic
QE quantum efficiency
SRH Shockley-Read-Hall
TE thermoelectrics
TPV thermophotovoltaics
TPX thermophotonics
TR thermoradiative

List of Figures

1.1 Blackbody spectrum obtained with Planck's law of radiation. . . . 9
1.2 Representation of a heat engine. . . . 10
1.3 Main physical phenomena occurring in semiconductors. . . . 11
1.4 Basic principle of conversion in light-emitting diodes and photovoltaic cells. . . . 12
1.5 Current-voltage characteristic of optoelectronic devices. . . . 13
1.6 Representation of the thermophotonic heat engine. . . . 16
1.7 Typical variation of the heat flux with the gap distance. . . . 18
1.8 Radiation modes occurring around an interface between vacuum and a body with higher refractive index. . . . 19
1.9 1D multilayered structure considered in the simulation of near-field radiative heat transfer in the z direction. . . . 19
1.10 Typical dielectric function obtained with a Drude model for the plasmonic contribution. . . . 23
1.11 Typical dielectric function obtained with a Lorentz oscillator for the optical phonon contribution. . . . 24
1.12 Dielectric function obtained for GaAs at room temperature with the model and parameters given in [Gonzalez-Cuevas *et al.* 2007]. . . . 25
1.13 Review of radiative heat engines. . . . 27
1.14 Best research-cell efficiency chart [NREL 2023]. . . . 28
1.15 Criticality of raw materials for the European Union (adapted from [European Commission *et al.* 2023]). . . . 29
1.16 State-of-the-art of the performance of radiative heat engines. . . . 32
1.17 Basic models for the variation of power generated with heat source temperature, obtained for different radiative heat engines. . . . 33

2.1 Representation of the luminescent heat engine. . . . 36
2.2 Variation of efficiency with chemical potential of radiation emitted by the cold absorber, considering complete above-E_g radiation. . . . 38
2.3 Entropy production in the passive emitter, normalised by the entropy flux coming from the heat source, as a function of the cut-off energy. . . . 40
2.4 Variation of efficiency with chemical potential of radiation emitted by the cold absorber for monochromatic radiation. . . . 41
2.5 Schematic of the energy flow through a thermophotonic heat engine at the radiative limit. . . . 45
2.6 Variation of power output with LED chemical potential. . . . 47
2.7 Variation of the efficiency at maximum power as a function of the temperature ratio $T_\mathrm{h}/T_\mathrm{c}$ for the monochromatic TPX device. . . . 48
2.8 (a) Variation of efficiency at maximum power with bandgap for $T_\mathrm{h} = 600$ K. (b) LED and PV cell chemical potentials at maximum power point for various heat source temperatures. . . . 49
2.9 Variation of the efficiency at maximum power of a TPX device as a function of the temperature ratio $T_\mathrm{h}/T_\mathrm{c}$ with complete above-bandgap radiation. . . . 52
2.10 Spectrum of the radiative heat flux exchanged between the LED and the PV cell for $(E_g - \mu)/k_\mathrm{B}T = \ln(2)$ and for $T_\mathrm{h} = 600$ K. . . . 53

2.11 Variation of the maximum power output and the related efficiency with radiation bandwidth. 54

3.1 Maximum power production of NF-TPX devices with constant interband dielectric function $10 + 1i$, with respect to the bandgap and the quantum efficiency. 60
3.2 (a) Variation of the power output with respect to the LED voltage, for TPV-like and true TPX behaviour. (b) Bandgap energy leading to maximum power output, computed for high quantum efficiencies. 61
3.3 Variation of maximum power with the bandgap mismatch, for materials with dielectric function $\varepsilon = 10 + 1i$ and for a PV cell bandgap of $E_g = 1$ eV. 63
3.4 Equivalent Raveau diagram for TPX heat engines at the radiative limit. 65
3.5 P-VV characteristic of an AlGaAs-GaAs NF-TPX device, respectively for (a) QE = 1, (b) QE = 0.9. 66
3.6 P-V_{LED} characteristic of an AlGaAs NF-TPX device. 67
3.7 Impact of series resistance on maximum power output. 68
3.8 Variation of power output for different solid-state heat engines, as a function of the heat source temperature. 69
3.9 Influence of the gap distance on the different energy flows circulating through the device, at maximum power point and for a QE of 0.9. 71
3.10 Spectral thermal heat flux density exchanged between the LED and the PV cell for different gap distances and for (a) undoped and (b) n-doped materials (5×10^{18} cm^{-3}). 72
3.11 η-VV characteristic of an AlGaAs-GaAs NF-TPX device, respectively for (a) QE = 1, (b) QE = 0.9. (c) η-V characteristics of AlGaAs-GaAs NF-TPX devices. . . 73
3.12 η-P characteristic of an AlGaAs NF-TPX device considering only above-bandgap photons. 74
3.13 η-V characteristic of an AlGaAs NF-TPX device considering only above-bandgap photons or complete spectrum. 75
3.14 Schematic of the AlGaAs-GaAs device considered, with exo-irreversibilities taken into account. 77
3.15 Flowchart of the Broyden's method based algorithm used to obtain the temperatures of both components at thermal equilibrium. 79
3.16 Flowchart of the secondary iterative process for self-consistent calculation of temperature and performance at maximum power point. 80
3.17 Impact of the QE on (a) the device performance, (b) the difference of temperature in the device for various reservoir thermal conductances, considering only above-bandgap photons. 81
3.18 Impact of (a) reservoir and (b) parasitic thermal conductance on the performance of the NF-TPX device, with only above-bandgap photons considered. 82
3.19 Impact of the QE (a) on the device performance, (b) on the difference of temperature in the devicefor various reservoir thermal conductance, considering the complete spectrum. 84
3.20 (a) Impact of reservoir conductance on the performance of the NF-TPX device, considering the complete spectrum. (b) Gap distance optimising the maximum power output as a function of the reservoir thermal conductance. 84

4.1 Impact of doping on the charge distribution (left: donor atom, right: acceptor atom). 91
4.2 Schematics of the main types of non-radiative recombinations. 92

4.3 Flowchart of the coupled radiative-electrical iterative solver proposed in [Callahan *et al.* 2021]. . . . 95
4.4 Basic semiconductor junctions. . . . 96
4.5 Band diagram for different abrupt junctions at equilibrium. . . . 97

5.1 Flowchart of the drift-diffusion solver for homostructures. . . . 107
5.2 Structure used for the validation of the drift-diffusion solver. . . . 108
5.3 Comparison of the results obtained by different 1D drift-diffusion solvers. . . . 109
5.4 Schematic of the AlGaAs-GaAs homostructure under consideration, obtained from optimisation algorithms. . . . 110
5.5 Local heat flux density (a) in the LED, (b) the PV cell obtained in the near field or in the far field. . . . 111
5.6 P-VV characteristic of the AlGaAs-GaAs homostructure. . . . 111
5.7 P-V_{LED} characteristic of the AlGaAs-GaAs homostructure. . . . 112
5.8 η-VV characteristic of the AlGaAs-GaAs homostructure. . . . 113
5.9 η-V_{LED} characteristic of the AlGaAs-GaAs homostructure. . . . 113
5.10 Impact of the gap distance on (a) the maximum power output and the transmitted radiative heat flux, (b) the efficiency of the AlGaAs-GaAs homostructure. . . . 114
5.11 Charge carrier density at MPP (a) in the LED, (b) in the PV cell. . . . 115
5.12 Effect of using the low-injection approximation to compute the local SRH recombination rate (a) in the LED, (b) in the PV cell at low voltage. . . . 116
5.13 Band diagrams at MPP (a) in the LED, (b) in the PV cell. . . . 117
5.14 Band diagrams obtained at low voltage (a) in the LED, (b) in the PV cell. . . . 118
5.15 I-V characteristics of the LED and the PV cell. . . . 119
5.16 Variation of power output with quantum efficiency obtained with the detailed-balance model. . . . 119
5.17 Local generation-recombination rates obtained at different voltages in components. 121
5.18 Total generation-recombination rate in a component given as a function of its voltage. 122
5.19 Variation of a component quantum efficiency as a function of its applied voltage. 123
5.20 Power production region obtained with the detailed-balance model, for different QEs. 123
5.21 Impact of the surface recombination velocity on the maximum power output of the AlGaAs-GaAs homostructure. . . . 124
5.22 Impact of the gap distance (a) on the LED quantum efficiency, (b) on the TPX device power production region. . . . 125
5.23 Schematic of the tail states inside the bandgap and the subsequent densities of states. 126
5.24 Comparison of the electroluminescent emission spectrum of an LED obtained from measurements and from Eq. (5.17). . . . 127
5.25 Variations of the maximum power output with the LED bandgap, controlled through the aluminium fraction. . . . 129
5.26 Transmission coefficient between the LED and the PV cell as a function of ω and k_ρ. 130
5.27 Power production region of a modified version of the structure shown in Figure 5.4, in which the doping level of intermediate layers is increased to 10^{18} W.cm^{-3}. 131

6.1 Advantages of heterostructures over homostructures. . . . 134
6.2 Transmission coefficient of charge carriers (here, electrons) through a heterojunction. 135
6.3 Representation of the different quantities useful for thermionic-field emission. . . . 138
6.4 Typical variation of the error ε obtained at each iteration, defined as the relative variation of the Slotboom variables. . . . 141

6.5 Flowchart of the drift-diffusion solver for heterostructures at $(U_{\mathrm{LED}}, U_{\mathrm{PV}}) = (U_i, U_j)$. 142
6.6 Typical deviation of the quasi Fermi level difference with respect to eU in a 600 K LED. . . . 143
6.7 Transmission coefficient between two layers separated by a distance d obtained for $\hbar\omega = 1.42$ eV, in an infinite medium with dielectric function $\varepsilon = 10 + i$. . . . 145
6.8 Non-optimised heterostructure-based TPX device used to compare the in-house solver with SCAPS. . . . 146
6.9 Comparison of the PV cell (a) I-V characteristic, (b) total generation-recombination rates obtained with the in-house algorithm and SCAPS. . . . 147
6.10 (a) Heterostructure-based AlGaAs/InGaP TPX device considered for optimisation. (b) Result of the active layer thickness optimisation. . . . 149
6.11 Power output estimate for different couples of active layer thicknesses, given by the optimisation process (a) at 10 nm, (b) at 100 nm. In (c) is given the variations of power output with active layer thicknesses at a 10 nm gap distance. . . . 150
6.12 Transmission coefficient of radiation between the LED and the PV cell at normal incidence and for a gap distance of (a) 10 nm, (b) 100 nm. . . . 151
6.13 P-V_{LED} characteristic of the two optimised TPX devices, at 10 and 100 nm gap distance. . . . 152
6.14 Influence of (a) the heterojunction model, (b) the iterative resolution of the photon chemical potential on the P-V_{LED} characteristic of the 10-nm-optimised TPX device. 153
6.15 Band diagrams at maximum power point in both components. . . . 154
6.16 Spatially-resolved electron and hole current densities related to drift and diffusion or to tunnelling at maximum power point in the LED and the PV cell. . . . 155
6.17 Influence of the SRH lifetime in AlGaAs (a) on the P-V_{LED} TPX characteristic, (b) on the maximum power output. . . . 157
6.18 Impact of the inclusion of temperature dependency for non-radiative recombination coefficients on (a) the P-V_{LED} TPX characteristic, (b) the local generation and recombination rate in the PV cell at MPP. . . . 158
6.19 Proposed InGaAs/InGaP TPX structure for the reduction of non-radiative recombinations. . . . 159
6.20 P-V_{LED} characteristic of the structure illustrated in Figure 6.19 for different scenarios, along with the LED QE at zero PV cell voltage. . . . 161
6.21 Influence of (a) the gap distance, (b) the heat source temperature on the maximum power output of the InGaAs/InGaP device. . . . 162
6.22 Performance of NF-TPX devices obtained from detailed balance (Chapter 3) and from the drift-diffusion modelling of charge transport in the InGaAs/InGaP device (Chapter 6), compared to thermoelectrics. . . . 164

A.1 Reproduction of the results provided in [Francoeur *et al.* 2010]. . . . 175
A.2 Schematic of the system considered in the radiative model. . . . 176

E.1 Schematic of the spatial grid. . . . 187

F.1 Impact of using low-field or field-dependent mobility on performance. . . . 193
F.2 P-V_{LED} characteristic of the AlGaAs/InGaP device represented in Figure 6.10a, either with or without the contribution of the photon flux internal to a component. 194
F.3 I-V characteristic of the PV cell from Figure 5.2 with an LED voltage of 1.15 V. 195

List of Tables

2.1 Bandwidth and quality factor of radiation emitted by common sources. 52

3.1 Performance of a NF-TPX AlGaAs-GaAs device. q is given at maximum power. . 76
3.2 Conductance at half power, given for the different cases studied in Figure 3.18. . 83

4.1 Pros and cons of available drift-diffusion solvers. 100

B.1 Material properties used to obtain the dielectric function of $Al_xGa_{1-x}As$ alloys. . 177
B.2 Material properties used to obtain the dielectric function of $In_{1-x}Ga_xP$ alloys. . . 178
B.3 Material properties used to obtain the dielectric function of $In_xGa_{1-x}As$ alloys. . 178
B.4 Charge transport properties of $Al_xGa_{1-x}As$ and $In_xGa_{1-x}As$ alloys. 179
B.5 Charge transport properties of $In_{1-x}Ga_xP$ alloys. 179

General introduction

In 2019, approximately 160,000 TWh of energy was consumed worldwide [IEA 2023]. However, only 30% of this was estimated to be useful energy: the remaining was lost as heat, either carried away by effluents or exhaust gases or directly released into the close environment through heat transfer [Forman *et al.* 2016]. In the current context of a global warming mostly caused by our energy consumption, making use of this waste heat to increase the efficiency of the primary energy conversion - and thus to reduce the need for energy production - becomes increasingly necessary. Consequently, many researchers and institutions have started to investigate the potential of waste heat recovery in industrial sites, incineration plants but also data centres [ADEME 2017], whose share of energy consumption became significant in the last few years.

Many possibilities are available to harvest this waste heat [Jouhara *et al.* 2018]. If the heat cannot be directly reused, for instance for preheating or in heat networks, heat engines can allow to convert a fraction of it into mechanical or electrical energy; this has for instance been investigated for increasing the efficiency of motorised vehicles [Wang *et al.* 2011]. When talking about heat engines, we generally think about mechanical engines based on the compression, expansion and phase transition of fluids, such as internal combustion engines but also Carnot, Stirling or Rankine engines. Such engines however face three major drawbacks, which are mainly related to the presence of mechanical parts:

- a lack of scalability, their performance dropping for small-scale applications due to decreased efficiency of the mechanical parts along with increased pressure drop occurring during the circulation of the working fluid;
- a significant need for maintenance;
- the presence of vibrations, which can be too detrimental in some applications (e.g. space probes).

In addition, if the mechanical energy they produce cannot be directly used, it must be further converted to another form of energy (typically electrical energy) which decreases the overall efficiency. To avoid such drawbacks, solid-state heat engines, which are based on electronics, can be used instead. One example of such an engine is the thermoelectric generator, which is based on the Seebeck effect. It is probably one of the most commonly used solid-state heat engine thanks to it satisfactory performance for low-grade heat recovery, which is interesting as the majority of waste heat is released at temperature below 100 °C [Forman *et al.* 2016, ADEME 2017]. Still, its efficiency remains significantly lower than that of usual engines [Melnick & Kaviany 2019], and research has been performed to develop solid-state waste heat harvesters with competitive performance even for low heat source temperature.

Recently, the concept of near-field thermophotonics have shown growing interest. This engine is closely related to thermophotovoltaics, in which a hot passive body - which is kept at high temperature thanks to the available heat - radiates towards a photovoltaic cell at room temperature, allowing to produce electrical power. In near-field thermophotonic heat engines, two main modifications are made:

- the passive emitter is replaced by a light-emitting diode, which allows increasing the amount of energy radiated by means of electroluminescence;
- the light-emitting diode and the photovoltaic cell are placed at a distance of the order

of tens to hundreds of nanometres to reach near-field operation, further improving the radiative transfer thanks to photon tunnelling.

While thermophotovoltaic operation is often limited to heat source temperature above 1000 °C, these two changes are expected to allow near-field thermophotonic devices to be suitable for low-grade heat recovery. However, only very limited research has been conducted on such devices. In this context, an international collaboration has been established between Aalto University, VTT, CNRS (through the CETHIL laboratory at INSA Lyon), Radboud University and Tf2 Devices to drive research on near-field thermophotonics forward. The work carried out in this manuscript is part of this common effort, and aims at developing the understanding of the physics and the thermodynamics of such engines and at giving pathways for their development based on theoretical and numerical analyses. It is divided into two distinct parts. In Part I, we introduce the concept of near-field thermophotonic energy harvesting and explore its operation through thermodynamics and detailed-balance approaches. In Part II, we aim at studying the performance of complete structures. To do so, the charge transport in semiconductors is simulated in one-dimension using the drift-diffusion equations.

In the first chapter, we start by describing the basic principle of thermophotonic engine operation, along with the different phenomena occurring in optoelectronic devices. Since we aim at extending classical thermophotonic heat engine to near-field operation, we also discuss the physics behind the radiative transfer enhancement obtained between two close bodies, which is related to the coupling of evanescent waves in the intermediate medium. The numerical model used to simulate one-dimensional near-field radiative heat transfer is also quickly described. We finish the chapter by reviewing the work performed in the literature on far-field and near-field thermophotonics and on closely-related engines, such as thermophotovoltaic and thermoelectric ones.

Chapter 2 focuses on the analytical development of fundamental efficiency limits for thermophotonic conversion, which differ from the usual limits due to the specific thermodynamics of radiation. We start by studying how the use of an active emitter modifies the maximum efficiency of a reversible radiative heat engine. This allows to highlight fundamental differences between thermophotovoltaics and thermophotonics. Then, we examine the efficiency at maximum power of irreversible thermophotonic engines, for which we derive an analytical expression in both monochromatic and broadband limits.

In Chapter 3, we perform the numerical analysis of thermophotonic engines operating in the near field based on detailed balance, in the idea of extending existing studies from the literature. We study the impact of bandgap energy and quantum efficiency, and pinpoint significant differences with thermophotovoltaics. For two different values of quantum efficiency, we analyse how power output and efficiency vary with the voltage applied on both components, and determine for which set of voltages the device is capable of operating as a heat engine. We also analyse the impact of having a finite thermal conductance with the reservoirs on the maximum power output.

Chapter 4 aims to introduce all the information necessary for the developments carried out in Part II. Namely, we describe briefly the key phenomena related to charge transport in semiconductors, along with the set of equations considered to simulate it.

After a short description of the model, Chapter 5 focuses on the analysis of PIN thin-film homostructures. Through an optimisation process, we are able to obtain a structure with promising performance. We however notice several differences with the results obtained from detailed-balance modelling, the cause of such deviations being investigated in regard to the non-radiative losses occurring during charge transport. Thereafter, we analyse how the performance

of such a structure is impacted by the inclusion of Urbach tails in the dielectric function, which reflects the possibility for interband transition to occur with photons of energy lower than the bandgap energy.

Chapter 6 covers the study of heterostructures, in which the use of confinement layers allows improving carrier separation. Different models being available for the charge transport through heterointerfaces, we analyse the sensitivity of the results to the model. By relaxing some of the idealising approximations assumed in the previous chapters, we then design and analyse a robust architecture which mitigates the drop of performance caused by non-radiative recombinations. Such studies shall pave the way to the numerical development of promising structures.

Finally, we provide a summary of this work and highlight interesting perspectives for future studies.

Part I

Thermodynamics and detailed-balance analyses of thermophotonic devices down to the nanoscale

Chapter 1

Concepts, key questions and state of the art

Contents

1.1 What is a thermophotonic device? 7
1.1.1 Thermodynamics and conversion of radiation 7
1.1.2 Basics of optoelectronics 10
1.1.3 Application to photovoltaics and electroluminescent cooling 13
1.1.4 Thermophotonics 14
1.2 Extension to near field 17
1.2.1 Physics of near-field radiation 17
1.2.2 Model for the simulation of near-field radiation 19
1.2.3 Main contributions to the dielectric function 22
1.2.4 Gap distance in near-field thermophotonic engines 26
1.3 State-of-the-art 26
1.3.1 Material for solar photovoltaics and other optoelectronic applications 28
1.3.2 Thermophotovoltaics 29
1.3.3 Electroluminescent cooling and related photonic cooling 30
1.3.4 Thermophotonic heat engine 31
1.3.5 Comparison of the different engines 33
1.4 To sum up 34

1.1 What is a thermophotonic device?

A thermophotonic device shows numerous similarities with thermophotovoltaic and thermoradiative engines. Globally, it is a *heat engine* based on *radiation* and its conversion through *optoelectronic* components. This first section will focus on the description of these main notions, allowing for a proper introduction of the concept of thermophotonics.

1.1.1 Thermodynamics and conversion of radiation

1.1.1.1 Wave and particle

Radiation corresponds to the transmission of energy through electromagnetic waves. Such waves emanate from the oscillation of electromagnetic dipoles related to the thermal agitation of charges in a medium at non-zero temperature. Energetically, this can be understood as the conversion of internal energy (the thermal agitation) into radiation. Symmetrically, radiation can be absorbed

and generates then thermal agitation. As a combination of waves, radiation will be exchanged in a given spectrum, i.e. in a range of wavelengths λ (or frequencies ν).

Wave formulation does not give a complete description of radiation. The work of Planck and Einstein shined a light on the wave-particle duality of electromagnetic radiation, which can also be seen as a flux of elementary particles called photons. These particles are elementary as the energy they carry is indivisible, which represents therefore the quantum of energy E of radiation. Using Planck-Einstein relation, E can simply be expressed as a function of its frequency ν or angular frequency $\omega = 2\pi\nu$ through

$$E = h\nu = \hbar\omega,$$

where h is the Planck constant and $\hbar$ the reduced Planck constant. This quantised vision of radiation was the key for Planck to derive its famous law of radiation.

1.1.1.2 Planck's law of radiation

In the end of the XIX$^{\text{th}}$ century, intensive research was conducted on the derivation of the maximum radiation emitted by a body at temperature T, called blackbody radiation (since such a body would absorb all the incoming light as a black body would do in the visible range of the spectrum). Such work has been carried out considering either the complete spectrum (Stefan & Boltzmann [Boltzmann 1884]) or any frequency (Wien, Rayleigh & Jeans). In 1901, Planck [Planck 1901] expresses the spectral radiance (i.e. the heat flux density per unit frequency and solid angle) as

$$B_\omega(T) = \frac{\hbar\omega^3}{4\pi^3 c^2} \frac{1}{\exp\left(\frac{\hbar\omega}{k_B T}\right) - 1}, \tag{1.1}$$

where c is the speed of light and k_B is the Boltzmann constant. Integrating over all the directions allows to obtain the spectral radiative heat flux density emitted; writing $[\exp(\hbar\omega/k_B T) - 1]^{-1}$ as the Bose-Einstein distribution $f_{\text{BE}}(\omega, T)$, we have

$$q_\omega(T) = \frac{\hbar\omega^3}{4\pi^2 c^2} f_{\text{BE}}(\omega, T). \tag{1.2}$$

This expression is represented in Figure 1.1 for different blackbody temperatures. Its further integration over the spectrum finally gives

$$q = \sigma T^4, \tag{1.3}$$

the Stefan-Boltzmann law.

1.1.1.3 Entropy of radiation

Up to now, we have discussed the energy of radiation. However, what ultimately limits the conversion of heat into useful work is the entropy carried by this heat. Generally, we can state that a heat flux q leaving a body at temperature T carries an entropy $s = q/T$. This is different for radiation; to understand why, we should study its thermodynamics. Instead of thinking of radiation just as a flux of energy leaving an emitter, we apply the laws of thermodynamics directly on radiation. Apart from its own energy (related to σT^4), it exchanges energy as heat with the emitter; but it also applies a pressure (called radiation pressure) on the interface of the emitter due to the change in momentum of photons when they get reflected or refracted. Taking into account this pressure allows to show that the entropy carried by radiation in equilibrium with a

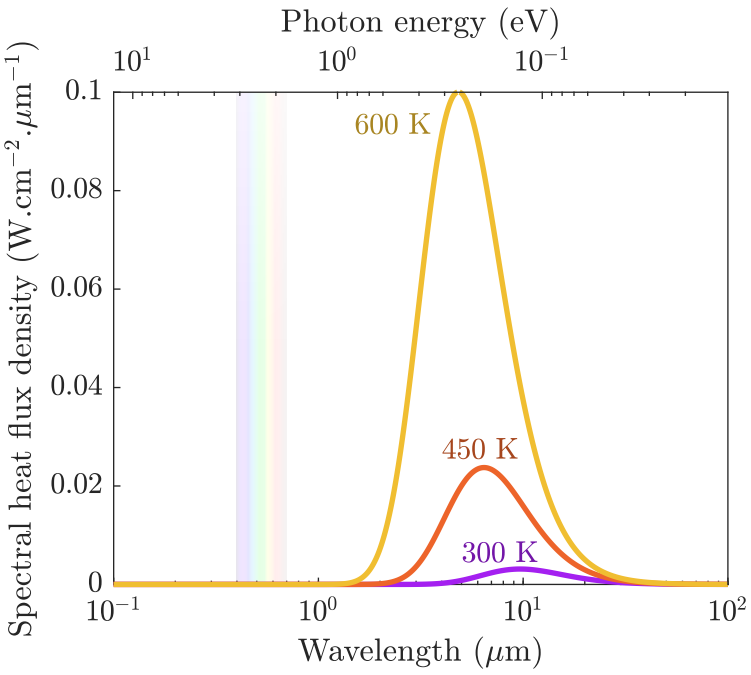

Figure 1.1: Blackbody spectrum obtained with Planck's law of radiation for different temperatures.

blackbody at temperature T is [Planck 1914]

$$s = \frac{4}{3}\sigma T^3 = \frac{4}{3}\frac{q}{T}, \tag{1.4}$$

hence larger by 1/3 than the entropy carried by the same amount of "usual" heat (e.g. conduction). Note that the factor 4/3 arises from the use of a blackbody spectrum, and would change for a different spectrum; still, except in some very specific cases, we have $s \neq q/T$. This has a significant impact on the conversion of radiation into work.

1.1.1.4 Conversion efficiency of radiative heat engines

A machine capable of converting heat into useful work is called a *heat engine*. Since entropy cannot be destroyed, only a fraction of the incoming heat q_{in} can be converted into work P, while the remaining must carry all the entropy - both incoming s_{in} and produced during conversion s_{prod} - towards a heat sink (i.e. a body at lower temperature). This is represented in Figure 1.2. In order to maximise the efficiency $\eta = P/q_{\text{in}}$, one should reduce as much as possible the outgoing heat flux q_{out}, thus the outgoing entropy flux s_{out}. The optimum case is therefore $s_{\text{prod}} = 0$, i.e. a reversible engine. If heat is exchanged with the engine through conduction or convection, then $s = q/T$ and the engine is a Carnot engine with efficiency

$$\eta = \frac{P}{q_{\text{in}}} = 1 - \frac{q_{\text{out}}}{q_{\text{in}}} = 1 - \frac{T_{\text{c}} s_{\text{in}}}{T_{\text{h}} s_{\text{in}}} = 1 - \frac{T_{\text{c}}}{T_{\text{h}}} = \eta_{\text{C}}, \tag{1.5}$$

η_{C} being the Carnot efficiency. Now, if we assume that the incoming heat is transferred through radiation, and that both heat source and engine behave as blackbodies, we have $q_{\text{in}} = q_h - q_e$ and $s_{\text{in}} = s_h - s_e$ where q_i and s_i are respectively obtained from Eq. (1.3) and (1.4) at the temperature of the heat source (subscript h) or of the engine (subscript e). The maximum efficiency is reached when the engine temperature T_{e} equals the heat sink temperature T_{c}; then,

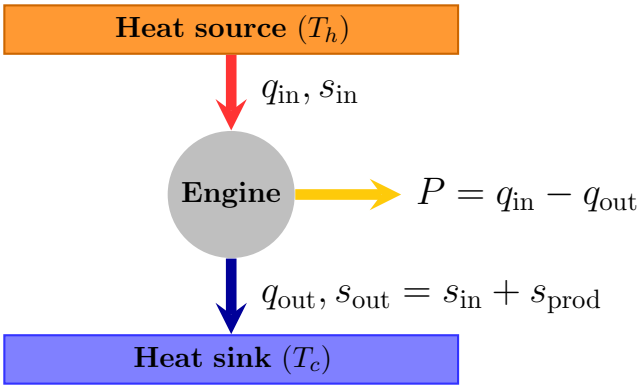

Figure 1.2: Representation of a heat engine.

the maximum efficiency is

$$\eta = 1 - \frac{q_{\text{out}}}{q_{\text{in}}} = 1 - \frac{T_{\text{c}}(s_{\text{h}} - s_{\text{e}})}{q_{\text{h}} - q_{\text{e}}} = 1 - \frac{4}{3}T_{\text{c}}\frac{T_{\text{h}}^3 - T_{\text{c}}^3}{T_{\text{h}}^4 - T_{\text{c}}^4} = \frac{1 - \frac{4}{3}\frac{T_{\text{c}}}{T_{\text{h}}} + \frac{1}{3}\left(\frac{T_{\text{c}}}{T_{\text{h}}}\right)^4}{1 - \left(\frac{T_{\text{c}}}{T_{\text{h}}}\right)^4} = \frac{\eta_{\text{L}}}{1 - \left(\frac{T_{\text{c}}}{T_{\text{h}}}\right)^4}, \quad (1.6)$$

which is closely related to the so-called Landsberg limit η_{L} [Landsberg & Tonge 1980] and definitely different from the Carnot efficiency. This makes clear that the usual thermodynamical limits derived for usual heat engines do not hold for radiative heat engines, which will require a specific treatment. This will be especially addressed in Chapter 2.

1.1.2 Basics of optoelectronics

In a broad sense, *optoelectronics* corresponds to the study of electronic devices capable of detecting, converting or controlling radiation; it includes devices like photodetectors, photovoltaic cells, or light-emitting diodes. All these devices are based on common physical phenomena which allow for the conversion of electricity into radiation (or the reverse). In all the manuscript, only optoelectronic devices based on inorganic semiconductors will be considered as they represent by far the most common solutions and allow to reach the best efficiencies, in comparison to organic devices for instance (see Section 1.3.1). Hereafter are presented the basics of the physical phenomena occurring in semiconductors, whose description is based on the very enlightening book on solar cells written by Würfel and Würfel [Würfel & Würfel 2016].

In any material, the available levels of energy of electrons can be described as an electronic band structure, in which alternate available and forbidden bands of energy. There is still a finite amount of energy levels in each of these available bands, which can therefore be more or less filled by electrons. In this band structure, two are of interest: the valence band and the conduction band. The valence band is defined as the last band (in terms of energy) being completely filled at 0 K. The next available band is the conduction band, in which electrons are freed from the coulombic attraction of the atom nucleus and can move inside the whole material. A semiconductor is defined as a material:

- whose conduction band is completely empty at 0 K (else, it is a metal);

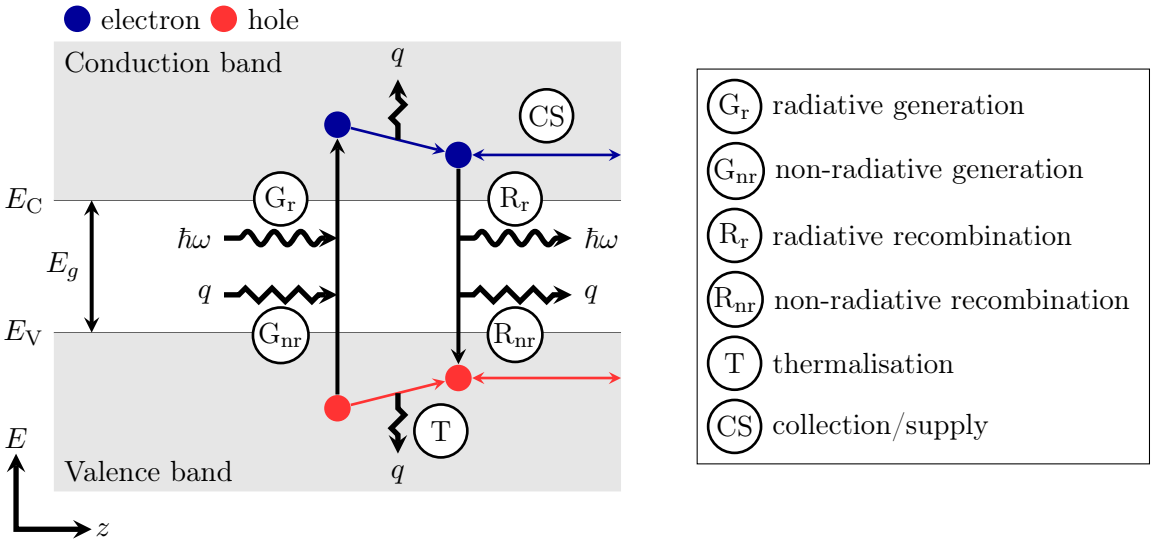

Figure 1.3: Main physical phenomena occurring in semiconductors.

- whose energy gap between valence and conduction bands (called bandgap) remains moderate[1] (else, it is an insulator).

If such a material is at a non-zero temperature, thermal agitation (i.e., the energy contained within the material lattice) can provide enough energy to promote electrons from the valence band to the conduction band, which can then help to conduct electricity (hence the name semiconductor). This energy can also come from other sources, e.g. from photons: any photon with energy $E = \hbar\omega$ greater than the bandgap energy E_g can promote electrons to the conduction band - this is the basic principle of the photovoltaic effect.

By moving to the conduction band, the electron leaves a hole in the valence band. At a non-zero temperature, this band is almost filled and other electrons of the valence band can quickly recombine with the hole due to thermal agitation - letting another hole behind. Instead of following the movement of electrons in the valence band, it is also possible to follow that of the holes instead; such holes in the valence band can be understood as particles with positive charges able to move in the material, similarly to electrons (with negative charge) in the conduction band. Thus, photons (or thermal agitation) not only promote an electron to the conduction band, but generates what is called an electron-hole pair. The energy provided to generate the electron-hole pair then corresponds to the sum of these particles' internal energy, and is stored inside the charges until they are collected at the boundaries of the system or recombine with a charge of opposite sign. In the latter case, it either gives rise to a photon (radiative process) or causes the release of the electron-hole pair energy into heat (non-radiative process).

Of course, it is also possible to supply the semiconductor with charge carriers by feeding it with an electrical current. By doing so, we largely increase the amount of both radiative and non-radiative recombinations. This especially means that much more photons are emitted above the bandgap energy E_g than in the standard case of thermal emission: this phenomenon is called electroluminescence. A similar effect can occur if the electron-hole pair supply is performed

[1] This definition is deliberately vague, as the delimitation between semiconductors and insulators is not strict and moves with temperature. For the temperature considered, materials with bandgaps larger than 5 eV can generally be considered to be insulators, although sometimes labelled as ultra-wide bandgap semiconductors (as for diamond).

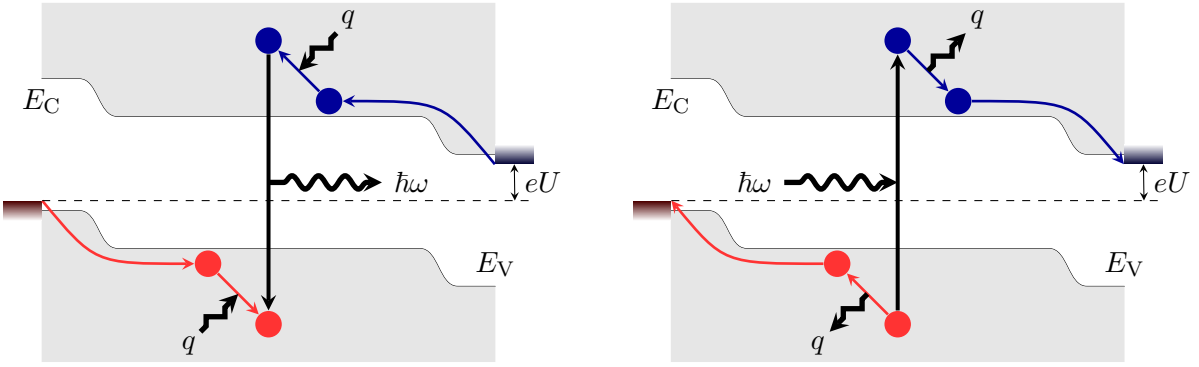

(a) Light-emitting diode

(b) Photovoltaic cell

Figure 1.4: Basic principle of conversion in light-emitting diodes and photovoltaic cells. The two rectangles at the ends of the band diagram correspond to electrical contacts.

through the illumination of the semiconductor with photons of energy greater than E_g. The increase of emission due to electron-hole pair recombinations can be obtained from the sum of both charge carrier electrochemical potentials: by recombining, the electrochemical potential of charges is converted into a chemical potential of photons. The Bose-Einstein distribution then takes the following generalised form for $\hbar\omega \geq E_g$ [Würfel 1982]:

$$f_{\mathrm{BE}}(\omega,\mu,T) = \begin{cases} f_{\mathrm{BE}}(\omega,T) & \text{if } \hbar\omega < E_g, \\ \dfrac{1}{\exp\left(\frac{\hbar\omega-\mu}{k_B T}\right)-1} & \text{if } \hbar\omega \geq E_g, \end{cases} \tag{1.7}$$

where μ represents the chemical potential of radiation. To make the impact of μ clearer, we can use the Boltzmann approximation, which holds if $\hbar\omega - \mu \gg k_B T$. In this case, the exponential term is much greater than 1 and $f_{\mathrm{BE}}(\omega,\mu,T) \approx \exp(\mu/k_B T) f_{\mathrm{BE}}(\omega,0,T)$: the above-bandgap heat flux increases exponentially with μ (while the below-bandgap heat flux remains unchanged). μ should be different from E_g to avoid the divergence of the Bose-Einstein distribution; this is always satisfied, as an entropy analysis allows to show that $\mu < E_g$ should hold to avoid destruction of entropy [Würfel 1982].

The different processes discussed above are represented in Figure 1.3. Along with radiative generation, non-radiative generation occurs in semiconductors due to thermal agitation and it should balance non-radiative recombination at equilibrium. It is however almost always negligible since the mean thermal energy of heat carriers in the lattice (around $k_B T$, equal to 26 meV at room temperature) is much smaller than the bandgap energy (commonly greater than 0.3 eV). One process which was not yet mentioned is thermalisation: it corresponds to the exchange of heat between the charge carriers and the lattice. In most cases, this reduces the energy of the carriers, hence making the electron move towards the minimum energy level in the conduction band E_C and the hole towards the maximum energy level in the valence band E_V (since this decreases the energy of electrons in the valence band). Still, note that thermalisation can also increase the energy of the carriers, making the electron-hole pair mean energy equal to $E_g + 3k_B T$ [Würfel & Würfel 2016] rather than E_g.

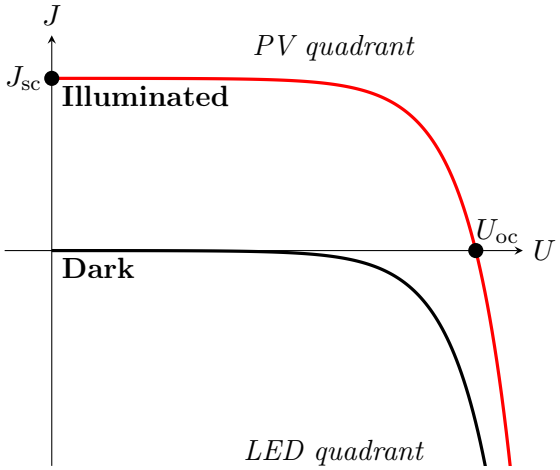

Figure 1.5: Current-voltage (I-V) characteristic of optoelectronic devices. In terms of sign convention, $U \cdot J > 0$ means that electrical power is produced.

1.1.3 Application to photovoltaics and electroluminescent cooling

These different phenomena form the basis of light-emitting diode (LED) and photovoltaic (PV) cell operation: we show in Figure 1.4 the principle of conversion of these two optoelectronic devices. Note that all the aforementioned processes occur for both components - we only show here the ones which allow the required conversion.

- An LED (Figure 1.4a) emits electroluminescent radiation above E_g thanks to the radiative recombination of electron-hole pairs supplied by an external circuit with a voltage bias U;
- a PV cell (Figure 1.4b) produces electrical power from the collection of electron-hole pairs generated by the absorption of photons with energy $\hbar\omega \geq E_g$.

From this description, it is clear that the photovoltaic cell is a radiative heat engine as it is able to convert radiation (which should come from a heat source for the net photon flux coming on the PV cell to be positive) into electricity, the remaining energy being lost as heat given to the lattice and ultimately to the environment. Since an LED can be understood as a PV cell working in the opposite fashion, it means that an LED can ideally be the opposite of a heat engine, hence a heat pump: it is able to pump heat from the lattice to emit electroluminescent radiation. The heat flux emitted exceeding the thermal radiation coming from the environment, this allows the LED and its surroundings to cool down: this phenomenon is called *electroluminescent cooling*. However, contrary to the PV cell, the LED is capable of working as a heat pump only if it is efficient enough: if part of the supplied electrical energy is lost into heat, less heat is pumped from the lattice, up to the point where the LED must reject heat to operate properly and does therefore not work as a heat pump any more.

The electrical behaviour of LEDs and PV cells is characterised by current-voltage (I-V) curves, which are strongly related to the different physical phenomena discussed above. Typical I-V characteristics are shown in Figure 1.5. At ambient temperature, no net radiation is observed for zero applied voltage and current is equal to zero: the device is at equilibrium. By increasing the applied voltage, both radiative and non-radiative recombination rates increase, making the power consumption rise along with the intensity of the emitted electroluminescent radiation ("Dark I-V"): this is typically the behaviour of an LED used for lighting applications. If the device is illuminated, electron-hole pairs are generated and a current consequently rises at zero

voltage, named short-circuit current J_{sc}. A non-zero voltage is then required to convert part of the incoming radiation into electricity as $P = U \cdot J$ ("Illuminated I-V"), which corresponds to PV operation. Similarly to the LED, the recombination rate increases in the same time, such that the current goes to zero for a given voltage called open-circuit voltage U_{oc}. For voltages larger than U_{oc}, the PV cell consumes electrical power and emits electroluminescent radiation, thus working as an LED. These different notions (I-V curve, J_{sc}, U_{oc}) will be regularly used throughout the manuscript.

One may have noticed that the band structure shown in Figure 1.4 is more complex than the one given in Figure 1.3. This is because using semiconductors for optoelectronic applications requires asymmetry: indeed, a homogeneous semiconductor cannot operate as an LED or a PV cell[2]. To illustrate this, imagine such a semiconductor with perfect (i.e. ohmic) electrical contacts at room temperature. If a difference of potential is applied at its contacts, a homogeneous electric field will rise. This makes electrons and holes move in opposite directions, but their local charge carrier densities remain constant, the carriers circulating through the layer at a steady rate. While the electrochemical potentials of electrons and holes vary spatially due to the field, they are locally opposite to each other. Thus the chemical potential of radiation, which is the sum of the carrier electrochemical potentials, is zero. The emitted radiation is therefore thermal, making this device unsuitable for LED applications. Similarly, if the semiconductor is illuminated, electrons and holes are generated but have the same probability to go to any of the two electrical contacts. Electron and hole currents cancel each other out and the short-circuit current is thus zero: such a device cannot properly operate as a PV cell.

In order to obtain a good conversion of charge carrier electrochemical potential into electrical energy (and vice-versa), it is therefore necessary to make the preferable paths of electrons and holes in the device opposite. This can be done by joining together semiconductors with different conductivities for electrons and holes. The conductivity is generally adjusted through the doping of semiconductors with impurity atoms, which allows to locally control the charge carrier density and hence the related conductivity. If the impurity atom can easily release electrons in the conduction band, the doped material is said to be n-doped; if conversely the atom can easily capture electrons from the valence band and create holes there, the material is p-doped. The study of semiconductor junctions will be performed in Part II of the manuscript, and will therefore be further described in Chapter 4 (see Section 4.1).

1.1.4 Thermophotonics

We now have all the building blocks to define thermophotonics. But the first question we should answer is: what is the motivation for developing such a device?

To do so, it is important to have in mind what thermophotovoltaics (TPV) is and what its limitations are. In contrast to solar photovoltaics, the radiation received by the PV cell is no longer emitted by the Sun, but rather by a hot emitter in TPV. This gives numerous advantages, among which:

- the radiation emitted by the PV cell, instead of being lost towards the sky, can be reabsorbed by the emitter and thus recycled, increasing the efficiency;
- the radiation comes from a much larger solid angle, thus increasing the power generation (see [Hirst & Ekins-Daukes 2011]);

[2] To be comprehensive, it can in fact function as an optoelectronic device, but requires then the asymmetry to be provided by the electrical contacts. This solution will not be considered here.

- the emitter can be designed as desired to tailor the emission spectrum; this allows transferring only above-bandgap radiation (being the only one useful for optoelectronic conversion) from the hot emitter to the PV cell.

Another strong advantage is that TPV devices can theoretically be used as a heat engine for any application, not only for solar energy conversion as with PV. While the heat source should be radiating towards the cell in PV, it can exchange heat in any form (conduction, convection, radiation) with the TPV emitter, which then converts this heat into radiation. In its recent industrial developments, TPV was for instance studied for large-scale electricity storage [Antora Energy 2023, Thermophoton 2023] or for mobile power generation [Mesodyne 2023] (see Section 1.3.2 for more details).

In all these applications however, the emitter must be kept at high temperature, usually above 1000 °C. There are two reasons for that. First, as the emitter temperature decreases, the peak wavelength of emission move towards mid-infrared: it then becomes more difficult to find semiconductors with adequate bandgap (which should remain close to the peak of emission to maximise the power generation [Shockley & Queisser 1961]) and good properties for photovoltaic conversion. Second, the PV cell power output is bounded by the incoming radiation, thus by Planck's law in the case of propagating radiation. Because thermal emission quickly increases with temperature ($\propto T^4$ for a blackbody), the output power is small at low emitter temperature. Consequently, TPV is not appropriate for moderate heat source temperature, e.g. for low-grade heat recovery. In order to make an optoelectronic device suitable for energy harvesting, it is therefore recommended to ensure that the emitter emission:

- exceeds Planck's law of radiation;
- is in the visible or near-infrared independently of its temperature, as bandgaps of most efficient semiconductors for PV conversion lie in this spectral region.

This perfectly fits the emission of an LED, which can largely exceed thermal radiation and be spectrally close to its bandgap thanks to electroluminescence. Having as the system emitter an LED with a bandgap close to that of the PV cell could therefore allow the PV cell to convert the radiation very efficiently. Since an LED consumes electrical power to emit electroluminescent radiation, a fraction of the electrical power generated by the PV cell should be redirected towards the LED. Such a device is called a thermophotonics (TPX) heat engine; it is represented in Figure 1.6. Even if we restrict our study to the analysis of the heat engine configuration in the frame of this manuscript, note that it can also work as a heat pump, the LED pumping the heat from the heat sink towards the PV cell and the heat source.

Often, one thinks that the LED should consume more electrical power than what produces the PV cell, preventing the device to produce electrical power. Such reasoning forgets that the LED pumps energy from the heat source: therefore, the LED can consume *in total* more energy, but *electrically* less, than what is produced by the PV cell. Its wall-plug efficiency, defined as the ratio of the radiation emitted and the electrical power consumed and written as η_{LED} in the following, can thus be greater than 1[3]. In fact, we can easily give a condition on η_{LED} to ensure that the thermophotonic engine generates power. Defining respectively P_{LED} and P_{PV} as the electrical power consumed by the LED and produced by the PV cell, q as the radiation exchanged between

[3]Note that in a TPX heat engine, the LED does not operate as a heat pump as it pumps heat from the hot side to the cold side. Still, because an LED is fundamentally a heat pump, it can function as an emitter with above-unity efficiency.

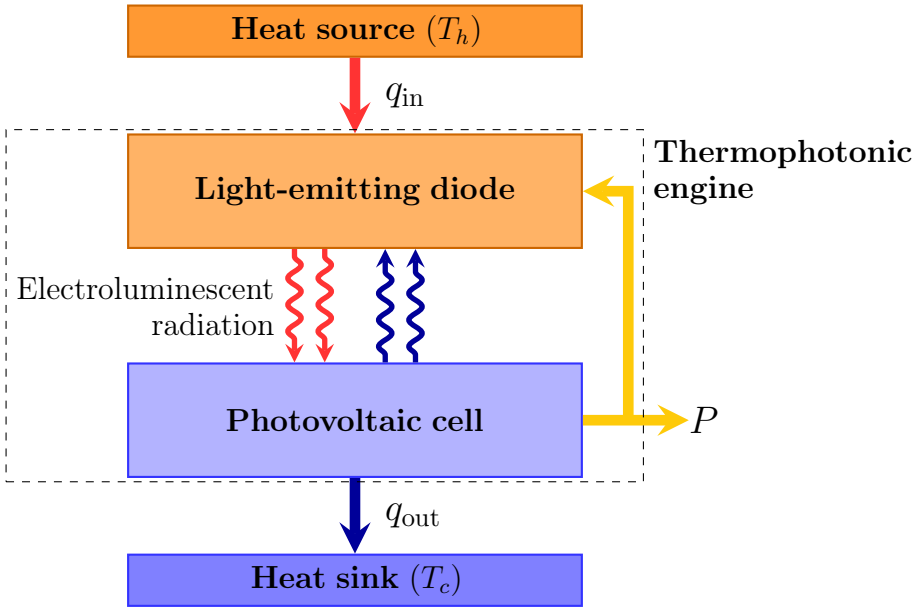

Figure 1.6: Representation of the thermophotonic heat engine.

the LED and the PV cell, and $\eta_{\text{PV}} = P_{\text{PV}}/q$ as the PV cell efficiency, we get

$$P \geq 0 \Leftrightarrow P_{\text{PV}} \geq P_{\text{LED}} \Leftrightarrow \frac{P_{\text{PV}}}{q}\frac{q}{P_{\text{LED}}} \geq 1 \Leftrightarrow \eta_{\text{LED}}\eta_{\text{PV}} \geq 1. \tag{1.8}$$

The most important challenge for the development of thermophotonic devices lies on the LED side. In TPV, the emitter is passive, which facilitates its assembly in complete devices and makes it doable to achieve good thermal stability. An LED, on the other hand, is connected to an external circuit and is generally composed of many layers to make it as efficient as possible. The increase of temperature can deteriorate the quality of the different contacts (e.g. because of thermal expansion mismatch) - even melt some materials if the temperature is really high. It can also cause the inter-diffusion of atoms between layers, reducing the purity of the LED and thus its efficiency. Even apart from its deterioration, the main physical properties of an LED change with temperature, making its performance vary. These different issues are the main reasons no experimental proof-of-concept has been elaborated to this date, the development of LED capable of electroluminescent cooling being already challenging at room temperature. More information on the impact of temperature can be found in the review by [Vaillon *et al.* 2020] for PV cells; in general, it has been sparsely studied above 100 °C as most of PV and LED applications are around room temperature.

For all these reasons, TPX heat engines can only be considered for moderate heat source temperature, most probably for low- to medium-grade energy harvesting applications, which include [Forman *et al.* 2016, ADEME 2017]

- industrial processes occurring for instance in food-processing industry, chemical industry or metallurgy, and in which large quantities of heat are available from various effluents (coolants, hot air, fumes) or directly from hot machines and equipments;
- data centres;
- personal equipment, from electronic equipments (phones, computers) to vehicles.

Quantitatively, the heat source temperature should most probably remain below 400 °C to avoid the aforementioned issues, this temperature being close to the maximum considered in the experiments gathered in [Vaillon *et al.* 2020] for PV cells. In most of the manuscript, the calculations will be performed for a temperature of 600 K (327 °C). While this may already be challenging to realise, it will give an idea of the best possible power output and efficiency that could be achieved by this device, these quantities increasing with the temperature difference. It will also facilitate comparison with literature, in which this temperature has been largely favoured [Zhao *et al.* 2018, McSherry *et al.* 2019, Zhao *et al.* 2019, Yang *et al.* 2022].

Lastly, we would like to discuss the question of the figure of merit of thermophotonic devices. The two most evident figures of merit are the maximum power and the maximum efficiency; in general, the operating point lies between these two, as the power at maximum efficiency is zero for irreversible engines. But in our specific case, the heat coming from the source is waste heat and is thus free. This basically means that efficiency is secondary, as long as heat is available in quantity. To illustrate this, imagine that 100 W of heat are available; then, it is preferable to recover 10 W from the whole 100 W (10% efficiency) than to recover 1 W from the use of 2 W of heat (50% efficiency), because these 100 W would be there anyway. This has been nicely discussed in [De Vos 1992]. Consequently, the power (and the related efficiency at maximum power) will be the main figure of merit of the thermophotonic heat engine.

1.2 Extension to near field

The use of an electroluminescent emitter is one solution, but not the only one, that can allow exceeding Planck's law. It has in fact been more common to do it by making use of *near-field radiation*. This section will focus on the physical ground of such radiation, the numerical methods used to compute it, along with its interest for TPV and TPX heat engines.

1.2.1 Physics of near-field radiation

Up to now, when mentioning radiation, we were in fact talking about *propagating* radiation, i.e. photons capable of travelling infinitely far in non-absorptive media. Planck's law typically correspond to the upper bound of emission of propagating radiation. If this holds perfectly for most everyday applications, it breaks down when the distance separating the two bodies exchanging radiation comes close to the characteristic wavelength λ of this radiation[4]. We review here how such distance modifies the radiation.

If the distance is much larger than λ, the amplitude of radiation emitted by a surface - which is exclusively propagating - remains constant. This corresponds to the usual macroscopic radiation, called *far-field* radiation. The first effects that arise from diminishing the distance are coherence effects such as interferences. As the distance varies, waves successively show constructive and destructive interferences and the energy carried by radiation thus oscillates. Such effects are caused by propagating waves; consequently, the heat flux remains bounded by Planck's law.

If the distance is further decreased, we reach the *near field* (NF) where *evanescent waves* come into play along with propagating waves. Such waves are localised at an interface and exhibit an exponentially decaying amplitude in the direction perpendicular to the interface, with a decay length of the order of λ. Generally, an evanescent wave carries no energy in the direction perpendicular to the surface (in average). But if an absorber is placed at a distance lower than

[4]This also happens when the size of the bodies are of the order of λ, but this will not be discussed here.

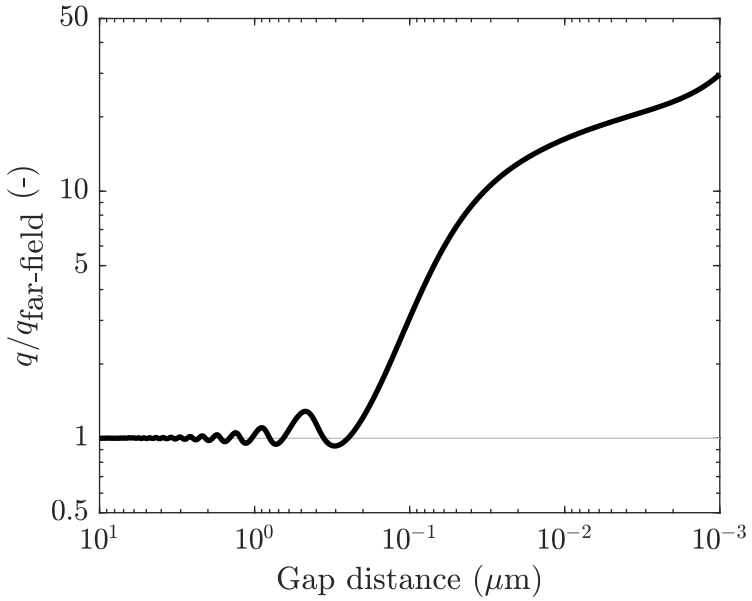

Figure 1.7: Typical variation of the heat flux with the gap distance, given with respect to the far-field value.

the decay length from the emitter, the evanescent wave will reflect or transmit across this second interface. The coupled standing wave, comprised of the original wave and its reflection, is capable to transfer energy from the emitter to the absorber (see e.g. [Tervo *et al.* 2018]). This new channel of energy transmission causes an increase of the radiative heat transfer in the near field as the distance decreases (as shown for example in Figure 1.7); for devices such as TPV and TPX, this allows to generate more electrical power.

Evanescent waves are generally subdivided into two different modes:

- *frustrated modes*, when the field is evanescent on one side of an interface and propagating on the other side;
- *surface modes*, when the field is evanescent on both sides of the interface.

These different modes of radiation are shown in Figure 1.8, considering an interface between vacuum and a body with higher refractive index. Physically, frustrated modes arise from the total internal reflection of propagating waves inside the body. Geometrical optics tells us that radiation coming from a high-refractive-index material onto an interface should undergo total internal reflection if its incidence angle is larger than the critical angle θ_c; in reality, evanescent waves should exist on the vacuum side to satisfy Maxwell equations. Regarding surface modes (also called surface waves), they are the consequence of the strong coupling of light with surface mechanical oscillations, under the form of quasi-particles called polaritons. Such couplings occur around the frequency of the mechanical oscillations, which can be caused by phonons in polar or dielectric materials (we then have surface phonon polaritons), or by the plasma formed by free electrons in metals or highly-doped semiconductors (surface plasmon polaritons).

The way to properly handle the contributions of such polaritons (or of electron-hole pair recombinations) to the near-field radiative heat transfer will be discussed in Section 1.2.3; we present first the basics of the model used to obtain the near-field radiative heat transfer.

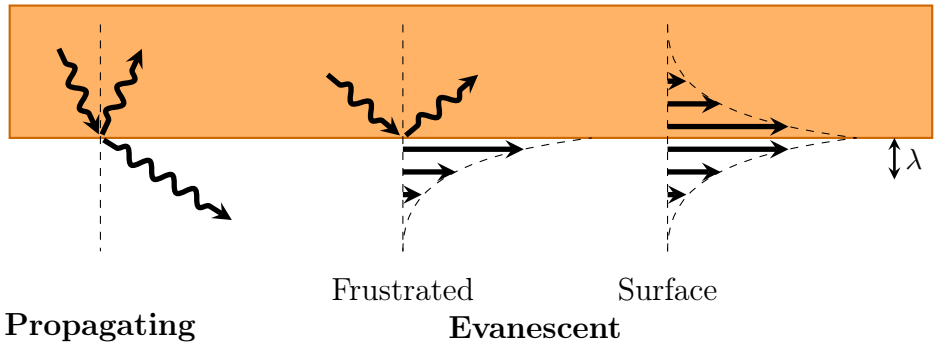

Figure 1.8: Radiation modes occurring around an interface between vacuum and a body with higher refractive index.

1.2.2 Model for the simulation of near-field radiation

Throughout this manuscript, near-field radiative heat transfer will be computed for 1D multilayered structures (shown in Figure 1.9), using the fluctuational electrodynamics framework first developed in [Rytov 1959] and applied in [Polder & Van Hove 1971] for thermal radiation. It is based on the simultaneous resolution of Maxwell's equations and fluctuation-dissipation theorem. The precise numerical method considered is presented in [Francoeur *et al.* 2009], and was extensively used and described in literature (see for instance [Blandre 2016]); for this reason, its description will be kept relatively short here. Fundamentally, the heat flux carried by radiation in the direction z (perpendicular to the interfaces) corresponds to the z-component of the time-averaged Poynting vector:

$$q_\omega(z) = \langle S_z(\omega, z)\rangle = 2\mathrm{Re}\big\{\langle \mathcal{E}_x \mathcal{H}_y^* - \mathcal{E}_y \mathcal{H}_x^*\rangle\big\}, \tag{1.9}$$

where $\boldsymbol{\mathcal{E}}$ is the electric field and $\boldsymbol{\mathcal{H}}^*$ is the complex conjugate of the magnetic field[5]. Such heat originates from the energy released by dipoles within the emitter: thermal agitation causes dipoles to move stochastically, making them generate an electromagnetic field and dissipate some of their energy. The fluctuation-dissipation theorem allows to express the time average of the spatial

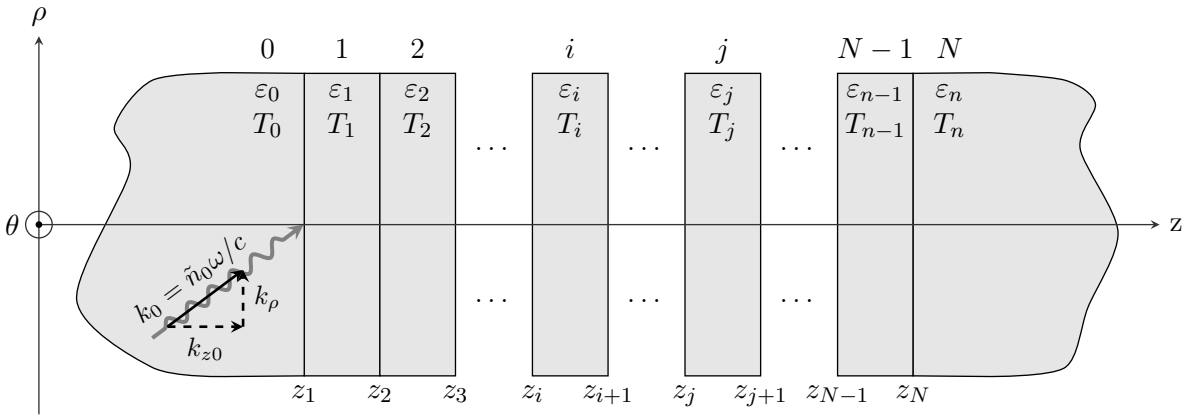

Figure 1.9: 1D multilayered structure considered in the simulation of near-field radiative heat transfer in the z direction. Schematic inspired by [Francoeur *et al.* 2009].

[5]The expression of the time-averaged Poynting vector provided here is four times larger than the commonly-known expression since only positive frequencies are considered [Zhang 2007].

correlation function of the stochastic current density $\boldsymbol{J}$ induced by the movement of dipoles:

$$\left\langle J_\alpha(\boldsymbol{r'},\omega)J_\beta(\boldsymbol{r''},\omega')\right\rangle = \frac{\varepsilon_\mathrm{v}\varepsilon''}{\pi}\omega\cdot\hbar\omega f_\mathrm{BE}(\omega,\mu,T)\delta(\boldsymbol{r'}-\boldsymbol{r''})\delta(\omega-\omega')\delta_{\alpha\beta}. \tag{1.10}$$

Here, α and β correspond to directions (x, y or z) and ε_v is the vacuum permittivity. ε'' is the imaginary part of the dielectric function of the material considered which quantifies the rate of energy dissipated by dipoles, thus the ability of a material to emit or absorb radiation. δ represents either the Dirac delta function or the Kroenecker delta; these δ mean that the fluctuations are correlated only locally (for $\boldsymbol{r'}=\boldsymbol{r''}$), for a common frequency ($\omega=\omega'$) and direction ($\alpha=\beta$). Last, we need to relate the current fluctuations at the point of emission $\boldsymbol{r'}$ to the electromagnetic field at any point $\boldsymbol{r}$; this can be done with dyadic Green's tensors $\bar{\bar{\boldsymbol{G}}}$:

$$\boldsymbol{\mathcal{E}}(\boldsymbol{r},\omega) = i\omega\mu_\mathrm{v}\int_V \bar{\bar{\boldsymbol{G}}}^{\mathcal{E}}(\boldsymbol{r},\boldsymbol{r'},\omega)\cdot\boldsymbol{J}(\boldsymbol{r'},\omega)d^3\mathbf{r'}, \tag{1.11a}$$

$$\boldsymbol{\mathcal{H}}(\boldsymbol{r},\omega) = \int_V \bar{\bar{\boldsymbol{G}}}^{\mathcal{H}}(\boldsymbol{r},\boldsymbol{r'},\omega)\cdot\boldsymbol{J}(\boldsymbol{r'},\omega)d^3\mathbf{r'}, \tag{1.11b}$$

μ_v being the permeability of vacuum. These four equations allow expressing the monochromatic heat flux as

$$\begin{aligned} q_\omega(z) =& \frac{2\varepsilon''(\omega)}{\pi}k_\mathrm{v}^2\hbar\omega f_\mathrm{BE}(\omega,\mu,T) \\ &\cdot \mathrm{Re}\left\{ i\int_V \left[G^{\mathcal{E}}_{x\alpha}(z,\boldsymbol{r'},\omega)G^{\mathcal{H}^*}_{y\alpha}(z,\boldsymbol{r'},\omega) - G^{\mathcal{E}}_{y\alpha}(z,\boldsymbol{r'},\omega)G^{\mathcal{H}^*}_{x\alpha}(z,\boldsymbol{r'},\omega)\right] d^3\mathbf{r'}\right\}, \end{aligned} \tag{1.12}$$

where $k_\mathrm{v}=\omega/c=\omega\sqrt{\varepsilon_\mathrm{v}\mu_\mathrm{v}}$ is the angular wavenumber of radiation in vacuum, z is the position where the heat flux is estimated and $\boldsymbol{r'}$ corresponds to one point of emission inside the emitting volume V. Einstein summation convention has been used for the product of the Green's tensor components. These components are the only remaining unknowns; since the system studied is one-dimensional, it is convenient to decompose Green's tensors in terms of plane waves, through a two-dimensional Fourier transform:

$$\bar{\bar{\boldsymbol{G}}}(z,\boldsymbol{r'},\omega) = \frac{1}{(2\pi)^2}\int_{-\infty}^{+\infty}\bar{\bar{\boldsymbol{g}}}(\boldsymbol{k}_\rho,z,z',\omega)e^{i\boldsymbol{k}_\rho(\boldsymbol{R}-\boldsymbol{R'})}d\boldsymbol{k}_\rho. \tag{1.13}$$

$\hat{\boldsymbol{x}}$ and $\hat{\boldsymbol{y}}$ being unit vectors, $R=x\hat{\boldsymbol{x}}+y\hat{\boldsymbol{y}}$ the in-plane position and $\bar{\bar{\boldsymbol{g}}}$ the Weyl representation of Green's tensor. It is a function of the in-plane (also called parallel) component of the wavevector $\boldsymbol{k}_\rho = k_x\hat{\boldsymbol{x}}+k_y\hat{\boldsymbol{y}}$ (see Figure 1.9), which is always real and remains constant for a given electromagnetic wave moving from one material to another. This quantity is directly related to the radiation mode: in a medium whose real part of the refractive index is n, $k_\rho \leq nk_\mathrm{v}$ means that radiation is propagating, $k_\rho > nk_\mathrm{v}$ that it is evanescent. In the case of propagating radiation, we in fact have $k_\rho = n\sin(\theta)k_\mathrm{v}$ (which must remain constant between materials due to Snell-Descartes law).

The next steps required to derive the complete expression of q_ω are the following:

1. switch to polar coordinates to simplify the expression, since the system is symmetric around the z-axis;
2. express the components of the Weyl representation of Green's tensors in terms of forward and backward travelling waves using Sipe's formalism [Sipe 1987] (developed analytically for simple cases in [Mulet 2004]);

3. express the spatial variation of amplitude of such waves as a function of the reflection at the interfaces and absorption in the different layers, using the scattering-matrix method.

These steps being not of primary importance for the understanding of the work presented in this manuscript, they are not developed here but rather in Appendix A; note that some corrections were made compared to the method presented in [Francoeur *et al.* 2009] regarding the emission location. Eventually, it allows obtaining an expression of $q_\omega(z)$ along with the related spectral photon flux density $\dot{N}_\omega(z)$ in the form of

$$\dot{N}_\omega(z) = \frac{1}{4\pi^2} f_{\mathrm{BE}}(\omega,\mu,T) \int_0^{+\infty} \mathcal{T}(\omega,k_\rho,z) k_\rho dk_\rho, \tag{1.14a}$$

$$q_\omega(z) = \hbar\omega \dot{N}_\omega(z). \tag{1.14b}$$

$\mathcal{T}(\omega,k_\rho,z)$ is the total transmission coefficient between the emitter and the point z, obtained from integration over the thickness of the emitter. It varies between 0 (no transmission) and 2 (complete transmission), being equal to the sum of the transmission coefficients for both transverse electric (TE) and transverse magnetic (TM) polarisations of light (ranging between 0 and 1). These expressions only give the flux received at one *point* from one *body*; if one rather wants the net heat flux received in a layer j from a layer i (which will be extensively used in the frame of this manuscript), it is expressed as

$$q_{\omega,ij} = \frac{\hbar\omega}{4\pi^2}(f_{\mathrm{BE},i} - f_{\mathrm{BE},j}) \int_0^{+\infty} \mathcal{T}_{ij}(\omega,k_\rho) k_\rho dk_\rho = \hbar\omega(f_{\mathrm{BE},i} - f_{\mathrm{BE},j})\mathcal{F}_{ij}(\omega). \tag{1.15}$$

$\mathcal{T}_{ij}(\omega,k_\rho)$ is the slab-slab transmission coefficient and $\mathcal{F}_{ij}$ is the related transmission function. The notation $f_{\mathrm{BE},i} = f_{\mathrm{BE}}(\omega,\mu_i,T_i)$ has been used for brevity. Considering that i is the emitting layer, $\mathcal{T}_{ij}$ can be computed as $\mathcal{T}(\omega,k_\rho,z_j) - \mathcal{T}(\omega,k_\rho,z_{j+1})$: what is absorbed by slab j is simply the difference between the incoming and outgoing radiation. Of course, the transmission coefficient should be reciprocal, and should therefore be unchanged if the layer j is considered to be emitting instead: $\mathcal{T}_{ij}(\omega,k_\rho) = \mathcal{T}_{ji}(\omega,k_\rho)$.

We should mention that this model is subject to numerical instabilities due to the bulk absorption term $\exp(-k''_{zi}\Delta z)$, where k''_{zi} is the imaginary part of the out-of-plane component of the wavevector in layer i[6]; this was already discussed in [Francoeur *et al.* 2009]. For large k''_{zi} - typically reached for surface waves - the exponential term can become tiny and cause numerical errors in calculations. Even worse, it could go strictly to zero if $k''_{zi}\Delta z$ is too large. Of course, it is $k''_{zi}\Delta z$, rather than k''_{zi} only, which impacts the value of the exponential; if these instabilities do not occur for thin layers, one should be cautious when considering thick layers (of the order of several micrometres for absorptive media). This is especially true for the emitter layer.

One way to circumvent such issues is to use analytical solutions when available; this will be done in particular in Chapter 3, where we will consider semi-infinite LED and PV cell separated by a vacuum gap. In this case, the transmission coefficient of γ-polarised radiation (either TM or TE) between the two semi-infinite media, denoted with indices 0 and 2, is [Mulet *et al.* 2002]

$$\mathcal{T}^\gamma_{02}(\omega,k_\rho) = \begin{cases} \dfrac{(1-|r^\gamma_{10}|^2)(1-|r^\gamma_{12}|^2)}{|1-r^\gamma_{10}r^\gamma_{12}e^{-2k'_{z1}d}|^2} & \text{if } k_\rho \le k_0, \\ 4e^{-2k''_{z1}d}\dfrac{\mathrm{Im}(r^\gamma_{10})\mathrm{Im}(r^\gamma_{12})}{|1-r^\gamma_{10}r^\gamma_{12}e^{-2k''_{z1}d}|^2} & \text{if } k_\rho > k_0. \end{cases} \tag{1.16}$$

[6] Since the angular wavenumber in a medium of complex refractive index $\tilde{n}$ is $\tilde{n}k_\mathrm{v}$, $k_{zi} = \sqrt{\tilde{n}^2k_\mathrm{v}^2 - k_\rho^2}$.

r_{ij} corresponds to the reflection coefficient at the interface between layers i and j, while k'_{zi} is the real part of k_{zi}. In this case, index 1 denotes vacuum.

In the end, the only material property on which the transmission coefficient depends on is the dielectric function ε of the different layers (related to the refractive index by $\varepsilon = \sqrt{\tilde{n}}$ for non-magnetic media), the reflection and transmission coefficients being functions of ε. This appears clearly in the analytical solution given above, but holds also in the more general case. It is thus essential to have precise expressions for the dielectric function.

1.2.3 Main contributions to the dielectric function

The phenomena impacting the behaviour of light in a material are various, and depends on the material considered. In a metal, the free electrons (in the form of plasmons, the quantum oscillation of plasma) are the particles with the largest impact, while it is optical phonons in a dielectric material. In a semiconductor, the recombination of electrons and holes (also called interband transitions) will affect the dielectric function, but plasmons and optical phonons can also play a role, depending on the charge carrier concentration and the polarity of the material. We will review these different contributions here. It has been shown in literature that such contributions could couple to one another [Kukharskii 1973]; still, we will neglect such coupling, allowing to study each contribution independently. We can then write the total dielectric function as

$$\varepsilon = \varepsilon_\infty + \tilde{\chi} = \varepsilon_\infty + \sum \tilde{\chi}_i \tag{1.17}$$

for each contribution i. ε_∞ is the high-frequency dielectric constant, i.e. the limit of ε as $\omega \to \infty$, and is the same whatever the number of contributions included. The effective susceptibility $\tilde{\chi}_i$, defined as $\tilde{\chi}_i = \varepsilon_i - \varepsilon_\infty$, therefore goes to zero as $\omega \to \infty$. If practical examples are to be given, aluminium gallium arsenide (AlGaAs) will be considered as this material will be regularly used in this manuscript.

1.2.3.1 Plasmonic contribution

As soon as free charge carriers are present in a medium, the formed plasma will contribute to radiative heat transfer. While we are mostly used to plasmas made of free electrons in metal, note that hole plasmas are also achievable in heavily p-doped semiconductors. The associated dielectric function is (see e.g. [Adachi 1994])

$$\varepsilon = \varepsilon_\infty \left(1 - \frac{\omega_\mathrm{p}^2}{\omega(\omega + i\Gamma)} \right). \tag{1.18}$$

ω_p is the plasmon frequency given by

$$\omega_\mathrm{p} = \sqrt{\frac{Ne^2}{m^* \varepsilon_\infty \varepsilon_0}}, \tag{1.19}$$

N being the charge carrier density (which will be approximated by the doping concentration for semiconductors), e the elementary charge and m^* the effective mass of the charge carriers (whose physical meaning is thoroughly explained in classical textbooks on PV, see e.g. [Nelson 2003, Würfel & Würfel 2016, Kitai 2018]). Last, Γ is the damping coefficient expressed as (see e.g. [Losego *et al.* 2009])

$$\Gamma = \frac{e}{m^* \mu}, \tag{1.20}$$

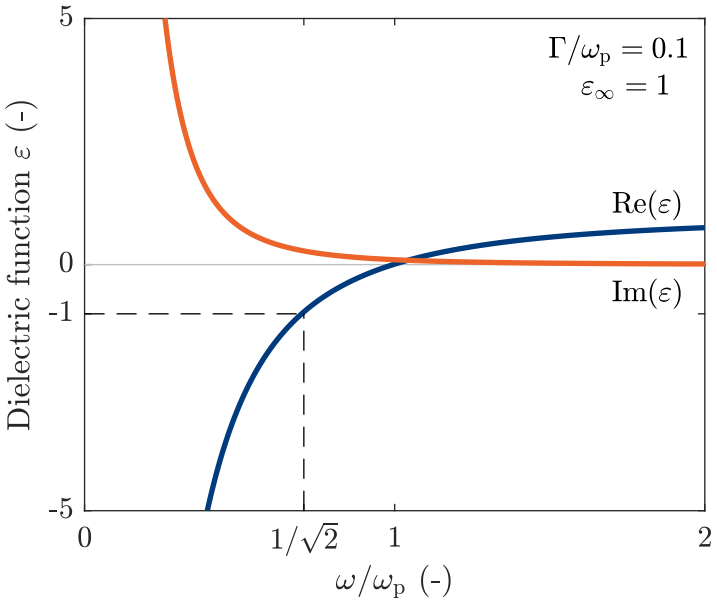

Figure 1.10: Typical dielectric function obtained with a Drude model for the plasmonic contribution.

μ being the mobility of the charge carrier, which links the velocity of charge carriers to the electric field magnitude and is directly related to the conductivity σ through $\sigma = eN\mu$. We show in Figure 1.10 a typical dielectric function obtained with this model (called Drude model) with arbitrarily chosen values for the different parameters. Clearly, plasmons impact the behaviour of radiation only around and below the plasmon frequency, ε going quickly to ε_∞ for frequencies larger than ω_p. Considering non-magnetic materials, the condition of resonance of the surface plasmon polariton (SPP) between layers 1 and 2 is $\varepsilon_1 + \varepsilon_2 = 0$. For an interface with vacuum, it is equivalent to $\varepsilon = -1$ which is reached for $\omega_{SPP} = \omega_p/\sqrt{1 + 1/\varepsilon_\infty}$ (considering $\varepsilon'' = 0$). This means one can expect significant radiative heat transfer in the near field around this frequency, which increases as the square root of N.

1.2.3.2 Phononic contribution

The contribution of optical phonons is generally modelled with a damped Lorentz oscillator:

$$\varepsilon = \varepsilon_\infty \left(1 + \frac{\omega_{LO}^2 - \omega_{TO}^2}{\omega_{TO}^2 - \omega^2 - i\omega\gamma}\right), \tag{1.21}$$

where ω_{LO} and ω_{TO} are respectively the longitudinal-optical (LO) and transverse-optical (TO) phonon frequencies, and γ is the damping coefficient. An example of dielectric function obtained with such Lorentzian oscillator is shown in Figure 1.11. The resonance condition of the surface phonon polariton (SPhP) is the same as for the SPP ($\varepsilon = -1$ for an interface with vacuum). Notice how the real part of ε equals -1 twice; SPhP resonance however occurs when the imaginary part is close to 0, and the resonance frequency at a vacuum interface is therefore $\omega_{SPhP} = \sqrt{(\varepsilon_\infty \omega_{LO}^2 + \omega_{TO}^2)/(\varepsilon_\infty + 1)}$.

As mentioned previously, optical phonons will contribute to the dielectric function only for dielectrics and polar materials such as III-V semiconductors (semiconductors made of group III and group V elements, GaAs for instance): the related increase of the near-field radiative

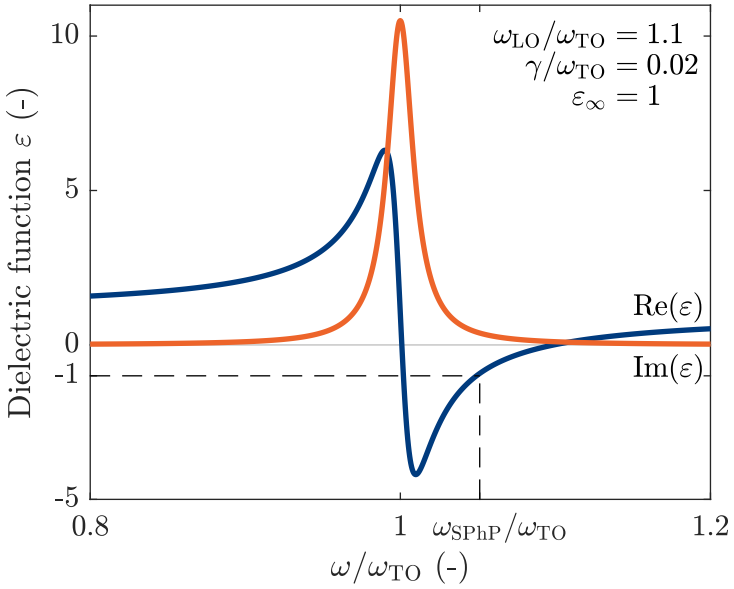

Figure 1.11: Typical dielectric function obtained with a Lorentz oscillator for the optical phonon contribution.

heat transfer due to SPhP can therefore only be observed in such materials. When several polar materials are alloyed (such as AlAs and GaAs into AlGaAs), the resulting material generally supports the optical phonons of each of the base components and one Lorentz oscillator should be considered for each, these oscillators being coupled to each other.

1.2.3.3 Electron-hole contribution

Properly taking into account the contribution of interband transitions for semiconductors is a bit more complex. In Section 1.1, we have discussed the bandgap energy, which represents the smallest energy required to go from the valence band to the conduction band. However, there are several extrema in these bands (for varying wavevectors): E_g represents the fundamental transition energy, but not the sole, and each of these transition energies will contribute differently to the dielectric function.

Since most of the radiation is generally emitted/absorbed close to E_g, a first-hand approximation is to consider only the contribution of this fundamental transition. This has been done for instance in [Lin *et al.* 2018] with the following expression:

$$\varepsilon = \begin{cases} B + \dfrac{A}{x^2}(2 - \sqrt{1+x} - \sqrt{1-x}) & \text{if } x < 0 \\ B + \dfrac{A}{x^2}(2 - \sqrt{1+x}) + i \cdot \dfrac{A}{x^2}\sqrt{x-1} & \text{if } x \geq 0, \end{cases} \tag{1.22}$$

with $x = \hbar\omega/E_g$ (A and B being two parameters). Such an expression can be obtained from Fermi's golden rule and Kramers-Kronig relations. In our case, we will work with a broader model based on the work of Adachi [Adachi 1987], in which similar expressions are derived for up to six different transitions and combined to obtain the complete interband contribution, which involves about ten different fitting parameters. The exact model used is the one given in [Gonzalez-Cuevas *et al.* 2007]; the resulting dielectric function for GaAs is given in Figure 1.12. We only show here the variations on the first eV since most of the transitions happen there, but the impact of

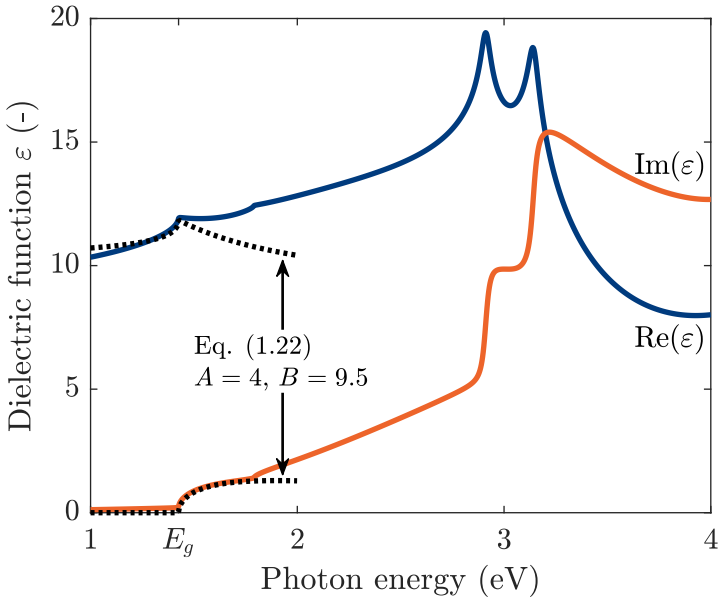

Figure 1.12: Dielectric function obtained for GaAs at room temperature with the model and parameters given in [Gonzalez-Cuevas *et al.* 2007].

interband transitions continues for larger photon energy. In comparison, simple models such as the one presented above can only depict accurately the dielectric function on the first tenths of eV above E_g.

1.2.3.4 Note on the accuracy and availability of data

As we will discuss at the beginning of Chapter 3, the devices considered throughout this work will be made of III-V (hence polar) semiconductors, and all three contributions mentioned above should be taken into account. The different material properties required to obtain the complete dielectric function are given in Appendix B.

Ideally, we would like to have properties with dependency on temperature (since the LED is at high temperature) and alloy composition when applicable. In reality, such data are seldom available. Most of them are given at room temperature only (e.g. in [Adachi 1989]), and the only alloy fractions studied are generally those allowing lattice-matching with pure III-V semiconductors (e.g. $In_{0.49}Ga_{0.51}P$ lattice-matched with GaAs, $In_{0.53}Ga_{0.47}As$ lattice-matched with InP). For this reason, several material properties used for the LED were obtained at room temperature (e.g. effective masses, optical phonon frequencies) - we have tried as much as possible to limit this to quantities we don't expect to vary dramatically with temperature. Similarly, in Chapter 6, some alloy properties will be taken from well-studied alloy fractions even if those are not the ones considered (since the alloy fraction required to ensure lattice-matching changes with temperature); we suppose that the change in properties will remain moderate as a first-hand approximation.

Still, some temperature- and alloy-fraction-dependent data are available, for instance for the electron-hole contribution to the dielectric function in many III-V semiconductors [Gonzalez-Cuevas *et al.* 2007]. However, we would like to mention that this source is not perfect. We cite here some detected issues:

- the fit with experimental results has variable quality, e.g. in comparison to the fit obtained in [Adachi 1989] for binary components; it is (at least partially) caused by the large number

of cases covered, studying quaternary III-V with arbitrary composition and temperature;

- the real part of the dielectric function obtained for GaAs with their model is different in their Figure 3 and 5, which makes us question the way these results were obtained;
- the obtained dielectric function does not satisfy Kramers-Kronig relations (which is actually an issue shared with [Adachi 1989])[7].

Even with such issues we choose to use the data from [Gonzalez-Cuevas *et al.* 2007], simply because the loss of accuracy would be even worse if the variations with temperature and composition are not taken into account in any way.

The lack of data (sometimes associated to their limited precision) strongly limits how accurate the numerical results can be. To illustrate this, we can quickly analyse the sensitivity of the maximum power generation to the dielectric function. If we increase by 1[8] the dielectric function given in [Gonzalez-Cuevas *et al.* 2007], then the maximum power output obtained in Section 3.3.1.2 varies by 5%. This gives an order of magnitude of the uncertainty we can expect for the end results, which can only be reduced through the further experimental study of semiconductors for different temperatures and compositions.

1.2.4 Gap distance in near-field thermophotonic engines

As we have seen previously, the radiative heat transfer between the LED and the PV cell in a thermophotonic device depends on the thickness of the gap (supposed to be made of vacuum to prevent heat transfer through conduction) separating the two elements. This thickness, called gap distance in the following, is chosen to be equal to 10 nm. Such particularly low value allows to emphasise the potential of near-field radiation for power generation enhancements, and was for this reason regularly used for different near-field radiative heat engines [Blandre *et al.* 2017, Zhao *et al.* 2018, Callahan *et al.* 2021, Papadakis *et al.* 2021]. It is however very hard to reach experimentally: in the state-of-the-art of his thesis[9], Lucchesi [Lucchesi 2020] has shown that the lowest distance achieved with plane-plane experiment is around 25 nm, while most of them are performed above 100 nm. Therefore, we will also give some insights about the performance of near-field thermophotonic devices at larger gap distances.

1.3 State-of-the-art

Now that the basic principle and motivation of the near-field thermophotonic heat engine has been explained, we should review the work performed on such devices. It will be preceded by a state-of-the-art of related technologies for context, which are summarised in Figure 1.13.

[7] Kramers-Kronig equations give a direct relation between the real and imaginary part of the susceptibility $\chi = \varepsilon - 1$; to be physical, a dielectric function ε should be defined such that the related susceptibility satisfies these relations. Often, to help to fit experimental data, we rather expect $\varepsilon - \varepsilon_\infty$ to satisfy these relations (as in [Adachi 1989]). In [Gonzalez-Cuevas *et al.* 2007], it is directly ε which satisfies them, and it is not clear if ε_∞ is deliberately omitted or not.

[8] An absolute error of 1 on ε may seem large, but it is actually plausible and roughly corresponds to the difference that can be found between different models.

[9] A briefer version of it can be found in [Lucchesi *et al.* 2021b], although the figure relating the experiments with the achieved gap distance is not shown there.

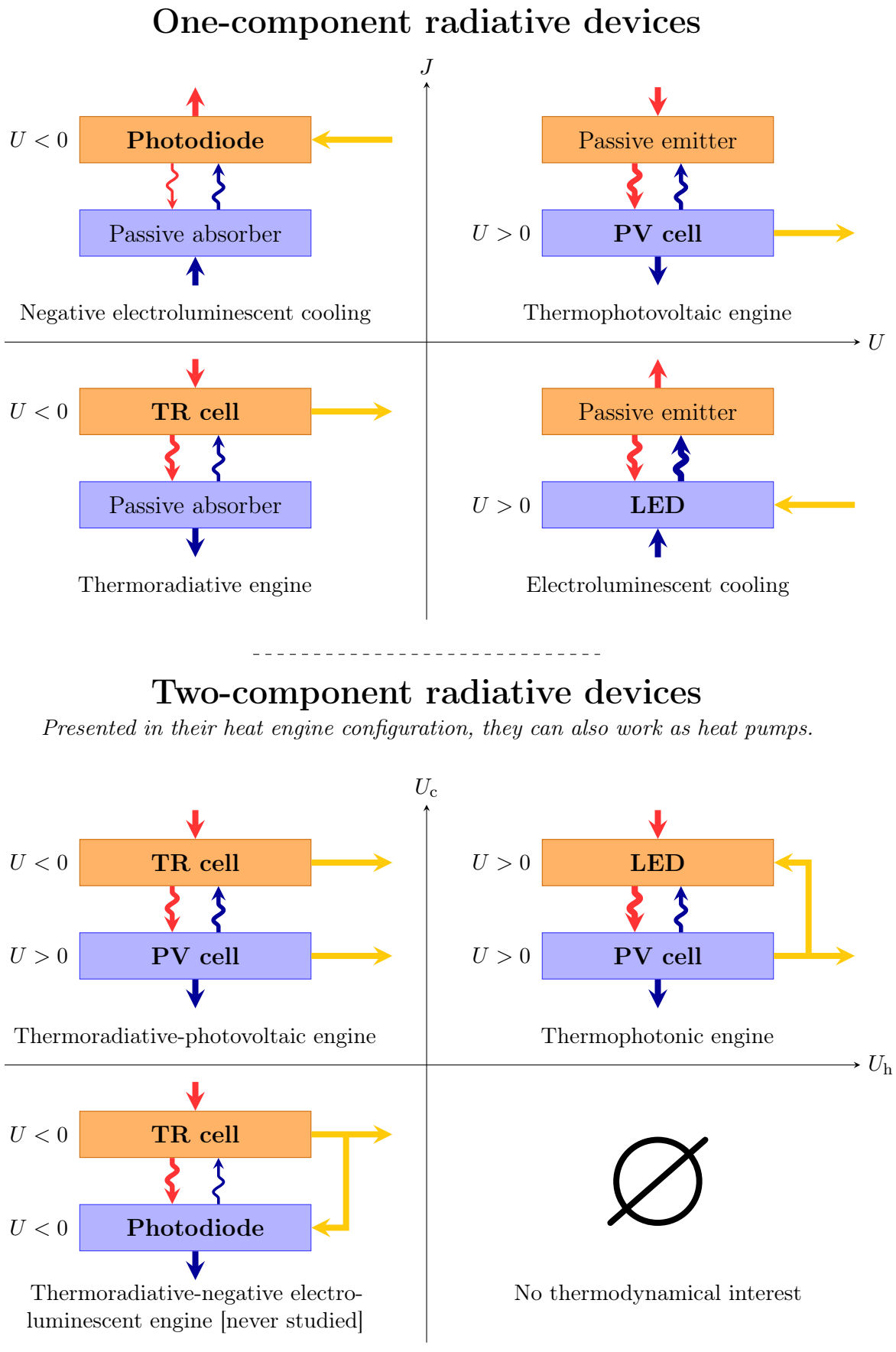

Figure 1.13: Review of radiative heat engines.

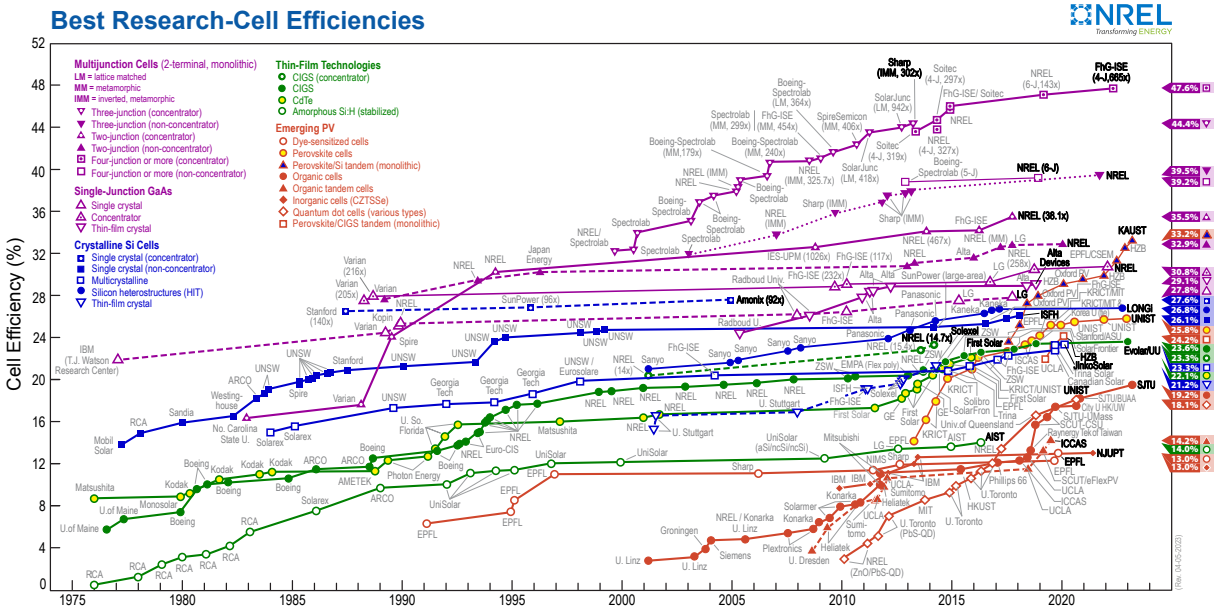

Figure 1.14: Best research-cell efficiency chart [NREL 2023].

1.3.1 Material for solar photovoltaics and other optoelectronic applications

We start this review with solar photovoltaics. While being relatively far from near-field thermophotonics in terms of operation and application, it is the domain with the most abundant literature. Monitoring of most efficient solar cells has been done since tens of years, e.g. in [Green *et al.* 2023] or in [NREL 2023]; the data gathered in the latter are given in Figure 1.14. As shown there, III-V-based junctions offer the best performance with efficiencies around 29% for GaAs single-junctions and above 40% for multijunctions. In comparison, monocrystalline silicon can achieve 26% efficiency, whereas polycrystalline silicon can only reach 23% efficiency.

But for terrestrial applications, cost - rather than efficiency - is generally the main metric of solar cells. While having the lowest efficiency, polycrystalline silicon solar cells represent a large majority of the installed power [IEA 2022], due to a historically much lower cost per unit electrical power. Nowadays, new solar cells are generally made of monocrystalline silicon, mainly because they are now cost-competitive with polycristalline ones. III-V-based solar cells, even with their higher efficiency, are almost never used due to their prohibitive cost per unit power which is more than two orders of magnitude larger than that of silicon cells [Horowitz *et al.* 2018]. They are consequently limited to applications where high efficiency is required (e.g. space applications).

Another important parameter for solar cells, although insufficiently considered, is the scarcity of raw materials and their subsequent supply risk. Apart from its impact on the cost, it is essential to take into account the criticality of materials per se: availability is key to ensure that a technology can be developed at a large scale and in the long term. We show in Figure 1.15 the supply risk and economic importance of most commonly used elements obtained from [European Commission *et al.* 2023], with a focus on the materials used in optoelectronic applications. It makes clear that III-V cells (based on gallium, arsenic, indium or aluminium for instance) could face a shortage in the coming years at the current rate of material consumption. Apart from semiconductors specifically, other elements used in optoelectronics - such as boron for doping, or silver for metallic contacts and mirrors - are already critical or close to becoming so. The long-term use of materials providing the best performance will therefore require finding ways to

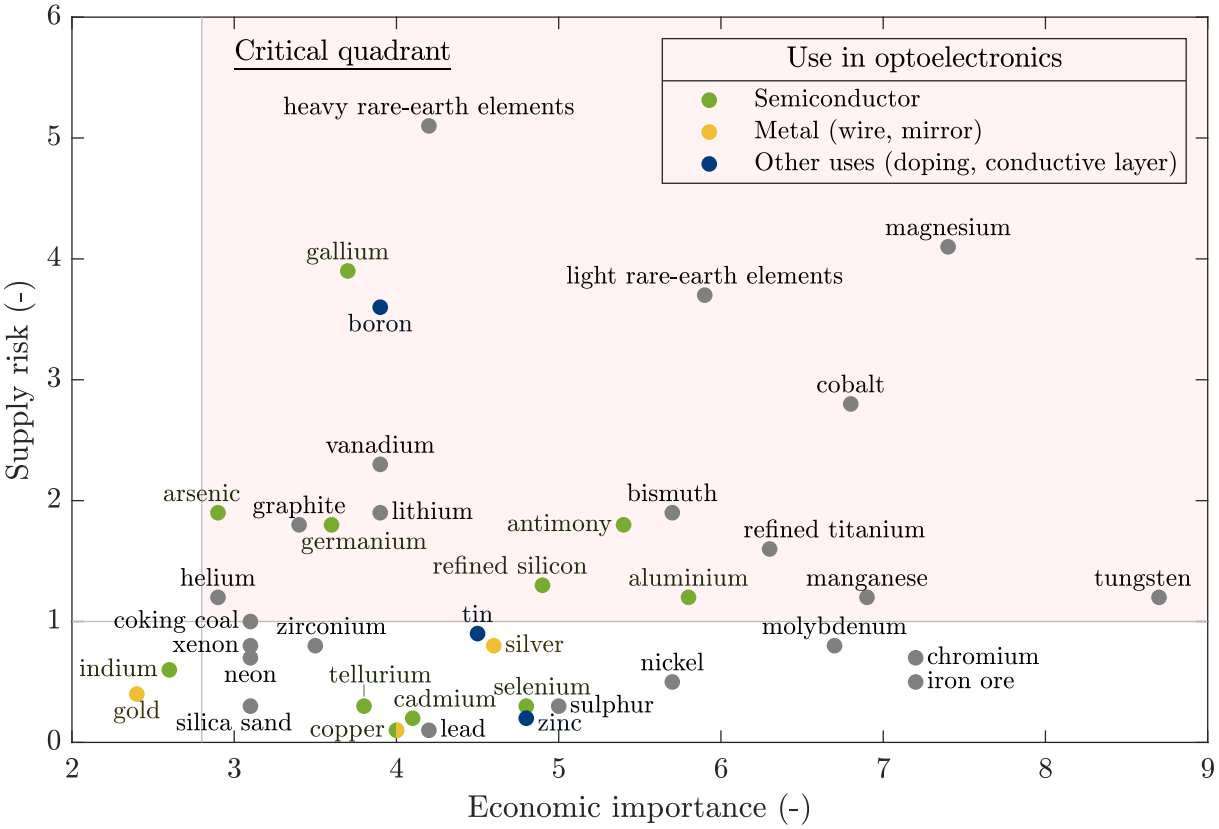

Figure 1.15: Criticality of raw materials for the European Union (adapted from [European Commission *et al.* 2023]).

efficiently recycle them.

In this manuscript, all the optoelectronic devices studied are made of III-V semiconductors (as in a large majority of the related literature, which will be shown in the following). While this may seem contradictory with the shortage issues mentioned above, it has to be kept in mind that the work performed here aims to present the potential of near-field thermophotonic devices in a best-case scenario, one of its goals being to help the development of a first experimental proof-of-concept. Such an experiment can hardly be performed without using the best possible materials due to the number of scientific and technical bottlenecks which need to be addressed. But if the first experiments with TPX were to be successful, and led to the further development of this technology, it would then be crucial to integrate the cost and scarcity issues to the research, the latter being dependent on the development of semiconductor recycling.

1.3.2 Thermophotovoltaics

A significant part of the research recently conducted on TPV focused on the development of efficient cells at high temperature, with [LaPotin *et al.* 2022, Tervo *et al.* 2022] having designed cells with 40% efficiency for an emitter temperature close to 2000 °C. Other teams have also worked on the improvement of the back-surface reflector to increase light absorption [Omair *et al.* 2019, Fan *et al.* 2020]. In all these works, the cells were made of different III-V semiconductors, as their bandgap energy can be controlled to decently match the energy of the incoming radiation. If the passive emitters considered in these examples were relatively simple (e.g. bulk silicon carbide, tungsten halogen bulb), they have been studied quite extensively in the past [Sakakibara

et al. 2019] and metamaterials are still under numerical [Wang *et al.* 2023b] and experimental investigation [Dyachenko *et al.* 2016, Shimizu *et al.* 2018]. Apart from this, the thermodynamical study of thermophotovoltaic devices has also recently regained interest [Giteau *et al.* 2023]. Complementary information on far-field TPV can be found in the review by [Burger *et al.* 2020].

Numerous articles have also examined the possibility to extend thermophotovoltaics, for instance with bifacial TPV [Datas 2023], hybrid thermionic-photovoltaic converters [Datas 2016] or thermoradiative-photovoltaic converters [Tervo *et al.* 2020] (thermoradiative (TR) systems being closely related to thermophotovoltaics [Tervo *et al.* 2018, Pusch *et al.* 2019, Callahan *et al.* 2021, Li *et al.* 2021b], see Figure 1.13). The most common extension is near-field thermophotovoltaics, which has been widely studied and reviewed in the past few years [Song *et al.* 2022, Mittapally *et al.* 2023] and even coupled to other concepts [Datas & Vaillon 2019, Choi *et al.* 2023, Wang *et al.* 2023a]. Experimentally, several teams successfully measured a near-field enhancement of the TPV cell power output by a factor 5 to 10 for gap distances varying between 60 and 140 nm [Fiorino *et al.* 2018, Inoue *et al.* 2019, Bhatt *et al.* 2020, Inoue *et al.* 2021, Lucchesi *et al.* 2021a, Mittapally *et al.* 2021], the maximum power output coming close to 1 W.cm^{-2}. In terms of efficiency, several of the devices designed in these papers achieved efficiencies above 10%, one of the devices from [Lucchesi 2020] even exceeding 20%. Numerically, [DeSutter *et al.* 2017] and [Papadakis *et al.* 2021] have analysed how entering the near field changes the cell luminescence and luminescence efficiency, while [Feng *et al.* 2022] investigated how geometry and doping change the performance of a near-field TPV device, all with a detailed-balance (i.e. 0D) approach. Several papers also focused on the design and performance of devices, either with detailed balance [Zhao *et al.* 2017], with a 1D resolution of the drift-diffusion equations in the low-injection approximation [Milovich *et al.* 2020], or more recently with a 2D resolution of these equations [Forcade *et al.* 2022]. In this last article, a TPV cell made of InAsSbP achieved a 14% efficiency and a maximum power output close to 1 W.cm^{-2} for a heat source temperature of 900 K and a 100 nm gap distance. The impact of common approximations used in the literature were also analysed, such as that of the low-injection approximation [Blandre *et al.* 2017] or that of the assumption that the chemical potential of emitted photons μ is related to the applied voltage through $\mu = eU$ [Callahan *et al.* 2021, Feng *et al.* 2021].

We discuss last the applications of thermophotovoltaics, which were already briefly mentioned previously. Because of its more complex structure (due to the additional emitter) and its greater cost (due to the use of III-V semiconductors), thermophotovoltaics cannot compete with silicon photovoltaics for solar energy conversion. The driving idea for TPV is rather to make use of its capability to generate electrical power on demand. Antora Energy [Antora Energy 2023] and Thermophoton [Thermophoton 2023] for instance work on the development of thermal batteries based on thermophotovoltaics: Joule effect is used to convert electricity into heat stored in materials (e.g. carbon blocks, molten silicon), which can be converted back to electricity when desired by placing a TPV cell in front. In both cases, the cell should even be capable of doing cogeneration, the fraction of heat not converted being sent to industry or heat networks. Another application, proposed by Mesodyne [Mesodyne 2023], is to couple the thermophotovoltaic device with a burner (used to heat up the emitter) into a mobile and scalable power generator - in this case TPV is not necessarily carbon-free.

1.3.3 Electroluminescent cooling and related photonic cooling

Electroluminescent cooling, in comparison to thermophotovoltaics, is a much narrower field. The first mention of such phenomenon can be found in [Lehovec *et al.* 1953], an experimental paper

studying silicon carbide LEDs. In the following years, EL cooling was mainly investigated in the frame of thermodynamics [Weinstein 1960, Landsberg & Evans 1968, Landsberg & Tonge 1980], sometimes compared to experimental results [Dousmanis *et al.* 1964], allowing to bring to light the heat pump behaviour of LEDs through the introduction of the concept of effective temperature of light (which takes into account the difference of entropy-to-energy ratio of radiation in comparison to conduction or convection). But this effective temperature has no physical meaning; this led Würfel to define the notion of chemical potential of radiation to handle non-thermal radiation [Würfel 1982], as explained in Section 1.1.2. Following this new paradigm, numerical results on EL cooling were quickly published [Berdahl 1985]. At this time however, the experimental proof of EL cooling was unachievable due to the limited efficiency of the LEDs. In the following years, the modelling of LEDs for EL cooling purposes continued to be improved (e.g. [Heikkilä *et al.* 2009]).

The first experimental proof of electroluminescent cooling came in the beginning of the 2010s thanks to the quick development of efficient III-V-based LEDs. It was initially performed at temperature higher than ambient [Santhanam *et al.* 2012], then at room temperature [Santhanam *et al.* 2013]. In these papers, cooling regime was achieved by applying very low voltage; this however means that the cooling rate also remained low. If some theoretical works were still performed regarding EL cooling [Xue *et al.* 2017], a large fraction of the related research has gone into different directions to achieve EL cooling with larger cooling rate. [Oksanen & Tulkki 2010] proposed to use a thermophotonic engine in a heat pump configuration, in which the radiation emitted by the cooled LED can be recycled into the PV cell. Near-field EL cooling was also investigated [Chen *et al.* 2015, Liu & Zhang 2016, Li *et al.* 2021a] and logically extended to near-field thermophotonic heat pump [Chen *et al.* 2017], in one case based on Schottky diodes [Song *et al.* 2020]. As of now, the only related device which achieved high-power EL cooling is a Double-Diode Structure (DDS) [Radevici *et al.* 2019], in which the PV cell is grown directly on the LED. While largely improving the radiation transmission, it is however limited by the significant conduction between the two components; as explained by the authors, "the DDS structure is designed to act as an intermediate research prototype [...], providing the necessary additional insight and evidence on the feasibility of both conventional EL cooling and thermophotonic cooling". A review on the advances on EL cooling can be found in [Sadi *et al.* 2020].

We should lastly mention that EL cooling is not the only way to obtain photonic cooling. Negative EL cooling, in which a photodiode is negatively biased to reduce emission and consequently cool a facing body, has also been recently studied [Chen *et al.* 2016] and experimentally demonstrated in the near field [Zhu *et al.* 2019]. We have also excluded here from the term "photonic cooling" the much broader research field of laser cooling [Nemova & Kashyap 2010, Seletskiy *et al.* 2016].

1.3.4 Thermophotonic heat engine

The thermophotonic heat engine was first mentioned at the beginning of the century [Harder *et al.* 2001, Tobias & Luque 2002, Harder & Green 2003], and was then meant to be used for solar applications, as an improvement of solar TPV. In parallel, highly efficient LEDs made once more of III-V materials (in this case, InGaP/GaAs heterostructures) were investigated for thermophotonic purposes [Lin *et al.* 2004].

After these first studies however, research was paused for several years, and started again only in the end of the 2010s owing to the good development of both thermophotovoltaics and electroluminescent/thermophotonic cooling devices. The new results published were essentially numerical and based on a detailed-balance approach, apart from a paper in which a thermophotonic

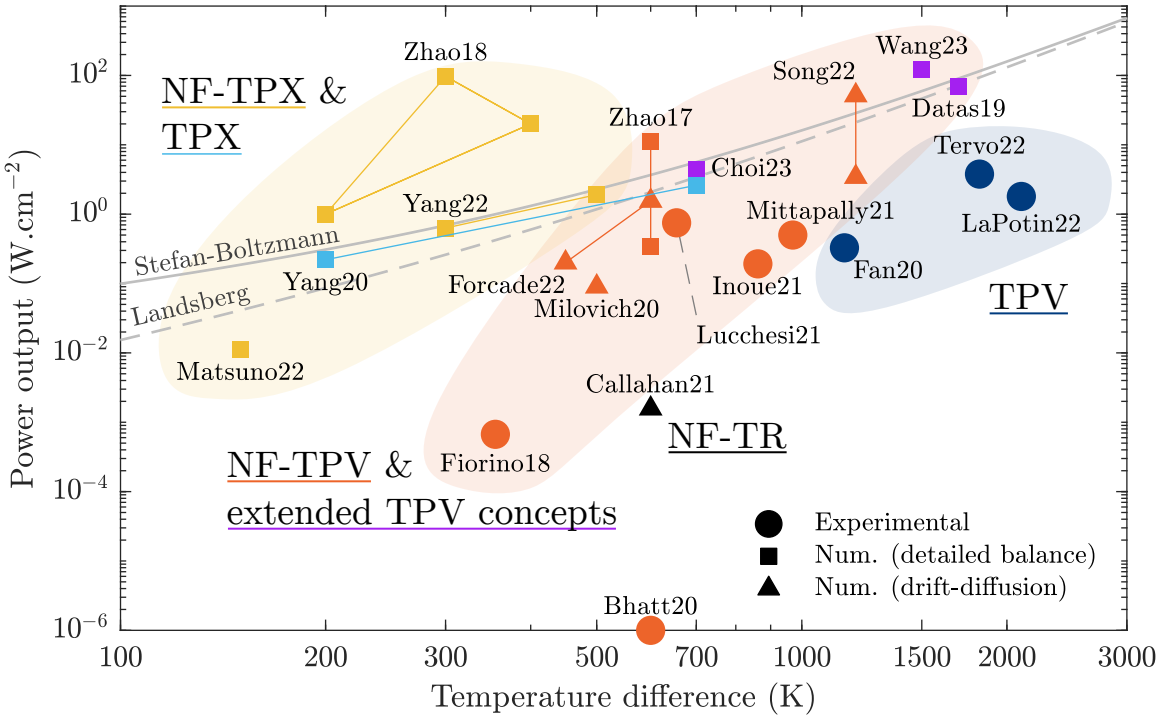

Figure 1.16: State-of-the-art of the performance of radiative heat engines. Connected points come from the same source. Stefan-Boltzmann law is expressed as $\sigma(T_\mathrm{h}^4 - T_\mathrm{c}^4)$, while Landsberg's limit corresponds to the power output $P = \eta_\mathrm{L}\sigma T_\mathrm{h}^4$ of a radiative engine receiving radiation from a blackbody and operating with Landsberg's efficiency (assuming a heat sink at ambient temperature).

device is used for DC voltage conversion [Zhao *et al.* 2021]. The impact of classical losses were analysed, such as the power loss due to imperfect connections with the thermal reservoirs [Yang *et al.* 2020] or due to non-radiative recombinations and series resistance [Sadi *et al.* 2022]. [McSherry *et al.* 2019] also studied how the radiation bandwidth (i.e. the spectral width of radiation) affects the efficiency of TPV and TPX systems, both in the far and near field. Several papers focused on the performance of specific devices, either made of AlGaAs alloys [Zhao *et al.* 2018], CdTe and InP [Yang *et al.* 2022] or black phosphorus [Matsuno *et al.* 2022]. All these devices are made of LEDs and PV cells with similar sizes. However, such devices cannot be self-sustaining as neither voltage nor current are similar in the two components, as explained in [Zhao *et al.* 2019]; they propose in this article a self-sustaining circuit based on multiple LEDs and PV cells (whose respective number should be different).

We should here make clear that the study of thermophotonic heat engines is an even smaller field of research than photonic cooling, therefore much smaller than thermophotovoltaics: while most of the TPX literature has been reviewed here, more than a thousand articles whose title include thermophotovoltaic/thermophotovoltaics can be found on the *Web Of Science* database. For this reason, it seems essential to draw inspiration from TPV for the development of TPX, for instance on:

- the development of the thermodynamical ground of TPX ([Landsberg & Tonge 1980] for PV, [Giteau *et al.* 2023] for TPV);
- the resolution of the drift-diffusion equations [Blandre *et al.* 2017, Forcade *et al.* 2022];

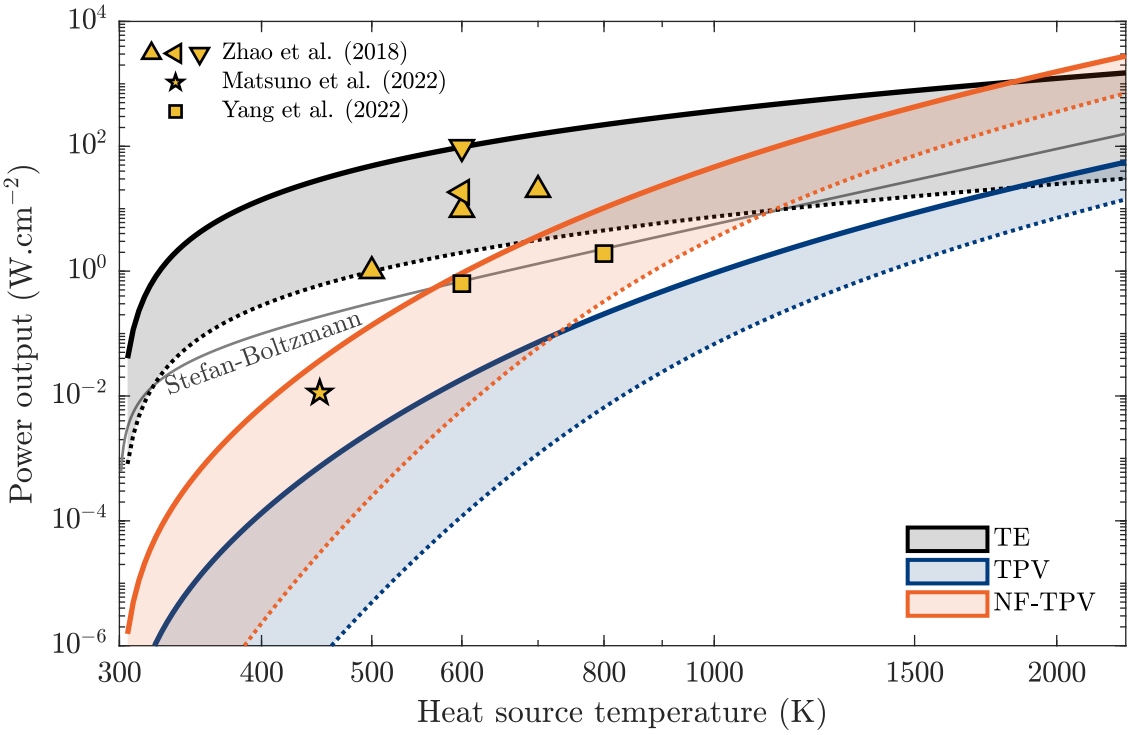

Figure 1.17: Basic models for the variation of power generated with heat source temperature, obtained for different radiative heat engines. Full and dashed line represent ideal and more realistic scenarios. For the data from [Zhao *et al.* 2018], several markers are used to denote the difference of hypothesis considered ($\triangledown$: ideal case, $\triangleleft$: with non-radiative recombinations, $\triangle$: with non-radiative recombinations and imperfect back mirrors).

- the study and the correction of usual approximations [Callahan *et al.* 2021].

Many of these points will be addressed throughout the manuscript.

1.3.5 Comparison of the different engines

We summarise in Figure 1.16 the performance of many of the devices cited throughout the review, differentiating experimental results from calculations made with a detailed-balance approach or with the resolution of the drift-diffusion equations. The power output is given as a function of the temperature difference between the heat source and the heat sink rather than heat source temperature, since in the experiment of [Lucchesi *et al.* 2021a], the cell is kept at cryogenic temperature. The connected points correspond to results obtained from the same source. This figure should make clear that the development of extended TPV concepts aims to decrease the operating temperature difference, more than to increase the power density - mainly since it gets harder and harder to ensure the good operation of a device as the power density increases, e.g. because of thermal management issues. Indeed, increasing the power output causes the heat flux densities supplied from the heat source and released to the heat sink to rise. Eventually, such high heat flux densities become impossible to sustain for the heating and cooling systems, causing a decrease of the overall temperature difference and limiting the achievable power output. The impact of such thermal management issues in NF-TPX devices will be investigated in Section 3.4.

To compare the results obtained throughout the manuscript for NF-TPX with the performance of other devices, it seemed interesting to have a common and simple modelling framework for

the aforementioned technologies, in a manner similar to [Okanimba Tedah *et al.* 2019]. This framework is described in Appendix C, and is based on a detailed-balance approach; the results are shown in Figure 1.17. The main difference with [Okanimba Tedah *et al.* 2019] is that all bodies are considered to be at constant temperature, so that thermal management issues arising at high heat source temperature are not observed. This means that the accuracy of these models are significantly degraded at high temperature, but this is not too much of an issue since NF-TPX devices operate at moderate heat source temperature. For each of the technologies considered (thermoelectrics (TE), thermophotovoltaics and near-field thermophotovoltaics), the dashed line roughly corresponds to current achievable performance, while the full line corresponds to ideal (or almost) operation. While NF-TPV can reach performances similar to TE only for heat source temperatures above 900 K, the first numerical results on NF-TPX tend to demonstrate that it can compete with TE at least for heat source temperatures above 500 K. To verify this, we will work in Chapter 3 to develop similar limits for NF-TPX.

1.4 To sum up

In this chapter, we introduced the basic principle of the near-field thermophotonic heat engine: it can simply be understood as the coupling of a radiative heat pump (the LED, pumping heat from the heat source to emit electroluminescent radiation) and a radiative heat engine (the PV cell, converting the incoming radiation into electrical power fed to the LED and extracted from the device). We motivated the interest of such devices for low-grade heat (300-700 K) recovery. The review of the related literature shined a light on the youth of the research of the subject, especially compared to similar technologies such as TPV. We have seen that all the TPX studies were performed numerically with a detailed-balance approach; still, due to the sparse published results, there is still room for gaining new insights on the capabilities of TPX devices through a more thorough analysis. The exclusive use of detailed-balance analysis in the literature also pinpoints the lack of a solid thermodynamical and analytical description of TPX devices, along with the absence of more refined analyses of charge transport and its impact on performance. The following chapters will aim at carrying out the aforementioned developments, from the ones based on the simplest models (thermodynamics and detailed balance, see Chapters 2 and 3) to the most complete ones (solution of the drift-diffusion equations, see Part II).

Chapter 2

Far-field performance of ideal thermophotonic engines

Contents

2.1 Maximum efficiency of luminescent heat engines 35
2.1.1 Luminescent engine with passive emitter: from Landsberg to Carnot 37
2.1.2 Luminescent engine with active emitter: a standard Carnot heat engine . . 40
2.2 Efficiency at maximum power of thermophotonic devices 42
2.2.1 Detailed-balance modelling of thermophotonic conversion 43
2.2.2 Monochromatic radiation 46
2.2.3 Above-bandgap radiation 48
2.2.4 Addition of below-bandgap losses 53
2.3 To sum up 54

Because solar energy conversion is based on radiative heat transfer, which is highly non-linear with temperature (varying as T^4 for blackbodies), the usual Carnot efficiency limit is not necessarily a proper metric, as mentioned in Section 1.1.1.4. For this reason, a great deal of work has been performed to estimate the ultimate efficiency of such conversion. Landsberg [Landsberg & Tonge 1980] and Shockley-Queisser [Shockley & Queisser 1961] limits are probably the most known derivations, obtained respectively for any reversible solar energy converter and for a single-junction solar cell. But many others have been developed throughout the years [De Vos 1992, Green 2006], and some of them have been extended to other radiative heat engines [Buddhiraju *et al.* 2018, Pusch *et al.* 2019, Park *et al.* 2022, Giteau *et al.* 2023]. This chapter focuses on the derivation of similar upper-bound efficiencies for TPV and TPX, based on the following remarks:

- most of these efficiencies are derived for solar PV, for which maximum efficiency and efficiency at maximum power are the same since the incoming radiation is constant; this is not the case for TPV and TPX as radiation can be recycled, and these two efficiencies should this be considered separately (resp. in Section 2.1 and 2.2);
- electroluminescent radiation emitted by the PV cell is generally not taken into account since it represents a loss; on the contrary, it is mandatory to consider it for TPX since its operation is based on LED electroluminescent radiation, and such radiation will thus be integrated into the developments.

2.1 Maximum efficiency of luminescent heat engines

The maximum efficiency of TPV and TPX devices is derived similarly to that of thermoradiative cells in [Pusch *et al.* 2019]. The device under consideration is shown in Figure 2.1 (named

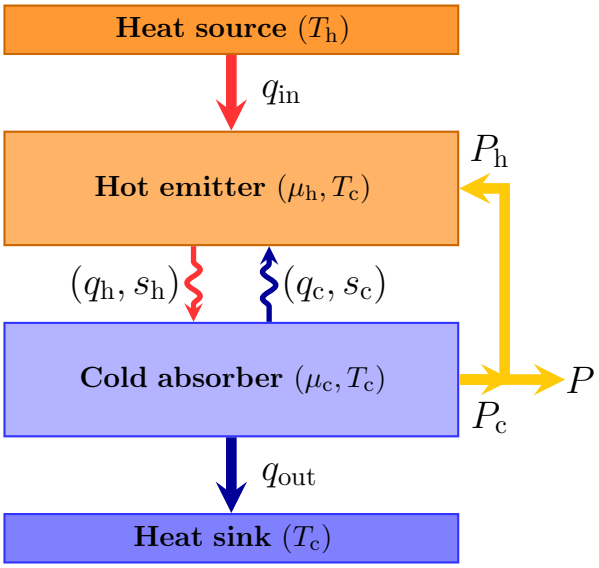

Figure 2.1: Representation of the luminescent heat engine.

Luminescent Heat Engine (LHE) thereafter). The way luminescent radiation is converted into electricity (or vice versa) is not of interest: it can be done with optoelectronic devices (as in TPX devices) or not. Rather, the LHE is considered to always operate in reversible regime, which means that any active component will not produce entropy - this is how most of the efficiencies cited at the beginning of the chapter were derived.

We consider that far-field luminescent radiation is only exchanged between a given cut-off energy E_g and $E_g + \Delta E$. In this range of frequency, the transmission coefficient of radiation from one semi-infinite body to the other is assumed to be maximum, the spectral heat flux density thus following Planck's law without luminescence. The main physical quantities related to radiation are defined as [Würfel 1982, Luque & Martí 1997]

$$\begin{aligned} q_i &= \frac{1}{4\pi^2 c^2 \hbar^3} \int_{E_g}^{E_g+\Delta E} \frac{E^3}{e^{(E-\mu_i)/k_B T_i} - 1} dE, \\ \dot{N}_i &= \frac{1}{4\pi^2 c^2 \hbar^3} \int_{E_g}^{E_g+\Delta E} \frac{E^2}{e^{(E-\mu_i)/k_B T_i} - 1} dE, \\ \dot{\Omega}_i &= \frac{k_B T}{4\pi^2 c^2 \hbar^3} \int_{E_g}^{E_g+\Delta E} E^2 \ln\left(1 - e^{-(E-\mu_i)/k_B T_i}\right) dE. \end{aligned} \tag{2.1}$$

q_i represents the heat flux density[1] emitted through luminescent radiation (i being either h or c) and $\dot{N}_i$ the related photon flux density. μ_i is the chemical potential of radiation, which must satisfy $\mu_i < E_g$. $\dot{\Omega}_i$, the grand potential flux density, can also be written as $q_i - T_i s_i - \mu_i \dot{N}_i$ and allows to obtain the related entropy flux density s_i. In this chapter, we will mainly study complete above-E_g radiation ($\Delta E = +\infty$), even if monochromatic radiation[2] ($\Delta E = \delta E$) will be briefly addressed.

[1] Strictly speaking, q_i represents the internal energy flux density of radiation. It is said to be a heat flux density to make the understanding easier.

[2] The term *monochromatic radiation* is an abuse of language, as true monochromatic radiation carries no energy. Rather, it refers to radiation with infinitely narrow bandwidth.

2.1.1 Luminescent engine with passive emitter: from Landsberg to Carnot

Assuming reversible operation, application of the first and second principles of thermodynamics on the absorber gives

$$q_\mathrm{h} = q_\mathrm{c} + q_\mathrm{out} + P_\mathrm{c}, \tag{2.2a}$$

$$s_\mathrm{h} = s_\mathrm{c} + \frac{q_\mathrm{out}}{T_\mathrm{c}}. \tag{2.2b}$$

Since the emitter is passive, the radiation it emits must be thermal which means that $\mu_\mathrm{h} = 0$. If the radiation sent back by the absorber can be recycled in the emitter, the efficiency is

$$\eta_\mathrm{passive} = \frac{P_\mathrm{c}}{q_\mathrm{h} - q_\mathrm{c}} = 1 - T_\mathrm{c}\frac{s_\mathrm{h} - s_\mathrm{c}}{q_\mathrm{h} - q_\mathrm{c}} = 1 - \frac{\frac{T_\mathrm{c}}{T_\mathrm{h}}\left(q_\mathrm{h} - \dot{\Omega}_\mathrm{h}\right) - \left(q_\mathrm{c} - \mu_\mathrm{c}\dot{N}_\mathrm{c} - \dot{\Omega}_\mathrm{c}\right)}{q_\mathrm{h} - q_\mathrm{c}}. \tag{2.3}$$

In comparison, if emission by the absorber cannot be recycled and is lost (as for solar PV), we get

$$\eta_\mathrm{passive,w/o\ rec} = \frac{P_\mathrm{c}}{q_\mathrm{h}} = 1 - \frac{q_\mathrm{c} + T_\mathrm{c}(s_\mathrm{h} - s_\mathrm{c})}{q_\mathrm{h}} = 1 - \frac{\frac{T_\mathrm{c}}{T_\mathrm{h}}\left(q_\mathrm{h} - \dot{\Omega}_\mathrm{h}\right) - \left(-\mu_\mathrm{c}\dot{N}_\mathrm{c} - \dot{\Omega}_\mathrm{c}\right)}{q_\mathrm{h}}. \tag{2.4}$$

The variation of both efficiencies with the chemical potential of radiation emitted by the absorber is depicted in Figure 2.2, for different cut-off energies and considering complete above-E_g radiation. The emitter and absorber temperatures are respectively equal to 600 and 300 K. In reversible operation, efficiency decreases with chemical potential if the emission from the absorber cannot be recycled, as the heat flux emitted increases with the chemical potential. This result can easily be obtained analytically by using $\partial\dot{\Omega}_i/\partial\mu_i = -\dot{N}_i$:

$$\frac{\partial\eta_\mathrm{passive,w/o\ rec}}{\partial\mu_\mathrm{c}}(\mu_\mathrm{c}) = -\frac{\mu_\mathrm{c}}{q_\mathrm{h}}\frac{\partial\dot{N}_\mathrm{c}}{\partial\mu_\mathrm{c}}(\mu_\mathrm{c}) \leq 0, \tag{2.5}$$

the equality holding only for $\mu_\mathrm{c} = 0$. By recycling the absorber emission, the maximum efficiency can be significantly increased and is reached for a non-zero chemical potential. The variations are however quite different according to the cut-off energy considered. To understand how this quantity impacts the efficiency, two limiting cases will be studied: $E_g \to 0$ and $E_g \to \infty$.

If $E_g \to 0$, the chemical potential must also go to zero, since $\mu < E_g$ should hold (see Section 1.1.2). Then, the radiation considered approaches that of blackbodies, and using $s_i = 4/3\sigma T_i^3$, we get back Landsberg limit [Landsberg & Tonge 1980] without absorber emission recycling:

$$\eta_\mathrm{passive,w/o\ rec} = \eta_L \equiv 1 - \frac{4}{3}\frac{T_\mathrm{c}}{T_\mathrm{h}} + \frac{1}{3}\left(\frac{T_\mathrm{c}}{T_\mathrm{h}}\right)^4. \tag{2.6}$$

Similarly, the efficiency with emission recycling can be expressed as

$$\eta_\mathrm{passive} = \frac{\eta_L}{1 - \left(\frac{T_\mathrm{c}}{T_\mathrm{h}}\right)^4}. \tag{2.7}$$

Such expressions correspond well to the results obtained for $E_g = 0.1\ k_\mathrm{B}T_\mathrm{h}$. Even if the chemical potential can indeed be non-zero, it is too small to have a significant impact on the energy transfer, and the efficiency remains almost constant.

We now move on to the $E_g \to \infty$ case. Looking for the chemical potential at maximum efficiency

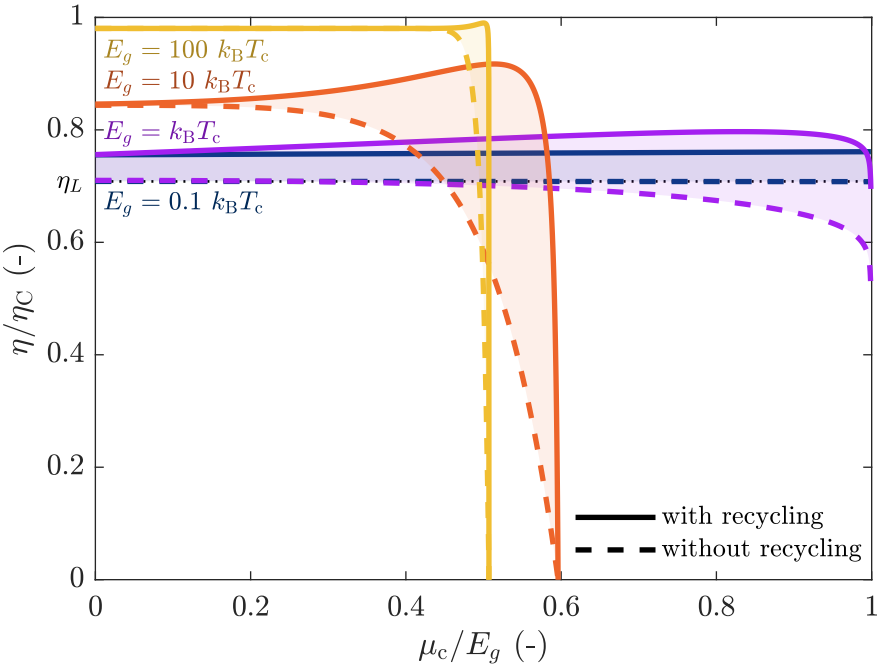

Figure 2.2: Variation of efficiency with chemical potential of radiation emitted by the cold absorber, obtained for $T_h = 600$ K and $T_c = 300$ K and for complete above-E_g radiation.

$\mu_{c,opt}$, we get

$$\frac{\partial \eta_{passive}}{\partial \mu_c}(\mu_{c,opt}) = 0 \Leftrightarrow \eta_{passive,max} = \mu_{c,opt} \frac{\frac{\partial \dot{N}_c}{\partial \mu_c}(\mu_{c,opt})}{\frac{\partial q_c}{\partial \mu_c}(\mu_{c,opt})} \tag{2.8}$$

This expression cannot be easily developed due to the integrals on both sides of the fraction. Generally, Boltzmann's approximation is used to simplify such an expression [Pusch *et al.* 2019], and the results that will be presented in this section can be similarly obtained with this approximation. However, it will be necessary to avoid it later in the chapter. Hence, a more general framework based on polylogarithm functions will be used instead of Boltzmann's approximation. A similar framework was used in [Green 2012a]. The different radiative quantities can be expressed as

$$q_i = \Lambda_{3,4}(E_g, \mu_i, T_i), \tag{2.9a}$$
$$\dot{N}_i = \Lambda_{2,3}(E_g, \mu_i, T_i), \tag{2.9b}$$
$$\dot{\Omega}_i = \Lambda_{2,4}(E_g, \mu_i, T_i), \tag{2.9c}$$

$\Lambda_{n,m}$ being a function defined as

$$\Lambda_{n,m}(E_g, \mu, T) = \frac{1}{4\pi^2 c^2 \hbar^3} \sum_{k=0}^{n} \frac{n!}{k!} (k_B T)^{m-k} E_g^k \cdot \mathrm{Li}_{m-k}\left(\exp\left\{\left(\frac{\mu - E_g}{k_B T}\right)\right\}\right). \tag{2.10}$$

Li_m is the polylogarithm of order m. These expressions of the radiative quantities are quite heavy and cannot be used to derive any efficiency as of now. However, we can use the fact that the polylogarithm function $\mathrm{Li}_m(x)$ increases as its order m decreases. Since the lowest order polylogarithm (Li_{m-n}) is associated with the largest power of $x_g = E_g/k_B T$ (x_g^n) in the last term of the sum, it becomes dominant in Λ_m for large enough cut-off energies. Then, Eq. (2.8)

becomes

$$\eta_{\text{passive,max}} = \mu_{\text{c,opt}} \frac{E_g^2 \operatorname{Li}_0\left(\exp\left\{\left(\frac{\mu_{\text{c,opt}}-E_g}{k_\text{B}T_\text{c}}\right)\right\}\right)}{E_g^3 \operatorname{Li}_0\left(\exp\left\{\left(\frac{\mu_{\text{c,opt}}-E_g}{k_\text{B}T_\text{c}}\right)\right\}\right)} = \frac{\mu_{\text{c,opt}}}{E_g}. \tag{2.11}$$

This expression can be inserted in Eq. (2.3) to obtain the maximum efficiency and the related chemical potential. Neglecting the grand potential (which is only proportional to E_g^2, against E_g^3 for q_i and $\mu_i E_g^2$ for $\mu_i \dot{N}_i$) and defining ζ as $\frac{T_\text{h}}{T_\text{c}} \frac{\operatorname{Li}_1\left(\exp\left\{\left(-\frac{E_g}{k_\text{B}T_\text{h}}\right)\right\}\right)}{\operatorname{Li}_1\left(\exp\left\{\left(\frac{\mu_{\text{c,opt}}-E_g}{k_\text{B}T_\text{c}}\right)\right\}\right)}$ ($\zeta > 0$) gives

$$\begin{aligned}
\eta_{\text{passive,max}} &= \eta_\text{C} - \frac{\mu_{\text{c,opt}}\dot{N}_\text{c} - \eta_\text{C} q_\text{c}}{q_\text{h} - q_\text{c}} \\
&= \eta_\text{C} - \frac{\mu_{\text{c,opt}} k_\text{B} T_\text{c} E_g^2 - \eta_\text{C} k_\text{B} T_\text{c} E_g^3}{k_\text{B} T_\text{h} E_g^3 \frac{\operatorname{Li}_1\left(\exp\left\{\left(-\frac{E_g}{k_\text{B}T_\text{h}}\right)\right\}\right)}{\operatorname{Li}_1\left(\exp\left\{\left(\frac{\mu_{\text{c,opt}}-E_g}{k_\text{B}T_\text{c}}\right)\right\}\right)} - k_\text{B} T_\text{c} E_g^3} \\
&= \eta_\text{C} - \frac{\frac{\mu_{\text{c,opt}}}{E_g} - \eta_\text{C}}{\zeta - 1} \\
&= \eta_\text{C} - \frac{\eta_{\text{passive,max}} - \eta_\text{C}}{\zeta - 1} \\
\Leftrightarrow &(\eta_\text{C} - \eta_{\text{passive,max}}) \frac{\zeta}{1-\zeta} = 0 \\
\Leftrightarrow &\eta_{\text{passive,max}} = \eta_\text{C}.
\end{aligned} \tag{2.12}$$

Hence, if the cut-off energy is large enough, the maximum efficiency comes close to the Carnot limit and is reached for a chemical potential $\mu_{\text{c,opt}} = \eta_\text{C} E_g$. In comparison, the maximum efficiencies obtained numerically and presented in Figure 2.2 approaches the Carnot limit quite slowly, but the chemical potential at maximum efficiency is already close to $\eta_\text{C} E_g$ for $E_g = 10 k_\text{B} T_\text{c}$. We can in fact show that for very high cut-off energies, maximum efficiency is reached when both power output and net heat flux equal zero: by using $\operatorname{Li}_n(x) \sim x$ as x approaches 0,

$$\begin{aligned}
q_\text{h} = q_\text{c} \Leftrightarrow & k_\text{B} T_\text{h} E_g^3 \operatorname{Li}_1\left(\exp\left\{\left(-\frac{E_g}{k_\text{B}T_\text{h}}\right)\right\}\right) = k_\text{B} T_\text{c} E_g^3 \operatorname{Li}_1\left(\exp\left\{\left(\frac{\mu_\text{c}-E_g}{k_\text{B}T_\text{c}}\right)\right\}\right) \\
\Leftrightarrow & \exp\left\{\left(\frac{E_g}{k_\text{B}T_\text{h}} + \frac{\mu_\text{c}-E_g}{k_\text{B}T_\text{c}}\right)\right\} = \frac{T_\text{h}}{T_\text{c}} \\
\Leftrightarrow & \mu_\text{c} = \eta_\text{C} E_g + k_\text{B} T_\text{c} \ln\left(\frac{T_\text{h}}{T_\text{c}}\right) \approx \eta_\text{C} E_g,
\end{aligned} \tag{2.13}$$

the last term being equal to $\mu_{\text{c,opt}}$ following Eqs. (2.11) and (2.12). By using Eq. (2.3) and a similar expansion of Li_n, we can also prove that for any chemical potential between 0 and $\eta_\text{C} E_g$, the efficiency tends towards the Carnot limit as the cut-off energy goes to infinity, which means that the efficiency will ultimately look like a step function around $\eta_\text{C} E_g$.

In the end, the LHE goes from the Landsberg to the Carnot efficiency as E_g increases. To understand why this happens, we have to identify why, even if the absorber is in reversible operation, the LHE does not always operate at the Carnot limit. As discussed in Section 1.1.1.3, radiation carries in general more entropy per unit energy than any other kind of heat transfer. Therefore, the only way to ensure both energy and entropy balance in the emitter is to have entropy produced there: the irreversibilities causing a decrease in efficiency comes from the conversion of the heat supplied to the hot emitter (through conduction or convection) into

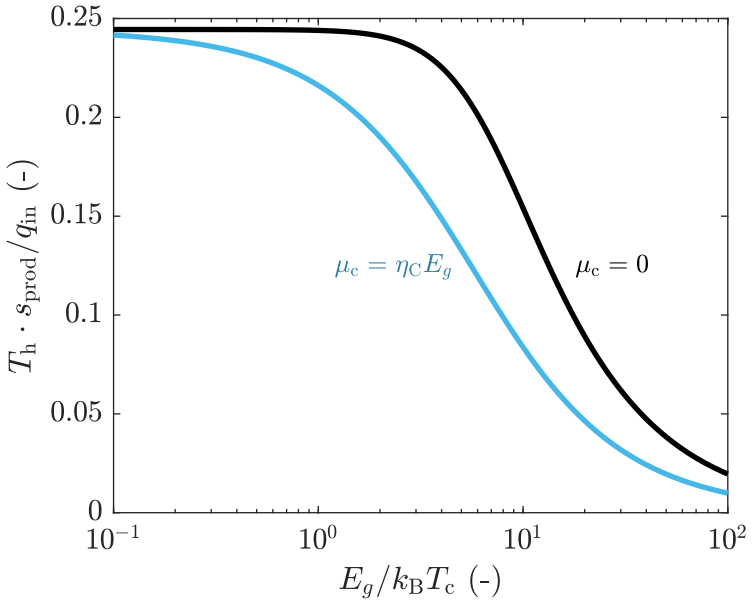

Figure 2.3: Entropy production in the passive emitter, normalised by the entropy flux coming from the heat source, as a function of the cut-off energy. The results are obtained for $T_h = 600$ K and $T_c = 300$ K.

radiation. This is also what makes Landsberg limit different from Carnot limit. However, as the cut-off energy increases, the entropy of radiation exchanged between the emitter and the absorber decreases, to come close to q_{in}/T_h. The entropy production in the emitter gets lower[3], as depicted in Figure 2.3, and the efficiency approaches the Carnot limit. However, the energy transferred through radiation simultaneously decreases, and the power output goes to zero for high cut-off energies, as expected.

The variation of efficiency with chemical potential in the monochromatic case is shown in Figure 2.4. If the results are quite different for low cut-off energies, they are mostly similar for E_g larger than $k_B T_c$. The ultimate values of $\mu_{c,opt}$ and $\eta_{passive,max}$ as cut-off energy goes to infinity can be derived in the same way and give the same result ($\mu_{c,opt} = \eta_C E_g$, $\eta_{passive,max} = \eta_C$). These ultimate values are in fact reached faster than for the complete above-E_g radiation, being almost correct for $E_g = k_B T_c$.

2.1.2 Luminescent engine with active emitter: a standard Carnot heat engine

If the emitter is now actively controlled, a set of equations similar to Eq. (2.2) should be considered for the emitter, along with the equation $P = P_c - P_h$. Defining $q = q_h - q_c$ and

[3]For $E_g \to 0$ and $T_h \gg T_c$, the entropy production can analytically be obtained using the Stefan-Boltzmann law. First, $s_h - s_c = 4/3\sigma(T_h^3 - T_c^3) \approx 4/3\sigma T_h^3$ which is approximately equal to $4/3 \cdot q_{in}/T_h$ since $q_{in} \approx \sigma T_h^4$. Thus the entropy production is $s_{prod} = s_h - s_c - q_{in}/T_h \approx 1/3 \cdot q_{in}/T_h$. If T_c is not negligible compared to T_h, the entropy production will be between 0 and $1/3 \cdot q_{in}/T_h$, as in the case considered here.

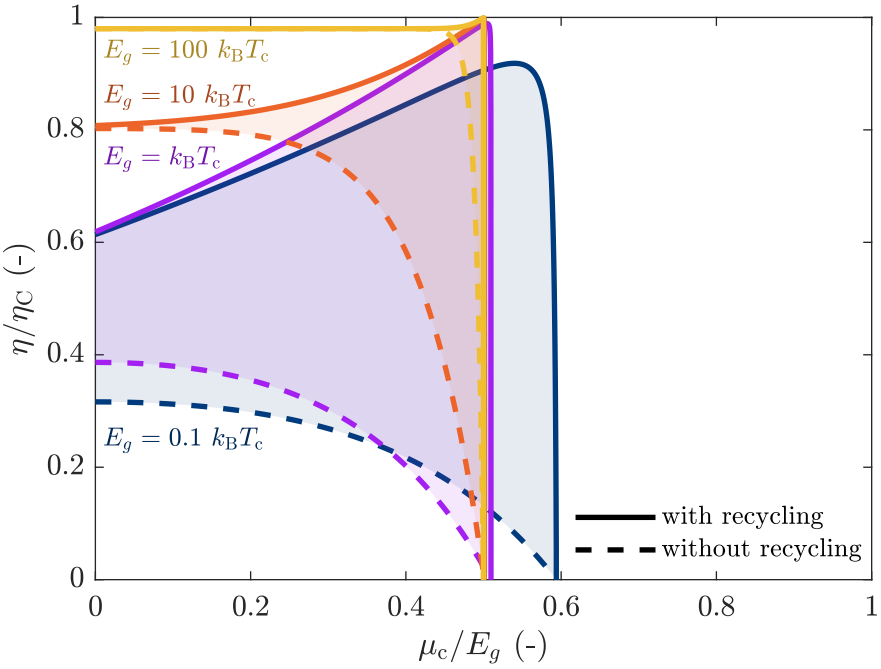

Figure 2.4: Variation of efficiency with chemical potential of radiation emitted by the cold absorber, obtained for $T_h = 600$ K and $T_c = 300$ K and for monochromatic radiation.

$s = s_h - s_c$, the efficiency of the system is:

$$\begin{aligned}\eta_{\text{active}} &= \frac{P}{q_{\text{in}}} \\ &= \frac{P_c - P_h}{q - P_h} \\ &= \frac{(q - T_c s) - (q - T_h s)}{q - (q - T_h s)} \\ &= \frac{T_h - T_c}{T_h} \\ &= \eta_C. \end{aligned} \tag{2.14}$$

For any cut-off frequency[4], chemical potential and temperature, the efficiency of this device is thus strictly equal to the Carnot efficiency. Such a result could in fact be expected. In the previous section, we have shown that the difference with the Carnot limit was due to the conversion of heat to radiation in the passive emitter; as the emitter is now active, we can ensure that it works at the reversible limit, hence reaching the Carnot limit. The expressions of q and s were not even necessary to obtain this result, which thus holds for any kind of radiation exchanged between the emitter and the absorber. In this configuration, the LHE is thus a standard Carnot heat engine, and reaches consequently higher efficiencies than with a passive emitter.

It is interesting to notice that the net power output of the LHE with an active emitter is simply expressed as $P = \Delta T(s_h - s_c)$. Therefore, it is not directly related to the energy carried by radiation, but rather to its entropy. This is important because while the heat flux density can

[4]In fact, this result even holds if the cut-off frequencies of the emitter and the absorber are different.

be infinitely large as the chemical potential of radiation comes close to E_g, the entropy flux density is actually bounded for any cut-off energy because $q - \mu\dot{N}$ remains bounded - this can be shown using the polylogarithmic expressions[5]. Consequently, the power output remains finite even for $\mu \to E_g$ and reaches its maximum for $\mu_\mathrm{h} \to E_g$ and $\mu_\mathrm{c} = 0$ (as we can prove from the polylogarithmic expression of s_i that it increases with μ_i).

2.2 Efficiency at maximum power of thermophotonic devices

We now come back to the specific case of TPX conversion. In comparison to the previous section, we don't force the entropy production to be zero any more, and the device hence operates irreversibly. Since we consider perfect connections with the thermal reservoirs, the engine is said to operate in an exoreversible configuration. As discussed in Section 1.1.4, the maximum efficiency point loses interest for irreversible engines as power output is zero - this is even truer in the case of TPX heat engines as their aim is to be used as energy harvesters. Therefore, we focus on the study of the efficiency at maximum power.

The most known efficiency at maximum power for standard heat engines (i.e. not based on radiative heat transfer) is the Curzon-Ahlborn limit, expressed simply as

$$\eta_\mathrm{CA} = 1 - \sqrt{\frac{T_\mathrm{c}}{T_\mathrm{h}}}. \tag{2.15}$$

It is derived for a reversible (i.e. Carnot) engine with imperfect thermal connections. Irreversibilities arising only from these connections, the engine is endoreversible. This expression can already give some insights about the efficiency at maximum power of TPX devices. We have established that a LHE with an active emitter is in fact a Carnot heat engine: this means that its efficiency at maximum power in endoreversible configuration must equals the Curzon-Ahlborn efficiency, which must represent an upper limit for TPX. On the contrary, [Giteau *et al.* 2023] have recently demonstrated that LHEs with passive emitter can have efficiencies at maximum power exceeding the Curzon-Ahlborn limit. This would mean that using an active emitter decreases the efficiency at maximum power, i.e. that TPX would be less efficient than TPV at maximum power. We will show in the next chapter that this is indeed correct, but that power output is increased in parallel. Intuitively, we would in fact say that efficiency decreases *because* power increases: as the energy flow through the device gets larger, the device must operate further from equilibrium, leading to a larger rate of entropy creation.

Along with the Curzon-Ahlborn efficiency, many other expressions were derived for different engines in the past [Schmiedl & Seifert 2008, Tu 2008], and related to each other by Apertet [Apertet *et al.* 2012b, Apertet 2014, Apertet *et al.* 2017]. The question is now to understand how the efficiency at maximum power of exoreversible TPX devices compares with these limits.

[5] The polylogarithmic expression of s_i can be obtained from

$$\begin{aligned}4\pi^2c^2\hbar^3 \cdot T_i s_i =&(E_g-\mu_i)E_g^2 k_\mathrm{B}T_i \,\mathrm{Li}_1\left(\exp\left(\frac{\mu_i-E_g}{k_\mathrm{B}T_i}\right)\right) + (4E_g-2\mu_i)E_g(k_\mathrm{B}T_i)^2\,\mathrm{Li}_2\left(\exp\left(\frac{\mu_i-E_g}{k_\mathrm{B}T_i}\right)\right)\\ &+(8E_g-2\mu_i)(k_\mathrm{B}T_i)^3\,\mathrm{Li}_3\left(\exp\left(\frac{\mu_i-E_g}{k_\mathrm{B}T_i}\right)\right) + 8(k_\mathrm{B}T_i)^4\,\mathrm{Li}_4\left(\exp\left(\frac{\mu_i-E_g}{k_\mathrm{B}T_i}\right)\right),\end{aligned}$$

coherent with the expression derived for thermal radiation in [Delgado-Bonal 2017].

2.2.1 Detailed-balance modelling of thermophotonic conversion

In this section, radiative heat and photon flux densities remain expressed similarly as in the previous section (see Eq. (2.1)), with the cut-off energy representing now the bandgap of both LED and PV cell. We consider in the following that $E_{g,\mathrm{LED}} = E_{g,\mathrm{PV}}$ as it should allow to reach the best performance:

- if $E_{g,\mathrm{LED}} > E_{g,\mathrm{PV}}$, all the energy above $E_{g,\mathrm{PV}}$ carried by photons coming from the LED is lost to the heat sink through thermalisation of the electron-hole pairs in the PV cell;
- if $E_{g,\mathrm{LED}} < E_{g,\mathrm{PV}}$, electrical power is consumed to make the LED emit electroluminescent radiation between $E_{g,\mathrm{LED}}$ and $E_{g,\mathrm{PV}}$, but this radiation cannot generate electron-hole pairs in the PV cell and directly goes to the heat sink (or worse, heat the PV cell).

This also helps with the derivation of analytical expressions. The impact of bandgap mismatch will be further discussed in Section 3.2.2.

The conversion of radiation into electricity (and vice-versa) is modelled through detailed balance in the radiative limit, in a manner mostly similar to [Harder & Green 2003]. This means we assume that

1. the absorption of one photon generates one electron-hole pair;
2. the recombination of one electron-hole pair causes the emission of one photon (i.e. there is no bulk non-radiative recombinations);
3. the transport of charge carriers towards the electrical contacts is ideal (i.e. there is no resistive losses);
4. the contacts are perfectly selective (i.e. there is no surface non-radiative recombinations).

In the general case, the electrical current density can be obtained from the electron-hole pair generation and recombination rates G and R:

$$J = e\big(\bar{G} - \bar{R}\big), \tag{2.16}$$

where e is the elementary charge and $\bar{X} = \int X(z)dz$. The above assumptions imply that only radiative events occur; since radiative generation and recombination are directly related to above-bandgap photon absorption and emission, it means that the net flow of charges inside a component is exactly the opposite of the net flow of above-bandgap photons. Radiative and electrical quantities are then linked through the simple relation

$$J = e\Big(\dot{N}_{\mathrm{abs}} - \dot{N}_{\mathrm{em}}\Big) = e\dot{N}_{\mathrm{net}}, \tag{2.17}$$

where subscripts "abs" and "em" correspond respectively to absorbed and emitted radiation ($J > 0$ means that an electrical current is generated). With an applied voltage U, the electrical power is expressed as

$$P = UJ = eU\dot{N}_{\mathrm{net}}. \tag{2.18}$$

This expression is a function of the chemical potential of absorbed and emitted radiation μ_{abs} and μ_{em}, and of the applied voltage U. However, μ_{em} and U should not be considered as two independent degrees of freedom, as they are strongly correlated. As explained in Section 1.1.2, μ_{em} is equal to the sum of electron and hole electrochemical potentials, and is often approximated by eU [Würfel 1982] (this will be further developed in Section 4.1.2). In this section and in

Chapter 3, we will assume that $\mu_{em} = eU$, this approximation being widely used in the literature (especially in detailed-balance analyses [DeSutter *et al.* 2017, Zhao *et al.* 2018, Sadi *et al.* 2020]). Its validity will be discussed in Part II of the manuscript (see Section 4.1.4), where charge carrier electrochemical potentials can be calculated.

Naturally, the net heat flux density exchanged between the LED and the PV cell q is different from the different electrical powers, and heat should be pumped from the heat source or released to the heat sink for the heat engine to work. However, it is important to understand that this heat is related to different physical phenomena, which impact differently the efficiency of the device. Taking the example of the LED (being mostly similar for the PV cell[6]), we have

- emission of below-bandgap radiation: as electron-hole pairs cannot generate below-bandgap photons, all the energy carried must be pumped from the heat source;
- charge supply: the electrons have a mean energy eU inside the electrical circuit, but that of electron-hole pairs in the semiconductor is close to E_g, and the difference of energy comes from the heat source;
- thermalisation: electroluminescent radiation is not only emitted at E_g, but also at higher energies, which means that some electron-hole pairs have an energy larger than E_g before recombining; the difference of energy with E_g is also provided by the heat source.

All these elements are gathered in Figure 2.5, in which $\dot{N} = \dot{N}_h - \dot{N}_c$ represents the net above-bandgap photon flux density. It illustrates that both q_{below} and $q_{above} - E_g\dot{N}$ (related to thermalisation) go completely from heat source to heat sink, and can therefore be considered as heat leakage: they have no impact on the power output, but decrease the efficiency as they increase the heat pumped from the heat source. Inversely, it means that the only energy that should be exchanged between the LED and the PV cell to reach the best efficiency is $E_g\dot{N}$. This analysis will guide the developments made in this section:

- the only way to satisfy $q = E_g\dot{N}$ with radiation is to consider monochromatic radiation at $E = E_g$ (Section 2.2.2); this allows to reach the largest efficiency, but comes at the cost of power which goes to zero as the spectral bandwidth goes to zero (since no energy is carried by purely monochromatic radiation);
- in order to have the largest power output, $\dot{N}$ should be as large as possible, and complete above-bandgap radiation should be considered (Section 2.2.3); then, some heat pumped from the heat source leaks to the heat sink ($q_{above} - E_g\dot{N}$) and the efficiency is decreased;
- the worst case scenario is to consider radiation over the complete spectrum (Section 2.2.4), which gives the same power output as the previous case but with lessened efficiency.

In the following of the chapter, the use of the chemical potential will be preferred to that of the voltage, expressing thus the net electrical power as $P = (\mu_c - \mu_h)\dot{N}$. This will allow to make the analytical derivations and the comparison with other energies (E_g,k_BT) easier. Also, μ will

[6]For the PV cell, we have:

- absorption of below-bandgap radiation: as it cannot be converted to charges, all the energy carried must go to the heat sink;
- charge collection: while electron-hole pairs have an energy close to E_g inside the component, the electron energy is the electrical circuit is only eU, and the difference of energy goes to the heat sink;
- thermalisation: after the absorption of a photon with energy $E > E_g$, the electron-hole pair has an energy E, but the surplus $E - E_g$ is quickly lost as heat to the heat sink.

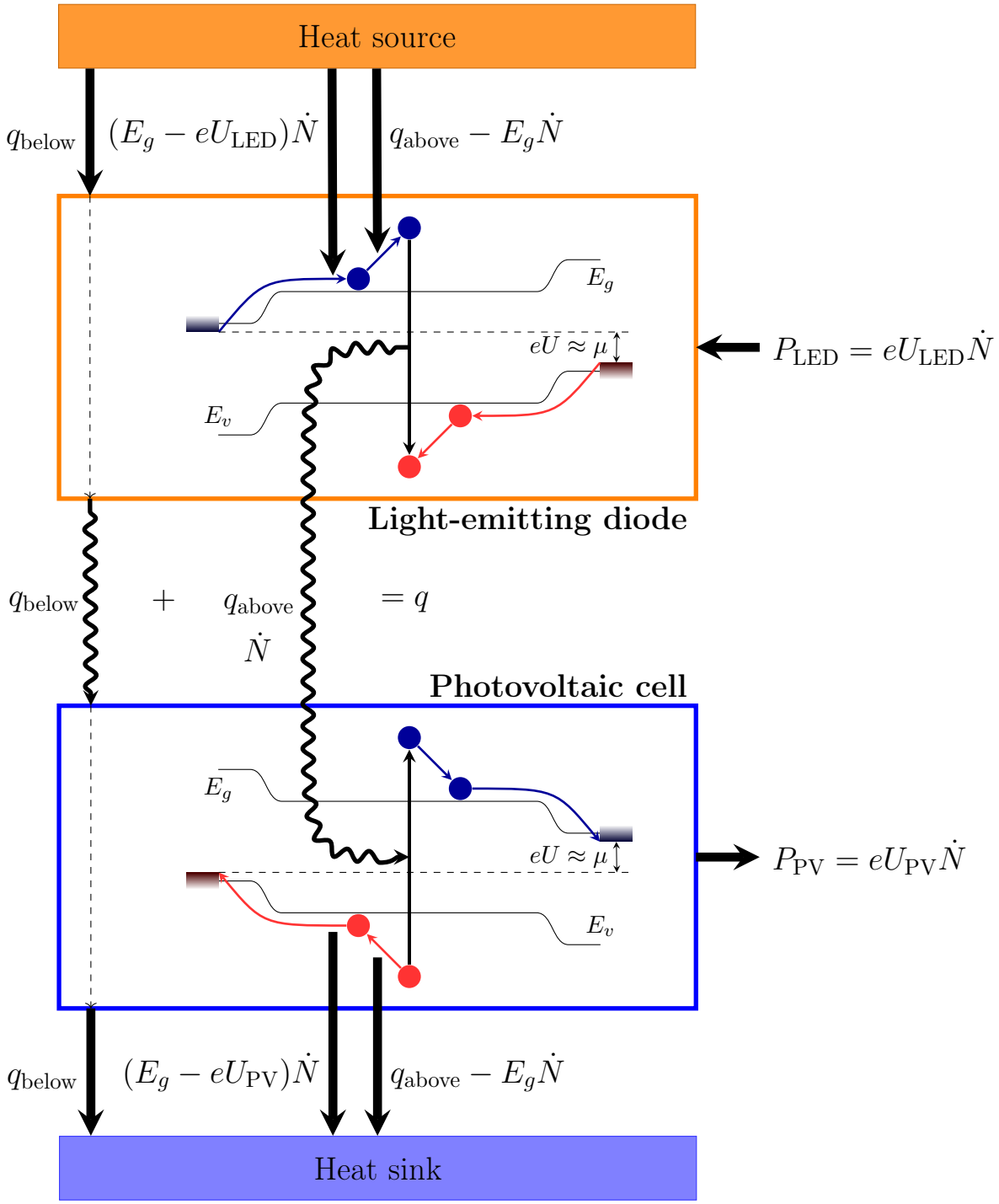

Figure 2.5: Schematic of the energy flow through a thermophotonic heat engine at the radiative limit.

simply be designated as the LED (resp. PV cell) chemical potential for the sake of brevity, even if it is strictly speaking the chemical potential of radiation emitted by the LED (resp. PV cell). Subscripts c and h will be used (while subscripts LED and PV could have been suitable and will often be used in the remaining of the manuscript) to improve the readability of the analytical developments.

2.2.2 Monochromatic radiation

We first consider monochromatic radiation exchanged at the bandgap energy E_g between the LED and the PV cell. The monochromatic efficiency of a TPX device is given by

$$\begin{aligned}\eta_\lambda &= \frac{P_\mathrm{c} - P_\mathrm{h}}{q - P_\mathrm{h}} \\ &= \frac{(\mu_\mathrm{c} - \mu_\mathrm{h})\dot{N}}{q - \mu_\mathrm{h}\dot{N}} \\ &= \frac{\mu_\mathrm{c} - \mu_\mathrm{h}}{E_g - \mu_\mathrm{h}},\end{aligned} \tag{2.19}$$

since $q = E_g\dot{N}$. The key to obtain the efficiency at maximum power is to determine the chemical potentials which satisfy

$$\frac{\partial P}{\partial \mu_\mathrm{h}}(\mu_\mathrm{h}, \mu_\mathrm{c}) = \frac{\partial P}{\partial \mu_\mathrm{c}}(\mu_\mathrm{h}, \mu_\mathrm{c}) = 0. \tag{2.20}$$

We focus on $\partial P/\partial \mu_\mathrm{h}$. Assuming that chemical potentials are uncorrelated ($d\mu_\mathrm{h}/d\mu_\mathrm{c} = 0$), we get from Eq. (2.18) that

$$\begin{aligned}\frac{\partial P}{\partial \mu_\mathrm{h}}(\mu_\mathrm{h}, \mu_\mathrm{c}) &= -\left(\dot{N}_\mathrm{h} - \dot{N}_\mathrm{c}\right) + (\mu_\mathrm{c} - \mu_\mathrm{h})\frac{\partial \dot{N}_\mathrm{h}}{\partial \mu_\mathrm{h}}(\mu_\mathrm{h}, \mu_\mathrm{c}) \\ &= \frac{1}{4\pi^2 c^2 \hbar^3} E_g^2 \delta E \left(f_{\mathrm{BE,c}} - f_{\mathrm{BE,h}}\left(1 - (f_{\mathrm{BE,h}} + 1)\frac{\mu_\mathrm{c} - \mu_\mathrm{h}}{k_\mathrm{B} T_\mathrm{h}}\right)\right),\end{aligned} \tag{2.21}$$

where $f_{\mathrm{BE},i} = (\exp\{((E_g - \mu_i)/k_\mathrm{B}T_i)\} - 1)^{-1}$ is the Bose-Einstein distribution of photons and δE the spectral bandwidth. Clearly, Eq. (2.21) is not easy to work with, mainly because of Bose-Einstein distributions. We can simplify these terms in two different ways:

- if $E_g - \mu \gg k_\mathrm{B}T$, the exponential term is much larger than 1 and f_BE can be written as $\exp\{((\mu - E_g)/k_\mathrm{B}T)\}$ (Boltzmann's approximation);
- if $E_g - \mu \ll k_\mathrm{B}T$, the Taylor expansion around 0 of $(\exp\{(x)\} - 1)^{-1}$ gives $f_\mathrm{BE} = k_\mathrm{B}T/(E_g - \mu)$.

There is no straightforward way to know which one of these two approximations is more correct; consequently, numerical results are used to discriminate them. We show in Figure 2.6 the maximum power output obtained for each LED chemical potential, for $T_\mathrm{h} = 301$ K and $T_\mathrm{h} = 3000$ K to consider a wide range of heat source temperatures. It appears that the maximum power is reached for $E_g - \mu_\mathrm{h} \ll k_\mathrm{B}T_\mathrm{c}$. Since $T_\mathrm{h} > T_\mathrm{c}$, it means that $E_g - \mu_\mathrm{h} \ll k_\mathrm{B}T_\mathrm{h}$ and Taylor's expansion should allow obtaining accurate results. Partial derivatives of the electrical power with respect to chemical potential using $f_\mathrm{BE} \approx k_\mathrm{B}T/(E_g - \mu)$ gives

$$\frac{\partial P}{\partial \mu_\mathrm{h}}(\mu_\mathrm{h}, \mu_\mathrm{c}) = \frac{1}{4\pi^2 c^2 \hbar^3} E_g^2 \delta E \left(-\frac{k_\mathrm{B}T_\mathrm{h}}{E_g - \mu_\mathrm{h}} + \frac{k_\mathrm{B}T_\mathrm{c}}{E_g - \mu_\mathrm{c}} + \frac{\mu_\mathrm{c} - \mu_\mathrm{h}}{E_g - \mu_\mathrm{h}}\frac{k_\mathrm{B}T_\mathrm{h}}{E_g - \mu_\mathrm{h}}\right) \tag{2.22a}$$

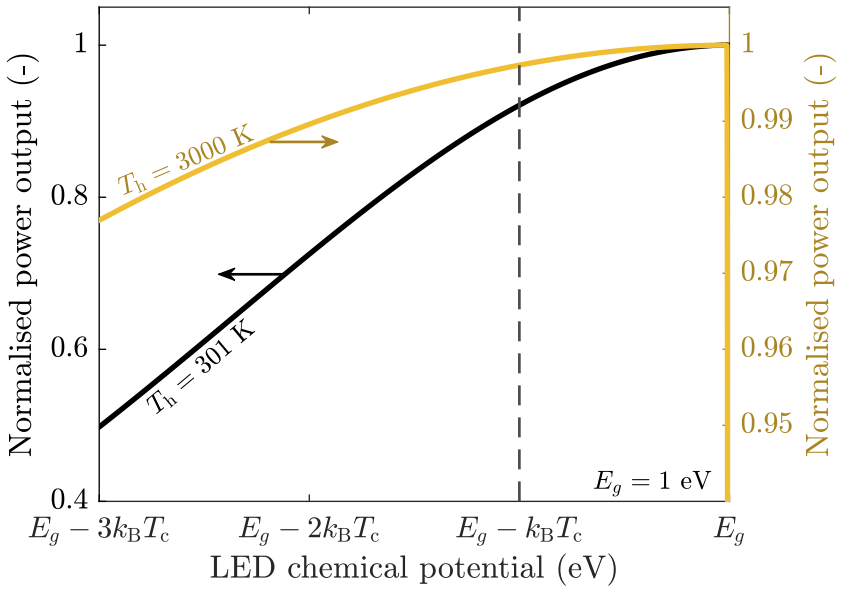

Figure 2.6: Variation of power output with LED chemical potential, for an LED temperature of 301 and 3000 K. Different scales are used for the two temperatures considered to improve readability.

Then,

$$\begin{aligned}\frac{\partial P}{\partial \mu_h}(\mu_h, \mu_c) = 0 &\Leftrightarrow -\frac{k_B T_h}{E_g - \mu_h} + \frac{k_B T_c}{E_g - \mu_c} + \frac{\mu_c - \mu_h}{E_g - \mu_h}\frac{k_B T_h}{E_g - \mu_h} = 0 \\ &\Leftrightarrow \frac{k_B T_c}{E_g - \mu_c} = \frac{k_B T_h}{E_g - \mu_h}\frac{E_g - \mu_c}{E_g - \mu_h} \\ &\Leftrightarrow \frac{E_g - \mu_c}{E_g - \mu_h} = \sqrt{\frac{T_c}{T_h}} \\ &\Leftrightarrow \eta_\lambda = 1 - \sqrt{\frac{T_c}{T_h}} = \eta_{CA},\end{aligned} \tag{2.23}$$

exactly the Curzon-Ahlborn efficiency. This was obtained using only one partial derivative in Eq. (2.20), but the second provides exactly the same result. The system of equations is thus underdetermined, and the maximum generated power is reached for an infinite number of chemical potential couples: using the Taylor expansion of f_{BE} allows obtaining a maximum power line rather than a maximum power point. While such a maximum power line cannot be observed when looking at the whole range of LED chemical potential in Figure 2.6 (since the maximum power output should be constant with the LED chemical potential to satisfy it), it is for $E_g - \mu_h \ll k_B T_c$, which is where the maximum power point is located. The maximum power output can then be written as

$$P_{max} = \frac{k_B T_h}{4\pi^2 c^2 \hbar^3} \eta_{CA}^2 E_g^2 \delta E. \tag{2.24}$$

The efficiency at maximum power obtained numerically with the complete expression of f_{BE} is shown in Figure 2.7, and matches perfectly the Curzon-Ahlborn efficiency. While derived for a monochromatic radiation with complete transmission of propagative waves (i.e. satisfying Planck's law), the same result can be obtained with any other value of transmission (partial transmission of propagative modes, participation of evanescent modes, etc.) since the transmission function anyway cancels out between the second and the third line of Eq. (2.19). This is an

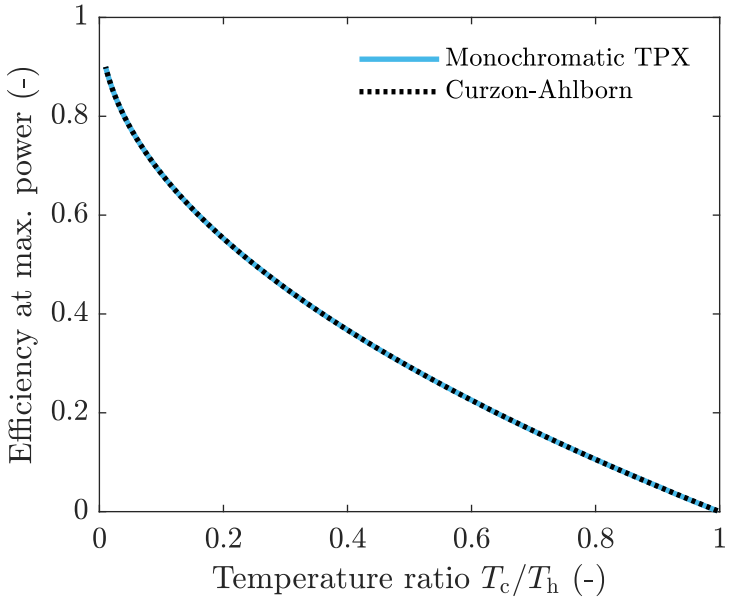

Figure 2.7: Variation of the efficiency at maximum power as a function of the temperature ratio T_h/T_c for the monochromatic TPX device (obtained for a 1 eV bandgap).

important result for TPX energy harvesting as it sets Curzon-Ahlborn efficiency as the upper limit for the conversion efficiency at maximum power, since monochromatic radiation shall lead to the best achievable efficiencies. This result is consistent with the qualitative discussion provided at the beginning of this section. It is interesting to notice that while the monochromatic TPX efficiency is (almost) equal to the Curzon-Ahlborn limit, the source of irreversilibities in the TPX devices (the conversion of heat into radiation) is completely different from the one considered in the original paper (imperfect connections with thermal reservoirs) [Curzon & Ahlborn 1975]. We should lastly mention that the efficiency at maximum power is in fact only weakly affected by the exact expression of f_{BE}. Indeed, if Boltzmann's approximation is considered (which is incorrect, as shown previously) the efficiency at maximum power point (MPP) obtained is

$$\eta_{\lambda,\mathrm{MPP}} = \frac{\eta_C^2}{\eta_C - (1-\eta_C)\ln(1-\eta_C)}, \tag{2.25}$$

which is exactly the result obtained in [Tu 2008] for a Feynman ratchet heat engine, and deviates from η_{CA} by only 5 percent points at most for T_c/T_h close to 0. The details of calculations are shown in Appendix D.1.

2.2.3 Above-bandgap radiation

We now consider the complete above-bandgap radiation ($\Delta E \to \infty$). Even more than with monochromatic radiation, assumptions will be required to be able to derive an efficiency at maximum power. To understand which ones could be accurate, we show in Figure 2.8 the efficiency at maximum power along with the LED and PV cell chemical potentials for different bandgap energies. Regarding the efficiency (Figure 2.8a), only the data obtained for $T_h = 600$ K is shown, since the variations with bandgap energy are mostly similar for other heat source temperatures. The efficiency at maximum power increases at a rapid rate roughly up to a bandgap of 1 eV, and seems to approach a plateau as the bandgap gets larger. This echoes the maximum efficiency obtained for the LHE with passive emitter in the first section of this chapter,

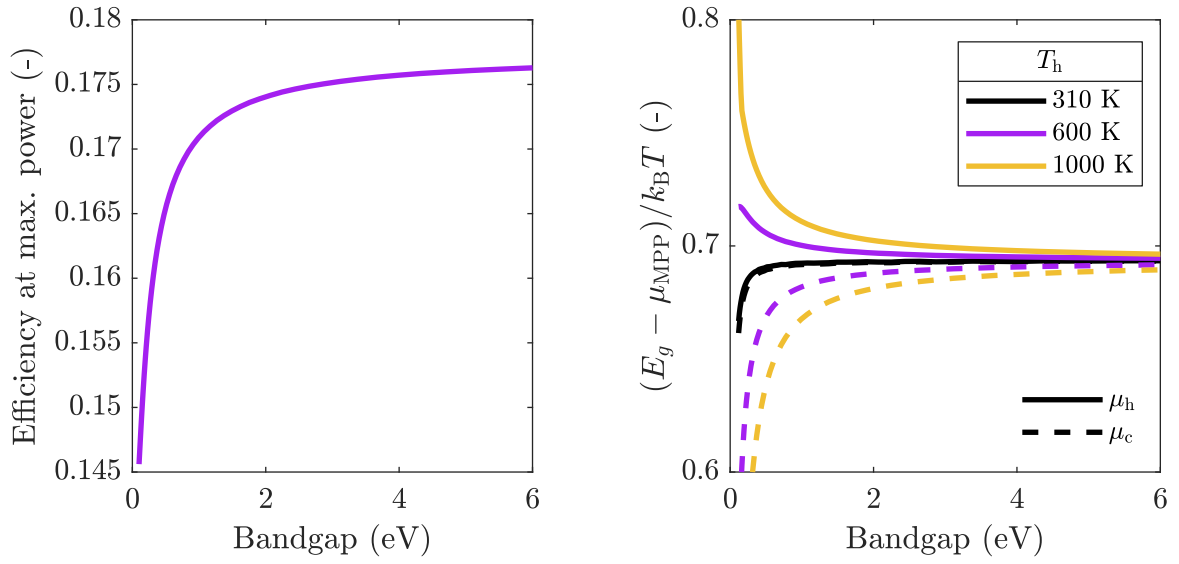

(a) (b)

Figure 2.8: (a) Variation of efficiency at maximum power with bandgap for $T_{\mathrm{h}} = 600$ K. (b) LED and PV cell chemical potentials at maximum power point given relatively to the bandgap and the energy $k_{\mathrm{B}}T$ (resp. $k_{\mathrm{B}}T_{\mathrm{h}}$ and $k_{\mathrm{B}}T_{\mathrm{c}}$) for various heat source temperatures.

which was increasing with bandgap energy as the net entropy carried by radiation was reduced. Apropos the optimum chemical potential (Figure 2.8b), much information are represented. We should just gather those of interest for the development of an expression of the efficiency at maximum power. For any of the two chemical potentials and the three temperatures considered:

- the ratio $(E_g - \mu_{\mathrm{MPP}})/k_{\mathrm{B}}T$ remains in a narrow interval (between 0.6 and 0.8) for all bandgaps except the smallest - in comparison to the monochromatic case, we have $E_g - \mu_{\mathrm{MPP}} < k_{\mathrm{B}}T$ but not $E_g - \mu_{\mathrm{MPP}} \ll k_{\mathrm{B}}T$;
- $(E_g - \mu_{\mathrm{MPP}})/k_{\mathrm{B}}T$ tends towards a value close to 0.7 as the bandgap gets larger.

Clearly, since $E_g - \mu_{\mathrm{MPP}}$ is close to $k_{\mathrm{B}}T$, neither of the two approximations of the Bose-Einstein distribution proposed for monochromatic radiation (Boltzmann's approximation or Taylor's expansion) can work for complete above-bandgap radiation. We will need therefore to use the complete expression based on polylogarithm shown in Eq. (2.9). As the main objective is to obtain an upper-bound efficiency for this broadband radiation, we can focus on large bandgaps where the largest efficiencies are reached; this should allow to simplify the polylogarithmic expression.

We first want to prove that in the limit of infinite bandgaps, $(E_g - \mu_{\mathrm{h,MPP}})/k_{\mathrm{B}}T_{\mathrm{h}} = (E_g - \mu_{\mathrm{c,MPP}})/k_{\mathrm{B}}T_{\mathrm{c}} = x$, where x is a value which remains to be found and should be close to 0.7 according to numerical results. To do so, we use the polylogarithmic expression but consider only the first-order polylogarithm to express the power output, this term being dominant for large bandgaps as long as $E_g - \mu$ does not go to infinity. We get

$$\begin{aligned} P &= (\mu_{\mathrm{c}} - \mu_{\mathrm{h}})\left(\dot{N}_h - \dot{N}_c\right) \\ &= \frac{E_g^2}{4\pi^2 c^2 \hbar^3}(\mu_{\mathrm{c}} - \mu_{\mathrm{h}})\left[\mathrm{Li}_1\left(\exp\left(\frac{\mu_{\mathrm{h}} - E_g}{k_{\mathrm{B}}T_{\mathrm{h}}}\right)\right)k_{\mathrm{B}}T_{\mathrm{h}} - \mathrm{Li}_1\left(\exp\left(\frac{\mu_{\mathrm{c}} - E_g}{k_{\mathrm{B}}T_{\mathrm{c}}}\right)\right)k_{\mathrm{B}}T_{\mathrm{c}}\right]. \end{aligned} \tag{2.26}$$

Defining x_i as $(E_g - \mu_i)/k_{\mathrm{B}}T_i$ and X_i as $\exp(-x_i)$ (i being either h or c) and using $\mathrm{Li}_1(x) =$

$-\ln(1-x)$ gives

$$\begin{aligned}
P &= \frac{E_g^2}{4\pi^2c^2\hbar^3}(\mu_\mathrm{c} - E_g + E_g - \mu_\mathrm{h})\left(k_\mathrm{B}T_\mathrm{h}\,\mathrm{Li}_1\left(e^{-x_\mathrm{h}}\right) - k_\mathrm{B}T_\mathrm{c}\,\mathrm{Li}_1\left(e^{-x_\mathrm{c}}\right)\right)\\
&= \frac{E_g^2}{4\pi^2c^2\hbar^3}(x_\mathrm{h}k_\mathrm{B}T_\mathrm{h} - x_\mathrm{c}k_\mathrm{B}T_\mathrm{c})\left(k_\mathrm{B}T_\mathrm{h}\,\mathrm{Li}_1\left(e^{-x_\mathrm{h}}\right) - k_\mathrm{B}T_\mathrm{c}\,\mathrm{Li}_1\left(e^{-x_\mathrm{c}}\right)\right)\\
&= \frac{E_g^2k_\mathrm{B}^2T_\mathrm{h}^2}{4\pi^2c^2\hbar^3}\left(x_\mathrm{h} - \frac{T_\mathrm{c}}{T_\mathrm{h}}x_\mathrm{c}\right)\left(\mathrm{Li}_1\left(e^{-x_\mathrm{h}}\right) - \frac{T_\mathrm{c}}{T_\mathrm{h}}\,\mathrm{Li}_1\left(e^{-x_\mathrm{c}}\right)\right)\\
&= \frac{E_g^2k_\mathrm{B}^2T_\mathrm{h}^2}{4\pi^2c^2\hbar^3}\left(\ln(X_\mathrm{h}) - \frac{T_\mathrm{c}}{T_\mathrm{h}}\ln(X_\mathrm{c})\right)\left(\ln(1-X_\mathrm{h}) - \frac{T_\mathrm{c}}{T_\mathrm{h}}\ln(1-X_\mathrm{c})\right).
\end{aligned} \tag{2.27}$$

Using this last expression, we can show that the power output reaches a maximum for $X_\mathrm{h} = X_\mathrm{c} = 1/2$; the details can be found in Appendix D.2. This means that the maximum is reached for $x = \ln(2)$: $\ln(2)$ being approximatively equal to 0.693, x is in perfect agreement with the numerical results shown in Figure 2.8b. The maximum power is then expressed as

$$P_\mathrm{max} = \frac{\left(\ln(2)E_gk_\mathrm{B}T_\mathrm{h}\eta_\mathrm{C}\right)^2}{4\pi^2c^2\hbar^3} \tag{2.28}$$

and tends to infinity as the bandgap increases; of course, this holds only because no other additional losses are considered (this will be further studied in the next chapter). Interestingly, the radiation exchanged between the LED and the PV cell at the maximum power point (and for infinitely large bandgaps) has some specific features. The main one is probably that $(E_g - \mu_\mathrm{h,MPP})/k_\mathrm{B}T_\mathrm{h} = (E_g - \mu_\mathrm{c,MPP})/k_\mathrm{B}T_\mathrm{c}$, which means that no radiation is exchanged at the bandgap energy. This is somewhat counterintuitive as the total radiative heat flux is then far from its maximum. Also, we can notice that for $x = \ln(2)$, $f_\mathrm{BE}(x)$ exactly equals 1. Still, we miss a physical explanation of why $f_\mathrm{BE}(x_\mathrm{h}) = f_\mathrm{BE}(x_\mathrm{c}) = 1$ gives maximum power - this could be an interesting development of the current work.

Anyway, we can now derive the efficiency at maximum power for above-bandgap radiation. The efficiency for any couple of chemical potentials can be expressed as:

$$\eta = \frac{(\mu_\mathrm{c} - \mu_\mathrm{h})\dot{N}}{q - \mu_\mathrm{h}\dot{N}} = \frac{\mu_\mathrm{c} - \mu_\mathrm{h}}{\frac{E_g}{\rho} - \mu_\mathrm{h}}, \tag{2.29}$$

where $\rho = E_g\dot{N}/q$ corresponds to the fraction of energy carried by photons which is useful to conversion. Then, using $(E_g - \mu_\mathrm{h,MPP})/k_\mathrm{B}T_\mathrm{h} = (E_g - \mu_\mathrm{c,MPP})/k_\mathrm{B}T_\mathrm{c} = x$, we find that

$$\frac{E_g - \mu_\mathrm{h,MPP}}{k_\mathrm{B}T_\mathrm{h}} = \frac{E_g - \mu_\mathrm{c,MPP}}{k_\mathrm{B}T_\mathrm{c}} \Leftrightarrow \frac{\mu_\mathrm{c,MPP} - \mu_\mathrm{h,MPP}}{E_g - \mu_\mathrm{h,MPP}} = \eta_\mathrm{C} \tag{2.30a}$$

$$\Leftrightarrow E_g - \mu_\mathrm{h,MPP} = x\cdot k_\mathrm{B}T_\mathrm{h} = \frac{x\cdot k_\mathrm{B}T_\mathrm{c}}{1-\eta_\mathrm{C}}$$

$$\Leftrightarrow \frac{E_g}{E_g - \mu_\mathrm{h,MPP}} = (1-\eta_\mathrm{C})\frac{E_g}{x\cdot k_\mathrm{B}T_\mathrm{c}}. \tag{2.30b}$$

Dividing by $E_g - \mu_\mathrm{h,MPP}$ at the numerator and denominator of the expression given in Eq. (2.29) allows obtaining

$$\eta_\mathrm{MPP} = \frac{\eta_\mathrm{C}}{1 + \left(\frac{1}{\rho} - 1\right)(1-\eta_\mathrm{C})\frac{1}{x}\frac{E_g}{k_\mathrm{B}T_\mathrm{c}}}, \tag{2.31}$$

in which the only remaining unknown is ρ, which should now be estimated. Since we work in the limit case of bandgaps much larger than the reference energy $k_\mathrm{B}T$, the terms with the largest powers of E_g should dominate the polylogarithmic expression. However, if only one term is kept for $\dot{N}_i$ and q_i, it gives

$$\rho = \frac{E_g \dot{N}}{q} = \frac{E_g \cdot (k_\mathrm{B}T_\mathrm{h} - k_\mathrm{B}T_\mathrm{c}) E_g^2 \,\mathrm{Li}_1(e^{-x})}{(k_\mathrm{B}T_\mathrm{h} - k_\mathrm{B}T_\mathrm{c}) E_g^3 \,\mathrm{Li}_1(e^{-x})} = 1 \Rightarrow \eta_\mathrm{MPP} = \eta_\mathrm{C}, \tag{2.32}$$

which cannot be correct as power output is zero when operating at the Carnot efficiency. Consequently, we use both first and second order polylogarithm to express $\dot{N}_i$ and q_i:

$$\begin{aligned}\rho &= E_g \frac{(k_\mathrm{B}T_\mathrm{h} - k_\mathrm{B}T_\mathrm{c}) E_g^2 \,\mathrm{Li}_1(e^{-x}) + 2(k_\mathrm{B}^2T_\mathrm{h}^2 - k_\mathrm{B}^2T_\mathrm{c}^2) E_g \,\mathrm{Li}_2(e^{-x})}{(k_\mathrm{B}T_\mathrm{h} - k_\mathrm{B}T_\mathrm{c}) E_g^3 \,\mathrm{Li}_1(e^{-x}) + 3(k_\mathrm{B}^2T_\mathrm{h}^2 - k_\mathrm{B}^2T_\mathrm{c}^2) E_g^2 \,\mathrm{Li}_2(e^{-x})} \\ &= \frac{E_g \,\mathrm{Li}_1(e^{-x}) + 2(k_\mathrm{B}T_\mathrm{h} + k_\mathrm{B}T_\mathrm{c}) \,\mathrm{Li}_2(e^{-x})}{E_g \,\mathrm{Li}_1(e^{-x}) + 3(k_\mathrm{B}T_\mathrm{h} + k_\mathrm{B}T_\mathrm{c}) \,\mathrm{Li}_2(e^{-x})}.\end{aligned} \tag{2.33}$$

Then,

$$\begin{aligned}\frac{1}{\rho} - 1 &= \frac{(k_\mathrm{B}T_\mathrm{h} + k_\mathrm{B}T_\mathrm{c}) \,\mathrm{Li}_2(e^{-x})}{E_g \,\mathrm{Li}_1(e^{-x}) + 2(k_\mathrm{B}T_\mathrm{h} + k_\mathrm{B}T_\mathrm{c}) \,\mathrm{Li}_2(e^{-x})} \\ &\sim \frac{k_\mathrm{B}T_\mathrm{h} + k_\mathrm{B}T_\mathrm{c}}{E_g} \frac{\mathrm{Li}_2(e^{-x})}{\mathrm{Li}_1(e^{-x})},\end{aligned} \tag{2.34}$$

and thus

$$\begin{aligned}\left(\frac{1}{\rho} - 1\right)(1 - \eta_\mathrm{C}) \frac{1}{x} \frac{E_g}{k_\mathrm{B}T_\mathrm{c}} &\sim \frac{T_\mathrm{c}}{T_\mathrm{h}} \left(1 + \frac{T_\mathrm{h}}{T_\mathrm{c}}\right) \frac{1}{x} \frac{\mathrm{Li}_2(e^{-x})}{\mathrm{Li}_1(e^{-x})} \\ &\sim (2 - \eta_\mathrm{C}) \frac{1}{x} \frac{\mathrm{Li}_2(e^{-x})}{\mathrm{Li}_1(e^{-x})}.\end{aligned} \tag{2.35}$$

$x = \ln(2)$ is in fact one of the few values for which we have an analytical expression of the polylogarithmic terms, which gives

$$\chi = \frac{1}{x} \frac{\mathrm{Li}_2(e^{-x})}{\mathrm{Li}_1(e^{-x})} = \frac{1}{\ln(2)} \frac{\frac{\pi^2}{12} - \frac{1}{2}\ln^2(2)}{\ln(2)} = \frac{1}{2}\left(\frac{1}{6}\left(\frac{\pi}{\ln(2)}\right)^2 - 1\right) \approx 1.21. \tag{2.36}$$

Therefore, the highest efficiency at maximum power is

$$\eta_\mathrm{MPP} = \frac{\eta_\mathrm{C}}{1 + (2 - \eta_\mathrm{C})\chi} \equiv \eta_{E_g \to \infty}. \tag{2.37}$$

This analytical expression is compared to numerical results in Figure 2.9, obtained respectively for $E_g = 1$ eV and $E_g = 100$ keV (labelled $E_g \to \infty$ in the figure). This last value may seem unnecessarily large, but is in fact required to reach the aimed precision, especially for the highest heat source temperature. The expression given in Eq. (2.37) shows a perfect agreement with the data obtained for $E_g \to \infty$. In comparison, the efficiency at maximum power obtained for a bandgap of 1 eV fits quite well the analytical result for low heat source temperature (i.e. $T_\mathrm{c}/T_\mathrm{h}$ close to 1) but gets further and further off as T_h increases, the approximation $E_g \gg k_\mathrm{B}T$ being less and less true. This is not a surprise, as we could already see in Figure 2.8a that the efficiency at $E_g = 1$ eV was notably lower than the maximum. The absolute difference with the expression of Eq. (2.37) is slightly lower than 1 percent point for $T_\mathrm{c}/T_\mathrm{h} = 0.5$ (at which $\eta_{E_g \to \infty} = 17.7\%$),

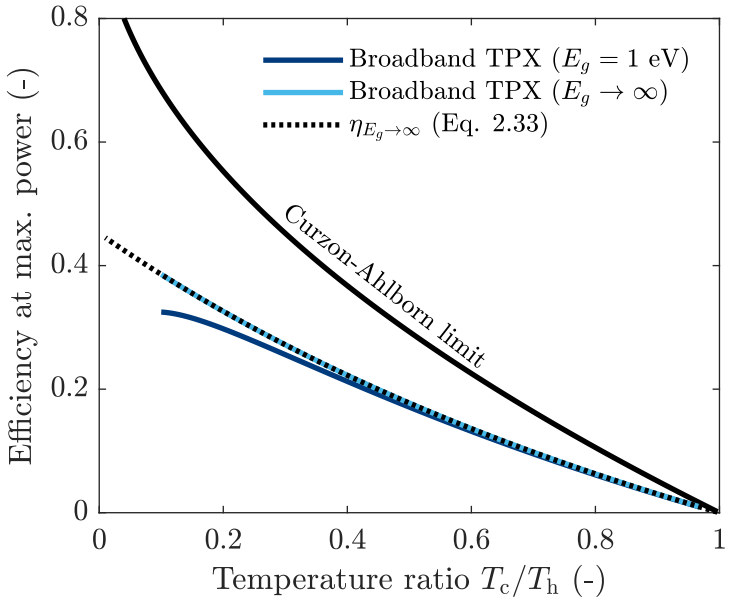

Figure 2.9: Variation of the efficiency at maximum power of a TPX device as a function of the temperature ratio T_h/T_c with complete above-bandgap radiation.

but goes up to 6% for $T_c/T_h = 0.1$.

In comparison to the Curzon-Ahlborn limit obtained for monochromatic radiation, $\eta_{E_g\to\infty}$ is significantly lower. Considering that T_c/T_h is close to one for instance, we can show that

$$\eta_{CA} \sim \frac{\eta_C}{2}, \tag{2.38a}$$

$$\eta_{E_g\to\infty} \sim \frac{\eta_C}{1+2\chi}, \tag{2.38b}$$

which means that in this range of temperature ratio $\eta_{E_g\to\infty}$ is only $2/(1+2\chi) \approx 60\%$ of the Curzon-Ahlborn efficiency. This gets even more important as T_h increases, since $\eta_{E_g\to\infty}$ does not reach 1 for $T_h \to \infty$ (contrary to usual efficiencies) but rather goes to $1/(1+\chi) \approx 45\%$. Since $\eta_{E_g\to\infty}$ is so far from the result obtained with monochromatic radiation, does this mean that the radiation exchanged is far from monochromatic? To answer this question, the spectrum of the radiation exchanged is shown in Figure 2.10 using $(E_g - \mu)/k_B T = \ln(2)$ for both the LED and the PV cell. We can notice that the normalised spectra obtained for a 1 eV bandgap or an infinite (100 keV) bandgap are mostly similar, the former being slightly broadened towards large energy. Even in this case, 99% of the heat flux is exchanged within a 0.3 eV bandwidth, with $E_{peak} = 1.03$ eV; in comparison, the radiation of a blackbody at temperature 6000 K peaks at 1.5 eV and has a bandwidth of 5 eV, while typical lasers have a bandwidth (called linewidth for this application) much smaller than 1 meV. These bandwidths are gathered in Table 2.1 along

Table 2.1: Bandwidth and quality factor of radiation emitted by common sources.

	Visible laser	Light-emitting diode	Blackbody (6000 K)
Bandwidth (eV)	$\ll 10^{-3}$	0.3	5
Quality factor (-)	$\gg 10^{3}$	3.4	0.3

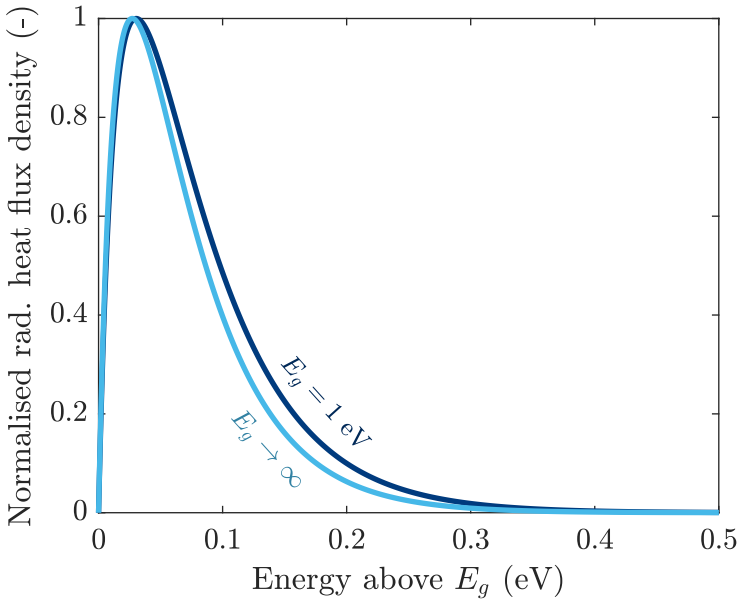

Figure 2.10: Spectrum of the radiative heat flux exchanged between the LED and the PV cell for $(E_g - \mu)/k_B T = \ln(2)$ and for $T_h = 600$ K.

with the associated quality factors $E_{peak}/\delta E$. It is clear that the electroluminescent radiation exchanged is not as broadband as thermal radiation, but far from the monochromatic radiation of a laser.

We finish this section by connecting the two analytical limits derived for monochromatic and complete above-bandgap radiation. We show in Figure 2.11 how the maximum power output and the related efficiency change with the transmission bandwidth ΔE used in Eq. (2.1) (as a reminder, assuming no radiation is exchanged above $E_g + \Delta E$), in a manner similar to the work done in [McSherry *et al.* 2019] for the maximum efficiency. The transition from η_{CA} (monochromatic) to $\eta_{E_g \to \infty}$ (complete above-bandgap radiation) appears clearly. This figure also allows to understand that the monochromatic approximation breaks down for bandwidths greater than 1 meV, while the complete spectrum limit is reached for bandwidths greater than 0.3, which is consistent with the spectra provided in Figure 2.10.

2.2.4 Addition of below-bandgap losses

A last question we could ask ourselves is: what is the impact of photons exchanged below the bandgap on efficiency? In the limit of infinitely large bandgaps, we can in fact assume that the thermal below-bandgap radiation corresponds to the complete thermal radiation, i.e. using the Stefan-Boltzmann law:

$$q_b = \sigma\left(T_h^4 - T_c^4\right). \tag{2.39}$$

The efficiency is then, keeping the same notation as before (i.e. q, $\dot{N}$ for above-bandgap quantities)

$$\eta = \frac{P}{q - \mu_h \dot{N} + q_b} = \frac{\eta_C}{1 + (2 - \eta_C)\chi + \frac{q_b}{\dot{N} x k_B T_h}}. \tag{2.40}$$

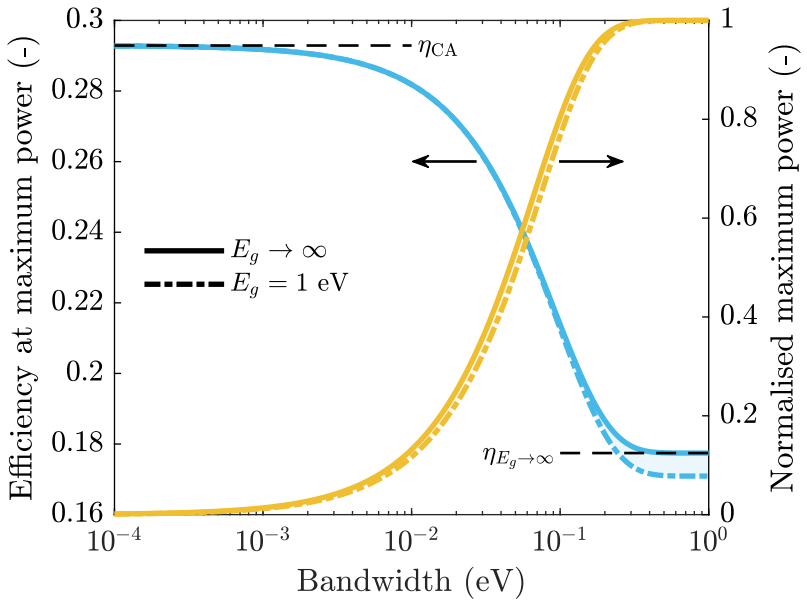

Figure 2.11: Variation of the maximum power output and the related efficiency with radiation bandwidth.

In the limit of large bandgaps, we have $\dot{N} \propto k_B(T_h - T_c)E_g^2 \,\mathrm{Li}_1(\exp(-x)) \to \infty$ as E_g goes to infinity; therefore, even with below-bandgap losses

$$\eta_{MPP} \sim \eta_{E_g\to\infty}. \tag{2.41}$$

Therefore, the efficiency at maximum power point should not be significantly changed by the addition of below-bandgap photons, as the electroluminescent radiation exchanged far exceeds the energy carried by below-bandgap radiation. This holds as long as the bandgap is large enough and no other losses are considered - we will see in the next chapter how additional conversion losses can change this result.

2.3 To sum up

This chapter helped to deepen the understanding of the thermodynamics of thermophotonic heat engines. First, we showed that radiative heat engines with an active emitter can ideally (i.e. without entropy generation) work at the Carnot limit. To reach such an efficiency with TPX would require to either work at the monochromatic limit, or with a multicolour converter [Green 2006] (i.e. an infinite stack of monochromatic converters) to prevent thermalisation losses if the complete above-bandgap heat flux is considered. Anyway, this holds for any bandgap for TPX, which means that a TPX device is simply a Carnot engine at the reversible limit. In contrast, the maximum efficiency of TPV systems goes from Landsberg limit to the Carnot limit as the bandgap increases. In this regard, a thermophotonic device can ultimately be a more efficient heat engine than a thermophotovoltaic device - even if a monochromatic/multicolour converter is more difficult to make for TPX than for TPV as both the absorber and the emitter should be properly designed.

Second, we highlighted that if the efficiency at maximum power for a monochromatic TPX device can reach the Curzon-Ahlborn limit, it decreases significantly (relatively by 40 to 55%) when considering the complete above-bandgap radiation because of thermalisation losses. Of course, it

is necessary to consider a non-monochromatic radiation to be able to generate any power: there is thus a trade-off between power and efficiency, and a limited bandwidth can be considered if the efficiency at maximum power obtained for broadband radiation is too low for a given application.

Note that the way the efficiency at maximum power was derived for TPX in the case of broadband radiation cannot be directly applied to TPV. In our case, both power and efficiency increases with the bandgap energy, and we could directly study the limiting case of $E_g \to \infty$. For TPV however, since the radiation coming from the emitter is inherently limited by Planck's law, it will go to zero as $E_g \to \infty$ - and so will do the power output. If one wants to study a TPV device around the true maximum power point, it is thus necessary to search for the optimum bandgap first. This is typically what has been done for PV in [Shockley & Queisser 1961], and derived analytically in [Green 2012a] - even if no complete analytical expression has been derived, since the optimum bandgap has only been expressed numerically in the literature.

Up to now, every component of the device was assumed to work at the radiative limit - i.e., that the energy carried by electron-hole pairs is ultimately converted to radiation or to electrical power. In the next chapter, we will see how non-radiative recombinations, which convert this energy into heat, impacts the performance - this will be done along with the consideration of near-field radiation.

Chapter 3

Detailed-balance analysis of GaAs-based devices in the near field

Contents

3.1 A small discussion on modelling . . . 57
3.1.1 Near-field radiation calculations: phenomenological vs. numerical . . . 57
3.1.2 On non-radiative recombinations and the vagueness of the quantum efficiency definition . . . 58
3.2 Why GaAs-based structures? . . . 60
3.2.1 Required properties for performant thermophotonics . . . 60
3.2.2 Aligning bandgaps for optimal conversion . . . 62
3.3 Performance of an AlGaAs-GaAs device in the near field . . . 63
3.3.1 Power-voltage characteristics . . . 64
3.3.2 Radiation in the near field . . . 69
3.3.3 Efficiency and below-bandgap photons . . . 72
3.4 Beyond the exoreversible limit . . . 76
3.4.1 Introduction . . . 76
3.4.2 Numerical resolution . . . 78
3.4.3 Performance for above-bandgap radiation . . . 81
3.4.4 Impact of below-bandgap photons . . . 83
3.5 To sum up . . . 85

3.1 A small discussion on modelling

3.1.1 Near-field radiation calculations: phenomenological vs. numerical

We now aim to derive the ideal performance of devices in the near field, and study how the main loss channels will impact the performance. In the far-field developments shown in the previous chapter, the modified Planck law sets an upper bound to absorption and emission. There is no such straightforward limit in the near field, as frustrated and surface modes participate to the heat transfer (see Section 1.2.1). The simplest way to account for them is to multiply the standard blackbody spectrum by a near-field enhancement factor f_{NF}, as done in [McSherry *et al.* 2019]. In general, such a factor lacks any physical basis, and is used to fit the enhancement at a given gap distance. Still, there is one value of interest for this parameter. Recall the expression of the near-field radiative heat transfer given in Eq. (1.15). If the transmission coefficient is assumed to be maximum (thus equal to 2), we get:

$$q_\omega = \hbar\omega\Delta f_{\mathrm{BE}}^0 \frac{k_{\rho,\max}^2}{4\pi^2} \tag{3.1}$$

For far-field radiation, we should only account for propagative modes and $k_{\rho,\max} = \omega/c$: we then get Planck's law back. If we now consider both propagative and frustrated modes, $k_{\rho,\max} = n\omega/c$ and thus $q_\omega = n^2 q_\omega^{BB}$, n being the refractive index of the emitter/absorber. Thus, $f_{\mathrm{NF}} = n^2$ corresponds to the perfect transmission of these two modes, surface modes being neglected[1]. Such a high transmission can only be reached for distance much smaller than the characteristic wavelength and for weakly absorbing materials, as discussed in [Zhang 2007]. Notice that the use of such near-field factors (independent of the wavelength) in the expressions derived in Chapter 2 will not change the efficiencies obtained, since it can directly be simplified (through factorisation in numerator and denominator).

Anyway, to avoid being limiting by these rather strong assumptions, we choose to compute numerically the integral over k_ρ of the transmission coefficient required to obtain the near-field radiative heat transfer between the LED and the PV cell. Both components are assumed to be semi-infinite, and the analytical expression of the transmission coefficient presented in Section 1.2.2 can be used to compute the heat flux density q and the photon flux density $\dot{N}$ (see Eq. (1.16)).

3.1.2 On non-radiative recombinations and the vagueness of the quantum efficiency definition

In this chapter, we will move away from the radiative limit and consider non-radiative recombinations. As explained in Section 1.1.2, when such recombinations occur, the energy carried by electron-hole pair is lost into heat rather than converted to radiation. To keep the model simple, we will not try to compute each contribution individually, but will simply express the total non-radiative recombination rate as a function of the radiative recombination rate and the fraction of recombinations being radiative (which will be manually set). One question is then: how to name this last parameter? In [Harder & Green 2003], it is called the external quantum efficiency; however, since the quantum efficiency has different definitions, we first review them.

Generally, two different quantum efficiencies can be considered: the Internal Quantum Efficiency (IQE) and the External Quantum Efficiency (EQE). In an LED, these two quantities describe the efficiency in converting electron-hole pairs into photons and are expressed as

$$\mathrm{IQE} = \frac{\bar{R}_{\mathrm{rad}}}{\bar{R}} = \frac{\bar{R}_{\mathrm{rad}}}{\bar{R}_{\mathrm{rad}} + \bar{R}_{\mathrm{nonrad}}}, \tag{3.2a}$$

$$\mathrm{EQE} = \frac{\bar{R}_{\mathrm{rad,ext}}}{\bar{R}} = \frac{\bar{R}_{\mathrm{rad,ext}}}{\bar{R}_{\mathrm{rad}}}\mathrm{IQE}. \tag{3.2b}$$

As in the previous chapter, $\bar{R}$ represents the total recombination rate obtained after integration over the whole thickness. The two definitions are quite close, the difference being that the IQE is computed from all the radiative recombinations happening *inside* the component $\bar{R}_{\mathrm{rad}}$, while the EQE focuses on the photons emitted by radiative recombinations which can *escape* the component $\bar{R}_{\mathrm{rad,ext}}$ (i.e. not being reabsorbed inside the component, which corresponds to photon recycling). These two quantities are related through the extraction efficiency $\bar{R}_{\mathrm{rad,ext}}/\bar{R}_{\mathrm{rad}}$. It is also possible

[1] A near-field radiative heat transfer model which can properly handle surface modes has actually been recently proposed [Papadakis *et al.* 2021], and is based on the parametrisation of the transmission coefficient. This model is however mainly made to model surface modes-dominated radiation, and remains phenomenological.

to find the EQE expressed as

$$\mathrm{EQE} = \frac{e\dot{N}}{J} = \frac{\bar{R}_{\mathrm{rad,ext}} - \bar{G}_{\mathrm{rad}}}{\bar{R} - \bar{G}}, \tag{3.3}$$

Since an LED emits much more light than it absorbs, $\bar{R} \gg \bar{G}$ and this expression is approximately equal to the previous one - this definition is sometimes preferred as it is based on physical quantities which are much easier to measure.

In a PV cell, the quantum efficiency is defined differently[2], and is given by

$$\mathrm{IQE} = \frac{J}{e\dot{N}_{\mathrm{abs}}} = \frac{\bar{G} - \bar{R}}{\bar{G}_{\mathrm{rad}}}, \tag{3.4a}$$

$$\mathrm{EQE} = \frac{J}{e\dot{N}_{\mathrm{incident}}} = A \cdot \mathrm{IQE}, \tag{3.4b}$$

These definitions focuses on the conversion efficiency of photons into charges, either taking the photons *absorbed* in the cell (IQE) or coming from *outside* the cell (EQE) as a reference. The absorptance of the cell A links these two quantities.

Coming back to the parameter we want to use to express the non-radiative recombinations (the fraction of recombinations being radiative), it is clear that it fits well the definition of the LED quantum efficiency. Since the radiative recombination rate is computed from the photon flux density emitted towards the opposite component, they correspond to $\bar{R}_{\mathrm{rad,ext}}$ and the LED EQE definition can be a suitable choice (done e.g. in [Harder & Green 2003]). But at the same time, assuming $\mu = eU$ leads the photon chemical potential to be constant throughout a component, therefore the net photon flux density between any couple of points inside the component to be zero. Since we suppose that all reabsorption occurs through interband transitions, it means that photon recycling - corresponding to the reabsorption of photons emitted inside a component - has no effect overall: $\bar{G}_{\mathrm{rec}} - \bar{R}_{\mathrm{rec}} = 0$. Consequently, we only need to compute external quantities, so that the total radiative recombination rate $\bar{R}_{\mathrm{rad}}$ we obtain equals $\bar{R}_{\mathrm{rad,ext}}$, and thus IQE = EQE: using the LED IQE definition is also a valid choice (and was used in our previous work [Legendre & Chapuis 2022a, Legendre & Chapuis 2022b]). To make clear that both definitions can equally work, this parameter will simply be referred to as the quantum efficiency (QE) in the following as long as there is no net contribution of photon recycling.

Now that this is settled, we can go back to the electrical modelling. The non-radiative recombinations are expressed from the QE:

$$\mathrm{QE} = \frac{\bar{R}_{\mathrm{rad}}}{\bar{R}_{\mathrm{rad}} + \bar{R}_{\mathrm{nonrad}}} \Leftrightarrow \bar{R}_{\mathrm{nonrad}} = \frac{1 - \mathrm{QE}}{\mathrm{QE}} \bar{R}_{\mathrm{rad}}. \tag{3.5}$$

As briefly discussed previously, non-radiative recombination comes along with non-radiative generation, which should remain constant with the applied voltage and cancel non-radiative recombination at zero voltage [Harder & Green 2003]. Therefore

$$\bar{G}_{\mathrm{nonrad}} = \frac{1 - \mathrm{QE}}{\mathrm{QE}} \bar{R}_{\mathrm{rad}}(U = 0). \tag{3.6}$$

[2] Actually, the radiative efficiency (IRE or ERE) is the PV quantity which has the same definition as the LED quantum efficiency [Green 2012b].

Using $\bar{G}_{\text{rad}} = \dot{N}_{\text{abs}}$ and $\bar{R}_{\text{rad}} = \dot{N}_{\text{em}}$, the current density can then be expressed as

$$\begin{aligned} J = e(\bar{G} - \bar{R}) &= e\left(\bar{G}_{\text{rad}} - \bar{R}_{\text{rad}} - \frac{1-\text{QE}}{\text{QE}}(\bar{R}_{\text{rad}} - \bar{R}_{\text{rad}}(U=0))\right) \\ &= J_{\text{rad}} - e\frac{1-\text{QE}}{\text{QE}}\left(\dot{N}_{\text{em}} - \dot{N}_{\text{em}}(U=0)\right), \end{aligned} \tag{3.7}$$

where $J_{\text{rad}} = e(\dot{N}_{\text{abs}} - \dot{N}_{\text{em}})$ corresponds to the expression of the current obtained at the radiative limit. The above expression will be used in the following of the chapter to compute the electrical current density/power of the LED and the PV cell. Notice that neither the current nor the voltage of the LED and PV cell are matched: this means the overall device would require additional electronics to operate. The study of self-sustaining TPX devices has been notably performed in [Zhao *et al.* 2019], but will not be further investigated in the frame of this manuscript.

3.2 Why GaAs-based structures?

3.2.1 Required properties for performant thermophotonics

The main input needed to compute the near-field radiative heat transfer is the dielectric function of the material considered. But as of now, the material which would lead to the best results is unknown. To tackle this issue, a basic model of dielectric function can be defined, which should be applicable to any of the materials of interest. Since this section will focus on the power output of TPX devices, only above-bandgap properties are needed, and the model can be restricted to interband contributions. A flat dielectric function $\varepsilon = 10 + 1i$ is chosen as a first estimation, the real and imaginary parts of most usual semiconductors being in this order or magnitude above

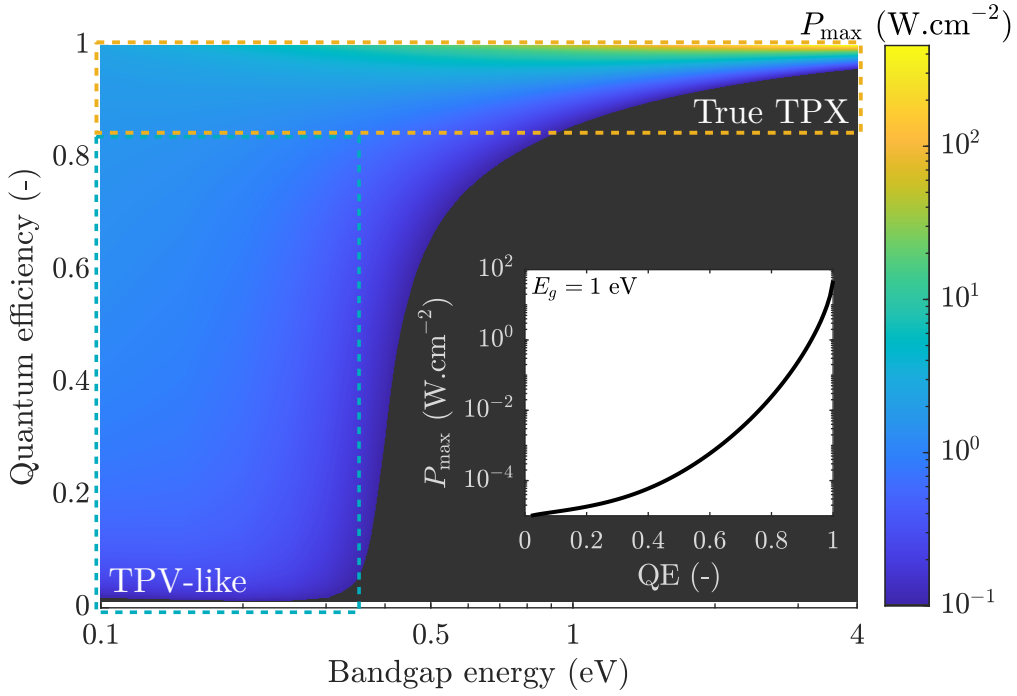

Figure 3.1: Maximum power production of NF-TPX devices with constant interband dielectric function $10 + 1i$, with respect to the bandgap and the quantum efficiency. The gap distance is set to 10 nm, the LED and PV cell temperatures to 600 K and 300 K respectively.

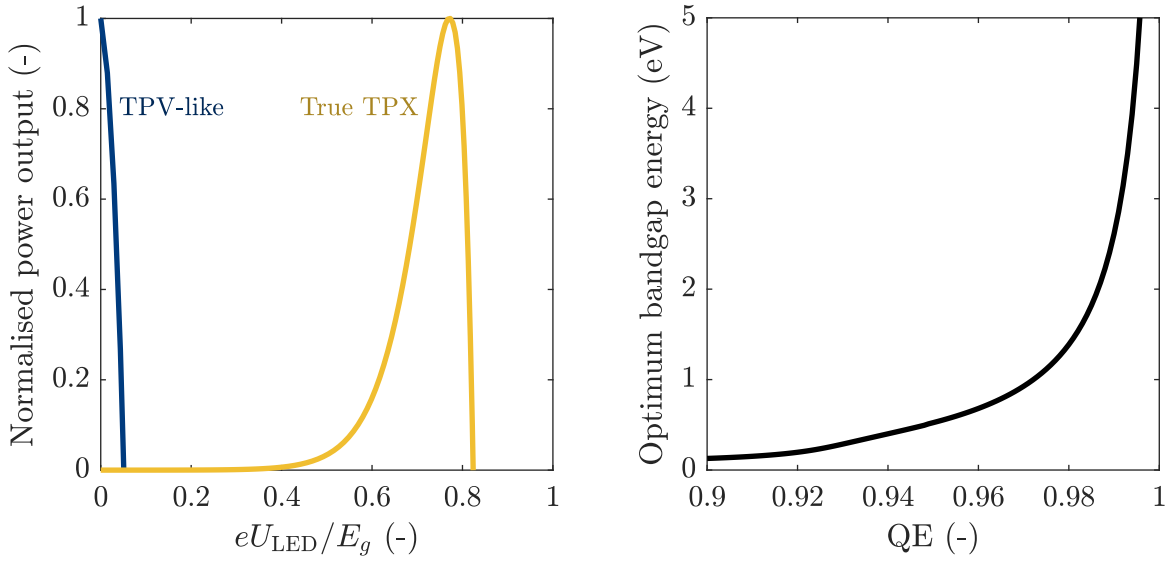

(a) (b)

Figure 3.2: (a) Variation of the power output with respect to the LED voltage, for TPV-like (QE = 0.1, $E_g = 0.2$ eV) and true TPX (QE = 0.95, $E_g = 1$ eV) behaviour. For each LED voltage, the power output shown corresponds to the maximum obtained by varying the PV cell voltage. In both cases, power output is normalised by the maximum power. (b) Bandgap energy leading to maximum power output, computed for high quantum efficiencies.

the bandgap. The model defined in [Lin *et al.* 2018] and provided in Eq. (1.22) has been used for verification, and gave almost the same results[3].

This being set, E_g and QE can be varied in Eq. (3.7) to examine their influence on the performance. In fact, the impact of each of these parameters has already been investigated individually for far-field TPX in [Sadi *et al.* 2022]. In Figure 3.1, we show the coupled effect of E_g and QE on maximum power output, obtained at a gap distance of 10 nm and for $T_{\mathrm{LED}} = 600$ K and $T_{\mathrm{PV}} = 300$ K. Two main regions of power production can be spotted. The first one is located at low bandgap ($E_g \leq 0.5$ eV) and for QE up to 0.8: this is a TPV-like region. Thermal radiation emitted by the LED peak at around $3k_{\mathrm{B}}T_{\mathrm{LED}} \approx 0.15$ eV photon energy, following Wien's law. With such small bandgaps, a significant fraction of thermal radiation can be converted by the PV cell, enabling efficient TPV conversion - for low QEs, the optimum bandgap is between 2 and $3k_{\mathrm{B}}T_{\mathrm{LED}}$, close to Shockley-Queisser limit for PV conversion ($2.2k_{\mathrm{B}}T_{\mathrm{LED}}$) [Shockley & Queisser 1961]. However, the LED is not efficient enough in this range of quantum efficiency and the maximum power point is reached for zero (or almost) LED voltage, hence the name "TPV-like". This is depicted in Figure 3.2a, where the variation of power output with the LED voltage is shown for a QE of 0.1 and a bandgap of 0.2 eV.

The second region can be found at high quantum efficiencies (QE ≥ 0.9). This would correspond to the "true TPX" region, as a significant LED voltage is required to generate substantial power (see Figure 3.2a, obtained with QE = 0.95 and $E_g = 1$ eV). The improvement of electrical power production with QE is dramatic there, especially at high bandgap: the order of magnitude of its increase rate from a QE of 0.9 to 1 is 10^2 and 10^7 for bandgaps of 1 and 4 eV, respectively.

[3]Note that since the components are supposed to be semi-infinite, the transmission coefficient is directly related to the reflection and transmission coefficients at the interfaces, and is thus mainly directed by the real part of the dielectric function as $\varepsilon' \gg \varepsilon''$.

While going towards higher QEs always helps to reach higher performance, there is actually an optimal bandgap energy for a given quantum efficiency: this optimum is shown in Figure 3.2b. Originally between 2 and $3k_BT_{LED}$, it first increases smoothly (reaching $E_g = 0.68$ eV for a QE of 0.96) before diverging when getting close to the ideal case - this divergence being consistent with results from the previous chapter (see Figure 2.8). Such an increase comes from the fact that for high quantum efficiencies, the LED can be strongly biased: the emitted radiation is then highly electroluminescent, and spectrally centred around the bandgap energy, so that it doesn't matter that thermal radiation at such high photon energy is negligible for the temperature considered.

In the end, what conclusions can be drawn from these results about the required materials properties? Regarding the bandgap energy, while it is constrained by the emitter temperature in TPV, it is not the case in TPX thanks to the electroluminescent radiation. But in order to have a true TPX behaviour, the QE must be high - at least 0.8, or even 0.9. This parameter should thus guide the decision. GaAs was selected among the plausible semiconductors, for several reasons. In terms of quantum efficiency, [Bender *et al.* 2013] reported an EQE larger than 0.99 for a GaAs-based cooling structure, and electroluminescent cooling was demonstrated with a GaAs-based LED [Radevici *et al.* 2019]. Furthermore, GaAs is a widely used material for high-efficiency solar PV, thanks to its high QE and 1.42 eV bandgap at room temperature. It has been used either in thin-films [Kayes *et al.* 2011] or in multijunctions, directly [Takamoto *et al.* 2014] or in alloys [France *et al.* 2022] (see Figure 1.14 for more details). Its properties were thus intensely studied and available for simulations. Note of course that other materials could be of interest for TPX applications (e.g., GaN) but will not be studied here.

3.2.2 Aligning bandgaps for optimal conversion

In the previous subsection, we only talked about choosing one material which has the required QE and bandgap. But GaAs, as other semiconductors, sees its bandgap energy decrease with temperature following Varshni's equation [Varshni 1967]:

$$E_g(T) = E_g(0\ \mathrm{K}) - \frac{\alpha T^2}{T + \beta}, \tag{3.8}$$

where α and β are two positive constants for a given material. For GaAs, $E_g(0\ \mathrm{K}) = 1.52$ eV, $\alpha = 0.55$ meV.K^{-1} and β=225 K [Gonzalez-Cuevas *et al.* 2006], which means the bandgap goes down to 1.28 eV at 600 K. In the previous chapter, we assumed the LED and PV cell bandgaps to be equal so that electroluminescent emission from the LED could generate as much electron-hole pairs as possible, but did not show what is the effect of bandgap mismatch. Using as a base scenario the "true TPX" example given in Figure 3.2a, we show in Figure 3.3 how abrupt the decrease of power produced is when the LED bandgap gets further from that of the PV cell. To generate at least 1% of the maximum achievable power, the LED bandgap should range from 0.99 to 1.09 eV considering a PV cell bandgap of 1 eV.

Of course, such narrowness also comes from the assumption that the absorption tail is abrupt at the bandgap (i.e. that there is no absorption due to interband transitions below the bandgap). In reality, this is not strictly correct as some states can be available inside the bandgap, causing some interband transitions to occur even with photons whose energy is tens or even hundreds of meV lower than E_g. Such effects, which will be analysed in Section 5.3, may smoothen the electrical power peak in Figure 3.3. Still, the abrupt-bandgap approximation being mostly correct, the LED and the PV cell shall not be made of the same material.

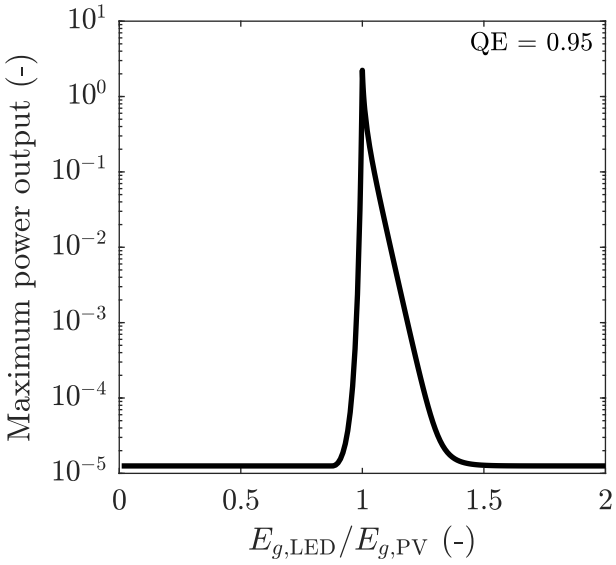

Figure 3.3: Variation of maximum power with the bandgap mismatch, for materials with dielectric function $\varepsilon = 10 + 1i$ and for a PV cell bandgap of $E_g = 1$ eV.

Surprisingly, the need for bandgap matching is not systematically considered in TPX literature. While [Zhao *et al.* 2018] takes it into account, [Matsuno *et al.* 2022] uses black phosphorus for both LED and PV cell; this might partly explain why the maximum power output obtained are much lower than other results. In the case of [Yang *et al.* 2022], two different materials are used but their bandgaps match only for a 520 K heat source temperature. However, they consider different heat source temperatures and bandgaps are therefore unmatched; to prevent excessive power drop, they assume that no electroluminescent radiation is exchanged below the highest bandgap (which in their case is the PV cell bandgap), which is a rather strong assumption.

In most of this manuscript, we choose to work with AlGaAs on the LED side. Alloying GaAs with AlAs increases the bandgap, which allows to counter its natural decrease with temperature on the LED side. Bandgaps can thus be matched for any LED temperature by carefully setting the alloy fraction. While other materials can show similar behaviour, using AlGaAs for the LED ensures that its properties are close to those of GaAs, which are those of interest to obtain highly efficient conversion. Moreover, AlGaAs lattice constant does not change with Al fraction, which makes growth on GaAs substrate easier. A similar choice was made in [Zhao *et al.* 2018], with the difference that the PV cell was also made of AlGaAs.

Other alloys could be attractive, for instance InGaAs on the PV cell side (since its bandgap is lower than that of GaAs at room temperature): with an InGaAs PV cell, the LED can be made of pure GaAs, and lower bandgaps can be reached. However, the careful selection of material for each component is not of major interest prior to the complete device design and analysis, and will thus be further discussed in Chapter 6.

3.3 Performance of an AlGaAs-GaAs device in the near field

The aim now is to study, for a given device, how electrical power output and efficiency vary with LED and PV cell voltages. Many studies on TPX (for energy harvesting or cooling purposes) show the variation of these quantities with LED voltage [Harder & Green 2003, Chen *et al.* 2017, Zhao *et al.* 2018, Matsuno *et al.* 2022, Yang *et al.* 2022], but the impact of the PV cell voltage is

always missing. In some articles, the QE is computed from material properties and thin-films are considered, but this is done to design devices. As in [Harder & Green 2003], we rather want to understand what the role of the different parameters in the model is and to keep the results general, so the QE is set manually in Eq. (3.7) and the same QE is considered for the LED and the PV cell. Also, both components are considered to be semi-infinite. Many of the results shown here were published in [Legendre & Chapuis 2022a], except Figure 3.8 which was published in [Legendre & Chapuis 2022b].

3.3.1 Power-voltage characteristics

3.3.1.1 Power production region and equivalent Raveau diagram

Instead of looking directly at the numerical results, we can first try to understand what are the range of LED and PV cell voltages in which power is generated, i.e. where is the power production region (PPR) in a $(U_{\mathrm{LED}}, U_{\mathrm{PV}})$ map. To do so, we derive analytically the solution to $P = 0$ and look for a relation between U_{LED} and U_{PV}, in order to delimit the PPR.

First, the electrical power circulating through each component should be compared. Eq. (3.7) gives $J_{\mathrm{LED}} = -e\left(\dot{N} + (1-\mathrm{QE})/\mathrm{QE} \cdot \dot{N}_{\mathrm{em,LED}}\right)$ and $J_{\mathrm{PV}} = e\left(\dot{N} - (1-\mathrm{QE})/\mathrm{QE} \cdot \dot{N}_{\mathrm{em,PV}}\right)$. In order to generate power, the LED should consume less than what the PV cell produces:

$$\begin{aligned} P \geq 0 &\Leftrightarrow P_{\mathrm{PV}} \geq -P_{\mathrm{LED}} \\ &\Leftrightarrow U_{\mathrm{PV}} \geq U_{\mathrm{LED}} \frac{-J_{\mathrm{LED}}}{J_{\mathrm{PV}}} \\ &\Leftrightarrow U_{\mathrm{PV}} \geq U_{\mathrm{LED}} \frac{\mathrm{QE} \cdot \dot{N} + (1-\mathrm{QE}) \cdot \dot{N}_{\mathrm{em,LED}}}{\mathrm{QE} \cdot \dot{N} - (1-\mathrm{QE}) \cdot \dot{N}_{\mathrm{em,PV}}}. \end{aligned}$$

Now, if the temperature difference between the LED and the PV cell is large enough, and if the applied voltage on the PV cell is not much larger than that of the LED, $\dot{N}_{\mathrm{em,LED}} \gg \dot{N}_{\mathrm{em,PV}}$ and thus $\dot{N} \approx \dot{N}_{\mathrm{em,LED}}$. If the QE is not too low, we have $\mathrm{QE} \cdot \dot{N} \gg (1-\mathrm{QE}) \cdot \dot{N}_{\mathrm{em,PV}}$ and the previous inequation transforms into

$$P \geq 0 \Leftrightarrow U_{\mathrm{PV}} \geq \frac{U_{\mathrm{LED}}}{\mathrm{QE}}. \tag{3.9}$$

This condition, approximative for $\mathrm{QE} < 1$ because of the assumptions presented above, is strictly correct for $\mathrm{QE} = 1$. For a given LED voltage, $U_{\mathrm{LED}}/\mathrm{QE}$ is therefore the minimum PV cell voltage for which power can be generated.

There is also a maximum PV cell voltage for a given LED voltage, which arises from the condition $\dot{N} \geq 0$. Indeed, if U_{PV} gets too large, the PV cell emission is sufficiently electroluminescent to surpass thermal (or slightly electroluminescent) radiation coming from the LED. Then, the PV works as an LED, the LED as a PV cell, and heat (at least above the bandgap) goes from cold to hot: the device has switched to a heat pump configuration. Note that $\dot{N} = 0$ is strictly equivalent to $P = 0$ only for $\mathrm{QE} = 1$: for $\mathrm{QE} < 1$, if $\dot{N} = 0$, both LED and PV cell consumes electrical power, and the device does not work as a heat engine nor as a heat pump. Still, the variation of current with voltage in this area is sufficiently sharp so that the line representing $\dot{N} = 0$ remains close to $P = 0$.

This limit can be derived similarly to Eq. (2.13) (obtained with a passive emitter). We assume

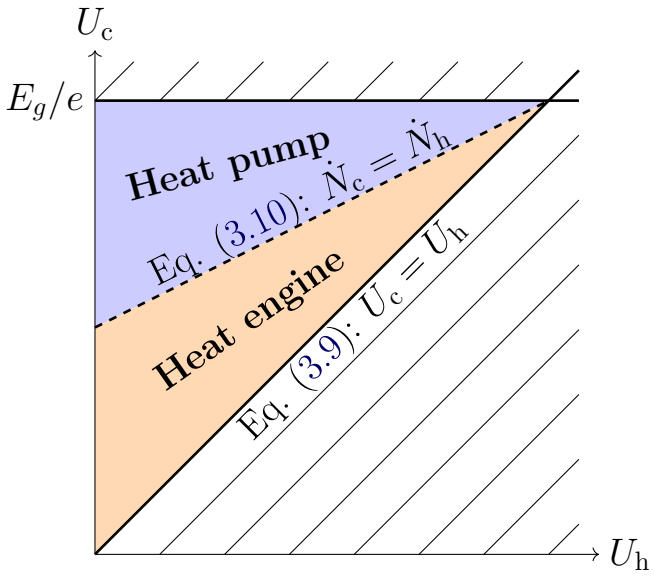

Figure 3.4: Equivalent Raveau diagram for TPX heat engines at the radiative limit (QE = 1).

that the transmission function varies as $(\hbar\omega)^n$ (n being an integer greater or equal to -2), so that the photon flux density can be expressed in terms of polylogarithms. Then, we suppose that E_g is much larger than $k_B T$ and eU, allowing to reduce the expression of $\dot{N}$ to one simple term (similarly to Boltzmann's approximation). Writing $(E_g - eU_i)/k_B T_i = x_i$ for simplicity, it gives

$$\begin{aligned}
\dot{N} \geq 0 \Leftrightarrow q \geq 0 &\Leftrightarrow k_B T_{LED} \exp(-x_{LED}) \geq k_B T_{PV} \exp(-x_{PV}) \\
&\Leftrightarrow -x_{PV} \leq -x_{LED} + \ln\left(\frac{T_{LED}}{T_{PV}}\right) \\
&\Leftrightarrow eU_{PV} \leq (1-\eta_C) eU_{LED} + \eta_C E_g + k_B T_{PV} \ln\left(\frac{T_{LED}}{T_{PV}}\right) \qquad (3.10a) \\
&\Leftrightarrow eU_{PV} \lesssim (1-\eta_C) eU_{LED} + \eta_C E_g. \qquad (3.10b)
\end{aligned}$$

Eq. (3.10a) can be simplified into Eq. (3.10b) since the last term is in general negligible: for $T_{LED} = 600$ K, $T_{PV} = 300$ K and $E_g = 1.42$ eV, $\eta_C E_g = 0.71$ eV and $k_B T_{PV} \ln(T_{LED}/T_{PV}) = 0.02$ eV. If the applied voltage comes close to the bandgap energy, the second approximation is not correct any more and the polylogarithmic expression should be used to obtain a non-linear relation between the two voltages. Anyway, the maximum admissible PV cell voltage is a function of the LED voltage, the ratio of temperature and the bandgap energy.

The results obtained in the derivations presented above are summarised in Figure 3.4, given for a QE of 1. Since the LED and the PV cell exchange their operation when crossing the isoline $\dot{N} = 0$ (Eq. (3.10)), these results are shown as functions of U_c and U_h, rather than U_{PV} and U_{LED}. Such figure can be understood as an equivalent Raveau diagram for TPX devices, giving the region where the device works as a heat engine or as a heat pump as a function of the cold and hot bodies voltages (in a usual Raveau diagram, these regions are given as a function of heat flux exchanged with heat source and sink). Notice how neither of the two limiting equations for the PPR depend on the photonic transmission function: the shape of this region should thus remain quite unaffected by the gap distance.

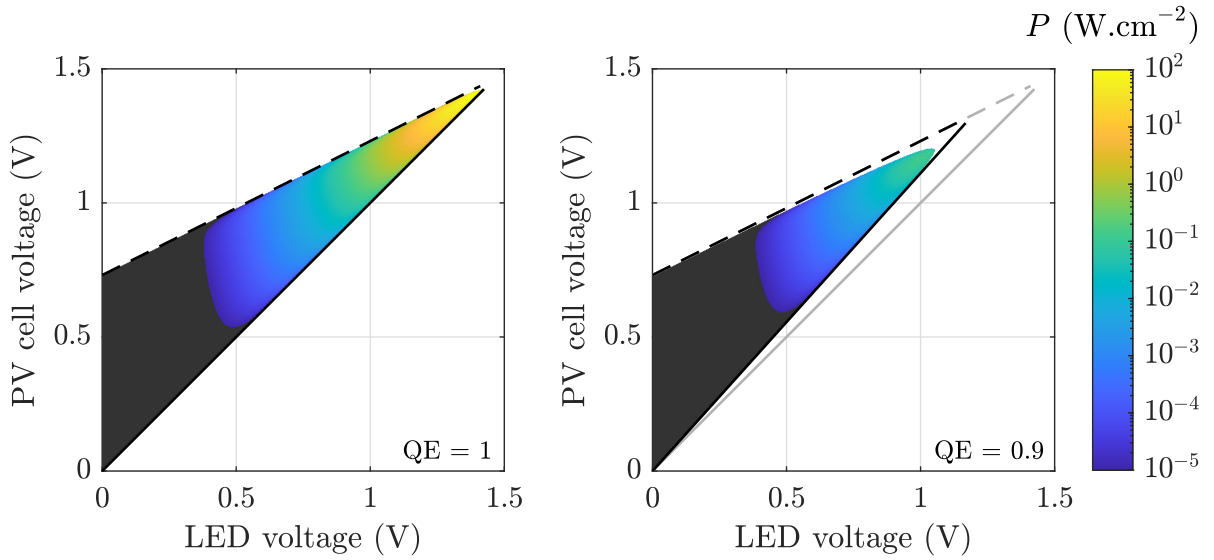

Figure 3.5: P-VV characteristic of an AlGaAs-GaAs NF-TPX device, for a 10 nm gap distance (T_{LED} = 600 K, T_{PV} = 300 K), respectively for (a) QE = 1, (b) QE = 0.9. The full line corresponds to Eq. (3.9), the dashed line to Eq. (3.10a).

3.3.1.2 P-VV characteristic of AlGaAs-GaAs devices

We can now have a look at the power generated by an AlGaAs-GaAs device as a function of the voltage, and compare the PPR with the one presented in the previous section. As a reminder, all the material properties used can be found in Appendix B; the data related to the phononic contribution having no dependency with temperature, they are taken at 300 K. For an LED heated at 600 K, the alloy fraction should be set to 12.1% to match bandgaps. The performance of such a device is simulated at a 10 nm gap distance, for a QE of 0.9 (supposedly achievable scenario) and 1 (ideal scenario). These results are shown in Figure 3.5, where the power output of the device is given as a function of both LED and PV cell voltages. Such figure will later be called "P-VV characteristic", similarly to "I-V" (current-voltage) or "P-V" (power-voltage) characteristics in PV and LED applications.

The first element which can be noticed is that the PPR delimited in the previous section matches well the numerical results, except maybe when the two limiting lines come close to each other for QE = 0.9. Actually, the maximum power point is in both cases close to the point where these two lines cross each other: if any voltage is increased from there, the power output abruptly drops to zero. The LED voltage at maximum power point is thus close but slightly smaller than the LED voltage at the line crossing, expressed using Eq. (3.9) and Eq. (3.10b) as

$$\frac{eU_{\mathrm{LED}}}{E_g} = \frac{\eta_{\mathrm{C}}\mathrm{QE}}{1-(1-\eta_{\mathrm{C}})\mathrm{QE}}. \tag{3.11}$$

Comparison of the two figures also reveals that power output at moderate voltages is similar for QE = 0.9 and 1, and significantly differs only under high voltage ($U_{\mathrm{LED}} \gtrsim 1$ V). This is better seen in Figure 3.6, in which the maximum power output obtained for each LED voltage is given (named in the following of the manuscript "P-V_{LED} characteristic"). In both cases, the power output starts by increasing almost proportionally to $\exp(eU_{\mathrm{LED}}/k_{\mathrm{B}}T_{\mathrm{LED}})$: this is due to P being

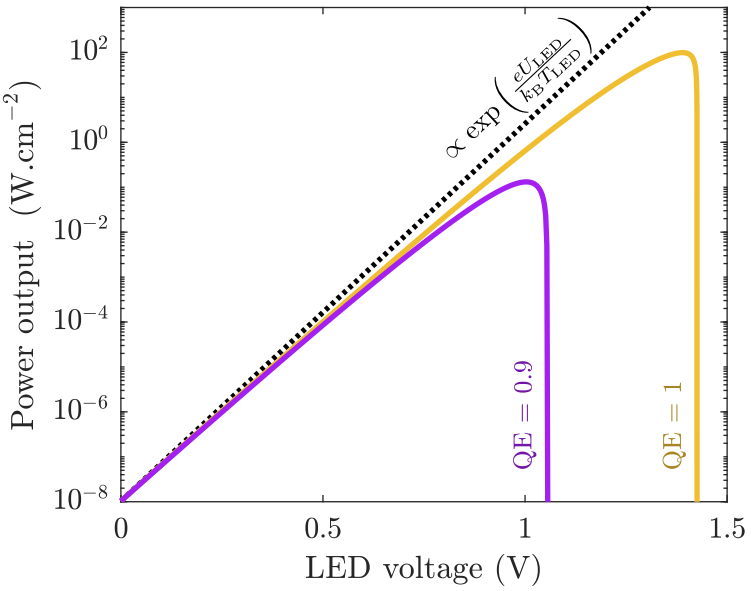

Figure 3.6: P-V_{LED} characteristic of an AlGaAs NF-TPX device.

strongly correlated to the above-bandgap heat flux, which itself roughly increases as such using Boltzmann's approximation and assuming the PV cell emission to be negligible compared to that of the LED. Following this exponential increase, power output reaches a maximum - for a given voltage varying with QE - before quickly dropping to zero. The respective maximum power output for QEs of 0.9 and 1 are 0.13 and 99 W.cm^{-2}, obtained for couples (U_{LED},U_{PV}) equal to (1 V,1.17 V) and (1.39 V, 1.41 V).

3.3.1.3 Additional losses due to series resistance

Apart from non-radiative losses taken into account through the QE, other losses could drive the maximum power output away from the QE = 1 optimum. One such loss source is series resistance, which consumes an electrical power density $R_s J^2$ in each component (R_s being the series resistance in Ω.cm^2 and J the current density in the component). Series resistance can for instance arise from the semiconductors forming the components or from the metallic contacts delivering/extracting the charge carriers.

The impact of series resistance on power output is illustrated in Figure 3.7 for QEs of 1 and 0.9. In both cases, power output starts to decrease towards zero above a given threshold of series resistance. Since higher electrical powers, and thus higher currents, are flowing through the device in the QE = 1 case, it is more sensitive to series resistance. Defining $R_{s,50\%}$ as the series resistance at which 50% of power has been lost, we find it to be equal respectively to 4×10^{-6} Ω.cm^2 and to 6×10^{-3} Ω.cm^2 for QEs of 1 and 0.9. This comes from the inverse variation of $R_{s,50\%}$ with respect to the maximum power output, which appears clearly when computing $R_{s,50\%}$ for different QEs (dashed line in the figure). As a result, the power output enhancement observed at a given series resistance when QE increases from 0.9 to 1 becomes more modest: originally close to 750, it goes down to 8 for $R_s = 10^{-2}$ Ω.cm^2 and to 3 for $R_s = 1$ Ω.cm^2.

To give meaning to these results, one of the lowest values of series resistance achieved for TPV cells is 6×10^{-3} Ω.cm^2 and was obtained in [Tervo *et al.* 2022], while some other devices cited in this paper reached values in the order of tens of mΩ.cm^2. It will therefore be a technical challenge

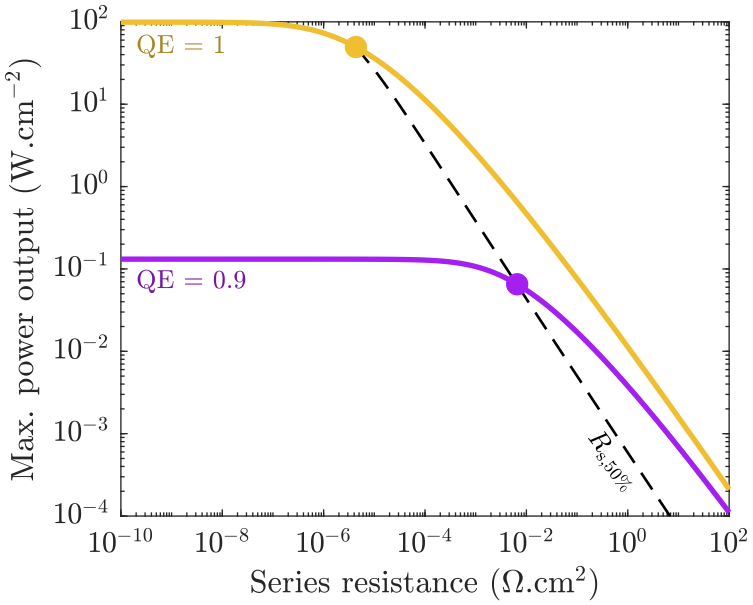

Figure 3.7: Impact of series resistance on maximum power output in the two cases considered in Section 3.3.1.2.

to reach sufficiently low series resistance to prevent significant Joule heating, and the interest of going towards unity QE is largely mitigated if series resistance is not simultaneously decreased.

In the remaining of the chapter, no series resistance will be considered with the aim of studying the most optimistic cases.

3.3.1.4 Comparison to other solid-state heat engines

To put the performance of NF-TPX devices into perspective, we show in Figure 3.8 a new version of Figure 1.17 completed with the variations of power output of NF-TPX devices with heat source temperature. As a reminder, two scenarios are considered for each of these technologies, one ideal (full line) and the other more realistic (dashed line). For NF-TPX, these two scenarios correspond to the QE = 1 and QE = 0.9 cases respectively, still with the AlGaAs-GaAs device and for a 10 nm gap distance.

As discussed previously, NF-TPX performance is highly sensitive to QE: compared to the ideal case, the power output drops by a factor 10^7 at 400 K, 10^4 at 500 K and 10^3 at 600 K in the more realistic scenario, even if the QE considered is much higher than that of TPV in the equivalent scenario (6×10^{-5}). NF-TPX is therefore the technology with the largest difference between the two scenarios. Nonetheless, the use of an LED as the active emitter allows to significantly increase power output for low heat source temperatures, NF-TPX surpassing NF-TPV around 400 K considering the realistic case. Interestingly, the upper limit of maximum power output obtained for NF-TPX almost matches that of TE. This means that NF-TPX can be competitive with TE for low-grade heat recovery; however, very high quantum efficiencies will be required to compete.

The comparison with literature results is not straightforward, as different bandgaps are considered for the PV cell (0.34 eV in [Matsuno *et al.* 2022], 1.34 eV in [Yang *et al.* 2022], 1.64 eV in [Zhao *et al.* 2018]) or even different gap distances (50 nm in [Matsuno *et al.* 2022]). But as shown in Section 3.2.1, the variation of performance with bandgap is not dramatic between 1.3 and 1.7 eV,

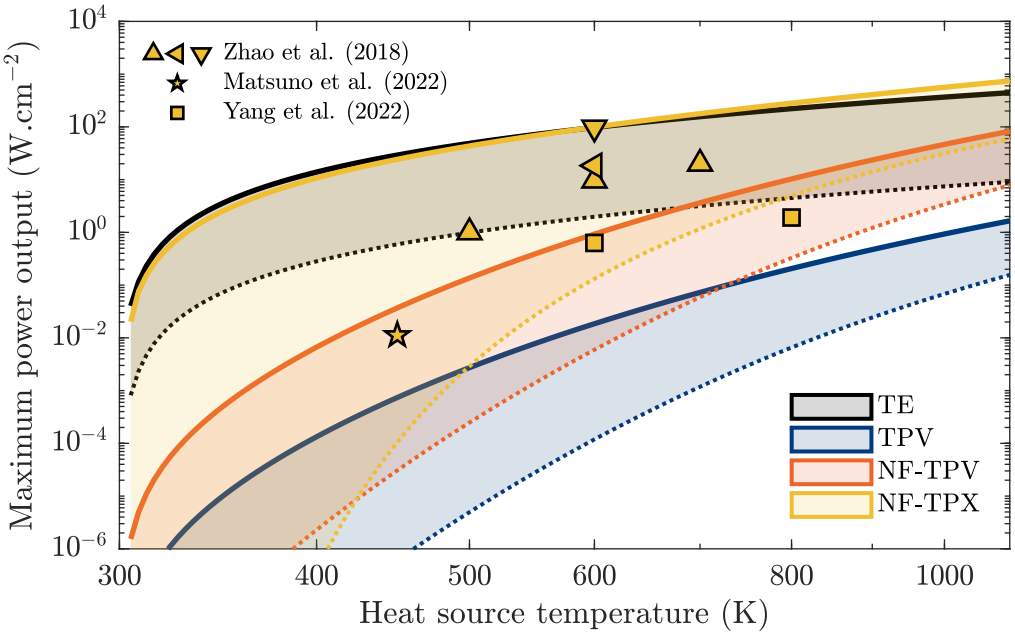

Figure 3.8: Variation of power output for different solid-state heat engines, as a function of the heat source temperature. Full and dashed lines represent ideal and more realistic scenarios (for NF-TPX, corresponding to the QE = 1 and QE = 0.9 cases).

so quantitative comparison with [Zhao *et al.* 2018] and [Yang *et al.* 2022] should make sense. The power output obtained at the radiative limit in [Zhao *et al.* 2018] (downward-pointing triangle) matches well our own result. In these two articles, QE was computed from material properties rather than set manually and can change with temperature: this explains why one result obtained in [Yang *et al.* 2022] is above the QE = 0.9 line, while the other is below. Apart from this last point, all the other results from literature are between the two limiting cases considered.

3.3.2 Radiation in the near field

3.3.2.1 From far to near field

Since the beginning of the chapter, the gap distance was fixed at 10 nm, but it is important to bear in mind how the performance of a TPX device varies with the gap distance. This can be analysed more precisely by studying how each type of electromagnetic mode impacts this performance, e.g. as done in [Bernardi *et al.* 2015] for NF-TPV.

The influence of the gap distance is shown in Figure 3.9. The variations of the different electrical power densities are drawn in Figure 3.9a along with those of the above-bandgap heat flux density (both total and per mode) exchanged between the LED and the PV cell, obtained at maximum power point for QE = 0.9. Globally, the different electrical quantities vary similarly to the above-bandgap heat flux. Note how close PV cell power production and LED consumption are, and how much larger they are compared to the net production: both P_{LED} and P_{PV} are around 35 times larger than P, for any gap distance. This means that most of the energy produced by the PV cell is directly used to power the LED.

If we now look at the variation of the heat transferred with the gap distance, four main regimes can be identified:

1. Above a few micrometres, only propagative modes participate to the heat transfer and

remain constant: this is far-field radiation. As a result, power output does not depend on distance.

2. Between hundreds of nanometres and a few micrometres, propagative modes are still dominant but oscillate due to interferences: this is a far-field coherent regime [Tsurimaki *et al.* 2017].

3. Between 30 nm and 200 nm, the heat transfer increase rate is at its highest. This happens mainly thanks to frustrated modes, which now dominate heat transfer through the nanogap. Consequently, this is also where the gain of power output is the largest.

4. Below 30 nm, the increase is much slower as transmission comes close to maximum for these two modes. At 1 nm gap distance, transmission through surface modes is significant but still lower than through frustrated modes.

The maximum heat transferred through propagative and frustrated modes can in fact be computed using the expression given in Eq. (3.1). The following assumptions are used:

- the heat flux is dominated by LED emission, so that every term related to the PV cell can be neglected;
- the Boltzmann approximation holds for the LED, so that electroluminescent enhancement can be taken into account independently of the integral over frequency;
- the LED refractive index is almost constant close to E_g, so that it can be taken out of the integral;
- the LED voltage at maximum power does not change with the gap distance.

Defining $F_{E_g}(T)$ as the fraction of blackbody radiation emitted above the bandgap by a body at temperature T, we get:

$$q_{\mathrm{max,prop}} = \exp\left(\frac{eU_{\mathrm{LED}}}{k_{\mathrm{B}}T_{\mathrm{LED}}}\right) \cdot F_{E_g}(T_{\mathrm{LED}})\sigma T_{\mathrm{LED}}^4, \tag{3.12a}$$

$$q_{\mathrm{max,frus}} = (n^2 - 1)q_{\mathrm{max,prop}}. \tag{3.12b}$$

This gives $q_{\mathrm{max,prop}} = 0.75$ W.cm^{-2} and $q_{\mathrm{max,frus}} = 8.9$ W.cm^{-2} for an LED temperature of 600 K and an LED voltage of 1 V (the optimum voltage for QE = 0.9), close to the numerical results obtained at 1 nm.

The variation of below-bandgap heat transferred through the different modes as a function of the gap distance is depicted in Figure 3.9b, for undoped materials. Globally, the same regimes can be found, but the transition between them occurs at larger distance. As shown in Section 1.2.1, near-field enhancements appear for ratios d/λ close to or lower than 1, λ being the wavelength. Since below-bandgap photons have larger wavelength, it is logical to reach the near field at larger gap distance. Contrary to above-bandgap heat transfer, surface modes have a significant role in below-bandgap heat transfer: already significant at a 100 nm gap distance, they are largely dominant at 10 nm where they increase as $1/d^2$, which is a standard result for extreme near-field heat transfer between semi-infinite materials [Loomis & Maris 1994, Pascale *et al.* 2023]. Consequently, the below-bandgap heat flux goes from 0.4 to 50 W.cm^{-2} from far field to a 10 nm gap distance. In comparison, above-bandgap heat flux obtained with $U_{\mathrm{LED}} = 1$ V increases from 0.4 to 6 W.cm^{-2} only, which means that the fraction of radiation exchanged above the bandgap

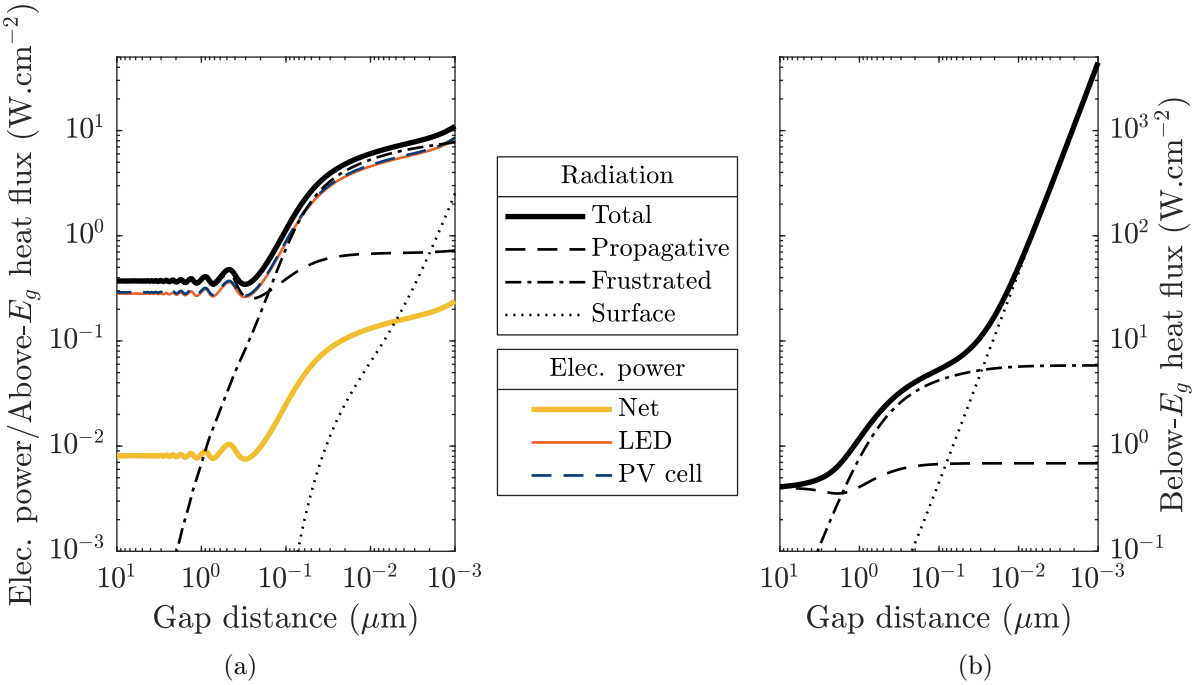

Figure 3.9: Influence of the gap distance on the different energy flows circulating through the device, at maximum power point and for a QE of 0.9. The different electrical powers and the above-bandgap heat transfer are provided in (a), while below-bandgap heat transfer is provided in (b).

goes down from 50% to 10%; without electroluminescence from the LED, it represents a negligible fraction of both far- and near-field heat transfer.

3.3.2.2 Radiation spectrum in the near field

When going in the near field, the total heat transferred not only increases but also changes spectrally. This is shown in Figure 3.10a, where the spectrum of heat transferred between undoped LED and PV cell is given in the far field and for a 10 nm nanogap. In the far field, the spectrum is mostly smooth (except around 40 meV photon energy) and the maximum spectral heat flux density is reached around 0.14 eV, close to the value dictated by Wien's law ($\sim 3k_{\mathrm{B}}T_{\mathrm{LED}} \approx 0.15$ eV). In contrast, the maximum is reached at only 36 meV in the near field, in the same range of energy where far-field heat flux quickly varies. This is due to surface phonon-polariton resonances, which give rise to huge heat transfer through surface modes at the resonance frequency. Actually, two separate resonances are visible (the second one being at 46 meV) due to GaAs-like modes and AlAs-like modes [Adachi 1994]. At these resonances, the near-field enhancement factor can be as high as 10^5, while it goes down to 10 for larger photon energy (coming close to the n^2 limit discussed previously). This explains the large impact of surface modes presented in the previous section.

Figure 3.10b depicts how doping modifies the heat transfer, both LED and PV cell being n-doped with a concentration of 5×10^{18} cm^{-3}. While largely decreased in the far field, it increases the below-bandgap heat flux to 1200 W.cm^{-2} for a 10 nm nanogap, caused by surface plasmon-polaritons showing a wide resonance around 0.1 eV. The resonance frequency increasing as the square root of the doping level (see Section 1.2.3), the effect is particularly visible in the case considered as the doping level is high. It is interesting to notice that due to this large plasmonic

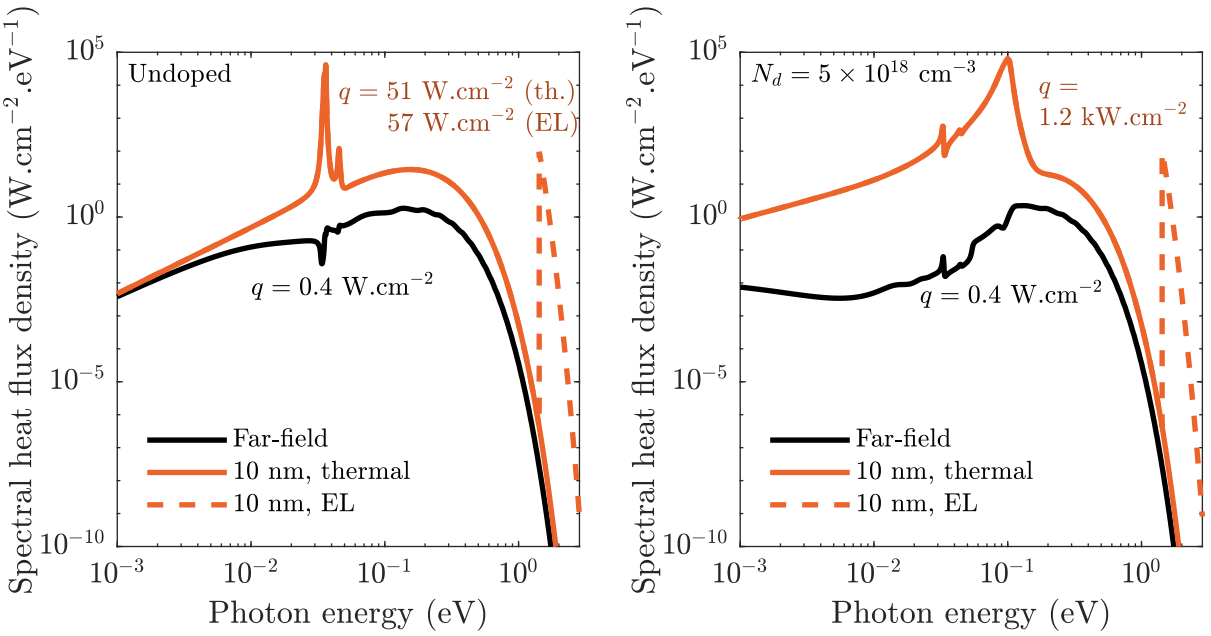

Figure 3.10: Spectral thermal heat flux density exchanged between the LED and the PV cell for different gap distances and for (a) undoped and (b) n-doped materials (5×10^{18} cm^{-3}). For the electroluminescent (EL) case, the voltages obtained at maximum power point for QE = 0.9 are taken. In panel (a), the value of the thermal (th.) heat flux density is also provided.

resonance, the surface phonon-polariton resonance is much weaker than in the undoped case.

Such a large below-bandgap heat flux could have a dramatic effect on power output and efficiency, as will be shown subsequently in this chapter. However, the scenario considered here is a worst-case scenario: with symmetrical and high doping levels in the LED and the PV cell, the resonance is maximum and reached at large photon energy. In order to study an intermediate between this worst-case scenario and the "no below-bandgap radiation" scenario, we will consider undoped materials for the remaining of the chapter.

3.3.3 Efficiency and below-bandgap photons

3.3.3.1 Above-bandgap efficiency

Along with power output, it is useful to understand how efficiency varies with voltage. We show in Figure 3.11 the η-VV and η-V characteristics of TPX devices, considering only above-bandgap photons to quantify how efficient the conversion is. We therefore neglect below-bandgap losses. Regarding the η-V characteristic, for a given LED voltage, we provide both the maximum achievable efficiency (in full line) and the efficiency at maximum power (in dashed line).

Looking first at the Figures 3.11a and 3.11b, it appears that the largest efficiencies are reached close to the line where the net photon flux density equals zero (dashed line), especially in the QE = 1 case. This means that maximum efficiency is reached when no current circulates in the components, i.e. at open-circuit voltage: this is where reversible operation can be approached, as discussed in Section 2.1. In the QE = 0.9 case, the maximum efficiencies move away from the $\dot{N} = 0$ limit as voltages increase, mainly since it is not strictly equivalent to open-circuit operation due to non-radiative losses. Regarding the minimum efficiencies, they are reached in

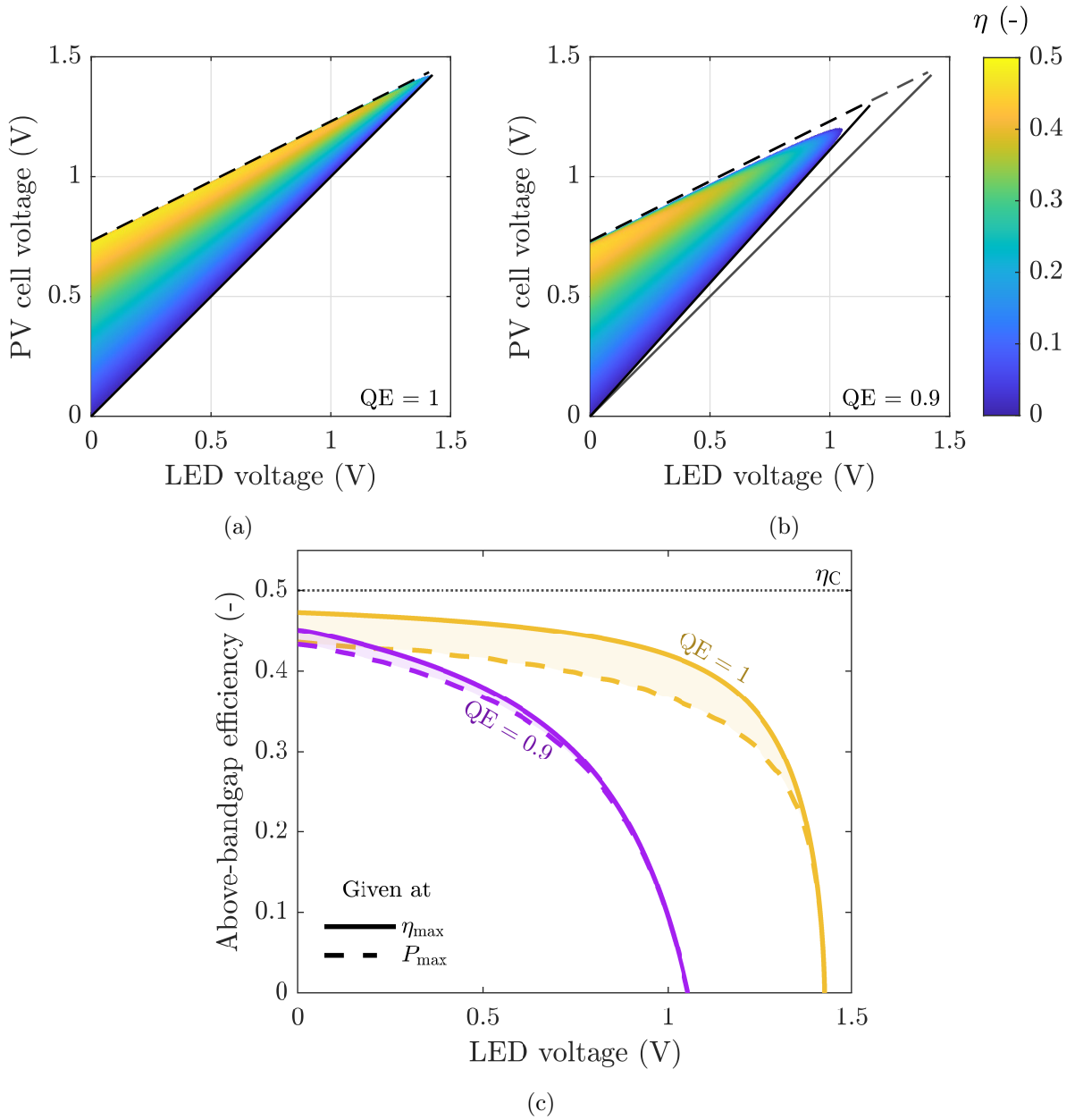

Figure 3.11: η-VV characteristic of an AlGaAs-GaAs NF-TPX device, for a 10 nm gap distance ($T_{\mathrm{LED}} = 600$ K, $T_{\mathrm{PV}} = 300$ K), respectively for (a) QE = 1, (b) QE = 0.9. The full line corresponds to Eq. (3.9), the dashed line to Eq. (3.10a). (c) η-V characteristics of AlGaAs-GaAs NF-TPX devices. In all these figures, only above-bandgap photons are considered.

both cases close to the $P = 0$ limit set by Eq. (3.9), since heat should be supplied to the LED to keep it at high temperature while no electrical power is generated. The variations of LED and PV cell efficiency with voltages are not shown here for the sake of brevity, but remains globally similar to those obtained for monochromatic radiation ($\eta_{\mathrm{LED}} = E_g/U_{\mathrm{LED}}$, $\eta_{\mathrm{PV}} = U_{\mathrm{PV}}/E_g$).

Results presented in Figure 3.11c clearly show that for a given LED voltage, maximum efficiency and efficiency at maximum power are close to each other: the maximum absolute difference between these two is close to 5 percent points for QE = 1 (around $U_{\mathrm{LED}} = 1.05$ V) and to 2% for QE = 0.9 (at $U_{\mathrm{LED}} = 0$ V). Globally, the maximum efficiency and efficiency at maximum power are respectively equal to 47% and 17% for QE = 1, and to 45% and 9% for QE = 0.9. In both cases, maximum efficiency is not far from the Carnot limit, but will not reach it due to thermalisation process happening for photons with energy higher than E_g. These maxima are reached at zero LED voltage, and are almost the same for the two QEs considered. However, achieving high QEs allows maintaining high efficiency for a wider range of LED voltage, the efficiency at maximum power for QE = 1 being thus twice larger than its QE = 0.9 counterpart. The value obtained at QE = 1 (17.3% with more precision) can also be compared to the limit derived for an ideal far-field spectrum in Section 2.2.3: with $T_{\mathrm{LED}} = 600$ K and $T_{\mathrm{PV}} = 300$ K, Eq. (2.37) gives 17.7%. While the case considered here (realistic emission/absorption profile in the near field) is pretty different from the assumptions taken in the previous chapter, the result obtained for QE = 1 matches well the analytical expression with only 2% relative error. This pinpoints the interest of using this equation as an upper bound for efficiency at maximum power.

To wrap up information about power output and efficiency, the TPX performance can be presented in an η-P diagram, as shown in Figure 3.12. The full line corresponds to the convex envelope of the set of achievable (η,P) couples, so that every couple inside (filled in colour) can be reached by properly setting the two voltages. Such representation allows to quickly obtain the power output and related efficiency at maximum power (on the right) and maximum efficiency (in the upper left corner), as well as the optimum performance in between these two points (along the full line).

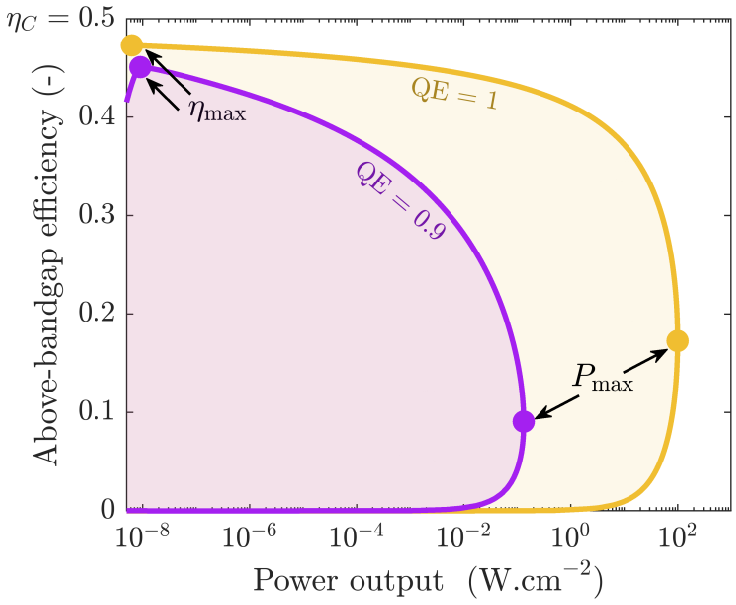

Figure 3.12: η-P characteristic of an AlGaAs NF-TPX device considering only above-bandgap photons, for a 10 nm gap distance ($T_{\mathrm{LED}} = 600$ K, $T_{\mathrm{PV}} = 300$ K). The full line represents the convex envelope in which any point can be reached by setting the voltages properly.

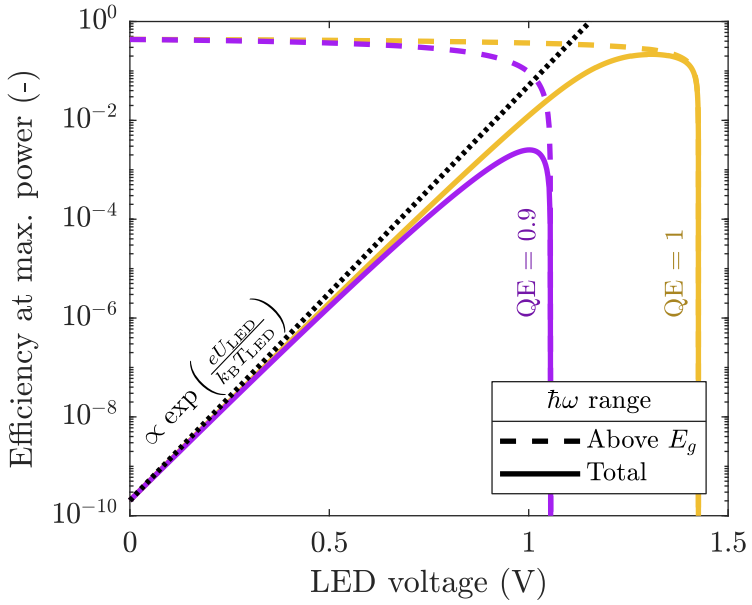

Figure 3.13: η-V characteristic of an AlGaAs NF-TPX device considering only above-bandgap photons or complete spectrum, for a 10 nm gap distance ($T_{\mathrm{LED}} = 600$ K, $T_{\mathrm{PV}} = 300$ K).

3.3.3.2 Total efficiency

As shown in Section 3.3.2.2, a large amount of heat is exchanged below the bandgap. Such heat is useless for conversion and will therefore decrease the efficiency. This total efficiency can be expressed as a function of the above-bandgap efficiency η_{a} as follows:

$$\begin{aligned}\eta &= \frac{P}{q - P_{\mathrm{LED}}} \\ &= \frac{q_{\mathrm{a}} - P_{\mathrm{LED}}}{q - P_{\mathrm{LED}}} \frac{P}{q_{\mathrm{a}} - P_{\mathrm{LED}}} \\ &= \frac{1 - \frac{P_{\mathrm{LED}}}{q_{\mathrm{a}}}}{\frac{q}{q_{\mathrm{a}}} - \frac{P_{\mathrm{LED}}}{q_{\mathrm{a}}}} \eta_{\mathrm{a}} \\ &= F_{E_g} \frac{\eta_{\mathrm{LED}} - 1}{\eta_{\mathrm{LED}} - F_{E_g}} \eta_{\mathrm{a}},\end{aligned} \tag{3.13}$$

where F_{E_g} represents the fraction of heat flux exchanged above the bandgap, and η_{LED} the LED wall-plug efficiency considering only above-bandgap photons. F_{E_g} is the factor with the largest impact: initially close to 0, it quickly increases with LED voltage thanks to electroluminescence, with a rate close to $\exp(eU_{\mathrm{LED}}/k_{\mathrm{B}}T_{\mathrm{LED}})$, before saturating to 1 for high LED voltage. Such an increase rate comes from the fact that under moderate voltage, $F_{E_g} \sim q_{\mathrm{a}}/q_{\mathrm{b}}$ (q_{b} representing below-bandgap heat flux), q_{a} roughly varying as $\exp(eU_{\mathrm{LED}}/k_{\mathrm{B}}T_{\mathrm{LED}})$ as discussed in Section 3.3.1.2. In comparison, the variations of the central ratio in Eq. (3.13) are much less significant, smoothly decreasing with LED voltage as $1\text{-}1/\eta_{\mathrm{LED}}$ (F_{E_g} being negligible for most voltages) before eventually going back up to 1 for F_{E_g} approaching 1.

The efficiency at maximum power obtained for complete spectrum is shown in Figure 3.13, assuming undoped materials. We clearly see there how the maximum efficiency corresponds to a trade-off between high above-bandgap efficiency (reached under low LED voltage) and high

Table 3.1: Performance of a NF-TPX AlGaAs-GaAs device. q is given at maximum power.

QE (-)	Spectrum	P (W.cm^{-2})	q (W.cm^{-2})	η_{MPP} (%)	$\eta_{\max}$ (%)
0.9	Above E_g	0.13	6.0	9.0	45
	Complete		57	0.25	0.25
1	Above E_g	99	8.2×10^3	17	47
	Complete		8.2×10^3	16	23

fraction of above-bandgap radiation (reached under high LED voltage). In the end, since F_{E_g} is much smaller than 1 at the maximum power point of the QE = 0.9 case, the efficiency decreases from 0.09 to 2.5×10^{-3}. Interestingly, the effect of F_{E_g} is so strong that the maximum efficiency obtained with the complete spectrum actually equals the efficiency at maximum power. In contrast, for the QE = 1 scenario, F_{E_g} is close to one at the maximum power point, and the efficiency at maximum power only goes down from 0.17 to 0.16.

If below-bandgap heat flux may not be an issue for the ideal scenario, it will most probably be one for any realistic device, even with electroluminescence largely increasing above-bandgap heat flux and with plasmonic resonance being neglected. It is thus necessary to limit below-bandgap heat flux. One solution is to go to the far field, or at least to a moderate near field, as we have shown in Section 3.3.2 that F_{E_g} decreases when going to the near field - this would be done however at the cost of power. Another solution, which could allow to keep high generation, would be to add at the front of each component a layer which do not support such resonances and is transparent in the above-bandgap range. This was done for instance for NF-TPV based on an InGaAs cell using a thick undoped silicon layer [Inoue *et al.* 2021]. This however will not be further studied in the course of the manuscript.

All the data obtained for this AlGaAs-GaAs device are summarised in Table 3.1.

3.4 Beyond the exoreversible limit

3.4.1 Introduction

Up to now, four loss phenomena have been considered:

- thermalisation, which arises from the non-monochromaticity of the radiation exchanged above the bandgap;
- below-bandgap heat transfer, which does not contribute to the production of electrical power;
- non-radiative recombinations, taken into account with the QE;
- series resistance.

All of these loss channels are related to the operation of the components, and are thus a source of irreversibilities inside the device: the NF-TPX heat engine operates in exoreversible regime. But losses could also arise from the thermal conductances between the device and the thermal reservoirs, as in the case of endoreversible engines [Curzon & Ahlborn 1975]. Any heat flow through these conductances leads to a difference of temperature with those of the reservoirs and thus worsens the performance, the difference of temperature between the LED and the PV cell being decreased (T_{LED} decreases while T_{PV} increases). By assuming that both LED and PV cell temperatures are respectively equal to heat source and heat sink temperatures, we implicitly

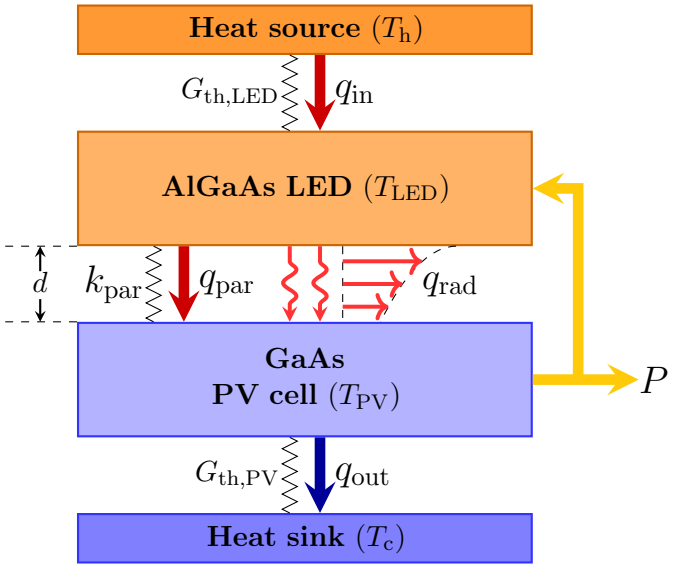

Figure 3.14: Schematic of the AlGaAs-GaAs device considered, with exo-irreversibilities taken into account.

neglected these losses, as in most of the literature about TPX. In [Yang *et al.* 2020], finite thermal conductances were actually considered, but were fixed for the whole study and not compared to the ideal contact scenario; additionally, the study was performed only in the far field. In this section, we aim to analyse in detail how the quality of the reservoir thermal conductances impact the performance of a NF-TPX device.

A schematic representation of the device considered is shown in Figure 3.14. The heat source is kept at 600 K and the heat sink at 300 K, but the temperature of the LED and the PV cell are now unknown - they are however still considered spatially constant. They are related to the heat source and heat sink temperatures through the following expressions:

$$q_{in} = G_{th,LED}(T_h - T_{LED}), \tag{3.14a}$$
$$q_{out} = G_{th,PV}(T_{PV} - T_c), \tag{3.14b}$$

where $G_{th,LED}$ (resp. $G_{th,PV}$) corresponds to the thermal conductance with the heat source (resp. heat sink), and T_h (resp. T_c) is the heat source (resp. heat sink) temperature. q_{in} is the heat flowing from the heat source, q_{out} the one flowing towards the heat sink. In all this section, $G_{th,LED}$ and $G_{th,PV}$ will be considered equal and written G_{th} (the reservoir thermal conductance). To complete the thermal study, a parasitic heat flux q_{par} is considered between the LED and the PV cell, and could physically correspond to conduction through air or nanopillars (placed between the two components to maintain distance) in the nanogap. The parasitic heat flux is obtained as a function of the parasitic thermal conductance $G_{th,par}$:

$$q_{par} = G_{th,par}(T_{LED} - T_{PV}). \tag{3.15}$$

LED and PV cell temperatures can be obtained from energy balance considerations:

$$P_{LED} + q_{in} = q_{rad} + q_{par}, \tag{3.16a}$$
$$P_{PV} + q_{out} = q_{rad} + q_{par}, \tag{3.16b}$$

the computation of the radiative heat flux q_{rad} and of the different electrical powers being done similarly to the previous section, for the same AlGaAs-GaAs device.

3.4.2 Numerical resolution

3.4.2.1 Core algorithm: energy balance

This system of coupled and non-linear equations is solved using Broyden's method [Broyden 1965], which corresponds to the extension of the secant method to multidimensional problems. Let f_{LED} and f_{PV} be two functions defined as

$$f_{\text{LED}}(T_{\text{LED}}, T_{\text{PV}}) = q_{\text{rad}} + q_{\text{par}} - P_{\text{LED}} - q_{\text{in}}, \tag{3.17a}$$

$$f_{\text{PV}}(T_{\text{LED}}, T_{\text{PV}}) = q_{\text{rad}} + q_{\text{par}} - P_{\text{PV}} - q_{\text{out}}. \tag{3.17b}$$

Using vector forms ($\boldsymbol{T} = (T_{\text{LED}}, T_{\text{PV}})$, $\boldsymbol{f} = (f_{\text{LED}}, f_{\text{PV}})$), this means that the equation which should be solved is simply $\boldsymbol{f}(\boldsymbol{T}) = \boldsymbol{0}$. Under the finite-difference approximation $\boldsymbol{J}_k \Delta \boldsymbol{T}_k = \Delta \boldsymbol{f}_k$, where k represents the iteration index, $\boldsymbol{J}_k$ is the system Jacobian, and $\Delta \boldsymbol{T}_k$ and $\Delta \boldsymbol{f}_k$ are respectively equal to $\boldsymbol{T}_{k+1} - \boldsymbol{T}_k$ and $\boldsymbol{f}_{k+1} - \boldsymbol{f}_k = \boldsymbol{f}(\boldsymbol{T}_{k+1}) - \boldsymbol{f}(\boldsymbol{T}_k)$. Then,

$$\begin{aligned} \boldsymbol{f}_{k+1} = 0 &\Leftrightarrow \boldsymbol{J}_k(\boldsymbol{T}_{k+1} - \boldsymbol{T}_k) = -\boldsymbol{f}_k, \\ &\Leftrightarrow \boldsymbol{T}_{k+1} = \boldsymbol{T}_k - \boldsymbol{J}_k^{-1}\boldsymbol{f}_k. \end{aligned} \tag{3.18}$$

In order to obtain a new estimation of the equilibrium temperatures, the inverse of the Jacobian at current iteration is required. Instead of computing at each iteration the Jacobian and its inverse, the Jacobian inverse is updated based on the previous iteration:

$$\boldsymbol{J}_k^{-1} = \boldsymbol{J}_{k-1}^{-1} + \frac{\Delta \boldsymbol{T}_{k-1} - \boldsymbol{J}_{k-1}^{-1}\Delta \boldsymbol{f}_{k-1}}{\Delta \boldsymbol{T}_{k-1}^T \boldsymbol{J}_{k-1}^{-1} \Delta \boldsymbol{f}_{k-1}} \Delta \boldsymbol{T}_{k-1}^T \boldsymbol{J}_{k-1}^{-1}. \tag{3.19}$$

The iterative process should also be initialised. Initialisation of $\boldsymbol{T}_0$ will be discussed in the next section. As for $\boldsymbol{J}_0$, it is obtained from $\boldsymbol{f}$ computed in three different cases: $\boldsymbol{f}(\boldsymbol{T}_0)$ ("reference"), $\boldsymbol{f}(\max(\boldsymbol{T}_0), \max(\boldsymbol{T}_0))$ ("hot") and $\boldsymbol{f}(\min(\boldsymbol{T}_0), \min(\boldsymbol{T}_0))$ ("cold"). This allows to get the variation of both f_{LED} and f_{PV} as any of the two temperatures vary between $\min(\boldsymbol{T}_0)$ and $\max(\boldsymbol{T}_0)$. Defining $\Delta T_0 = \max(\boldsymbol{T}_0) - \min(\boldsymbol{T}_0)$, each component of $\boldsymbol{J}_0$ can then be calculated using finite difference:

$$\begin{aligned} \boldsymbol{J}_0 &= \begin{pmatrix} \frac{\partial f_{\text{LED}}}{\partial T_{\text{LED}}} & \frac{\partial f_{\text{LED}}}{\partial T_{\text{PV}}} \\ \frac{\partial f_{\text{PV}}}{\partial T_{\text{LED}}} & \frac{\partial f_{\text{PV}}}{\partial T_{\text{PV}}} \end{pmatrix}_{T_{\text{LED}}, T_{\text{PV}}} \\ &\approx \frac{1}{\Delta T_0} \begin{pmatrix} f_{\text{LED,ref}} - f_{\text{LED,cold}} & f_{\text{LED,hot}} - f_{\text{LED,ref}} \\ f_{\text{PV,ref}} - f_{\text{PV,cold}} & f_{\text{PV,hot}} - f_{\text{PV,ref}} \end{pmatrix}. \end{aligned} \tag{3.20}$$

After initialisation has been done, iterations can be performed and will stop once the stopping criterion is reached, which here is that $||\boldsymbol{T}_{k+1} - \boldsymbol{T}_k||_\infty$ (i.e. the maximum of the difference) is lower than the tolerance ζ set by the user. The summarised flowchart (named "core algorithm" thereafter) is provided in Figure 3.15. Of course, since electrical and radiative quantities are functions of the voltage vector $\boldsymbol{U} = (U_{\text{LED}}, U_{\text{PV}})$, the equilibrium temperature will also depend on $\boldsymbol{U}$ and the iterative process described above should thus be performed for all the $\boldsymbol{U}$ considered.

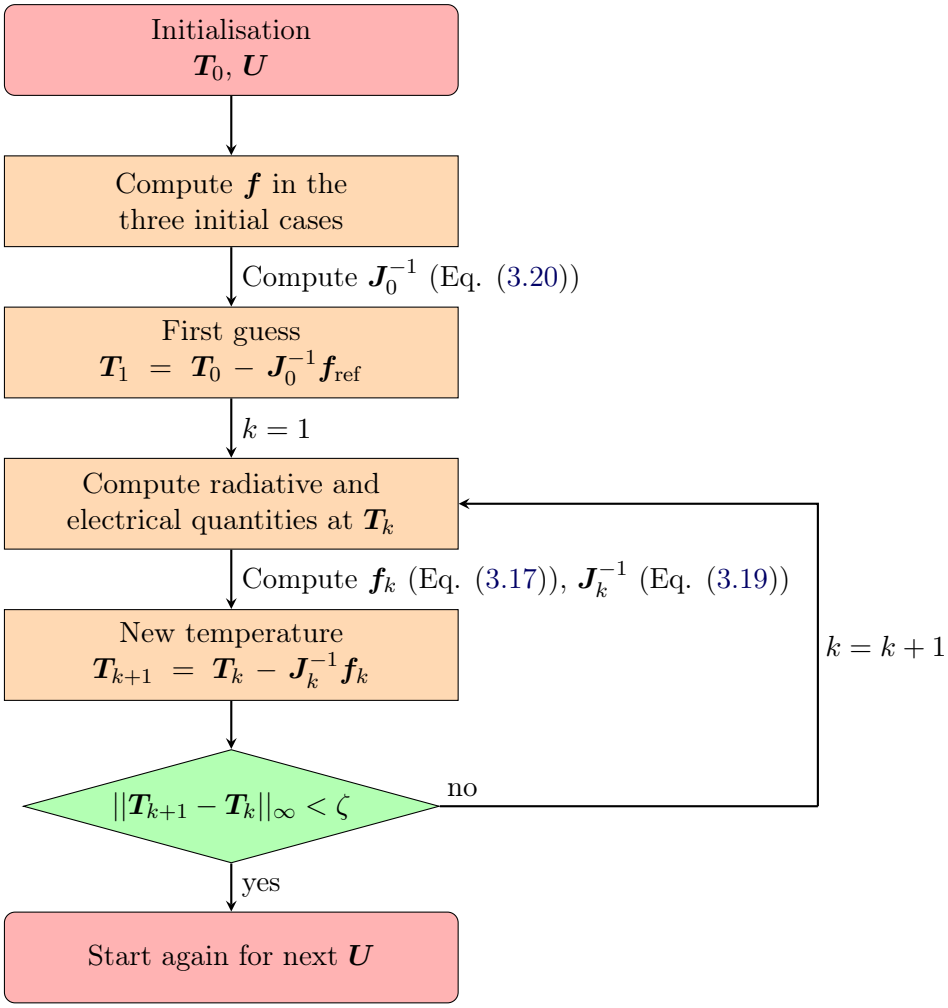

Figure 3.15: Flowchart of the Broyden's method based algorithm used to obtain the temperatures of both components at thermal equilibrium.

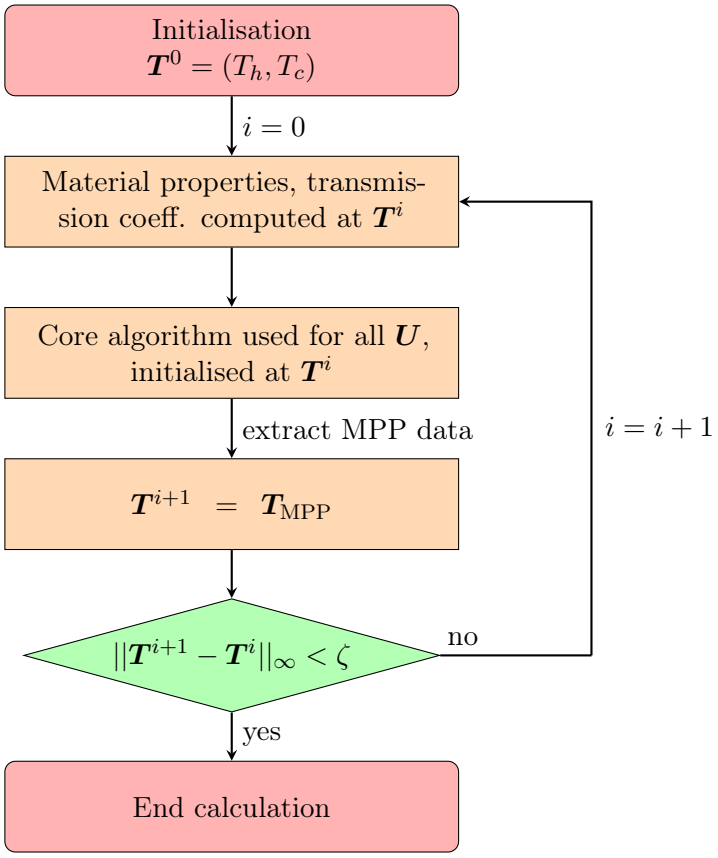

Figure 3.16: Flowchart of the secondary iterative process for self-consistent calculation of temperature and performance at maximum power point.

3.4.2.2 Secondary iterative process: material properties

As shown in Figure 3.15, the radiative and electrical quantities should be computed at each iteration to obtain $\boldsymbol{f}_k$. But since material properties depend on temperature (e.g. bandgap, dielectric function, etc.), it means that the complete calculation (near-field transmission coefficient, photon and heat flux density, electrical characteristics) should be performed for each $\boldsymbol{U}$ and at each iteration. The complexity of the calculation increases therefore at a rapid rate. To prevent this, we choose to focus, not on the full TPX characteristic, but rather on the MPP only. More precisely, a new iterative process is set in which the computation of the material properties and transmission coefficients (performed only at one given couple of temperatures) and the core algorithm alternates, using the temperatures at MPP obtained by the latter (noted $\boldsymbol{T}^i$ at iteration i) to update the former. The initial temperature $\boldsymbol{T}_0$ in the core algorithm at iteration i is simply $\boldsymbol{T}^{i-1}$ (or (T_h,T_c) if it is the first iteration). This allows to obtain self-consistent results at MPP. The corresponding flowchart is shown in Figure 3.16.

As discussed in Section 3.2.2, the temperature changes considered here will most probably cause the LED and PV cell bandgaps to deviate from their initially-matched value, causing a further decrease of performance. To properly separate the impact of the reduction of ΔT and of bandgap mismatch on the performance, two limiting cases are considered:

- the fraction of Al in the LED is set to match the bandgaps when both components are resp. at the heat source and heat sink temperatures; this is the worst-case scenario, in which both the reduction of ΔT and bandgap mismatch will worsen the performance ("Set bandgap"

scenario);

- the fraction of Al in the LED is set to match the bandgaps at the exact temperatures of the components; this is the best-case scenario since bandgaps are always matched ("Matched bandgap" scenario). Such scenario can be practically approached if the reduction of ΔT is properly anticipated.

Unless otherwise specified, the following results are obtained for heat source and heat sink temperatures of 600 and 300 K respectively, a QE of 0.95 (chosen as an intermediate between the two values previously considered), a zero parasitic conductance and a reservoir thermal conductance of 1 W.cm^{-2}.K^{-1}. Such value corresponds to a high-quality thermal connection, typically reached for convective boiling or conduction through few centimetres of aluminium, and of the order of usual thermal contact conductances. As for the efficiency in the previous section, the study will be first restricted to above-bandgap quantities, before addressing the impact of using the complete spectrum.

3.4.3 Performance for above-bandgap radiation

In Figure 3.17a, we compare the power output obtained for ideal contacts (i.e. with infinitely large reservoir thermal conductances, as in Section 3.3) and for the two limiting cases described above, as a function of the QE. In Figure 3.17b is given the related difference of temperature between the LED and the PV cell at thermal equilibrium. As the reservoir thermal conductances are symmetrical, the temperature shift of the LED and the PV cell (compared to the heat source and heat sink temperatures) are almost equal.

Without electroluminescence, the above-bandgap heat transfer is almost zero and no temperature shift is expected. But as discussed in Section 3.3.1.2, the different energy fluxes rise exponentially with LED voltage (since only above-bandgap photons are considered): there is thus a threshold value above which temperature shifts start to be significant (e.g. greater than 1 K). Since LED

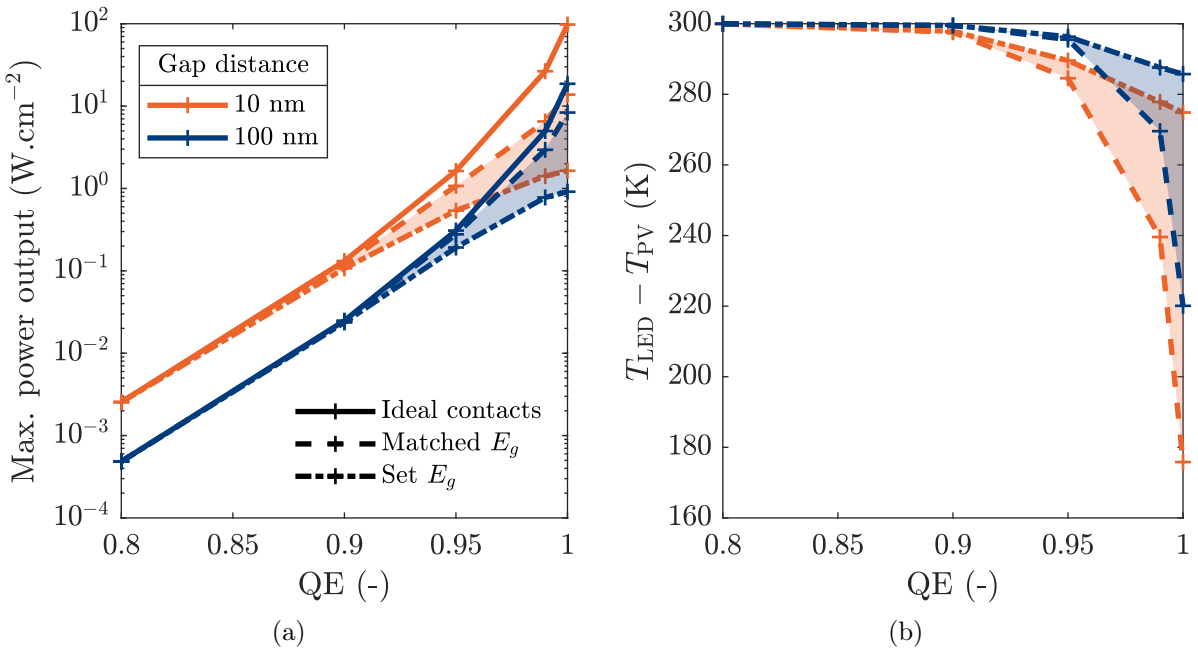

Figure 3.17: Impact of the QE on (a) the device performance, (b) the difference of temperature in the device for various reservoir thermal conductances, considering only above-bandgap photons.

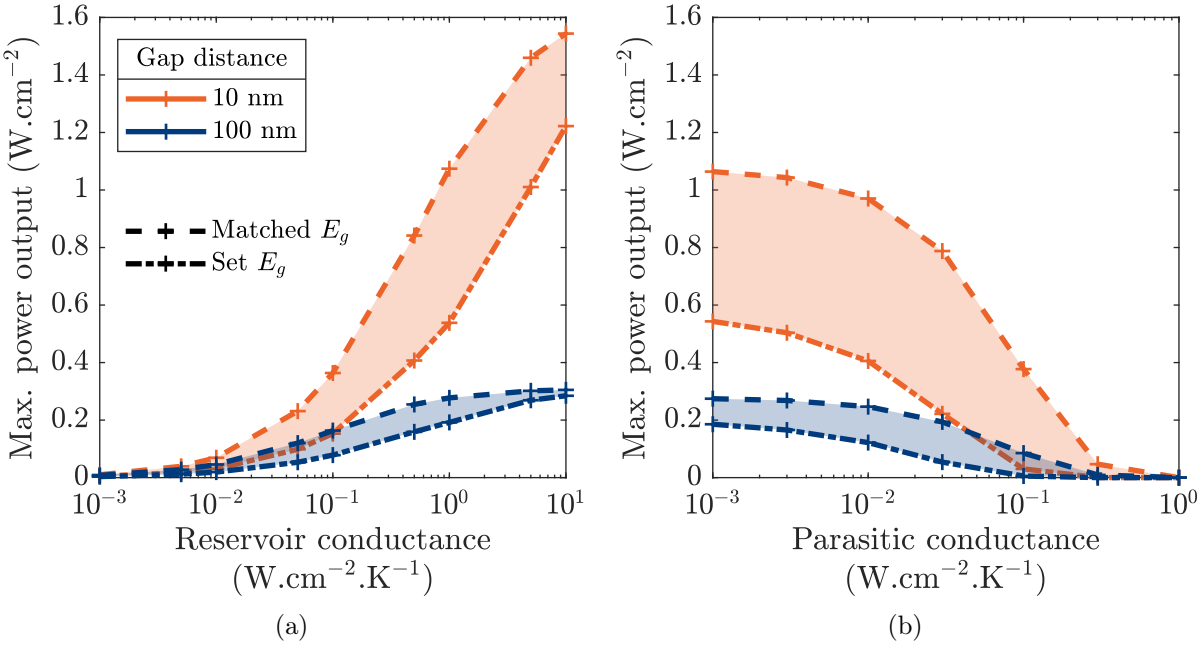

Figure 3.18: Impact of (a) reservoir and (b) parasitic thermal conductance on the performance of the NF-TPX device, with only above-bandgap photons considered.

voltage at MPP increases with QE, this threshold can instead be defined in terms of QE and is located slightly above 0.9 for a 10 nm nanogap and slightly below 0.9 for a 100 nm nanogap, corresponding to a power output of 0.1 W.cm^{-2}. These values only hold for a reservoir thermal conductance of 1 W.cm^{-2}.K^{-1}, the threshold value increasing as the thermal conductance gets larger (since more energy can flow for the same temperature shift).

For QE > 0.9, the three scenarios start to diverge. In the 10 nm nanogap case, the reduction of power output solely due to the decrease of ΔT between LED and PV cell (matched bandgaps scenario) is of the order of one third for QE $= 0.95$ and reaches almost 90% for QE $= 1$. For this last case, ΔT is decreased by almost one half, to 170 K: despite the large reduction of ΔT caused by the exchange of highly electroluminescent radiation, it remains beneficial in terms of power to operate at high voltage. The situation is actually opposite if bandgap mismatch is taken into account: the power reduction it could cause is so large that ΔT should remains as close to 300 K as possible, and voltages thus stay moderate. This translates into a further decrease of the maximum power output compared to the matched bandgap scenario, globally similar to the decrease from ideal to matched bandgap scenario.

In comparison, the 100 nm nanogap case is more weakly affected by these thermal management issues, since the transmission of photons between the LED and the PV cell is lower: while the power output is more than five times larger for the 10 nm nanogap than for the 100 nm nanogap for any QE in the ideal scenario, it is only 65% larger in the matched bandgap scenario for QE $= 1$. The interest of going to extreme near-field for highly efficient devices is thus mitigated if thermal management is not properly performed.

In Figure 3.18 is presented the impact of the reservoir and parasitic thermal conductances. The variation of power output with these quantities is slow: taking the example of a 10 nm nanogap, the increase over four decades of reservoir thermal conductance is not sufficient to reach ideal power output (around 1.6 W.cm^{-2}). If the trend of the different curves shown in this figure

Table 3.2: Conductance at half power, given for the different cases studied in Figure 3.18.

Conductance	Gap distance (nm)	Scenario	$G_{50\%}$ (W.cm^{-2}.K^{-1})
Contact	10	Matched	0.5
		Set	3
	100	Matched	0.09
		Set	0.5
Parasitic	10	Matched	0.06
		Set	0.02
	100	Matched	0.06
		Set	0.02

are mostly similar, they are slightly shifted in terms of conductance: ideal power output is approached quicker for matched bandgaps than for set bandgaps for instance. We quantify this by computing the conductance for which 50% of the maximum power is reached (noted $G_{50\%}$) through interpolation. The results are summarised in Table 3.2. Consistently with the previous results, the 100 nm nanogap case requires lower reservoir thermal conductances to operate close to the ideal contact limit, $G_{50\%}$ being five to six times smaller. The parasitic conductance has similar impact for the two nanogaps considered, and should be lower than 0.01 W.cm^{-2}.K^{-1} (i.e. one hundred times smaller than the reservoir conductances) for power output to approach its upper limit. Taking the example of parasitic heat transfer through conduction, such value of conductance will still be easier to reach for a 100 nm gap distance as $G_{\mathrm{th,par}} = k_{\mathrm{par}}/d$, where d is the gap distance (and k_{par} is the thermal conductivity of the medium conducting the heat).

3.4.4 Impact of below-bandgap photons

In Section 3.3, we have demonstrated that most of the heat flux is in fact exchanged below the bandgap, especially in the near field where polaritonic resonances occur. If the effect on efficiency was already discussed in Section 3.3.3, we show in Figure 3.19a that these below-bandgap photons have a considerable impact on power output when imperfect thermal contacts are considered. These data are obtained with below-bandgap spectra similar to those considered in the efficiency analysis.

The device with a 100 nm gap distance actually performs better for any QE (the difference with the 10 nm nanogap being larger at small QE). The reason behind appears clearly when looking at the related ΔT in Figure 3.19b. At low QE, above-bandgap heat flux is negligible and below-bandgap heat flux is thus the sole cause of temperature variation. As the gap distance decreases, below-bandgap heat flux rises quickly because of the phonon-polariton resonance. For a 100 nm nanogap, it is still small enough to change ΔT by a few kelvins only. However, it becomes very large for the reservoir conductance considered when the gap is only 10 nm thick. ΔT drops then by 75 to 100 K for QE = 0.8 (depending on the scenario), and it gets even worse for larger QE, causing a dramatic reduction in power output. For a QE of 1 and in the matched bandgap scenario, the device generates respectively 7 and 8 W.cm^{-2} of electrical power for a 10 and 100 nm gap distance (for comparison, $P = 14$ and 8 W.cm^{-2} with only above-bandgap photons, and 99 and 19 W.cm^{-2} with ideal contacts).

Of course, the performance obtained at 10 nm can be largely improved if the reservoir thermal conductance becomes large enough to properly handle all the energy flowing through the device. This is represented in Figure 3.20a: while the device performs better with a gap distance of

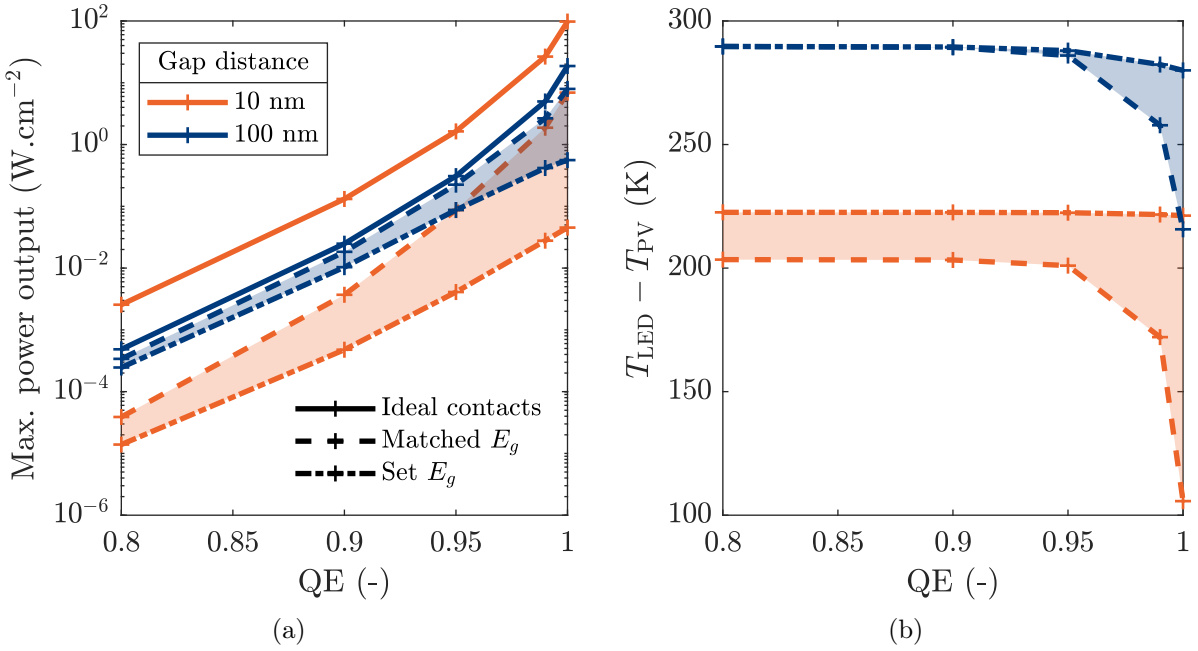

Figure 3.19: Impact of the QE (a) on the device performance, (b) on the difference of temperature in the devicefor various reservoir thermal conductance, considering the complete spectrum.

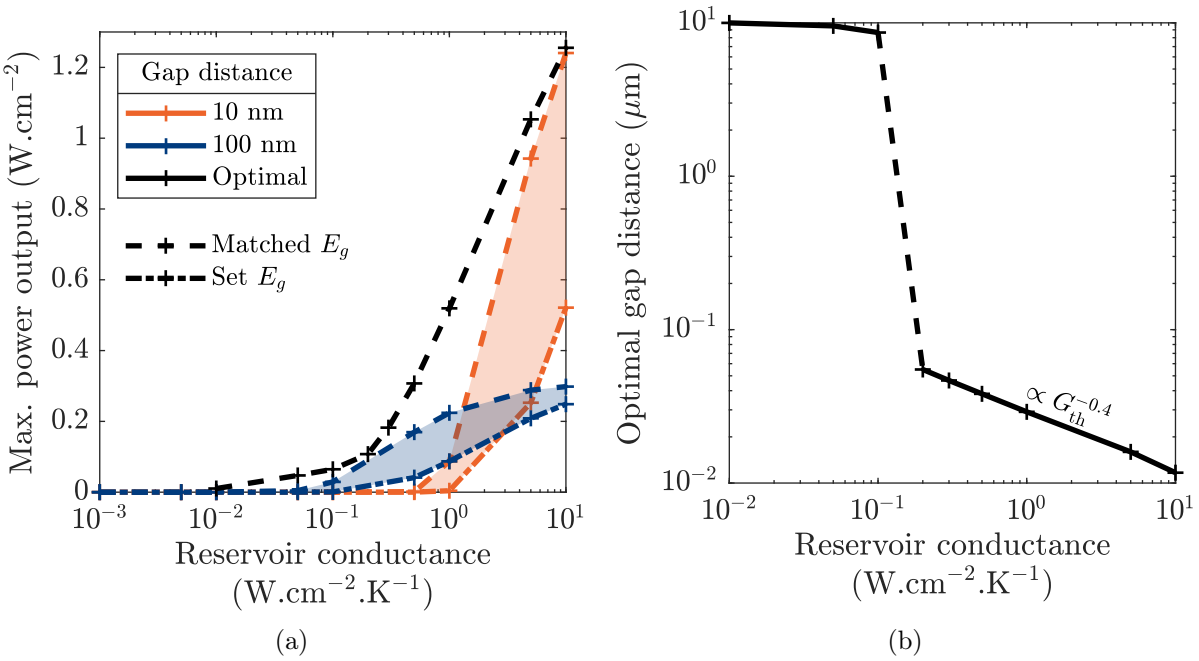

Figure 3.20: (a) Impact of reservoir conductance on the performance of the NF-TPX device, considering the complete spectrum. (b) Gap distance optimising the maximum power output as a function of the reservoir thermal conductance.

100 nm for low conductances, a 10 nm gap distance becomes better for conductances exceeding approx. 2 W.cm^{-2}.K^{-1}. This means that for a given reservoir conductance, there is an optimum gap distance allowing to obtain as much above-bandgap photons as possible, while keeping the total heat flux in a range in which ΔT remains close to $T_\mathrm{h} - T_\mathrm{c}$. The optimum gap distance obtained in the matched-bandgap scenario and for a QE of 0.95 is displayed in Figure 3.20b, while the power output at the optimum is shown in Figure 3.20a. It indicates that when the complete spectrum is considered and nothing is done to reduce the polaritonic resonance, there is simply no interest in going to the near field if the reservoir conductance is too low. Once a certain threshold is reached (between 0.1 and 0.2 W.cm^{-2}.K^{-1} for a QE of 0.95), entering the near field becomes beneficial and the optimum gap distance decreases like $G_\mathrm{th}^{-0.4}$ with the reservoir conductance. Above this threshold, the power output increases faster, power varying logarithmically with G_th.

3.5 To sum up

This chapter focused on the fine study of a thermophotonic device in the near field. The first step was to set the materials used in the device. If the bandgap energy is probably the most important parameter for (thermo-)photovoltaic energy conversion and for LED lighting, it is not the case for thermophotonics thanks to the electroluminescent enhancement of above-bandgap heat transfer. Instead, since the LED should pump heat with wall-plug efficiencies larger than 1, the quantum efficiency should be as large as possible and at least greater than 0.8. For this reason, the device studied is made of a GaAs PV cell and an AlGaAs LED, which ensure bandgap matching between the two components.

This device was analysed for a heat source temperature of 600 K and for two different quantum efficiencies: 1, i.e. an ideal case corresponding to the radiative limit, and 0.9, i.e. a supposedly achievable case. After demonstrating that energy harvesting could take place only in a specific region of the voltage space, we thoroughly studied the variation of power output and efficiency with voltage. Power output roughly increases exponentially with LED voltage, and the maxima are thus found at highest voltages: the maximum power for QE = 0.9 and QE = 1 are resp. equal to 0.13 and 99 W.cm^{-2}, and are reached for LED voltages of 1 and 1.39 V. Even for a QE of 0.9, such a device theoretically already outperforms far-field and near-field TPV, and should be competitive with TE for sufficiently high QE. Regarding the radiation in the near field, we shined a light on the fundamental difference between above- and below-bandgap radiation: while the first is dominated by frustrated modes - thus inherently limited by the n^2 limit - the second is dominated by surface modes due to polaritonic resonances and will thus increase much more in the near field. This causes the efficiency to drop considerably when accounting for these below-bandgap photons when operating in the extreme near field.

We have also studied how other kind of losses could impact the performance, e.g. series resistance or imperfect thermal contacts. Regarding the latter, near-field enhancements are mitigated or even shattered if the thermal conductances are not good enough, causing a large drop of power output - once more, especially when below-bandgap photons are considered. In this case, an optimum gap distance can be found for each reservoir conductance. While the relation between these two quantities has only been found numerically, it would be interesting for a future work to check if such an optimum comes from the matching of reservoir thermal conductances with the radiative conductance between the LED and the PV cell, as demonstrated for thermoelectrics in [Apertet *et al.* 2012a]. The additional difficulty would then be that near-field radiation is highly non-linear with ΔT.

Part II

Physics and design of GaAs-based near-field thermophotonic devices

Chapter 4

Charge transport in semiconductors

Contents

4.1 Charge carriers in semiconductors 90
4.1.1 Charge distribution at equilibrium 90
4.1.2 Quasi Fermi levels and out-of-equilibrium conditions 91
4.1.3 Sources of non-radiative recombinations 92
4.1.4 Radiative recombinations: radiative vs. electrical framework 94
4.1.5 Joining semiconductors for charge carrier separation 95
4.2 Drift-diffusion modelling 97
4.2.1 The drift-diffusion equations 97
4.2.2 Why using our own drift-diffusion solver? 99
4.2.3 Material properties 100
4.3 To sum up 101

Thanks to their simplicity, detailed-balance approaches are useful to quickly understand how energy flows through the device and what is the impact of the main physical parameters on power generation. However, this simplicity makes them unsuitable for the fine analysis and optimisation of specific structures which we aim to perform in Part II of this manuscript, the losses related to the transport of charge carriers to the contacts being very approximately taken into account. Regarding non-radiative recombinations for instance, we either neglected them (Chapter 2) or indirectly set them through the quantum efficiency (Chapter 3) in Part I. In reality, they are caused by different physical phenomena and are directly related to the local charge carrier densities, which are highly variable with position[1]. To properly estimate such losses, we should therefore compute the spatial variation of the charge carrier densities; we do so in the following using the drift-diffusion equations, which is the standard method for such kind of devices (see Section 1.3.5). The study will be restricted to one-dimensional simulations, as there is already a lot of physics to explore in 1D; this however means that some inherently 2D effects, for instance sidewall recombination or current crowding close to the front metallic grid, will be neglected. The current chapter reviews the main phenomena occurring during charge transport together with a presentation of the drift-diffusion equations, with the aim of providing all the information necessary to understand the developments presented in Chapters 5 and 6.

[1] In some articles on TPX based on detailed balance [Zhao *et al.* 2018, Yang *et al.* 2022], the precise expressions of non-radiative recombination rate were used. However, the charge carrier densities were assumed to be constant throughout the device, which is a strong approximation and makes the interest of using the precise expressions questionable - especially since the way these densities are obtained is not explained.

4.1 Charge carriers in semiconductors

4.1.1 Charge distribution at equilibrium

The charge carrier density in a semiconductor can be obtained from two different quantities:

- the density of states at a given energy in the corresponding band $D_{\mathrm{C/V}}$;
- the carrier distribution function f which gives the probability of a state at a given energy to be occupied, depending on the thermal agitation of the carriers; this function corresponds to a Fermi-Dirac distribution for charge carriers.

For electrons for instance, the distribution function at equilibrium is expressed as $f_n(E) = [\exp((E - E_{\mathrm{F}})/k_{\mathrm{B}}T) + 1]^{-1}$ where E_{F} is the Fermi level, which corresponds to the energy at which half of the available states are occupied. Using the Boltzmann approximation of the Fermi-Dirac distribution ($\exp((E - E_{\mathrm{F}})/k_{\mathrm{B}}T) \gg 1$) leads the electron density in the conduction band to be expressed as [Würfel & Würfel 2016]

$$n = \int_E D_{\mathrm{C}}(E')f_n(E')dE' = N_{\mathrm{C}} \exp\left(-\frac{E_{\mathrm{C}} - E_{\mathrm{F}}}{k_{\mathrm{B}}T}\right). \tag{4.1}$$

N_{C} corresponds to the effective density of states in the conduction band and is equal to $2(m_n^* k_{\mathrm{B}}T/2\pi\hbar^2)^{3/2}$. Similarly, we get for the hole density in the valence band

$$p = N_{\mathrm{V}} \exp\left(-\frac{E_{\mathrm{F}} - E_{\mathrm{V}}}{k_{\mathrm{B}}T}\right), \tag{4.2}$$

with the effective density of states in the valence band N_{V} being equal to $2(m_p^* k_{\mathrm{B}}T/2\pi\hbar^2)^{3/2}$. Since $E_{\mathrm{C}} - E_{\mathrm{V}} = E_g$, we get that at equilibrium np is constant and equal to

$$np = N_{\mathrm{C}}N_{\mathrm{V}} \exp\left(-\frac{E_g}{k_{\mathrm{B}}T}\right). \tag{4.3}$$

Intrinsic semiconductors

The case of a pure (i.e. without any impurity atom) semiconductor at equilibrium corresponds to the simplest scenario. Since each electron in the conduction band should be related to a hole in the valence band, $n = p$ and thus

$$n = p = n_{\mathrm{i}} = \sqrt{N_{\mathrm{C}}N_{\mathrm{V}}} \exp\left(-\frac{E_g}{2k_{\mathrm{B}}T}\right), \tag{4.4}$$

n_{i} being the intrinsic carrier concentration. The Fermi level is equal to the intrinsic energy level E_{i} and is given by

$$E_{\mathrm{F}} = E_{\mathrm{i}} = \frac{E_{\mathrm{V}} + E_{\mathrm{C}}}{2} - \frac{k_{\mathrm{B}}T}{2} \ln\left(\frac{N_{\mathrm{C}}}{N_{\mathrm{V}}}\right) \tag{4.5}$$

and is therefore close to the middle of the bandgap $(E_{\mathrm{V}} + E_{\mathrm{C}})/2$ for moderate temperatures.

Doped semiconductors

In order to break the condition $n = p$, one must find a way to add electrons to the conduction band without adding holes in the valence band (or the opposite). This can be done by doping the material, i.e. through the addition of impurity atoms. For instance, let us replace one atom

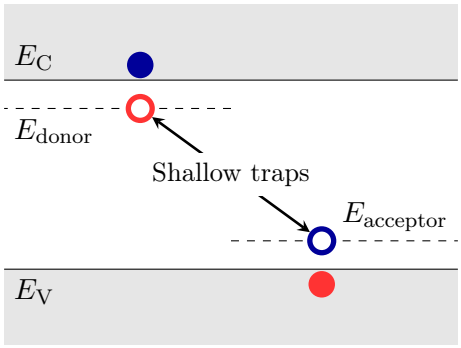

Figure 4.1: Impact of doping on the charge distribution (left: donor atom, right: acceptor atom).

from the crystal lattice by another having one more valence electron. This last electron cannot be shared with surrounding atoms, since their valence band is already full, and is thus very weakly bound to the atom. Thus, the energy of this valence electron is close to E_C, and thermal agitation is sufficient to promote the electron to the conduction band. The hole left behind cannot be defined as a particle in the valence band since its energy is much larger than E_V. Rather, it should be understood as a *shallow trap*, i.e. a new available level of energy in which free electrons are easily captured or conversely sent back to the conduction band. As they don't capture charge carriers for long, the degradation of charge transport due to these traps is negligible. The overall concept is represented in Figure 4.1. Since the impurity atom adds an electron to the conduction band, it is called a donor. Of course, we could instead add an atom with one less valence electron; it would then very easily capture an electron from the valence band (thus called an acceptor atom), leaving behind a hole in the valence band.

If the dopant concentration (either in donor N_d or acceptor N_a) is large enough, the charge carrier density can be significantly changed. For $N_d \gg n_i$ for instance, we obtain $n \approx N_d$; in the same time, $np = n_i^2$ should still hold since the semiconductor is still at equilibrium, so that $p \approx n_i^2/N_d$. The Fermi level is then

$$E_F = E_i + k_B T \ln\left(\frac{n}{n_i}\right) \approx E_i + k_B T \ln\left(\frac{N_d}{n_i}\right) \tag{4.6}$$

and comes closer to the conduction band as the donor density is increased. Similar expressions can be derived considering acceptor doping instead.

4.1.2 Quasi Fermi levels and out-of-equilibrium conditions

When an optoelectronic device is illuminated (PV cell) or supplied with electricity (LED), additional carriers are present in the semiconductor and the different expressions of n and p given above do not hold any more, the device being out of equilibrium. Especially, the notion of Fermi level is no longer relevant, as having both more electrons and holes than in equilibrium would mean that E_F comes simultaneously closer to the conduction band and to the valence band, which is obviously impossible. Instead, we should now use different levels for the two kinds of charge carriers, called quasi Fermi levels. They represent an extension of the Fermi level which

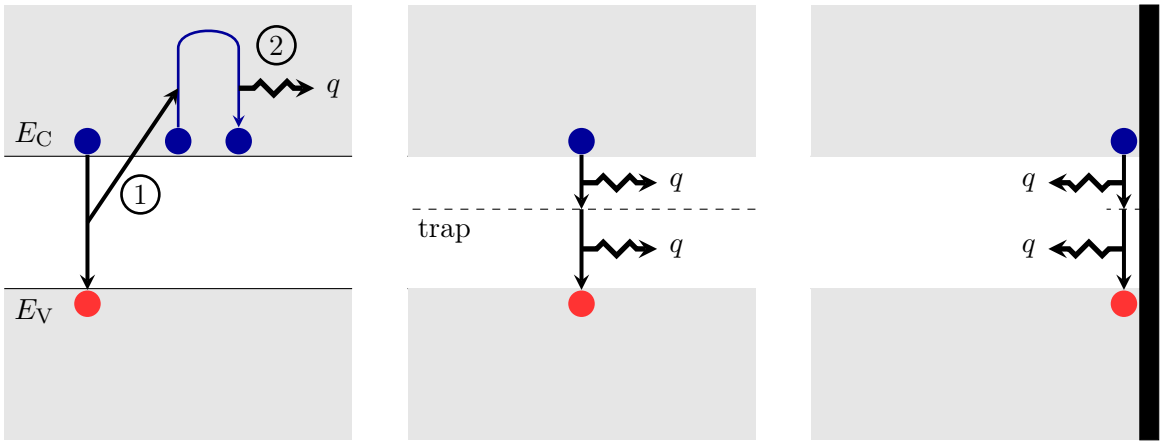

(a) Auger (b) Shockley-Read-Hall (c) Surface

Figure 4.2: Schematics of the main types of non-radiative recombinations.

works also in out-of-equilibrium conditions:

$$n = N_C \exp\left(-\frac{E_C - E_{Fn}}{k_B T}\right), \tag{4.7a}$$

$$p = N_V \exp\left(-\frac{E_{Fp} - E_V}{k_B T}\right), \tag{4.7b}$$

while at equilibrium $E_{Fn} = E_{Fp} = E_F$. These quasi Fermi levels are directly related to the electrochemical potential η of the charge carrier ($\eta_n = E_{Fn}, \eta_p = -E_{Fp}$). Notice that now, the product np is a function of the difference of quasi Fermi levels, thus of the local chemical potential of the emitted photons since $\mu = \eta_n + \eta_p = E_{Fn} - E_{Fp}$:

$$np = n_i^2 \exp\left(\frac{E_{Fn} - E_{Fp}}{k_B T}\right) = n_i^2 \exp\left(\frac{\mu}{k_B T}\right). \tag{4.8}$$

Thus, the larger $E_{Fn} - E_{Fp}$ (or μ) gets, the further away the device is from equilibrium.

4.1.3 Sources of non-radiative recombinations

As stated at the beginning of this chapter, different physical phenomena can cause the non-radiative recombination of electron-hole pairs. In the following, we review these phenomena which are represented in Figure 4.2.

Auger recombination

Auger recombination (Figure 4.2a) is a three-particle phenomenon, which can occur with two electrons and a hole or one electron and two holes; we describe here only the former case for brevity. The energy released by the recombination of an electron and a hole, instead of being converted into a photon, is transferred to another electron in the conduction band (step 1). Being far from the lowest energy level in the conduction band, this second electron will quickly thermalise, the initial energy being lost as heat to the lattice (step 2). Of course, such a process will take place more often when more particles are present. In the case of an electron-electron-hole (*eeh*) Auger recombination, the recombination rate is simply given by $R_n = C_n n^2 p$, where C_n is the *eeh* Auger recombination coefficient. As stated in Section 1.1.2, any non-radiative recombination should

be accompanied by a non-radiative generation that cancels it at equilibrium. Since $np = n_i^2$ at equilibrium, the net recombination rate (still written R_n for simplicity) is $R_n = C_n n(np - n_i^2)$. Considering also electron-hole-hole recombination, it gives finally

$$R_{\text{Auger}} = (C_n n + C_p p)(np - n_i^2). \tag{4.9}$$

Shockley-Read-Hall recombination

The notion of a bandgap in which no energy levels are available holds only for perfect crystals. In reality, some energy levels will be present due to the presence of defects in the crystalline lattice (e.g. vacancy, dislocation); such levels represent traps just as the shallow traps introduced through doping. During a Shockley-Read-Hall (SRH) recombination, the electron in the conduction band will move to these traps instead of directly recombining with the hole, releasing the difference of energy as heat. The net SRH recombination rate can be expressed as

$$R_{\text{SRH}} = \frac{np - n_i^2}{\tau_n(p + p_t) + \tau_p(n + n_t)}, \tag{4.10}$$

where τ corresponds to the SRH lifetime of each charge carrier, and n_t and p_t are the charge carrier densities obtained when their quasi Fermi level equals the trap energy. The traps with the most important impact are those located in the middle of the bandgap [Grundmann 2016][2], as thermal agitation is insufficient to free carriers from there. Such traps are called *deep traps*. In consequence, we will assume in the following that $n_t = p_t = n_i$ (since for an intrinsic semiconductor at equilibrium, the Fermi level is close to the middle of the bandgap, as shown in Section 4.1.1).

When the doping level is large enough, the majority carrier density is mostly insensitive to illumination or voltage bias and remains close to the doping level. In such situations, the low-injection approximation (LIA) can be used to simplify R_{SRH}: assuming $n = n_{\text{eq}} \approx N_d \gg p$ (n_{eq} being the electron carrier density at equilibrium) we get that in highly n-doped layers

$$R_{\text{SRH}} = \frac{p - p_{\text{eq}}}{\tau_p}. \tag{4.11}$$

The implication of using such an approximation has been analysed in [Blandre *et al.* 2017], and will be quickly investigated in Section 5.2.4. In the remaining of the manuscript, the complete expression provided in Eq. (4.10) will be used.

Surface recombination

Surface recombinations are similar to SRH recombinations, the only difference being that the defects are caused by dangling bonds at the interface between two media. Their net rate is expressed as

$$R_{\text{surf}} = \frac{np - n_i^2}{\frac{1}{S_n}(p + p_t) + \frac{1}{S_p}(n + n_t)}, \tag{4.12}$$

where S corresponds to the surface recombination velocity. Under the LIA, R_{surf} becomes simply expressed as $S_n(n - n_{\text{eq}})$ (considering a p-doped layer); in the frame of this thesis however, the complete expression provided above will be retained. As for SRH recombinations, we will assume in the following that $n_t = p_t = n_i$.

[2]The exact expression of the trap energy level with the largest impact is provided in page 373 of [Grundmann 2016], and is in fact slightly shifted compared to the Fermi level of an intrinsic semiconductor.

4.1.4 Radiative recombinations: radiative vs. electrical framework

In Part I of the manuscript, the radiative recombination rate was computed directly from the photon emission rate. Without precising it, we in fact supposed that the quasi Fermi levels were constant which implied that $\mu = eU$. In the case of drift-diffusion simulations, quasi Fermi levels can be computed but are available only *at the end* of the simulation, while μ is needed *before* the use of the drift-diffusion solver to have the correct radiative quantities. To circumvent this issue, the radiative recombination rate is often expressed from electrical quantities instead of radiative quantities, allowing to use the correct value of μ:

$$R_{\text{rad}} = B_{\text{rad}}(np - n_{\text{i}}^2) = B_{\text{rad}} n_{\text{i}}^2 \left(\exp\left(\frac{\mu}{k_{\text{B}}T} \right) - 1 \right). \tag{4.13}$$

This expression requires Boltzmann's approximation in order to be obtained, and thus holds only if $E_g - \mu \gg k_{\text{B}}T$. The radiative recombination coefficient B_{rad} directly depends on the local thermal emission rate of a device at equilibrium $\dot{N}_{\text{em}}$ through $B_{\text{rad}} = \dot{N}_{\text{em}}/n_{\text{i}}^2$. It should therefore depend on the position of emission, on the structure itself (material, thickness) and on its surroundings if they modify the emission rate (as in the case of near-field radiation). In practice, it is almost always considered to be constant as the use of a local coefficient complicates the study. Most of the time, it is taken as a material property (e.g. [Blandre *et al.* 2017, Milovich *et al.* 2020]). Occasionally, it is calculated from the van Roosbroeck-Shockley relation (e.g. in [Forcade *et al.* 2022]) which partially allows the geometry to be taken into account and takes the form:

$$B_{\text{rad}} = \frac{1}{n_{\text{i}}^2 \hbar^3 c^2} \int_0^\infty n(E)^2 \alpha_{\text{IB}}(E) \frac{E^2}{\exp\left(\frac{E}{k_{\text{B}}T} \right) - 1} dE, \tag{4.14}$$

n being here the layer refractive index and α_{IB} representing the absorption coefficient relative to interband transitions. If the use of such a coefficient B_{rad} is convenient, it however has several drawbacks. One first issue is related to photon recycling: while it allows including the complete photon emission (whether they escape the component or get eventually reabsorbed), it however does not include the subsequent increase in radiative generation rate caused by photon recycling. Therefore, it fails to satisfy detailed balance and cause the generation-recombination rate to be underestimated. In addition, it has recently been shown that neither of these two approaches allows including interference effects [Feng *et al.* 2022] or the surroundings influence [DeSutter *et al.* 2017]. This reduces the interest of Eq. (4.13) as the precision gained on the electroluminescence enhancement factor $\exp(\mu/k_{\text{B}}T)$ is offset by the precision lost on the spatial variation of thermal emission $\dot{N}_{\text{em}}$. For far-field applications, and especially if the different layers are thick enough, it may still be a satisfactory approximation. It is also mostly valid for structures in which the rate of radiative recombination events is small or even negligible in comparison to generation or non-radiative recombination. However, with our device working in the near field and with radiative recombinations expected to be dominant at least in the LED, this method would be highly erroneous and must therefore be avoided in NF-TPX applications.

A numerical method has been recently proposed to relax the $\mu = eU$ approximation while still using radiative quantities to express R_{rad} [Callahan *et al.* 2021]; it is summarised in Figure 4.3. In this model, radiative calculations are coupled to drift-diffusion simulations: the chemical potential μ obtained from charge transport ($\mu = E_{\text{F}n} - E_{\text{F}p}$) is used to update photon absorption and emission rates. Drift-diffusion equations can then be solved once more. These two steps are iterated up until a stopping criterion is reached, which can be either on μ or on R_{rad}. Such a model allows to obtain the correct expression for radiation, both in terms of electroluminescent

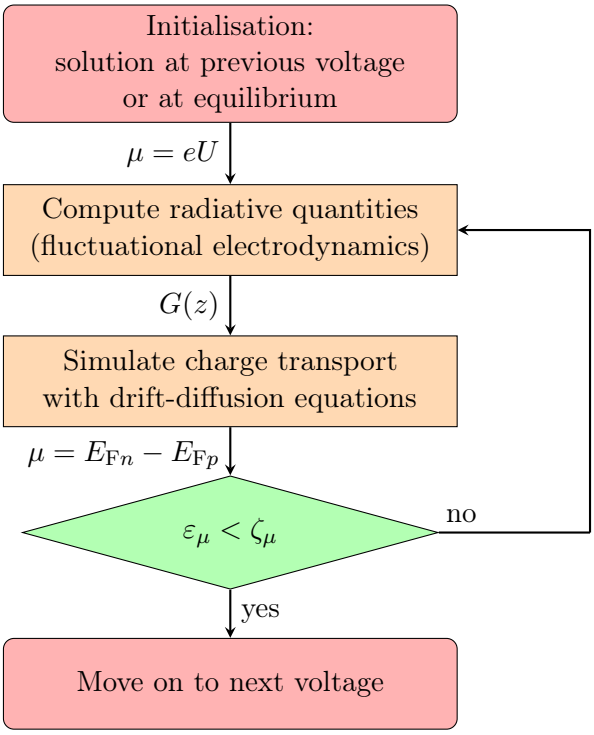

Figure 4.3: Flowchart of the coupled radiative-electrical iterative solver proposed in [Callahan *et al.* 2021].

enhancement and of spatial variation. On paper, we may want to use this method systematically; however, we should keep in mind that it increases the solver complexity and may give rise to convergence issues. As NF-TPX simulations will already be relatively complex due to the LED-PV cell coupling, we decided to keep the $\mu = eU$ approximation for the first 1D simulations performed in this Part[3]. The accuracy of this approximation will be examined in subsequent chapters, and the iterative process implemented if necessary.

Ultimately, the net and local generation-recombination rate in a component is expressed as follows:

$$G(z) - R(z) = \frac{d\dot{N}_{\mathrm{net}}}{dz}(\mu, z) - R_{\mathrm{Auger}}(z) - R_{\mathrm{SRH}}(z). \tag{4.15}$$

4.1.5 Joining semiconductors for charge carrier separation

As explained in Chapter 1, a homogenous semiconductor cannot be directly used for optoelectronic applications but should rather be joined with semiconductors with different properties to obtain components with good performance (see Section 1.1.3). We finish this section by reviewing the different kind of junctions that are generally used along with the physical phenomena occurring at the junction.

4.1.5.1 Types of junctions

The simplest structure, presented in many solar cell textbooks ([Nelson 2003, Würfel & Würfel 2016, Kitai 2018]), is the PN junction (Figure 4.4a). It simply corresponds to the junction of a p-doped

[3]Since the temperature is supposed to be constant throughout a component, this also means that the net photon flux exchanged between two layers of a component is supposed to be equal to zero (as $\dot{N} \propto \Delta f_{\mathrm{BE}}$).

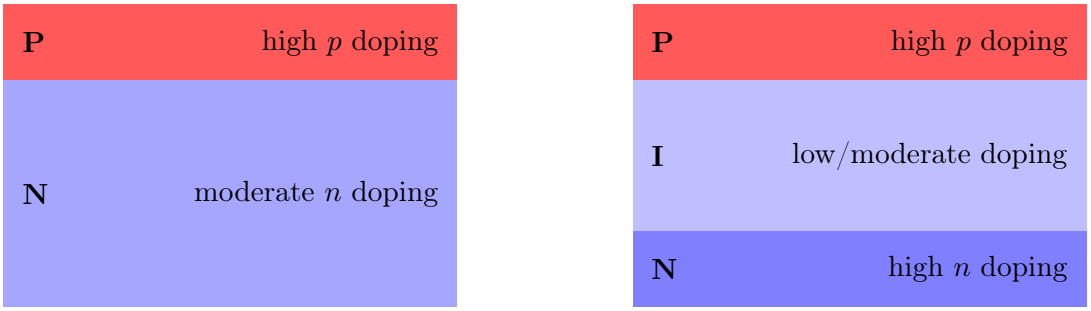

(a) PN junction (b) PIN junction

Figure 4.4: Basic semiconductor junctions.

material (hence having an improved hole conductivity) and an n-doped layer (improved electron conductivity). The difference of conductivity gives opposite preferable paths for electrons and holes, electrons being more likely to go to the contact on the n-doped layer side and holes to the one on the p-doped layer side. A slightly more complex structure is the PIN junction (Figure 4.4b), in which two thin and highly-doped layers (the P and N layers) are placed around a thick layer (layer I). Even if I stands for intrinsic, this layer is always at least slightly doped, due to unintentional doping by impurities[4]. Contrary to the PN junction, in which the thicker layer is limited in terms of doping level to prevent excessive non-radiative recombinations, both P and N layers can be highly doped in the PIN structure. They have thus very different electron and hole conductivity, which gives them good selectivity and sets the preferable path of charge carriers more efficiently than in the case of the PN junction.

Along with the structure itself, the choice of the materials composing the different layers will obviously have a significant impact. The use of a unique material for the different layers corresponds to the simplest case both in terms of simulation and manufacture. Such a component is called a *homostructure* (or homojunction). Often, materials with higher bandgaps are used for the highly doped layers, as their reduced intrinsic carrier concentration (see Eq. (4.4)) along with the potential barrier created at the junction (see Figure 4.5b) largely reduce the minority charge carrier density: it therefore improves their selectivity. Such a component made of different materials is called a *heterostructure* (or heterojunction).

In this Part, we will study PIN homostructures (Chapter 5) and heterostructures (Chapter 6), which correspond to the structures currently considered for NF-TPV applications [Forcade *et al.* 2022]. Note that more complex (thus more efficient) structures have been examined for LEDs and PV cells, such as multijunction cells in which several cells are stacked [LaPotin *et al.* 2022] (see also Figure 1.14) or multiple quantum well structures [Green 2006]; such structures will not be considered in the frame of this work as the physical understanding of TPX structure should first be developed on simpler architectures.

4.1.5.2 Physical phenomena occurring at junctions

The junction of semiconductors gives rise to specific physical phenomena in the region close to the interface (the *space-charge region*). As the density of free charge carriers is different on either side of the interface, carriers will diffuse towards the regions of lower density, electrons for instance diffusing in the p-doped layer. Initially neutral, the space-charge region becomes charged

[4] In the following chapters, we will sometimes intentionally dope this layer to minimise non-radiative recombinations. Nonetheless, we will keep the denomination PIN for simplicity.

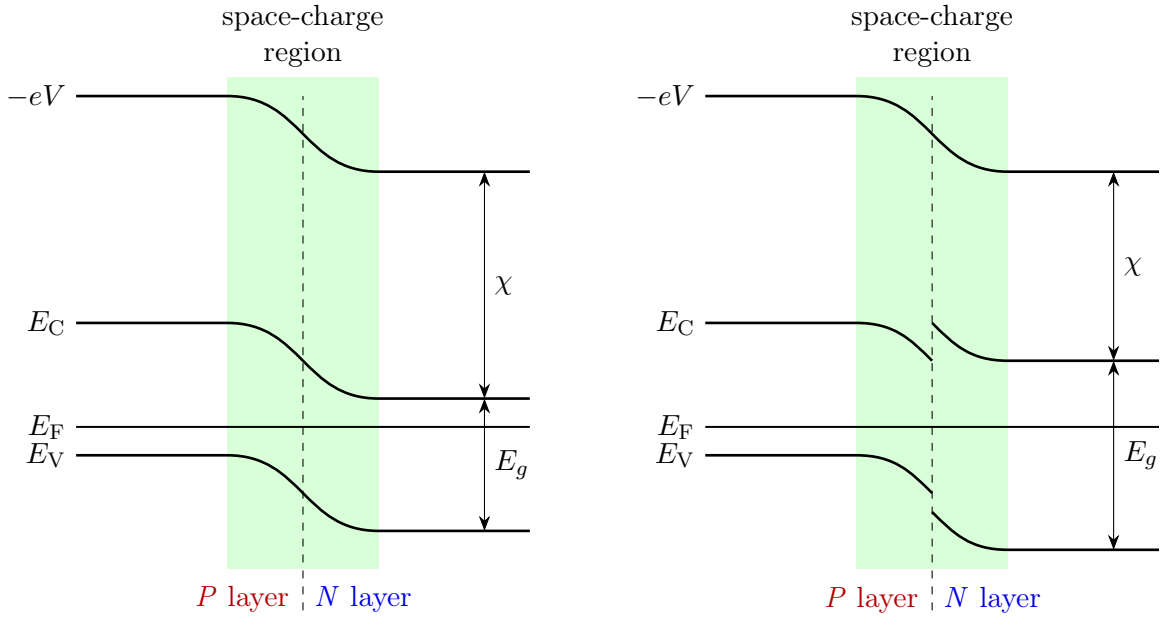

(a) Homojunction (b) Heterojunction

Figure 4.5: Band diagram for different abrupt junctions at equilibrium.

(hence the name), giving rise to an electric field which exerts a force in the direction opposite to diffusion; equilibrium is reached once diffusion and drift caused by the built-in electric field cancel each other out. Because of the electric field, the conduction and valence bands bend inside the space-charge region. Their exact variations can be obtained from the electrostatic potential V[5], related to the electric field through $\mathcal{E} = -\mathrm{d}V/\mathrm{d}z$, and from the electron affinity $\chi = -eV - E_C$, which is a material property independent of the doping level. The resulting band diagram is shown in Figure 4.5a.

Furthermore, if the two materials forming the junction are different, potential barriers will appear due to the energy band misalignment. E_C and E_V are discontinuous at an abrupt junction and must satisfy $\Delta E_C = -\Delta\chi$ and $\Delta E_V = -\Delta\chi - \Delta E_g$. This causes also a discontinuity in the charge carrier density at the interface. The only two quantities which remain continuous are the electrostatic potential, since the interface is supposed to be uncharged, and the Fermi level which is always constant at equilibrium. The corresponding band diagram is represented in Figure 4.5b. Out of equilibrium, these barriers give rise to specific charge transport phenomena (thermionic emission, tunnelling), which will be detailed in Chapter 6.

4.2 Drift-diffusion modelling

4.2.1 The drift-diffusion equations

We now introduce the set of equations which will be used to model both the LED and the PV cell, centred on the drift-diffusion equations. Note that while it is by far the most common way to model charge transport in optoelectronic devices, it is not the only way. For instance,

[5]The electrostatic potential V, which spatially varies within a junction and is directly related to the electric field, should not be confused with the applied voltage U, which corresponds to the difference of the electron and hole quasi Fermi levels at the boundary of the components. In Figure 4.5 for instance, V varies spatially due to the built-in electric field whereas U is zero.

the Boltzmann transport equation (BTE), from which drift-diffusion equations can be derived, describes with much more precision the different physical phenomena involved and the statistical behaviour of charge carriers [Kivisaari *et al.* 2015]. In our case, the additional precision it can provide is outweighed by the increase in model complexity, which is why the drift-diffusion model is preferred.

The first two equations of the set are continuity equations, which were in fact already used in the previous chapters, although not in their local form. They ensure the conservation of charge carriers, whose density can only be changed during transport due to generation or recombination events:

$$\frac{\mathrm{d}J_n}{\mathrm{d}z}(z) = -e(G(z) - R(z)), \tag{4.16a}$$

$$\frac{\mathrm{d}J_p}{\mathrm{d}z}(z) = \quad e(G(z) - R(z)), \tag{4.16b}$$

where J_i corresponds to the current density associated to carrier i, and G and R are respectively the local generation and recombination rate. Surface recombinations, which are not taken into account in the previous equations as they only happen at the electrical contacts, are included through boundary conditions. For the minority carriers at the interface with the contact, the current density is simply expressed as

$$J_{\mathrm{min}} = \pm e \cdot R_{\mathrm{surf}}, \tag{4.17}$$

the sign on the right side depending on the carrier type and on which boundary is considered - the sign should be the same as the one in front of $R(z)$ in the continuity equation. The total current density is equal to J_n+J_p. Since the boundary condition is given at the opposite ends for the two equations, the total current is expressed as

$$J(z) = J_n(z) + J_p(z) = e\left(\int_z (G(z) - R(z))dz - R_{\mathrm{surf,tot}}\right) = J, \tag{4.18}$$

a constant in steady state. This integrated expression corresponds to the equation used in the detailed-balance approaches of Part I.

To model charge transport, we must relate current density to the various phenomena contributing to the movement of charges. Two different driving forces are considered:

- the electric field, which causes the drift of carriers;
- the gradient of carrier density, which causes their diffusion.

The resulting equations are the drift-diffusion equations:

$$J_n(z) = \sigma_n \mathcal{E}(z) + eD_n \frac{\mathrm{d}n}{\mathrm{d}z}(z), \tag{4.19a}$$

$$J_p(z) = \sigma_p \mathcal{E}(z) - eD_p \frac{\mathrm{d}p}{\mathrm{d}z}(z), \tag{4.19b}$$

where D_i is the diffusion coefficient. Using $\sigma_n = e\mu_n n$ and $\sigma_p = e\mu_p p$ along with Einstein relation

$(D_i = \mu_i \cdot k_\mathrm{B}T/e)$ gives

$$J_n(z) = \mu_n\left(n(z)\frac{\mathrm{d}(-eV)}{\mathrm{d}z}(z) + k_\mathrm{B}T\frac{\mathrm{d}n}{\mathrm{d}z}(z)\right), \tag{4.20a}$$

$$J_p(z) = \mu_p\left(p(z)\frac{\mathrm{d}(-eV)}{\mathrm{d}z}(z) - k_\mathrm{B}T\frac{\mathrm{d}p}{\mathrm{d}z}(z)\right), \tag{4.20b}$$

where the electrostatic potential V has been used to make the energy eV appear.

The last required equation is Poisson equation. Derived from Maxwell-Gauss equation, it connects the variation of the electrostatic potential to the local charge, which can be due to free carriers or to shallow traps remaining on dopant atoms:

$$\frac{\mathrm{d}^2V}{\mathrm{d}z^2}(z) = \frac{e}{\varepsilon_\mathrm{s}\varepsilon_\mathrm{v}}(n(z) - p(z) + N_a(z) - N_d(z)). \tag{4.21}$$

ε_s is the static dielectric constant, which corresponds to the limit of ε as $\omega \to 0$. The modelling of charge transport therefore requires to solve this set of five equations to obtain the electrostatic potential along with the charge carrier densities and current densities. We still need two additional hypotheses, which will bring the remaining boundary conditions:

- the majority charge carriers at an electrical contact are supposed to be at equilibrium with the charges inside the contact. This means the quasi Fermi level remains constant through the interface, i.e. that $E_{\mathrm{Fn,maj}} = eU$ and $E_{\mathrm{Fp,maj}} = 0$ (the difference of these two representing the applied voltage).
- the regions close to the contacts are supposed to be uncharged.

4.2.2 Why using our own drift-diffusion solver?

Numerous softwares are capable of solving these equations. They can be divided into three main categories:

- commercial multiphysic softwares such as COMSOL;
- commercial softwares specialised on semiconductor physics such as Sentaurus or Silvaco TCAD;
- specialised free softwares such as PC-1D [Basore 1990], SCAPS [Burgelman *et al.* 2000] or Sesame [Gaury *et al.* 2019].

The pros and cons of these softwares are shown in Table 4.1. All the commercial softwares have been grouped in a unique category as their characteristics are mostly similar; specialised softwares may have more precise and robust models, but this is of limited interest for us in view of the simplicity of the structures considered. In the end, no software is perfect. Commercial softwares are the most complete ones but are quite heavy to handle and can be expensive. Each of the specialised softwares, while sharing basic features with the others, have specific capabilities (implementation of thermionic emission and tunnelling for SCAPS, 2D resolution and easy coupling with external near-field radiation solver for Sesame). Furthermore, the capacity of any of these softwares to properly handle the coupled modelling of the LED and PV cell is unknown, and may not be straightforward; the few TPX calculations made with SCAPS were for instance quite cumbersome.

Table 4.1: Pros and cons of available drift-diffusion solvers (✓yes, ∼ depends on software, ✗ no, ? unknown).

	Commercial softwares	Specialised free softwares	Own algorithm
2D simulation	✓	∼	✗
3D simulation	✓	✗	✗
Complete physics (thermionics, tunnelling)	✓	∼	✓
Fermi-Dirac statistics	✓	✗	✗
Coupling with ext. near-field code	✓	∼	✓
Easy/quick to handle	✗	✓	✓
Free	✗	✓	✓
LED-PV coupling	?	?	✓

As an in-house drift-diffusion solver was already developed in the past at our lab for TPV [Blandre *et al.* 2017], we chose to start from it to make our own drift-diffusion solver for TPX applications. This guarantees the quality of the communication between the radiative and electrical solvers, and simplifies the LED-PV cell coupled modelling. It also enables the model to be progressively refined, for example with the implementation of thermionic emission and charge tunnelling carried out in Chapter 6 - this might have proved difficult with external softwares. Furthermore, the development of a solver enhances the understanding of the underlying physics. It however comes at the cost of time, and requires validation - this will be done in the subsequent chapters.

4.2.3 Material properties

Since effective masses and carrier mobilities were already required for near-field radiation calculations, the drift-diffusion solver needs only few additional material properties, namely the electron affinity and the different non-radiative recombination coefficients. Their respective value can be found in Appendix B. As for radiative properties however, it proves difficult to find data which are temperature- and composition-dependent. Regarding non-radiative recombination coefficients for instance, no clear data was found for AlGaAs. Consequently, GaAs data was used instead - a similar choice was done in [Oublon 2023]. Since there is no consensus on the variation of these coefficients with temperature, we also take room temperature data as a first-hand approximation in Chapter 5. The impact of including these two dependencies will be analysed in Chapter 6. While it may seem that too many approximations are being used, we have to make clear that even GaAs properties are not precisely known. Looking at the GaAs SRH lifetime at room temperature for instance, a wide variety of values can be found in the literature:

- $\tau_{\mathrm{SRH}} = 10$ ns in [Maros *et al.* 2015];
- $\tau_{\mathrm{SRH}} = 900$ ns in [Perl *et al.* 2017];
- $\tau_{\mathrm{SRH}} = 3$ μs in [Sadi *et al.* 2019a];
- $\tau_{\mathrm{SRH}} = 16.7$ μs in [Zhao *et al.* 2018] (given for any AlGaAs alloy).

A significant uncertainty can therefore be expected due to this variability.

4.3 To sum up

In this chapter, we reviewed the main mechanisms related to charge transport in semiconductors. This provided the opportunity to introduce several important physical quantities - such as quasi Fermi levels and charge carrier densities - along with their interrelations. We also presented the expressions adopted to calculate the rates of radiative and non-radiative events, after discussing the various possibilities available and commonly used in the literature. We then introduced the set of equations that allows modelling charge transport in semiconductors in 1D, which gathers the drift-diffusion equations, the continuity equations and the Poisson equation. Finally, and although several commercial and free drift-diffusion solvers are available, we explained our decision to develop our own solver: succinctly, it allows for much more flexibility in terms of modelling. With the main equations and the associated material properties defined, we can proceed to the simulation of realistic structures.

Chapter 5

Study of AlGaAs-GaAs PIN homostructures

Contents

5.1 Numerical methods 103
5.1.1 Details on the algorithm 103
5.1.2 Validation of the solver 107
5.2 Study of an optimised structure 108
5.2.1 Description of the structure 108
5.2.2 Radiative heat transfer 110
5.2.3 Maximum power and related efficiency 110
5.2.4 Local charge distribution at maximum power point 115
5.2.5 Fundamental asymmetry between LED and PV operation 117
5.2.6 Impact of non-radiative recombinations 120
5.2.7 Quantum efficiency in the near field 124
5.3 Impact of bandgap misalignment in the case of non-abrupt bandgaps . 125
5.3.1 Urbach tails: definition and implementation 125
5.3.2 Influence of Urbach tails on TPX performance 128
5.3.3 Analysis of the resonance modes close to E_g 129
5.4 To sum up 131

To study realistic TPX devices, we must first decide what kind of structure we want for each component. Since no studies of this sort have been carried out previously in the literature, we choose to start with relatively simple structures. The simplest is the PN junction; TPX devices composed of such structures have been studied in [Legendre & Chapuis 2022a]. In this chapter, we directly consider TPX devices made of PIN homostructures, whose additional complexity compared to PN structures remains modest but which display significantly better performance, as mentioned in the previous chapter.

5.1 Numerical methods

5.1.1 Details on the algorithm

While all the required equations have been presented in the previous chapter, they cannot be easily solved in their current form. Rather, several modifications are required and are presented thereafter. The first step is to relate the carrier density to the electrostatic potential. To do so,

we express the charge carrier densities as a function of the intrinsic concentration:

$$n = n_\mathrm{i} \exp\left(\frac{E_{\mathrm{F}n} - E_\mathrm{i}}{k_\mathrm{B}T}\right), \tag{5.1a}$$

$$p = n_\mathrm{i} \exp\left(\frac{E_\mathrm{i} - E_{\mathrm{F}p}}{k_\mathrm{B}T}\right). \tag{5.1b}$$

In Eq. (4.5), the intrinsic energy level E_i was given relatively to E_C and E_V. Following the energy diagrams shown in Figure 4.5, these two levels can be expressed as $E_\mathrm{C} = E_0 - eV - \chi$ and $E_\mathrm{V} = E_0 - eV - \chi - E_g$. E_0 is the reference energy, which corresponds to the energy of a free electron in vacuum with no kinetic energy and at a zero electrostatic potential, taken equal to zero in the energy diagrams. The complete expression of E_i is then

$$E_\mathrm{i} = E_0 - eV - \chi - \frac{E_g}{2} - \frac{k_\mathrm{B}T}{2} \ln\left(\frac{N_\mathrm{C}}{N_\mathrm{V}}\right), \tag{5.2}$$

which varies with position. To simplify this expression, the zero energy level - and consequently the value of E_0 - is chosen so that $E_\mathrm{i}(z = 0, V = 0) = E_\mathrm{F}$, which is possible because E_F is constant. This gives

$$E_\mathrm{i}(z) = E_\mathrm{F} - eV(z) - (\chi(z) - \chi(0)) - \frac{E_g(z) - E_g(0)}{2} - \frac{k_\mathrm{B}T}{2} \ln\left(\frac{N_\mathrm{C}(z)}{N_\mathrm{C}(0)} \frac{N_\mathrm{V}(0)}{N_\mathrm{V}(z)}\right). \tag{5.3}$$

In this chapter, we work with homostructures. Therefore χ, E_g, N_C and N_V are constant and

$$E_\mathrm{i}(z) = E_\mathrm{F} - eV(z). \tag{5.4}$$

Defining the normalised electrostatic potential Ψ as $eV/k_\mathrm{B}T$ and using the Slotboom variables $\Phi_n = \exp((E_{\mathrm{F}n} - E_\mathrm{F})/k_\mathrm{B}T)$ and $\Phi_p = \exp((E_\mathrm{F} - E_{\mathrm{F}p})/k_\mathrm{B}T)$ [Slotboom 1973] finally gives

$$n = n_\mathrm{i} e^{+\Psi} \Phi_n, \tag{5.5a}$$

$$p = n_\mathrm{i} e^{-\Psi} \Phi_p. \tag{5.5b}$$

To make the analysis easier, we will consider E_F to be the zero reference level for quasi Fermi levels, which means they have a different reference energy than $-eV$. This corresponds to the standard approach [Blandre 2016, Vasileska *et al.* 2017], although rarely explicitly mentioned.

Looking at the aforementioned references, one may notice that the signs applied on the quasi Fermi levels are actually the opposite of ours. We suspect this comes from a difference in the definition of the quasi Fermi levels, as only our expression satisfies $np/n_\mathrm{i}^2 = \exp((E_{\mathrm{F}n} - E_{\mathrm{F}p})/k_\mathrm{B}T)$. We will show in Section 5.1.2 that this difference of definition does not impact the resolution as our algorithm is capable of reproducing results from [Blandre 2016].

Using Eq. (5.5), the drift-diffusion equations can easily be simplified into [Blandre 2016]

$$J_n(z) = \quad eD_n(z) n_\mathrm{i} e^{+\Psi(z)} \frac{\mathrm{d}\Phi_n}{\mathrm{d}z}(z), \tag{5.6a}$$

$$J_p(z) = -eD_p(z) n_\mathrm{i} e^{-\Psi(z)} \frac{\mathrm{d}\Phi_p}{\mathrm{d}z}(z). \tag{5.6b}$$

Similarly, Poisson equation can be expressed using normalised quantities. We define $\tilde{N}_\mathrm{dop} = (N_a - N_d)/n_\mathrm{i}$ and $\tilde{z} = z/z_{\mathrm{D,i}}$ where $z_{\mathrm{D,i}}$ is the intrinsic Debye length which equals $\sqrt{\varepsilon_\mathrm{s}\varepsilon_\mathrm{v} k_\mathrm{B}T/e^2 n_\mathrm{i}}$.

We then get

$$\frac{\mathrm{d}^2\Psi}{\mathrm{d}\tilde{z}^2}(z) = \left(e^{\Psi(z)}\Phi_n(z) - e^{-\Psi(z)}\Phi_p(z) + \tilde{N}_{\mathrm{dop}}(z)\right). \tag{5.7}$$

The five unknowns of the system are therefore Ψ, J_n, J_p, Φ_n and Φ_p.

5.1.1.1 At equilibrium

At equilibrium, these equations can be simplified since $E_{\mathrm{F}n} = E_{\mathrm{F}p} = E_{\mathrm{F}}$, which means that $\Phi_n = \Phi_p = 1$. The net electron and hole currents are zero, and only the Poisson equation (Eq. (5.7)) has to be solved to obtain Ψ. This is done with an iterative process to handle its non-linearity. At each iteration, the linearised Poisson equation is solved using a tridiagonal matrix algorithm (TDMA), allowing Ψ to converge towards the correct solution. This process has already been presented in the literature - although boundary conditions were either not given [Vasileska *et al.* 2017] or incorrect [Blandre 2016] - and will consequently not be detailed here. The complete development, holding for both equilibrium and out-of-equilibrium conditions as well as for homostructures and heterostructures, can be found in Appendix E.

5.1.1.2 Out of equilibrium

The five equations being coupled, they have to be solved iteratively to make the different physical quantities converge. The usual methodology for PV applications is as follows [Blandre *et al.* 2017, Vasileska *et al.* 2017]:

1. the first guess taken for the different unknowns at an applied voltage U_i corresponds to the converged solution obtained for the previous voltage U_{i-1};
2. continuity and drift-diffusion equations are combined to obtain two second-order differential equations of the Slotboom variables Φ_n and Φ_p, which no longer depend on the current densities and are solved using a TDMA;
3. the normalised electrostatic potential Ψ is updated using the iterative solver of the Poisson equation mentioned above, using the newly obtained Φ_n and Φ_p;
4. steps 2 and 3 are repeated until a given stopping criterion is reached.

This allows to reduce the system to three equations in the iterative process, current densities being computed only once convergence is reached. However, when trying to implement it, we noticed that the total current obtained was not spatially constant, especially around interfaces. Consequently, we chose to solve the system differently. The exact value taken by current densities and Slotboom variables are known at one boundary, being respectively related to the surface recombination rate and to the applied voltage as explained in Section 4.2.1. The variations of these quantities being given by first-order differential equations, they can in fact be obtained from integration. The second step given above is therefore replaced by the following:

2a. charge carrier current densities are obtained from the integration of continuity equations, using the minority carrier current density at the boundary of the component $J_i(z_0)$ which is related to surface recombinations; for instance for electron current,

$$J_n(z) = J_n(z_0) - e\int_{z_0}^{z}(G(z') - R(z'))dz'; \tag{5.8}$$

2b. Slotboom variables are computed through the integration of the drift-diffusion equations;

the quasi-Fermi level of majority carriers at a boundary z_0 being related to the applied voltage, we for instance get for electrons

$$\Phi_n(z) = \exp\left(\frac{eU}{k_\mathrm{B}T}\right) + \int_{z_0}^{z} e^{-\Psi(z')} \frac{J_n(z')}{eD_n(z')n_i} dz'. \tag{5.9}$$

In the expressions given above, the recombination rate $R(z)$ and the diffusion coefficients $D_i(z)$ depend on the charge carrier concentrations. Therefore, they must be updated at the beginning of each iteration. The diffusion coefficient is obtained from the carrier mobility, which is expressed using a Caughey-Thomas model:

$$\mu_{n/p} = \mu_\mathrm{min} + \frac{\mu_\mathrm{300K}\left(\frac{300}{T}\right)^{\theta_1} - \mu_\mathrm{min}}{1 + \left(\frac{N}{N_\mathrm{ref,300\ K}}\left(\frac{300}{T}\right)^{\theta_2}\right)} \tag{5.10}$$

The different parameters are taken from [Sotoodeh *et al.* 2000] and are different for electrons and holes. Here, we consider that N corresponds to the total number of free carriers: $N = n + p$. Indeed, the more carriers are present, the more they interact with each other, thus reducing their mobility. In fact, the mobility of each carrier even depends on the nature of the carriers around, but this will be neglected here. Often, N is simply supposed to be equal to the doping level [Blandre 2016]; while this is mainly correct in highly-doped layers, it breaks down for low-doped or intrinsic semiconductors and is therefore unsuitable for the study of PIN structures. We should also mention that the above expression is correct only when carriers are in a low electric field. If $\mathcal{E}$ becomes infinitely high, the carrier velocity must saturate and the related mobility should thus go to zero. This makes the Caughey-Thomas model incorrect close to interfaces, where the electric field is the highest. However, we show in Appendix F.1 that this error induces little difference in the final electrical characteristic of the device, and we will consequently use the low-field expression everywhere for simplicity.

Regarding the stopping criterion, we assume that convergence is reached once the maximum relative variation ε of the local charge carrier concentrations between two consecutive iterations $k-1$ and k is lower than a given tolerance ζ (which is set to values of the order of 10^{-6}). Given as an equation, the stopping criterion is

$$\varepsilon = \max\left(\left\|\frac{n_k - n_{k-1}}{n_{k-1}}\right\|_\infty, \left\|\frac{p_k - p_{k-1}}{p_{k-1}}\right\|_\infty\right) < \zeta. \tag{5.11}$$

Everything mentioned above relates to the electrical modelling of one component. Of course, in the case of a TPX device, the charge transport in both the LED and the PV cell should be resolved. These two components are coupled through radiation; as long as the chemical potential of emitted radiation μ is related to the applied voltage U through $\mu = eU$, the different radiative quantities are perfectly known for any couple of voltages before charge transport calculations. Therefore, the electrical modelling of the LED and the PV cell can be performed independently. The sole difference with PV simulation is that the current density must be computed on a 2D voltage space, both voltages being between 0 and E_g (E_g excluded). The first guess taken for the different quantities at $(U_\mathrm{LED}, U_\mathrm{PV}) = (U_i, U_j)$ is chosen as follows:

- if $U_i > 0$, it corresponds to the solution obtained at (U_{i-1}, U_j);
- if $U_i = 0$ and $U_j > 0$, it corresponds to the solution obtained at $(0, U_{j-1})$.

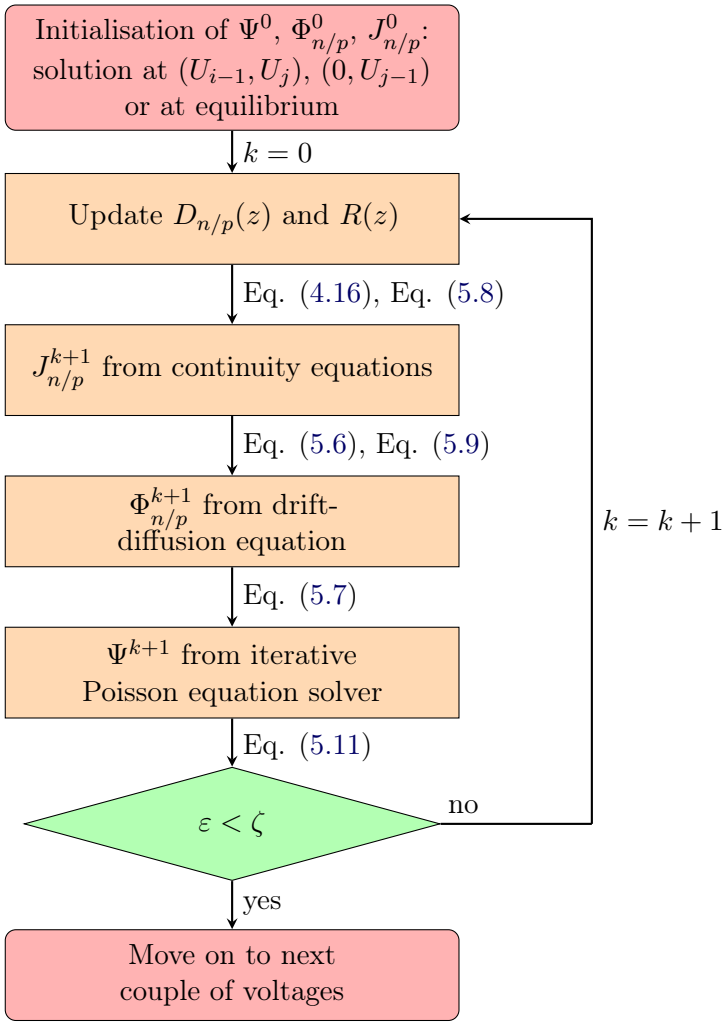

Figure 5.1: Flowchart of the drift-diffusion solver for homostructures at $(U_{\mathrm{LED}}, U_{\mathrm{PV}}) = (U_i, U_j)$.

- if $U_i = U_j = 0$, it corresponds to the solution obtained at equilibrium.

The drift-diffusion algorithm is summarised in the flowchart shown in Figure 5.1.

5.1.2 Validation of the solver

To validate our solver, we try to reproduce the results obtained in [Blandre 2016] for an InSb PIN homostructure. The structure considered is shown in Figure 5.2, the InSb cell being cooled down to 100 K to limit non-radiative recombinations. This cell is used in a NF-TPV device, which consequently allows to validate both radiative and electrical solvers along with their coupling. Since the code used in [Blandre 2016] was available to us, the data shown below comes directly from it rather than from the digitalisation of figures, and matches well the published results (see e.g. Figure V.22 of [Blandre 2016] for the I-V characteristic). To complete the validation, we compare our results with those obtained by SCAPS, using as an input the radiative generation rate computed by our solver. To match the calculations made in [Blandre 2016], the PV cell radiative recombination rate is computed using Eq. (4.13) with $B_{\mathrm{rad}} = 5 \times 10^{-11}$ cm^{-3}.s^{-1} instead of using the photon emission rate.

We show in Figure 5.3a the I-V characteristic computed by the different algorithms. All three

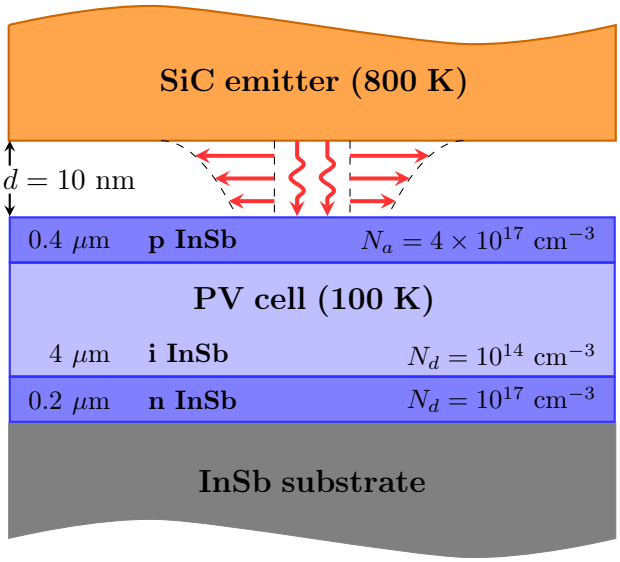

Figure 5.2: Structure used for the validation of the drift-diffusion solver.

are mostly similar, with a short-circuit current of the order of 15 A.cm^{-2} and an open-circuit voltage close to 17.7 mV. The match is especially good between our algorithm and the one used in [Blandre 2016], the small difference of J_{sc} coming from the generation rate obtained from the radiative solver. The results obtained by SCAPS deviate slightly more from our results; however, we noticed some unphysical phenomena in SCAPS. We show in Figure 5.3b the spatial variation of the electron density under illumination and at zero voltage. While we expect n to be continuous in a homostructure, which is satisfied for both our solver and Blandre's solver, we noticed in SCAPS a discontinuity at the P-I interface. We suspect this may be the cause of the larger density found elsewhere in the cell, which leads to more frequent recombinations and therefore to a lower J_{sc}. Increasing the cell temperature to 200 K makes the discontinuity disappear, and the low temperature considered must therefore cause convergence issues in SCAPS.

5.2 Study of an optimised structure

Now that the drift-diffusion solver has been described and verified, we can move on to the study of TPX homostructures. In the present section, we will analyse in detail the performance of an optimised structure along with the charge transport in the two components, with the aim of highlighting the major differences with detailed-balance results. Most of the following results have been published in [Legendre & Chapuis 2022b]. Since the publication of this article, the expression used for the hole effective mass has been changed, as it was supposed to be equal to the heavy hole effective mass in [Legendre & Chapuis 2022b]. Quantitatively, this makes the hole effective mass change from 0.51 to 0.53 for GaAs at room temperature. One may therefore notice a small discrepancy between the published results and the data shown below, of the order of 10% for the maximum power output for instance. Apart from these small numerical differences, all the conclusions drawn in [Legendre & Chapuis 2022b] remain valid.

5.2.1 Description of the structure

As discussed in Chapter 3, a high quantum efficiency is required for TPX devices to reach significant power output. This quantity being directly related to the non-radiative recombination

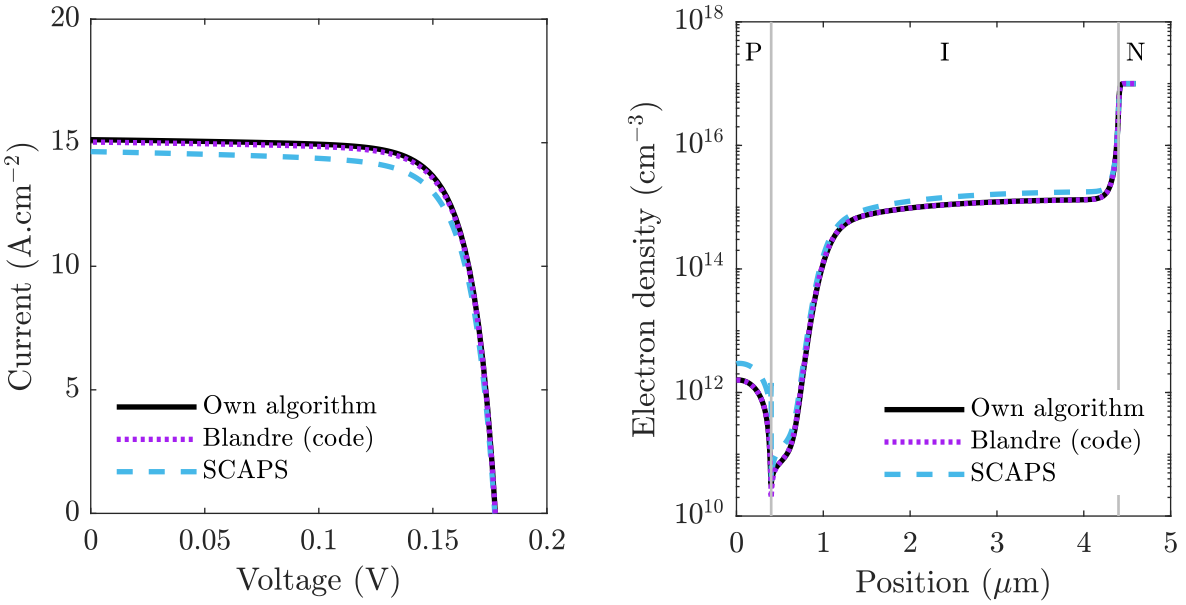

(a) I-V characteristic

(b) Electron density at zero voltage

Figure 5.3: Comparison of the results obtained by different 1D drift-diffusion solvers for the reference device shown in Figure 5.2.

rate, it will consequently be highly dependent on the structure. For example, the thickness of the two components should be precisely tuned to allow significant emission and absorption of photons while limiting non-radiative recombinations. In order to obtain a promising structure with high maximum power, the thickness and doping level of the different layers forming the components are computed using the MATLAB optimisation function *surrogateopt*. Perfect mirrors are placed at the back of the two components to prevent photon losses. To perform the optimisation, we assume that both the LED and the PV cell are PIN homojunctions with the P layer in front. The intermediate layer is assumed to be n-doped.

The optimisation is performed for a 10 nm gap distance, for a 600 K $Al_{0.121}Ga_{0.879}As$ LED and a 300 K GaAs PV cell, and for a surface recombination velocity S of 100 cm.s^{-1}. This last value is chosen arbitrarily, as it is not a material property but rather depends on the interface quality. It is however quite low in comparison to the values found in the literature: in the case of highly-doped layers, the surface recombination velocity at metallic contact is generally equal to hundreds or thousands of m.s^{-1} [Blandre *et al.* 2017], decreasing only for lower doping levels [Forcade *et al.* 2022] or in the case of partial surface covering by the metallic contacts [Saint-Cast *et al.* 2010]. The reason we have chosen such a low value is simply to limit the impact of surface recombinations on the performance: as we will see later (see Figure 5.21), large surface recombination velocities can significantly worsen the performance as they cause a reduction in quantum efficiency. This is due to the imperfect separation of charge carriers in homostructures, and is one of the main reasons why heterojunctions are often preferred. By using a low value of S, we therefore do not expect to catch the true performance of a TPX device made of homostructures, but rather to analyse the different physical phenomena related to charge transport in a relatively simple device, helping for the design and the physical understanding of heterostructures in Chapter 6.

The resulting device is given in Figure 5.4, and consists of a 200 nm LED and a 1 µm PV cell.

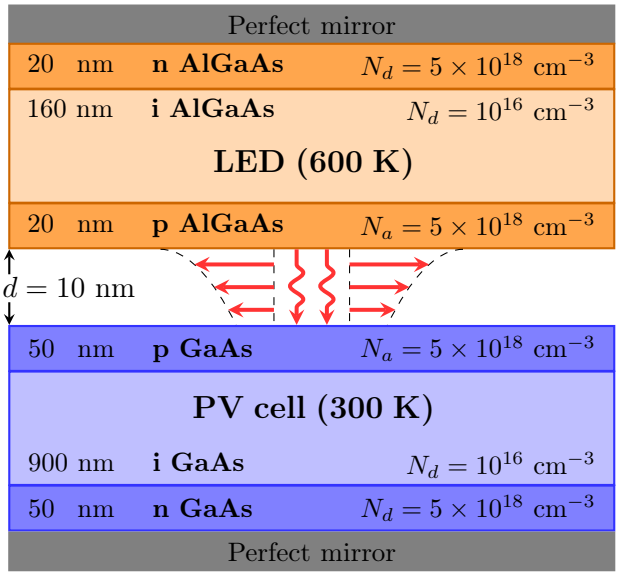

Figure 5.4: Schematic of the AlGaAs-GaAs homostructure under consideration, obtained from optimisation algorithms.

The highly-doped layers have a doping level of 5×10^{18} cm^{-3}; for intermediate layers, it is equal to 10^{16} cm^{-3}, but these layers can be considered intrinsic as lowering the doping does not impact noticeably the performance.

5.2.2 Radiative heat transfer

First, we study the local above-bandgap radiative heat transfer obtained in the LED and the PV cell. Three cases are considered: far-field thermal radiation, near-field thermal radiation and near-field electroluminescent radiation. The results can be found in Figure 5.5. Overall, the different spatial profiles show the same trends, the difference being mainly the amplitude. In all cases, q goes to zero at the back due to the presence of perfect mirrors. Far from them, q roughly varies exponentially, either increasing in the LED due to emission or decreasing in the PV cell due to absorption. The absence of a peak in heat flux density close to the front surface highlights the negligible contribution of surface modes to the heat transferred above the bandgap, in line with the results from Section 3.3.2. Reducing the gap distance to 10 nm allows to increase the local heat flux density by a factor 10 to 15 in most of the components, the factor being even larger close to the back surface. In comparison, the application of a 1 V bias on the LED further increases the flux by a factor 2.5×10^8, which corresponds to $\exp(eU_{\mathrm{LED}}/k_{\mathrm{B}}T_{\mathrm{LED}})$ as Boltzmann's approximation holds for such a voltage.

5.2.3 Maximum power and related efficiency

We start by investigating the electrical power production of the TPX device for a 10 nm gap distance, its P-VV characteristic being displayed in Figure 5.6. The resulting power production region (PPR) is within the one obtained for QE = 1 in Chapter 3, designated as the *ideal case* in the following. This could be expected, as electrical power can only be produced in the heat engine region of the equivalent Raveau diagram shown in Figure 3.4. The shape of the device PPR is however quite different from previous results, being divided into a "TPV-like" region and a "true TPX" region. This also appears clearly in the $P - V_{\mathrm{LED}}$ characteristic shown in Figure 5.7, with a large zone without power production between 0.05 and 0.4 V. At higher voltage, the

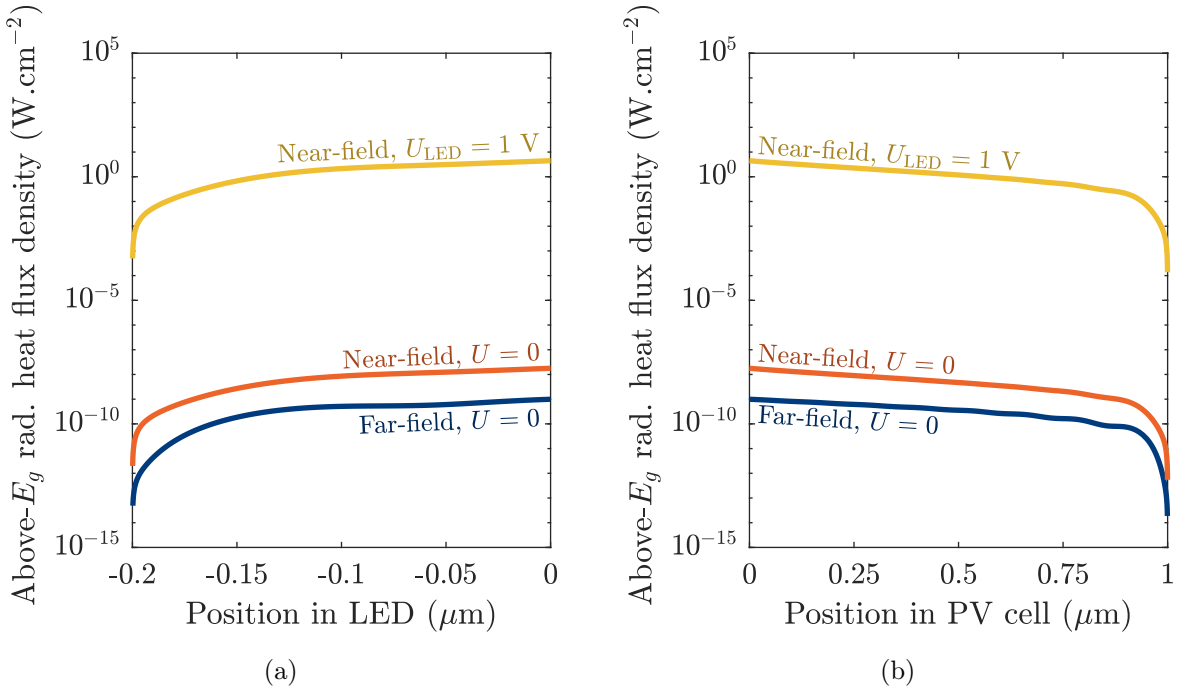

Figure 5.5: Local heat flux density (a) in the LED, (b) the PV cell obtained in the near field ($d = 10$ nm) or in the far field. In all cases, the PV cell voltage is zero.

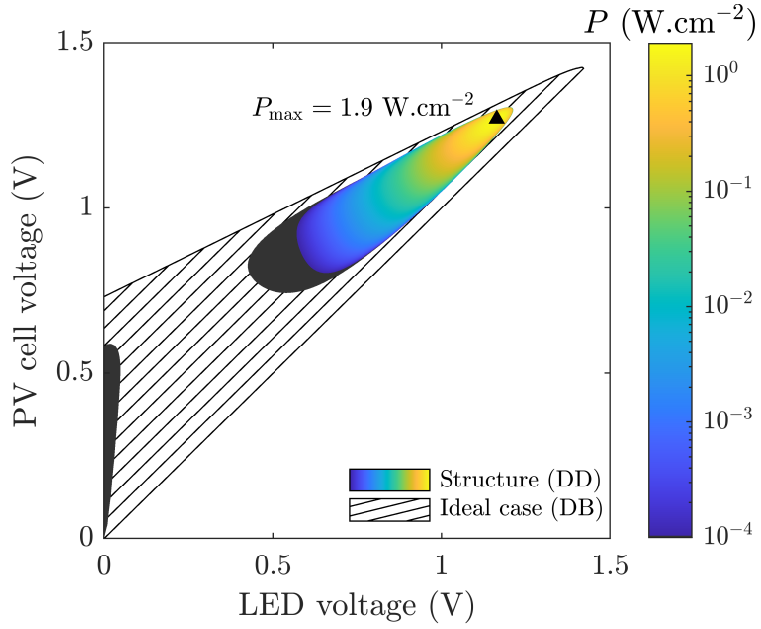

Figure 5.6: P-VV characteristic of the AlGaAs-GaAs homostructure.

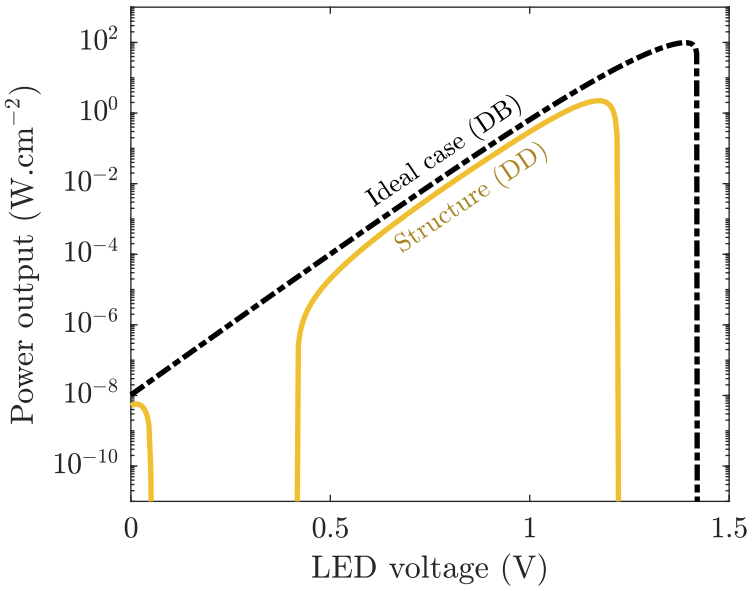

Figure 5.7: P-V_{LED} characteristic of the AlGaAs-GaAs homostructure.

characteristic is mostly similar to detailed-balance results. The maximum power output is equal to 1.9 W.cm^{-2} and is reached for $U_{LED} = 1.16$ V and $U_{PV} = 1.27$ V.

Along with its power output, the device efficiency should of course by studied; its η-VV characteristic is shown in Figure 5.8. As in the case of detailed-balance calculations, the highest efficiency at a given LED voltage is reached for large PV cell voltage, i.e. for voltages at which PV cell electroluminescence starts to have a significant impact on the radiative heat flux. The associated characteristic η-V_{LED} is depicted in Figure 5.9. It clearly highlights the loss of efficiency in comparison to the ideal case, which is mainly caused by non-radiative recombinations - although the use of thin-film components may also play a role in this drop. One can also notice the very tiny difference between maximum efficiency and efficiency at maximum power at a given LED voltage, being at most one percent point apart from each other. This makes the efficiency "ridge" visible in Figure 5.8 a pretty interesting region where both power and efficiency are maximised at a given LED voltage. Globally, the maximum efficiency is still obtained for zero LED voltage and is equal to 28%, reached for $U_{PV} = 0.47$ V. The efficiency at maximum power equals 12%, being thus five percent points lower than η_{MPP} obtained in the ideal case and with the far-field analytical expression derived in Chapter 2.

By changing the gap distance, we obtain the variation of power output displayed in Figure 5.10a. A large drop appears clearly around 78 nm, the maximum power output decreasing from 3×10^{-4} to 2×10^{-9} W.cm^{-2}. This sudden drop delimits two different regions of operation:

- below 78 nm, the above-bandgap heat flux at maximum power $q_{a,MPP}$ is highly electroluminescent, being order of magnitude larger than the thermal above-bandgap heat flux $q_{a,U=0}$, and the device therefore operates as a true TPX device;
- above 78 nm, $q_{a,MPP} \approx q_{a,U=0}$ as the LED is almost unbiased: the device operates in the TPV-like region, explaining why the power output is significantly lower.

For the device considered, near-field enhancements are therefore *mandatory* to reach TPX operation. This is a fundamental difference with TPV devices, in which power output always varies smoothly with the gap distance [Milovich *et al.* 2020, Forcade *et al.* 2022], or even with TPX

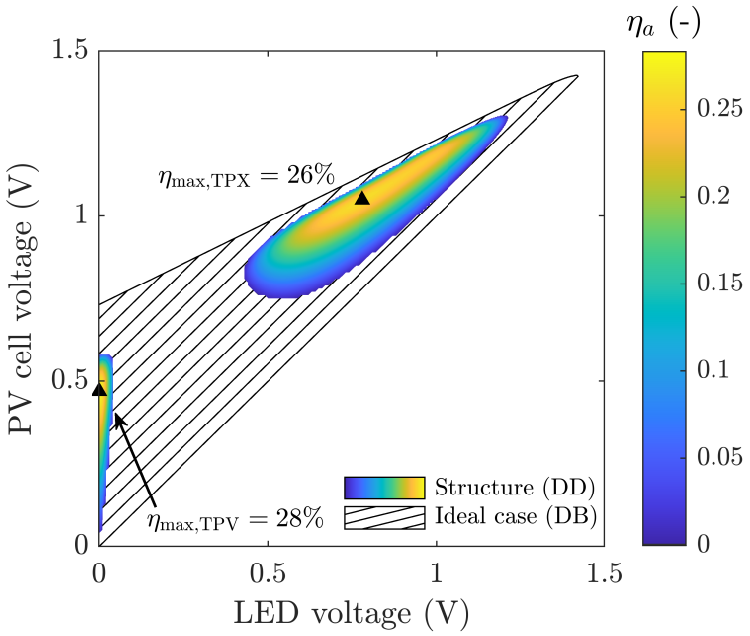

Figure 5.8: η-VV characteristic of the AlGaAs-GaAs homostructure.

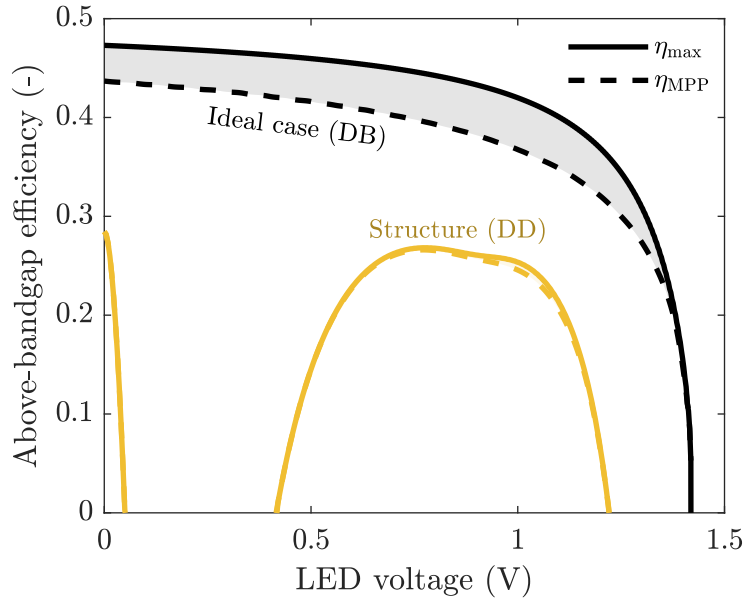

Figure 5.9: η-$\mathrm{V_{LED}}$ characteristic of the AlGaAs-GaAs homostructure.

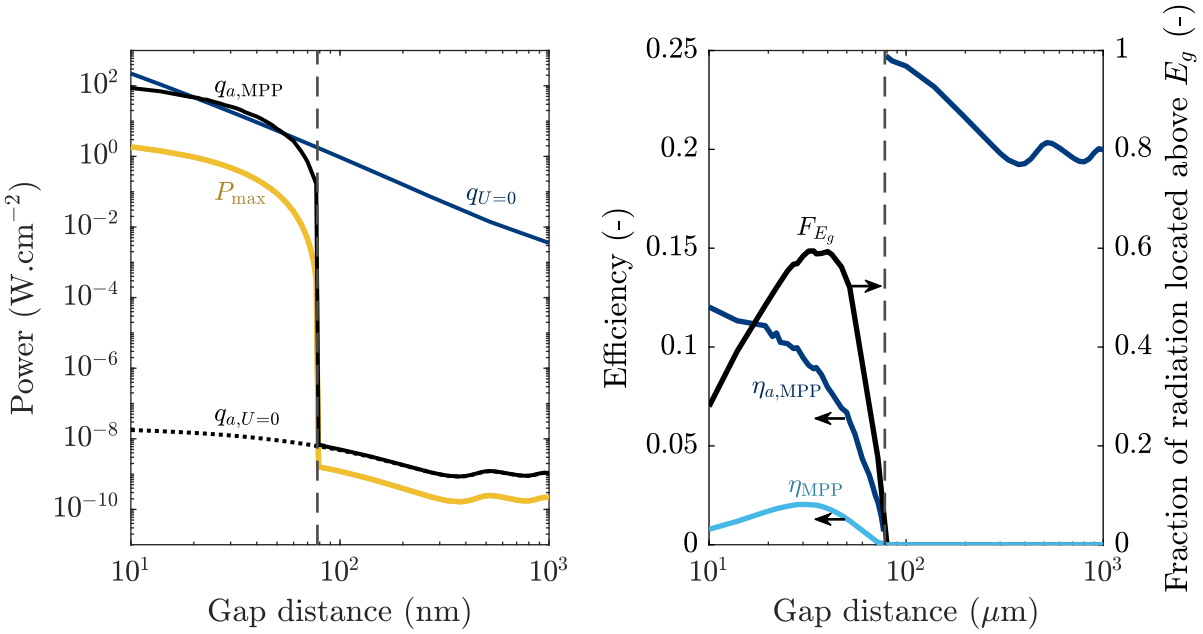

Figure 5.10: Impact of the gap distance on (a) the maximum power output and the transmitted radiative heat flux, (b) the efficiency of the AlGaAs-GaAs homostructure.

devices modelled with the detailed-balance approach of Chapter 3 (see Figure 3.9a). Understanding the cause of this drop along with the absence of power production in the low LED voltage range is a key element of this chapter, and will be explored in the following subsections.

We also show in Figure 5.10a the variation of total thermal radiative heat flux $q_{U=0}$ with gap distance. As discussed in Section 3.3.2, it is largely dominated by below-bandgap radiation and varies roughly as $1/d^2$ for low gap distances as surface modes prevail. One can notice that the above-bandgap electroluminescent heat flux becomes larger than $q_{U=0}$ for gap distances between 20 and 55 nm. This means that the fraction of radiation exchanged above the bandgap F_{E_g} must be relatively high in this distance range, and the total efficiency therefore be improved. To confirm this, the variation of efficiency with gap distance is provided in Figure 5.10b. The small oscillations which can be observed in the results are related to the large sensitivity of q with voltage: while variations of P are almost negligible close to MPP, q still depends exponentially on voltages and a small deviation from the MPP can lead to a noticeable change of q, hence of η. For gap distances lower than 78 nm, the above-bandgap efficiency at maximum power rises as d decreases - near-field effects therefore increase both power output and related efficiency when restricted to above-bandgap radiation. In the same time, F_{E_g} reaches, as expected, a maximum value of 0.59 for d between 30 and 40 nm. Consequently, the total efficiency at maximum power peaks at 0.02 for a gap distance $d = 30$ nm: if below-bandgap photons are not filtered, it may be more favourable to operate at such a gap distance than at 10 nm. If we now take a look at the gap distance range above 80 nm, the above-bandgap efficiency jumps from 7×10^{-3} to 0.25 at $d = 78$ nm, which is simply caused by the higher efficiencies reached in TPV-like operation. But simultaneously, F_{E_g} becomes very small and the total efficiency therefore remains close to 0, the bandgap of GaAs being way too large for the device to properly work as a TPV device.

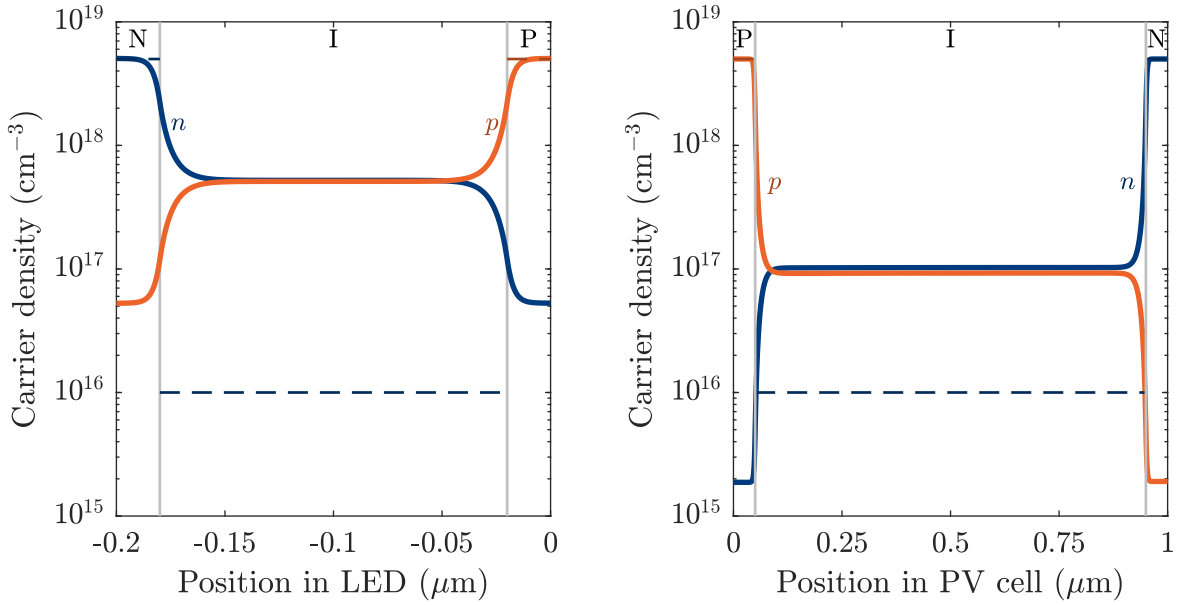

Figure 5.11: Charge carrier density at MPP (a) in the LED, (b) in the PV cell.

5.2.4 Local charge distribution at maximum power point

Thanks to the one-dimensional resolution of the drift-diffusion equations, we also have access to the spatial variation of the charge carrier densities inside both components; the data obtained at MPP can be found in Figure 5.11. The trends are mostly similar in the LED and the PV cell, with n and p being almost symmetric with respect to the centre of each component. Still, charge carrier concentrations are globally higher in the LED due to the quick increase of the intrinsic concentration n_i with temperature. In dashed line are represented the doping level in each layer. While the density of majority carriers in highly-doped layers approaches the doping level, this is untrue in the intermediate layer in which both carrier densities exceed the doping concentration. This layer is therefore subject to high-injection conditions, which justifies the complete resolution of the drift-diffusion equations over the use of the low-injection approximation (LIA) [Blandre *et al.* 2017]. With the LIA, majority carrier density would be wrongly assumed to always remain equal to the doping concentration. As mentioned in Chapter 4, the SRH recombination rate in an n-doped layer is for instance expressed as

$$R_{\mathrm{SRH}} = \frac{p - p_{\mathrm{eq}}}{\tau_{p,\mathrm{SRH}}}, \tag{5.12}$$

p_{eq} being the hole concentration at equilibrium. We show in Figure 5.12 how such an expression compares with the complete expression given in Chapter 4 under low voltage bias, where the difference is maximum. While the error is relatively small in highly-doped levels - especially in the PV cell - it becomes dramatic in I layers where the approximated expression can locally be off by a factor as large as 10^{17} in the PV cell. This makes the total SRH recombination rate obtained with the simplified expression larger than the correct rate by a factor 3×10^{10} in the PV cell and 5×10^{4} in the LED. At the MPP, the error is lower but still significant, this factor decreasing to 2 in both components.

The band diagrams can bring complementary information to the local carrier densities, and the

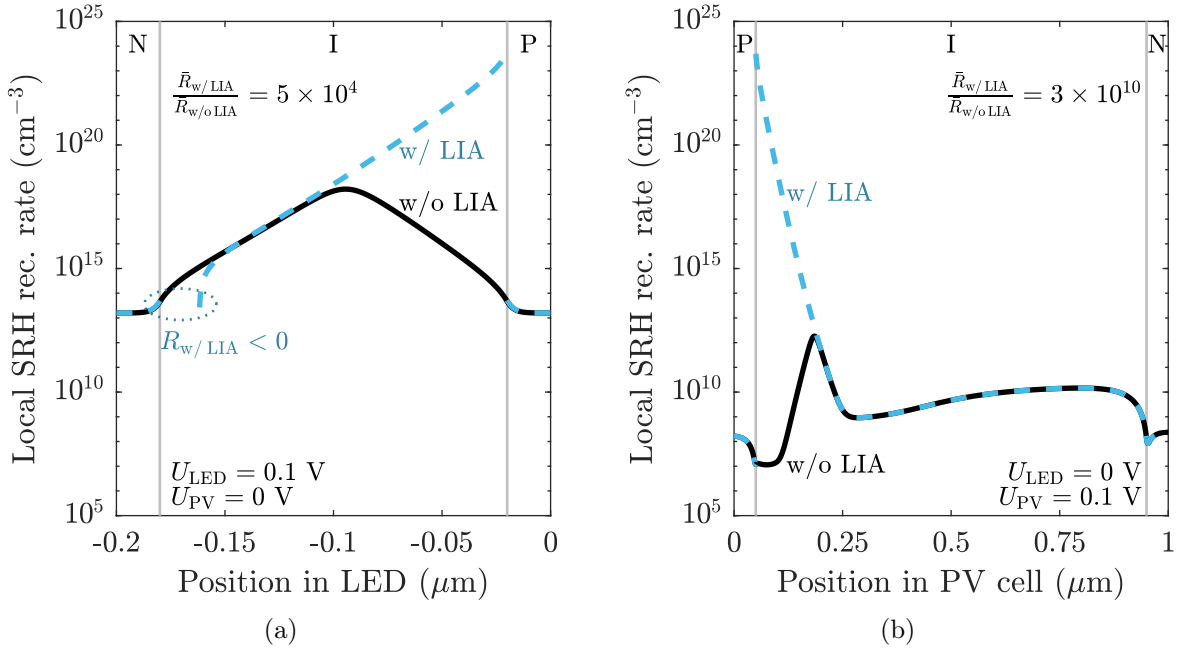

Figure 5.12: Effect of using the low-injection approximation to compute the local SRH recombination rate (a) in the LED, (b) in the PV cell at low voltage. The values of n and p used correspond to those obtained with the drift-diffusion solver, i.e. without the LIA.

diagrams obtained at MPP are therefore represented in Figure 5.13. Since the applied voltage is high in both components, the variation of electrostatic potential around junctions is relatively low and E_{C} and E_{V} show little variations in space. Quasi Fermi levels in the LED and the PV cell are almost flat, with variations of the order of the tenth of meV on the complete thickness. Thus, the approximation $\mu = eU$ holds well at MPP. However, $E_{\text{F}n}$ goes into the conduction band in the n-doped layers as the doping level is larger than N_{C}, the difference between $E_{\text{F}n}$ and E_{C} being for instance of the order of $3k_{\text{B}}T$ in the LED. In these layers, the semiconductor is therefore degenerate. This has several implications:

- several physical phenomena, which occurs in degenerate (or very highly doped) semiconductors, are neglected; we can for instance mention two competing effects:
  - the Moss-Burstein effect, which causes an increase in apparent bandgap as the energy levels in the bands which are closest to the band edges are completely filled [Grundmann 2016];
  - bandgap narrowing, which corresponds to a decrease of the apparent bandgap as the impurity density is so large that their energy levels form a band that extends the semiconductor band inside the bandgap [Sze 2006];
- the Boltzmann approximation used to simplify the Fermi-Dirac distribution is no longer correct in the case of degenerate semiconductors, which makes our model imprecise in such semiconductors.

The relaxation of Boltzmann's approximation is not straightforward in drift-diffusion models [Kantner 2020], especially since we work with the Slotboom variables, which naturally include the Boltzmann approximation. Therefore, we could not analyse the impact of this assumption, which might introduce non-negligible errors in the end results. This question shall be addressed

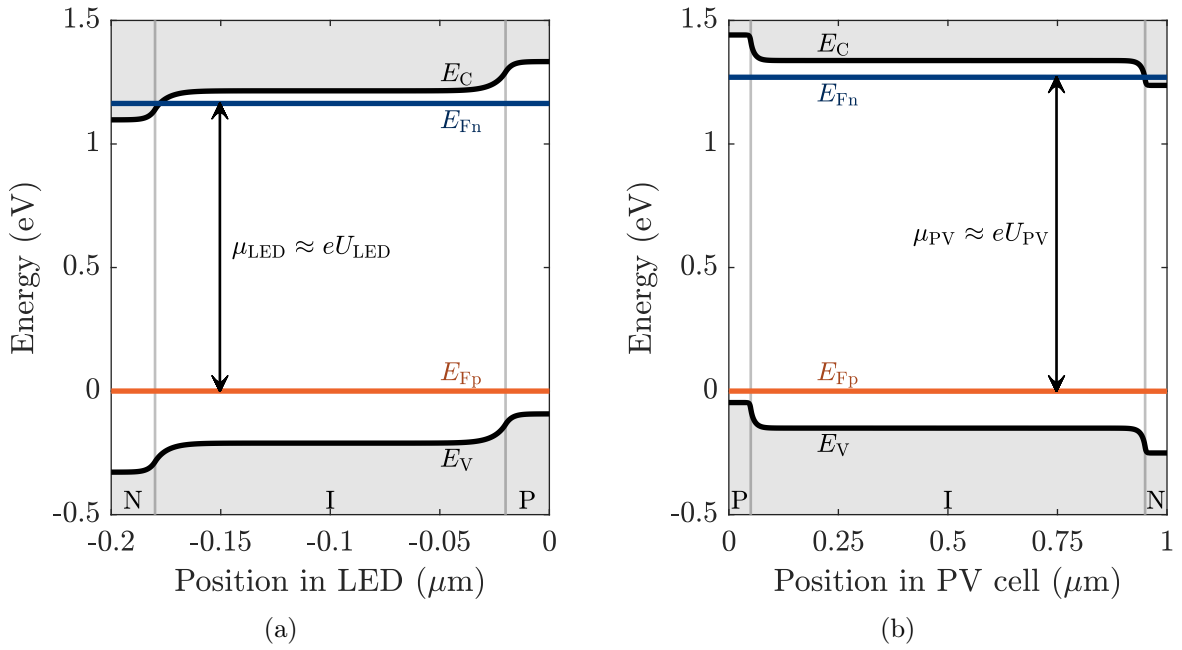

Figure 5.13: Band diagrams at MPP (a) in the LED, (b) in the PV cell.

in future work. Regarding the additional physical phenomena, we expect their impact to be limited as both effects compete with each other; also, the bandgap energy of GaAs being already quite large, the relative change in bandgap should remain limited. The impact should be even less important in Chapter 6, in which the highly-doped layers will have a higher bandgap and will not impact the above-bandgap radiative transfer (as they are transparent for photons with energy close to $E_{g,\mathrm{GaAs}}$).

5.2.5 Fundamental asymmetry between LED and PV operation

Several similarities were found between the LED and the PV cell at MPP, the band diagrams and the charge carrier concentrations being for instance mostly similar. This however hides a fundamental asymmetry in their behaviour at lower voltage. We show in Figure 5.14 the band diagrams obtained for the LED and the PV cell at low voltage. More precisely, a voltage of 0.1 V is applied to the component under consideration, while the other component remains unbiased. The resulting band diagram obtained for the LED is mostly similar to the one obtained at MPP. However, this is not the case for the PV cell as the quasi-Fermi levels vary significantly in space. The approximation $\mu = eU$ is thus incorrect in this case, since $\mu > eU$ instead. Still, this is not too much of an issue as we are mainly interested in the MPP. Furthermore, we do not expect this larger chemical potential to significantly change the PV cell current or the net radiative heat flux, and the resulting performance should thus remain mostly similar.

What happens in the PV cell is that the separation of quasi Fermi levels is caused by the LED illumination rather than the application of a voltage bias. Thus, the PV cell operation is strongly related to the LED voltage. This may be easily understood by looking at the I-V characteristics displayed in Figure 5.15, which are obtained by varying one voltage while keeping the other one at zero. If the LED voltage is varied (Figure 5.15a), both currents vary roughly as $\exp(eU_{\mathrm{LED}}/k_{\mathrm{B}}T_{\mathrm{LED}})$, since radiative recombinations - and thus the related LED emission - vary as such with the approximation $\mu = eU$. Non-radiative recombinations cause the small deviation from the exponential rate in the LED, but happen too sparsely in the PV cell to change

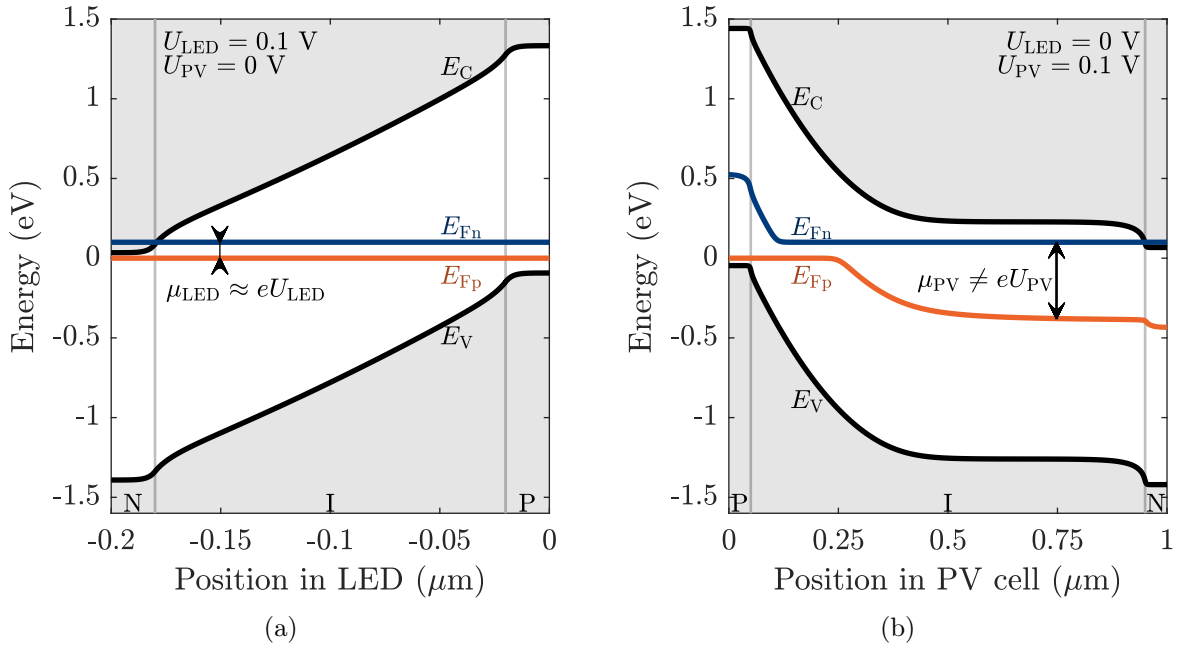

Figure 5.14: Band diagrams obtained (a) in the LED, (b) in the PV cell, with a voltage applied to the component under consideration equal to 0.1 V while the opposite component remains unbiased.

significantly its short-circuit current. In comparison, if we change the PV cell voltage instead (Figure 5.15b), both currents remain constant at first as the increase of the recombination rate in the PV cell is not sufficient to noticeably change the PV cell current or the radiative heat flux exchanged between the component - and thus the LED current. Of course, if the PV voltage becomes large enough, it will in fact operate as the LED, and then currents then increase as $\exp(eU_{PV}/k_B T_{PV})$ - but this happens outside the TPX heat engine operation region. In this region, most of the important quantities are therefore driven by the LED voltage rather than the PV cell voltage.

From what we have written above, we can also notice the difference of impact of recombinations on the two components. In the LED, they drive the current for any voltage. In contrast, they become significant in the PV cell only close to the open-circuit voltage. This means both components are very differently impacted by the rate of non-radiative recombinations, hence by their QE, as discussed in [Würfel & Würfel 2016]. To illustrate this, we use again the detailed-balance model of Chapter 3, but this time with different QEs for the LED and the PV cell - which are supposed to be semi-infinite for this calculation. The result obtained is depicted in Figure 5.16. If decreasing the QE_{PV} while keeping QE_{LED} equal to one deteriorate the power output, it is much worse if QE_{LED} is decreased instead: in comparison to the radiative limit QE = 1, power output is reduced by a factor 40 if $QE_{PV} = 0.5$, against 6×10^7 if $QE_{LED} = 0.5$ (keeping the other QE equal to unity). The results obtained with symmetric QE are in fact close to those obtained with $QE_{PV} = 1$: the impact of QE_{PV} is therefore moderate, and the power output is mainly limited by QE_{LED}. We shall thus investigate the variation of QE_{LED} with voltage in the studied homostructure.

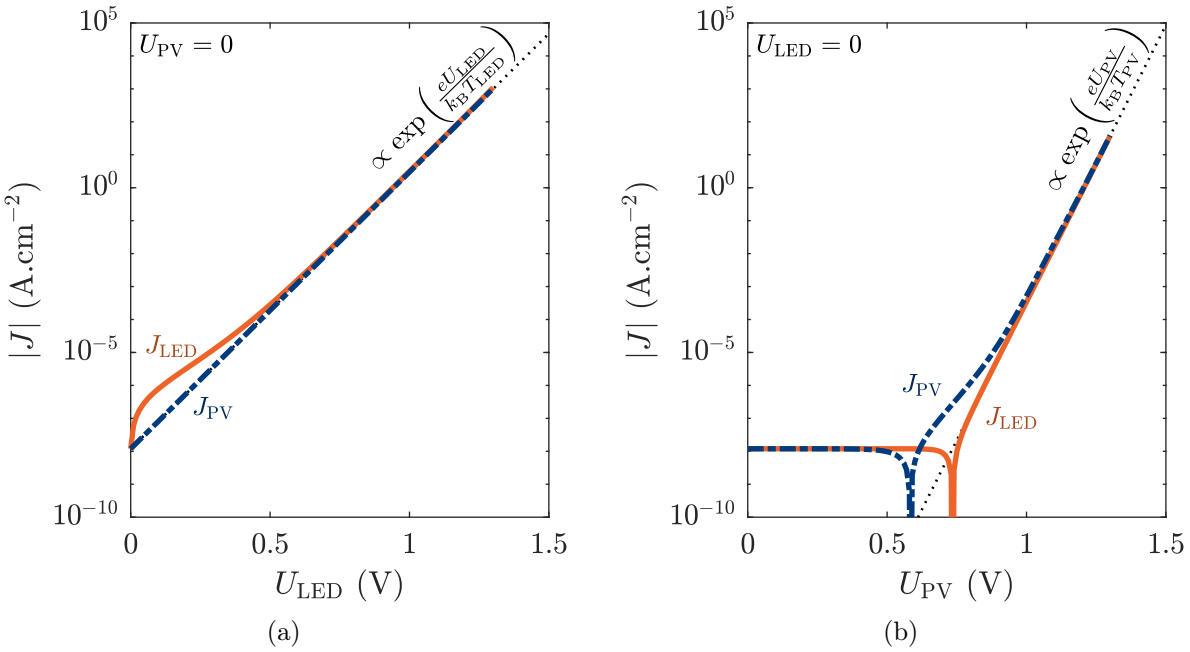

Figure 5.15: I-V characteristics of the LED and the PV cell, obtained by varying (a) U_{LED}, (b) U_{PV}.

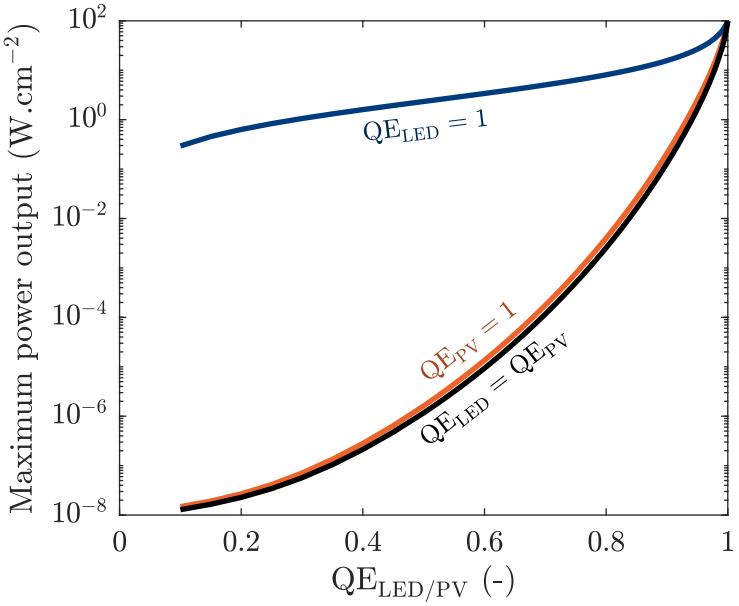

Figure 5.16: Variation of power output with quantum efficiency obtained with the detailed-balance model.

5.2.6 Impact of non-radiative recombinations

We start by looking at the local radiative and non-radiative generation-recombination rates in the LED and in the PV cell, which are represented in Figure 5.17. In any of the cases considered, SRH events mostly occur in the intrinsic region while Auger recombination rate is maximised in highly-doped layers. This is a standard result which comes from the difference of physics between the two phenomena. Traps capture carriers more efficiently if both kinds of carriers are equally available, while Auger recombination being a three-carrier phenomenon, it occurs more often in regions where many carriers are available. This can easily be obtained from the governing equations shown in Section 4.1.3 by using some simplifying approximations. Let us suppose that $\tau_{n,\mathrm{SRH}} = \tau_{p,\mathrm{SRH}}$ and $C_n = C_p$. If we assume that n_i is small enough in comparison to $n + p$ and that np is spatially constant and equal to $n_\mathrm{i}^2 e^{eU/k_\mathrm{B}T}$, we can easily obtain that R_Auger and R_SRH are respectively proportional and inversely proportional to $n + p$:

$$R_\mathrm{SRH} \approx \frac{1}{n+p} \frac{n_\mathrm{i}^2 \left(e^{\frac{eU}{k_\mathrm{B}T}} - 1 \right)}{\tau_\mathrm{SRH}}, \tag{5.13a}$$

$$R_\mathrm{Auger} \approx (n+p) \cdot C n_\mathrm{i}^2 \left(e^{\frac{eU}{k_\mathrm{B}T}} - 1 \right). \tag{5.13b}$$

Since we assume that np is a constant, this leads to $n+p$ being minimum for $n = p$ and increasing as the difference of carrier densities increases.

We can also notice the recombination rate of these two non-radiative phenomena vary differently with voltage. SRH recombinations are the most common at low voltages (panels (a,b)), while under large bias, Auger recombination rate becomes similar to (panel (d)) or greater than R_SRH (panel (c)). Using once more the above-mentioned approximations, we can in fact show that

$$R_\mathrm{SRH} \propto e^{\frac{eU}{2k_\mathrm{B}T}} - 1, \tag{5.14a}$$

$$R_\mathrm{Auger} \propto e^{\frac{eU}{k_\mathrm{B}T}} - 1, \tag{5.14b}$$

since in highly-doped layers $n+p$ equals approximatively the doping concentration. This captures the lower increase rate of R_SRH, and is actually the basis for the two-diode model in which the I-V characteristic is simply fitted using the expression $J = J_\mathrm{sc} + J_{01}(e^{eU/k_\mathrm{B}T} - 1) + J_{02}(e^{eU/2k_\mathrm{B}T} - 1)$ [Würfel & Würfel 2016]. In comparison to radiative events, the rate of non-radiative recombinations is quite low in most cases, except in the LED at low voltage (panel (a)) in which the SRH recombination rate far exceeds the radiative recombination rate. The LED quantum efficiency must therefore be significantly lower than one in this case.

To better quantify the QE, the generation-recombination rate is integrated over the whole thickness. The resulting total rate is given in Figure 5.18, along with the resulting QE. Globally, the dependency of non-radiative recombination rates with voltage found in Eq. (5.14) fits well those obtained numerically. The main exception comes probably from the constancy of Auger recombination rate at low voltage in the PV cell: this is due to the separation of the quasi-Fermi levels being much larger than eU in highly-doped layers, because of the LED illumination. Surface recombinations can also be displayed in such a figure, and show similar rates to Auger recombinations. Therefore, they have a significant impact even for the low surface recombination velocity considered. In the PV cell, the net radiative generation-recombination rate goes to 0 for a voltage of 0.73 V as the PV cell emission perfectly counterbalances the LED illumination there; radiative events are therefore dominated by generation for lower voltages, and by recombination

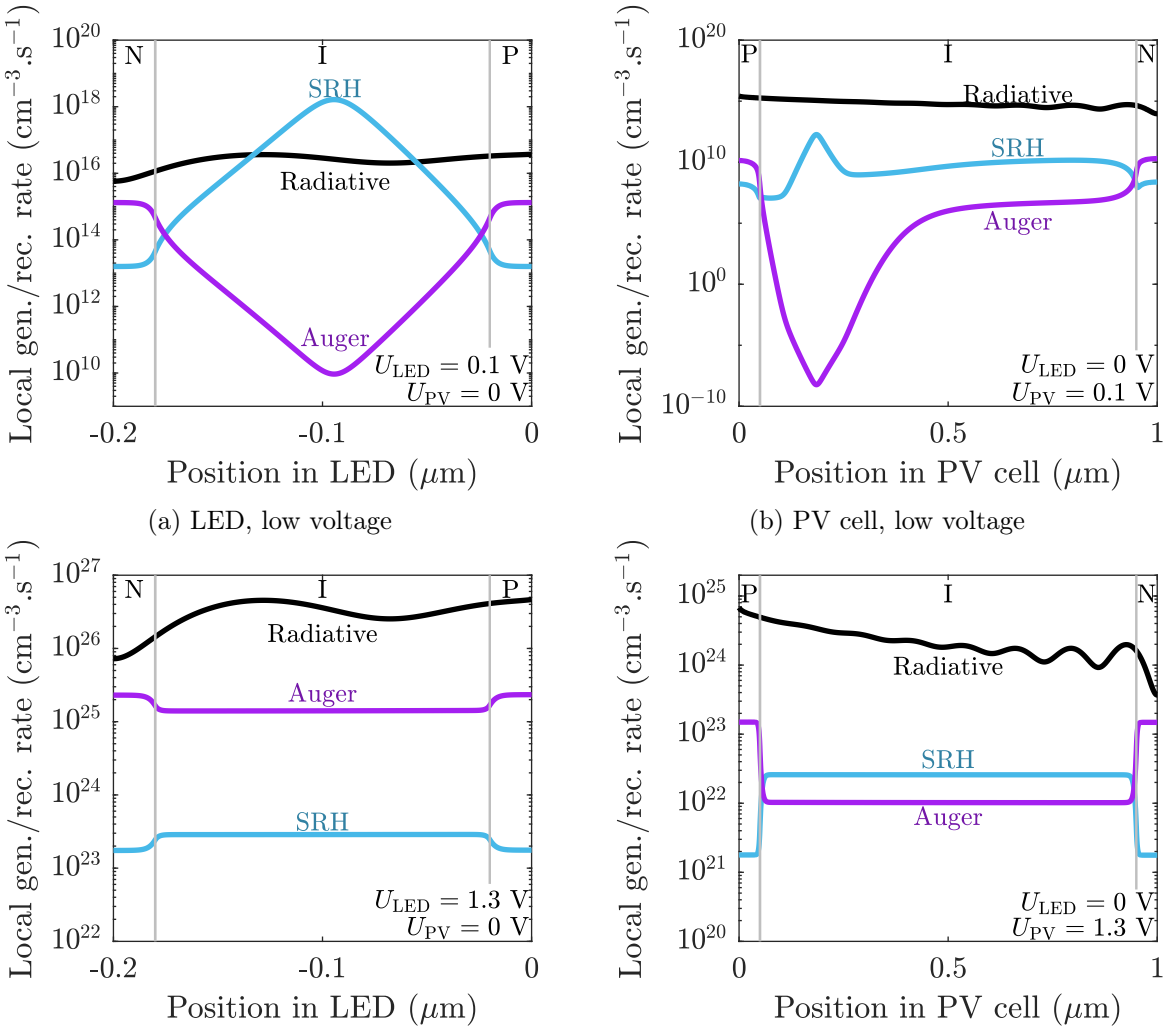

(a) LED, low voltage

(b) PV cell, low voltage

(c) LED, high voltage

(d) PV cell, high voltage

Figure 5.17: Local generation-recombination rates obtained at different voltages (a) in the LED, (b) in the PV cell. In all four panels, the rates are given in absolute value. Only for radiative events in the weakly biased PV cell is the generation rate greater than the recombination rate.

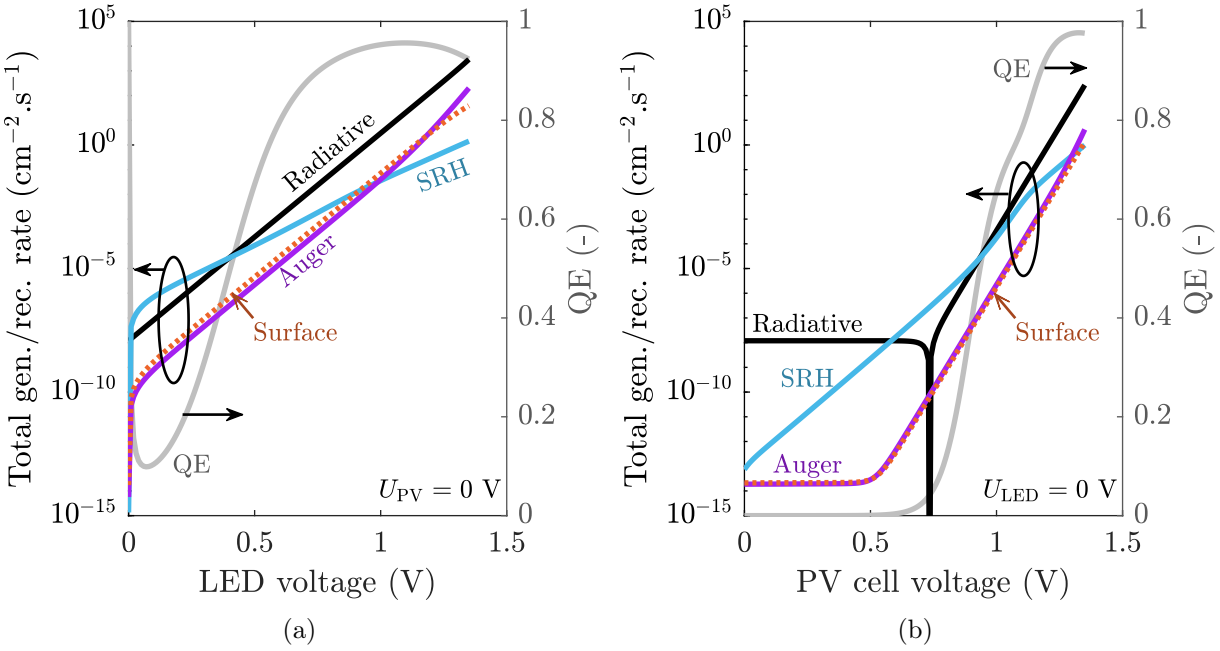

Figure 5.18: Total generation-recombination rate (a) in the LED, (b) in the PV cell, given as a function of the component voltage. The rates are given in absolute value.

for larger ones. This voltage corresponds to the maximum open-circuit voltage U_{oc} possible for the PV cell. Since the SRH recombination rate equals the radiative generation rate for $U_{PV} = 0.58$ V, the PV cell U_{oc} is consequently close to 0.58 V and non-radiative recombinations cause a decrease of U_{oc} of 0.15 V. This also implies that close to U_{oc}, QE_{PV} is quite low - at least at $U_{LED} = 0$ V. In fact, the QE of the PV cell only starts to increase around 0.75 V.

In the LED, the QE is non-monotonic:

1. for a zero voltage, it is equal to unity, as the LED thermally radiates towards the PV cell due to the temperature difference, the net non-radiative generation-recombination rate being almost zero;

2. it reaches quickly its minimum for a voltage close to 0.07 V due to SRH recombinations;

3. then, it goes up to 0.957 for $U_{LED} = 1.09$ V, at which all non-radiative recombinations occur approximately at the same rate;

4. for very large voltage, the QE drops again, this time due to Auger and surface recombinations.

These two QE profiles were obtained with one voltage equal to zero; to extract more information from the QE, the influence of both voltages should be investigated. We therefore show in Figure 5.19 how the QE profile of both LED and PV cell changes with the opposite component voltage bias, the pale area corresponding to the superimposition of all the obtained QE profiles. These profiles are only given in the range of voltage in which the component operates as expected: the PV cell QE is only given up to U_{oc}, while for large PV cell voltages the LED QE is only given above a certain voltage - the LED working as a PV cell at low bias. The results presented in Figure 5.19 pinpoints that as long as the LED operates as expected, its QE shows no dependency to the PV cell voltage. In comparison, QE_{PV} decreases with U_{LED}; however, U_{oc} increases with U_{LED}, and QE_{PV} at U_{oc} comes thus closer to unity as U_{LED} increases (black line in Figure 5.19).

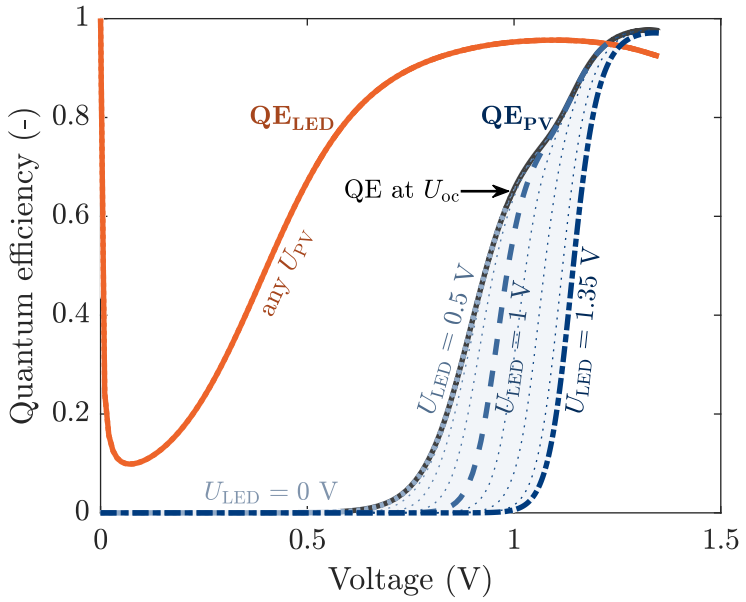

Figure 5.19: Variation of a component quantum efficiency as a function of its applied voltage, given in the voltage range in which the component behaves as expected (i.e. below U_{oc} for the PV cell and above U_{oc} for the LED). In the case of the PV cell, the QE profile varies with LED voltage and is therefore plotted every 0.1 V of U_{LED}. The value of the PV cell QE at U_{oc} is also represented in dark grey.

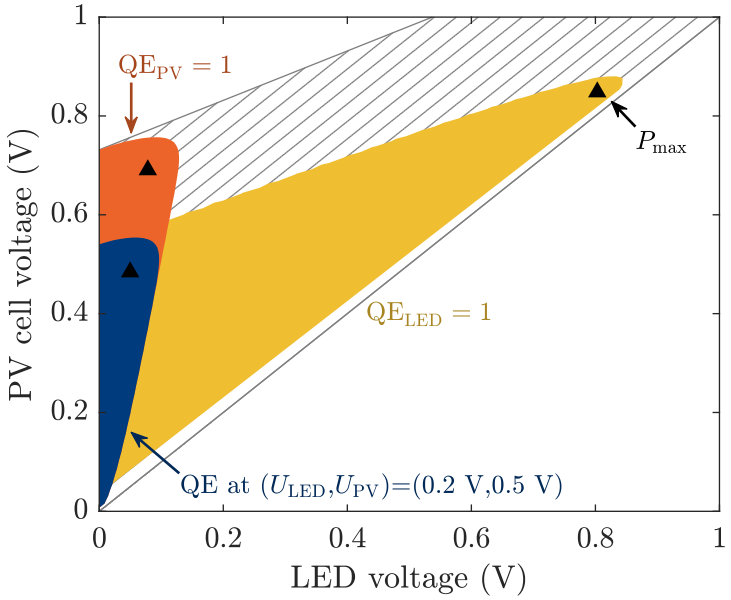

Figure 5.20: Power production region obtained with the detailed-balance model, for different QEs. The hatched region corresponds to the heat engine operating region obtained at the radiative limit in 3.3.1.1.

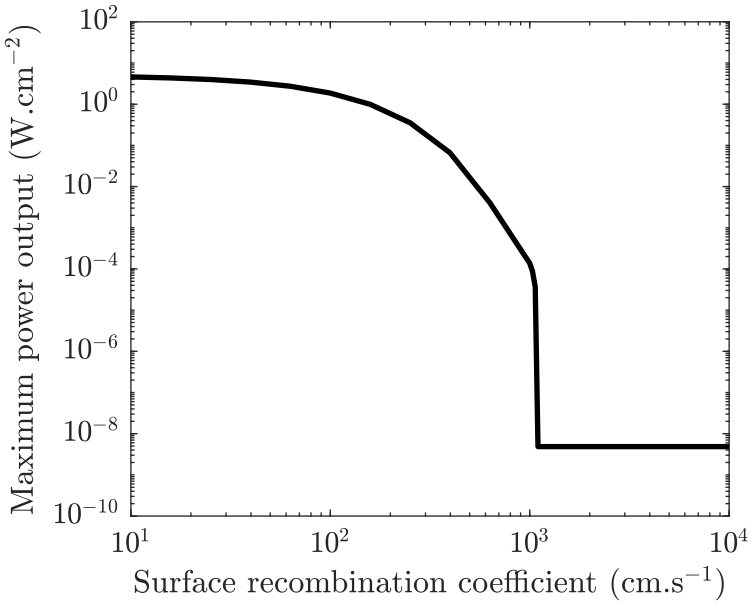

Figure 5.21: Impact of the surface recombination velocity on the maximum power output of the AlGaAs-GaAs homostructure.

At the MPP, LED and PV QEs equal 0.955 and 0.97 respectively, and QE_{LED} is therefore close to its maximum. In comparison, for $U_{LED} = 0.2$ V and $U_{PV} = 0.5$ V - which lies inside the power gap - they are only equal to 0.174 and 6.1×10^{-4}. In Section 5.2.5, we showed that QE_{LED} leads the variation of P. But as QE_{PV} is much smaller than QE_{LED}, one may think that QE_{PV} could play a significant role. In order to discard this hypothesis, we display in Figure 5.20 the PPR given by the detailed-balance model with the aforementioned QEs or with one of them equal to 1. Increasing QE_{PV} mainly allows to enhance the PV cell U_{oc} but does not increase significantly the available LED voltage range, in contrast to the $QE_{LED} = 1$ case. Therefore, even if QE_{PV} is the lowest of the two QEs, QE_{LED} is the sole cause of the power drop in the low-voltage range. Physically, it means that SRH recombinations are too frequent in the LED to allow the TPX device to produce power at low voltage. Similarly, as QE_{LED} decreases in the high-voltage range, we may expect a larger maximum power output if Auger recombination rate was reduced. As shown in Figure 5.21, increasing the surface recombination velocity - which lowers the LED QE - has a dramatic effect on the maximum power output. A power drop similar to the one obtained by varying the gap distance (see Figure 5.10) can be observed for $S_{n/p} \approx 10^3$ cm.s^{-1}.

5.2.7 Quantum efficiency in the near field

We shall now investigate the cause of this power drop. This will be done with respect to the gap distance, but the reasoning is similar if surface recombination velocity is considered instead. Since we have highlighted how the LED quantum efficiency is a critical parameter for the TPX power generation, we display in Figure 5.22a the profiles obtained at different gap distances. For any voltage, decreasing the gap distance allows enhancing QE_{LED}. This effect was already pinpointed for TPV cells, as it was shown that the radiative recombination rate increases more quickly as d decreases than the non-radiative recombination rate [DeSutter *et al.* 2017, Papadakis *et al.* 2021]. But in the case of the LED, lowering d has an even more important effect as the rate of non-radiative recombinations varies negligibly with d [Chen *et al.* 2015]: by decreasing d from 100 to 10 nm, QE_{LED} roughly increases by 0.3 at 0.5 V and by 0.1 at 1 V.

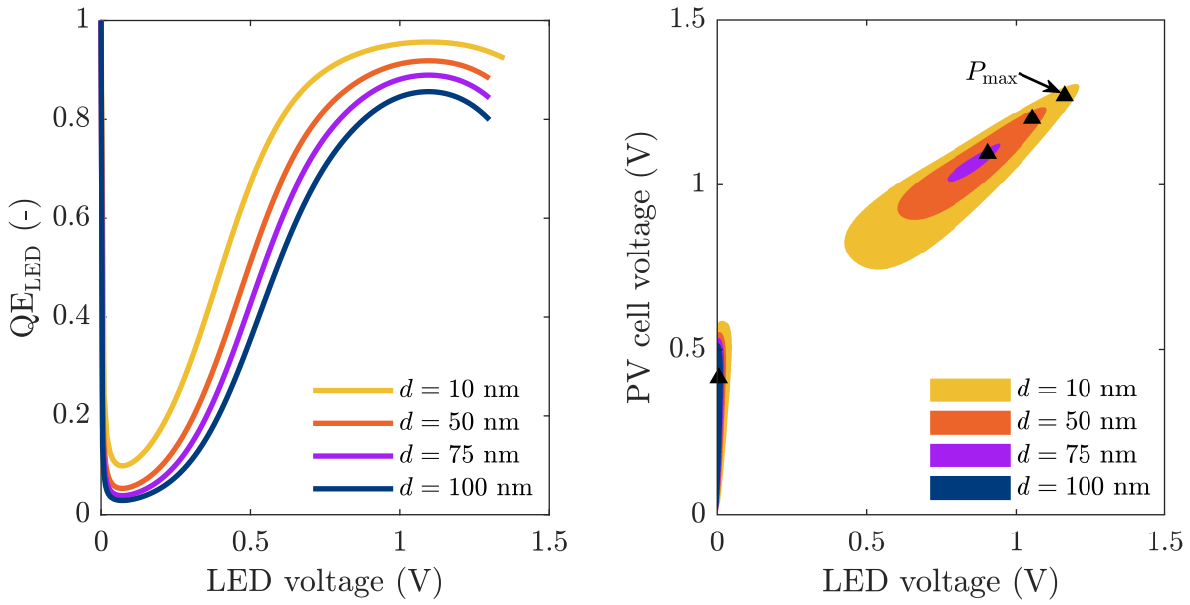

(a) (b)

Figure 5.22: Impact of the gap distance (a) on the LED quantum efficiency, (b) on the TPX device power production region.

As discussed previously, the LED quantum efficiency profile determines the size of the PPR. Since QE$_{\mathrm{LED}}$ diminishes as d increases, the PPR must shrink simultaneously: this is shown in Figure 5.22b. The effect is particularly significant in the true-TPX region: while at $d = 10$ nm this region is still quite large, it becomes very narrow for $d = 75$ nm. As the gap distance further increases, the true-TPX region continues to shrink up to the point where it completely disappears, which happens around $d = 78$ nm. The MPP, initially in the true-TPX region, moves then abruptly towards the TPV-like region as it is the only region where power can be generated - causing the drop of power output as well as the increase in above-bandgap efficiency mentioned in Section 5.2.3. Note that this drop, and especially its amplitude, is also related to the large SRH recombination rate at low voltage: this is because the low-voltage quantum efficiency is so small that the PPR is divided in two, causing ultimately the power drop as d is decreased.

5.3 Impact of bandgap misalignment in the case of non-abrupt bandgaps

5.3.1 Urbach tails: definition and implementation

In the results provided above, the bandgaps of the LED and the PV cell were matched. Indeed, we have shown in Section 3.2.2 that it allows to maximise the power output when considering an abrupt bandgap, i.e. that the densities of states equal zero inside the bandgap. However, this hypothesis of abrupt bandgap is strictly correct only for a perfect (i.e. without impurities) and infinite lattice. In reality, densities of states are found to decay exponentially as energy moves away from E_{C} or E_{V} due to tail states, as depicted in Figure 5.23. Consequently, interband transitions can occur with photons with energy close to but lower than E_g, changing the electroluminescent spectrum and possibly modifying the impact of bandgap misalignment on the power output of the device; in this section, we aim at analysing this impact.

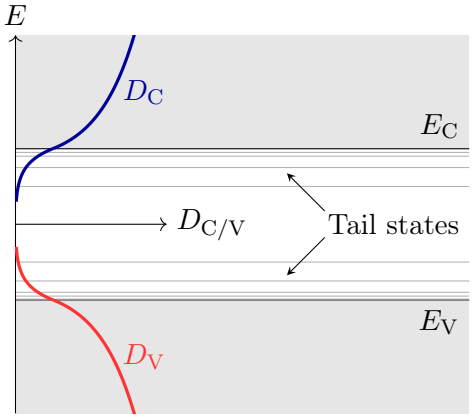

Figure 5.23: Schematic of the tail states inside the bandgap and the subsequent densities of states.

To account for these below-bandgap transitions, we should modify the interband contribution to the dielectric function. As of now, the emission and absorption of photons below E_g are neglected, i.e. the absorption coefficient is supposed to be zero for $E < E_g$[1]. This corresponds to the most common approach (see e.g. [Adachi 1988]). But if the tail states are considered, the absorption coefficient below the bandgap is most commonly expressed as

$$\alpha(E) \propto \left(-\frac{E - E_g}{E_U}\right), \tag{5.15}$$

where E_U is the Urbach energy, which does not have a particular physical meaning but is rather chosen to fit experimental data - the increase of E_U broadening the absorption tail. This tail is associated with above-bandgap data through convolution [Katahara & Hillhouse 2014]:

$$\alpha(E) = \frac{1}{2E_U}\int_{-\infty}^{+\infty} \exp\left(-\left|\frac{E - E'}{E_U}\right|\right)\alpha_{abrupt}(E')dE'. \tag{5.16}$$

Note that this expression does not perfectly correspond to the data from [Katahara & Hillhouse 2014], in which an additional E_g term is present in the exponential. This is because they define $\alpha_{abrupt}(E)$ as the absorption coefficient at $E - E_g$, while we consider it directly to be the absorption coefficient at E. Anyway, we can easily verify that our expression works in the limit of infinitely low Urbach energy: associated to the prefactor, the exponential term becomes then a Dirac delta function $\delta_E(E')$, and we therefore find back $\alpha(E) = \alpha_{abrupt}(E)$.

The question is then to understand how the Urbach tail changes the emission spectrum of an LED. Since far-field spectroscopy measurements of the emission spectrum of an InGaP/GaAs heterostructure were performed by Wissal Sghaier at room temperature at our lab, we can in fact compare the measurements with numerical results obtained with or without an Urbach tail.

[1] In fact, the absorption coefficient obtained from [Gonzalez-Cuevas *et al.* 2007] is non-zero below the bandgap. However, it decreases very slowly as E decreases, and would result in a significant change of near-field radiative heat flux transferred from the LED to the PV cell. Since there is no mention of tail states, this slow decrease could very well come from the numerical error related to data fitting, and we therefore preferred to cut interband transitions at E_g.

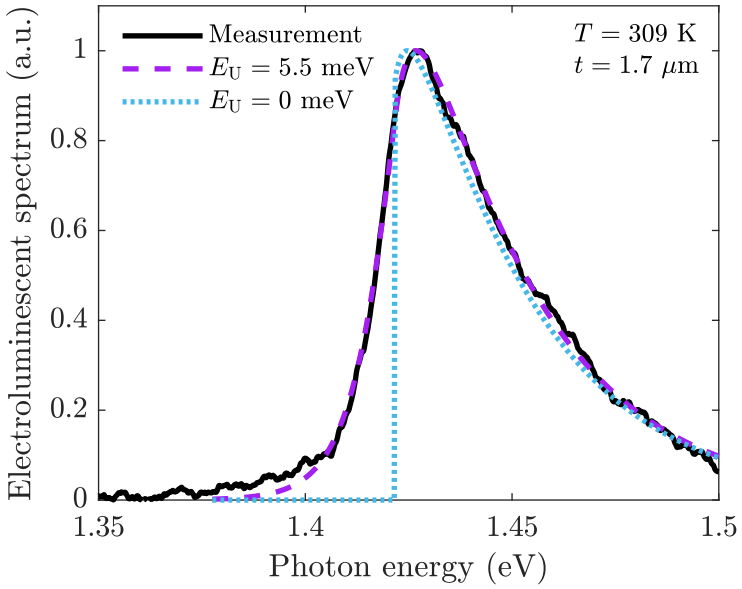

Figure 5.24: Comparison of the electroluminescent emission spectrum of an LED obtained from measurements and from Eq. (5.17).

Following the developments from [Katahara & Hillhouse 2014], we assume that

$$\dot{N}(E) \propto (1 - \exp(-\alpha t)) \frac{E^2}{\exp\left(\frac{E-\mu}{k_B T}\right)}, \tag{5.17}$$

t corresponding to an effective thickness. Note that this expression of $\dot{N}$ is much too simple in regard to the complex heterostructure considered in the measurements - its only aim is to allow a quick comparison with experiment. It is fitted with experimental data using E_U, t and T as degrees of freedom. We focus only on the variations of the spectrum, i.e. not to its amplitude; under the Boltzmann approximation, the applied voltage therefore plays no role. The result is given in Figure 5.24; clearly, an abrupt absorption coefficient cannot properly represent the entirety of the LED spectrum, the measured photon flux density smoothly decreasing to zero towards low photon energies. In contrary, the simple model described above captures quite well the spectrum global variations, the values obtained for the different degrees of freedom being plausible - although limited attention should be given to them as the model is once again very simple. We can also notice that a significant fraction of electroluminescent radiation is in fact exchanged in the below-bandgap energy range, being as large as 25% considering the numerical results. We can therefore expect the TPX power output to potentially rise when considering Urbach tails, but the efficiency to decrease as the bandwidth gets larger (see Section 2.2).

If Eq. (5.16) allows to include an absorption tail in the absorption coefficient, we still need to modify the dielectric function accordingly to implement the tail in the near-field radiation solver. These quantities are related through the following relations:

$$\alpha = 2\frac{\omega}{c}\sqrt{\frac{|\varepsilon| - \varepsilon'}{2}}. \tag{5.18}$$

This sole equation does not allow to obtain both the real and imaginary part of ε from α, and should be coupled with Kramers-Kronig relation to obtain them precisely. To avoid iterating

between these two, we will rather assume that ε' remains unchanged by the convolution, since α depends mostly on ε'' in the frequency range considered[2], and Eq. (5.18) can then give ε'' from ε' and α.

The addition of interband transitions with photons with energy lower than E_g can however give rise to divergence in the modified Bose-Einstein distribution. As shown previously (see Eq. (1.7)), it depends directly on $\hbar\omega - \mu$ and goes to infinity as μ approaches $\hbar\omega$. Without an absorption tail, $\mu < E_g \leq \hbar\omega$ and f_{BE} is always finite, but this is no longer true as interband transitions can occur at $\hbar\omega < E_g$. Some corrections are proposed in [Katahara & Hillhouse 2014] to prevent this unphysical divergence to occur; however, they cannot be straightforwardly applied to thin-films and to near-field radiation, and require further information about the occupation of the bands. Instead, we simply limit the range of admissible Urbach energy so that the lowest photon energy able to promote electrons to the conduction band $\hbar\omega_{\mathrm{min}}$ satisfies $\mu_{\mathrm{max}} \approx eU_{\mathrm{max}} < \hbar\omega_{\mathrm{min}}$ - this lowest photon energy corresponding to the energy at which ε'' gets below an arbitrarily chosen threshold. Considering a threshold of 10^{-3}, the Urbach energy should for instance be lower than 13 meV in the PV cell to keep $\hbar\omega_{\mathrm{min}}$ above 1.35 eV.

5.3.2 Influence of Urbach tails on TPX performance

Now that the whole framework has been introduced, we can come back to the effect of LED and PV cell bandgap misalignment in the case of a non-abrupt bandgap. In fact, this question has already been partially addressed in [Oehler 2022], in which the impact of the LED Urbach energy on the PV cell efficiency was investigated, the LED being heated at 350 K. Using a detailed-balance approach, they found out that the PV cell bandgap should in fact be around 0.1 eV lower than that of the LED to maximise the PV cell efficiency. Although the variations of efficiency of the cell have been studied in depth and compared to in-house experiments, this study lacks a global analysis of the variation of the TPX power output with Urbach energy.

The analysis is performed based on the optimised geometry presented in Figure 5.4, using the 1D drift-diffusion solver. One could wonder why we do not do this with a detailed-balance approach as in Section 3.2.2: this is mainly because the spectral heat flux density q_ω does not go to zero as ε'' goes to zero using the transmission coefficient given in Eq. (1.16), precisely because the components are semi-infinite. While this is not an issue in the case of an abrupt bandgap, it becomes one when considering an Urbach tail as q_ω does not go to zero as the photon energy decreases below E_g: the resulting spectrum is therefore erroneous below E_g. In terms of Urbach energy, that of the PV cell will be considered equal to 10 meV, roughly corresponding to the value given in [Greeff & Glyde 1995]. For the hot LED, it is set at 15 meV. This last value is chosen quite arbitrarily: while E_{U} is known to increase with temperature, its exact variations have been sparsely analysed [Greeff & Glyde 1995]. Also, note that these two values could in reality be smaller or larger depending on the device quality as well as its doping level, values between 5 and 40 meV being for instance reported in [Chen *et al.* 2021] for GaAs.

The variation of power output with LED bandgap is diplayed in Figure 5.25, the bandgap being changed through the aluminium fraction in the AlGaAs alloy forming the LED. When no Urbach tail is considered (blue curve), the trend is mostly similar with the one found in Chapter 3, the maximum power output being reached exactly when bandgaps are matched and decreasing quickly with bandgap mismatch - especially for LED bandgaps lower than the PV cell bandgap. However, as long as an Urbach tail is implemented for the LED emission, the variations are

[2] Close to E_g - and especially below - we have $\varepsilon'' < \varepsilon'$ (see Figure 1.12). In the limiting case $\varepsilon'' \ll \varepsilon'$, we obtain $|\varepsilon| - \varepsilon' \sim \varepsilon''/2$, and α then depends only on ε''.

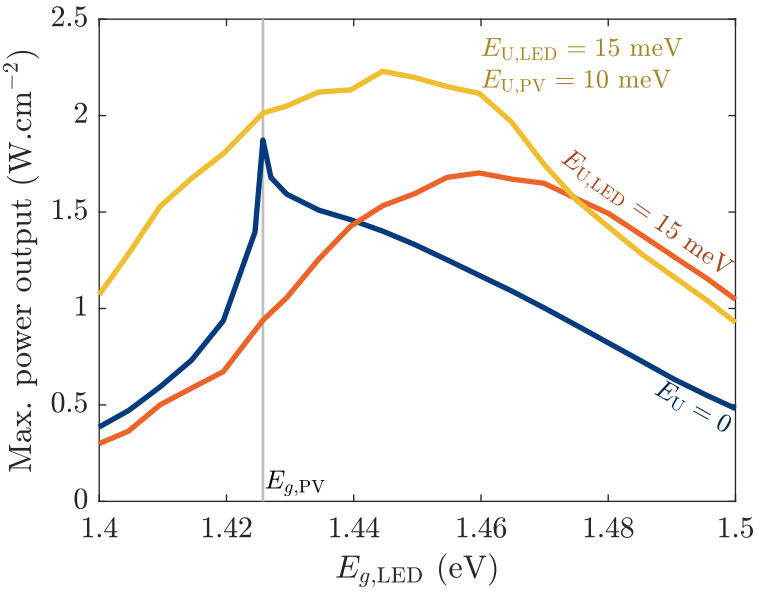

Figure 5.25: Variations of the maximum power output with the LED bandgap, controlled through the aluminium fraction.

much slower around the maximum. For an abrupt PV cell bandgap (orange curve), maximum power is reached for $E_{g,\mathrm{LED}}$ between 1.45 and 1.46 eV, hence for a 30 meV bandgap mismatch. This value is significantly lower than the ∼100 meV given in [Oehler 2022], as the goal was in their case to optimise the cell efficiency rather than the TPX power output. The temperature of the LED, equal to 350 K in [Oehler 2022], can also impact the optimal bandgap mismatch. As the PV cell bandgap is abrupt, the LED bandgap must be larger than $E_{g,\mathrm{PV}}$ to ensure that the electroluminescent radiation emitted below the LED bandgap can still be converted by the PV cell. However, if an Urbach tail is also implemented on the PV cell side (yellow curve), it can absorb photons with energy below its bandgap and the need for a significant bandgap mismatch is reduced. The LED bandgap at maximum power is consequently reduced to 1.44 eV, corresponding to a bandgap mismatch of approximately 15 meV. Variations of power output are even slower around the maximum in this case, almost reaching a plateau between 1.425 and 1.46 eV. Considering realistic emission and absorption profiles, the condition of exact bandgap matching is therefore relaxed. This shall be helpful for the experimental proof of concept of thermophotonics, as matching the bandgaps would require to control the aluminium concentration with a precision of the order of the tenth of percent, which is hardly achievable.

5.3.3 Analysis of the resonance modes close to E_g

One may notice the results shown above lack smoothness. This is due to the presence of resonant modes below the bandgap, which can be observed in an $\omega - k_\rho$ plot of the transmission coefficient, represented in Figure 5.26. Above the bandgap energy, the transmission coefficient varies smoothly with k_ρ for a given photon energy. On the contrary, resonances appear for photon energy below E_g at specific values of k_ρ, the transmission coefficient becoming locally much larger than for most of the admissible k_ρ. This makes the integration over k_ρ very sensitive to the mesh, and would require an adaptative mesh to ensure precision in the integration for any frequency. As it is not the case of our mesh, there are some imprecision in the integration below the bandgap which are causing the small variations observed in the results in Figure 5.25 - except for the case $E_{\mathrm{U}} = 0$, in which no such variations can be observed as no interband transitions occur below the

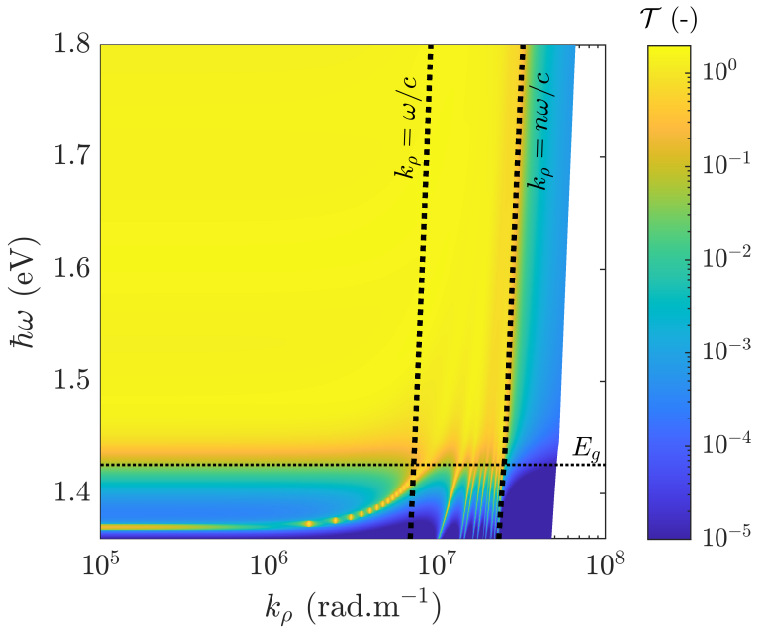

Figure 5.26: Transmission coefficient between the LED and the PV cell as a function of ω and k_ρ.

bandgap.

These resonances are mostly observed for frustrated modes, i.e. for $\omega/c < k_\rho < n\omega/c$, n corresponding to the refractive index of GaAs which is close to that of AlGaAs. In fact, we can notice that these resonances are also visible above the bandgap, but are much less impactful as the transmission coefficient is high even out of resonances due to the imaginary part of the dielectric function being significant. To trace the cause of these resonances back, we consider a simpler system composed only of the GaAs and AlGaAs layers facing each other, still with perfect mirrors at the back (here considered to be semi-infinite). With this set of five layers, the dependency of the transmission coefficient with ω and k_ρ is known analytically [Francoeur *et al.* 2010]. Using this analytical expression, we found the different resonant branches to perfectly coincide with the condition of resonance in the intermediate cavity:

$$\mathrm{Re}\left(R^\gamma_{\mathrm{LED}} R^\gamma_{\mathrm{PV}} e^{2ik_{z,\mathrm{gap}}d}\right) = 1, \tag{5.19}$$

where R^γ_i correspond to the global reflection coefficient of layer i for polarisation γ, whose expression is given in [Francoeur *et al.* 2010][3] and depends on the reflection coefficients at the interface along with the layer thickness and the value of k_z in the layer. Therefore, these peaks in the transmission coefficient come from the resonance of the electromagnetic field in the cavity. The leftmost branch is of particular interest, as for low values of k_ρ the related frequency remains constant. By meticulously designing the TPX device, this resonance could occur close to E_g, enabling a significant increase of the transmission coefficient and thus of the radiative heat transfer at a 10 nm gap distance.

[3]Note that in [Francoeur *et al.* 2010], the expression given for the global reflection coefficient R_{LED} (corresponding to R_1 in the article) is correct only if the semi-infinite layers at both ends and the intermediate layer are made of the same material. This is not the case here and R_{LED} should thus be slightly modified in comparison to the original expression.

5.4 To sum up

In this chapter, we performed the first complete 1D analysis of the performance of a TPX device. One aim of such an analysis is to obtain a better estimate of the achievable power output, which was found here to be equal to 1.9 W.cm^{-2} with an AlGaAs LED and a GaAs PV cell, considering a 300 K temperature difference. This is made possible by the large LED QE achieved, which is close to 0.955 at MPP and remains above 0.95 for LED voltages between 1 and 1.2 V. 1D analyses also allow highlighting specific behaviours which are difficult to grasp with simpler detailed-balance approaches. For instance, we studied how the presence of Urbach tails in the absorption and emission profiles relaxes the bandgap-matching requirement. We have also investigated the strong influence of the LED quantum efficiency on the overall TPX performance, which annihilates the capacity of the component to generate power in the low-voltage range due to SRH recombinations. In fact, this was also found to be one of the main phenomena hindering the development of electroluminescent cooling [Sadi *et al.* 2019b].

If this power gap is not an issue when operating at a 10 nm gap distance, it becomes one when going towards the far field: for a gap distance above 78 nm, we found that our device was not capable of generating significant amount of power, the true-TPX power production region having disappeared due to the global reduction of the LED quantum efficiency. The question could then be: how can we avoid such power loss in the far field? One solution is quite straightforward: since the low QE is mainly due to SRH recombinations, which occur mainly in the low-doped layers as $n \approx p$ there, we may simply want to further dope the intermediate layer. This will reduce the SRH recombination rate, at the cost of increased Auger recombination rate - and therefore reduced power output at a 10 nm gap distance. We show for instance in Figure 5.27 the power production region obtained if the intermediate layer doping level is equal to 10^{18} cm^{-3}. While the maximum power output is reduced to 1.7 W.cm^{-2} due to Auger recombination, no power gap is found in the low-voltage range at a 10 nm gap distance, and the device is still able to operate in the true-TPX region for a 100 nm gap distance - although the maximum power output is already

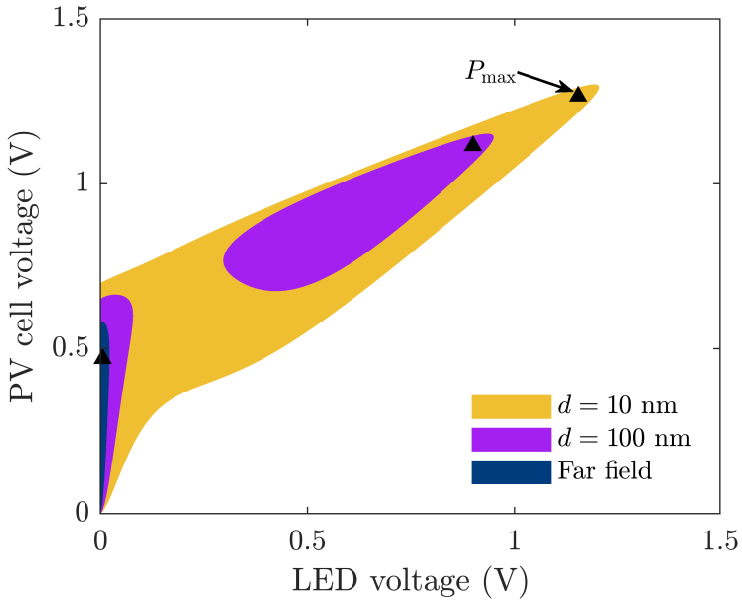

Figure 5.27: Power production region of a modified version of the structure shown in Figure 5.4, in which the doping level of intermediate layers is increased to 10^{18} W.cm^{-3}.

largely reduced, being only equal to 4×10^{-3} W.cm^{-2}. Moreover, for larger gap distances, the LED quantum efficiency continues to decrease such that this device is not capable of generating power in the far field either.

One other solution, which is more complex, was recently proposed in [Santhanam *et al.* 2020]. By precisely tailoring the dopant profile close to a heterojunction, they were able to locally control the carrier concentration and ensure that $n = p$ (which maximises R_{SRH}) occurs only in the high-bandgap material in which the impact of recombination is greatly lowered. This allowed them demonstrating a significant reduction of the total SRH recombination rate. However, this requires to work with heterostructures, and thus cannot be applied directly to the device considered in this chapter. In the following chapter however, heterostructures will be used and this solution could be implemented if SRH recombinations were found to be limiting.

Chapter 6

Extension to heterostructures for efficient charge transport

Contents

6.1 Physics and modelling of heterojunctions 133
6.1.1 Charge transport at heterojunctions 134
6.1.2 Drift-diffusion solver for heterostructures 139
6.1.3 Numerical stability issues 139
6.1.4 Back to the chemical potential 143
6.1.5 Photon recycling and thoughts on the locality approximation 144
6.1.6 Comparison to SCAPS 146
6.2 Analysis of TPX devices based on AlGaAs/InGaP heterostructures . . 147
6.2.1 Structure optimisation of AlGaAs/InGaP devices 148
6.2.2 Performance of optimised AlGaAs/InGaP heterostructures 151
6.2.3 Impact of the heterojunction model on TPX performance 152
6.2.4 Charge transport at maximum power point 153
6.3 Towards more realistic and performant TPX devices 156
6.3.1 Temperature and alloy fraction dependency of non-radiative recombination coefficients 156
6.3.2 InGaAs/InGaP heterostructures for robust TPX devices 158
6.4 To sum up 162

6.1 Physics and modelling of heterojunctions

In Chapter 4, we have briefly mentioned that materials with high bandgaps are often used for the highly-doped layers to form performant heterostructures. An important question we should answer before working with such heterostructures is: why do they perform better than homostructures? Or more precisely, why using high-bandgap materials for the highly-doped layers improve the performance of a device? The main advantage of such layers is that they significantly improve the separation of charge carriers, due to different phenomena which are detailed below and summarised in Figure 6.1.

- As shown in Eq. (4.4), n_i decays exponentially with E_g. np is proportional to n_i^2, and since the majority carrier concentration can be supposed to be constant in highly-doped layers, the minority carrier density largely decreases with E_g (considering a constant quasi Fermi level difference). Therefore, the difference of density between majority and minority carriers is increased: their separation is improved, allowing for a significant reduction of Auger and surface recombinations.

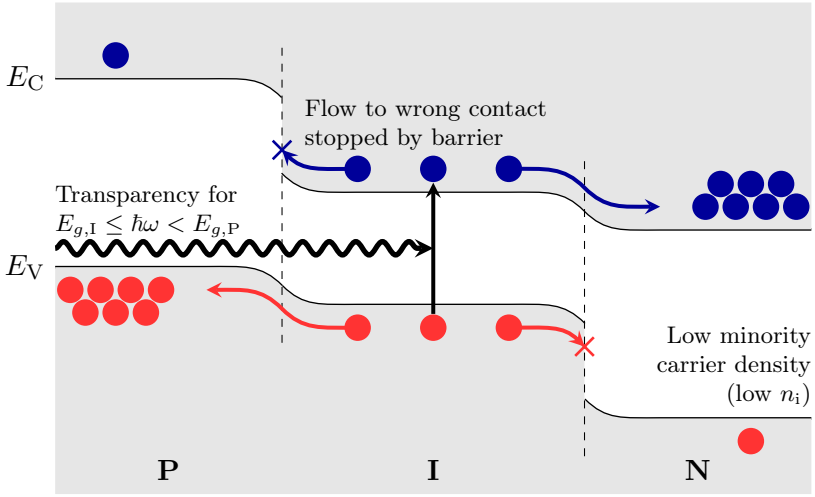

Figure 6.1: Advantages of heterostructures over homostructures.

- These high-bandgap materials are almost transparent close to the bandgap energy of the intermediate layer. This prevents the generation of minority carriers in highly-doped layers.
- In the case of abrupt junctions, the difference of E_g and χ at the interface causes the formation of a potential barrier in the conduction and valence bands. If the high-bandgap materials are chosen well, it can allow blocking the flow of carriers towards the wrong contact. However, this requires to use different materials for p-doped and n-doped layers. In our case, only InGaP layers will be considered, and the barriers will mainly be present in the valence band, as we will show afterwards.

While displaying better performance, such heterostructures are more difficult to grow than homostructures due to the abrupt variation in material properties at the junction and to the simultaneous need for a high-quality interface, as the formation of dislocations around the interface would significantly increase non-radiative events. They are also more complex to model, as the transport of charge carriers is modified at the heterojunction.

6.1.1 Charge transport at heterojunctions

In the following, only abrupt heterojunctions will be considered. As shown in Figure 6.1, the difference of bandgap energy and electron affinity causes the formation of potential barriers at the interfaces. Such barriers cause asymmetry in charge carrier transport: looking at the P-I interface for instance, it is clear that electrons in the P region can easily fall in the I region, while electrons in the I regions are blocked by the barrier. Because of this asymmetry, quasi Fermi levels are discontinuous at the heterointerface. Often, the variations of quasi Fermi levels are sufficiently small to make the assumption of continuity through the interface valid; in the frame of this work however, we will see that this approximation is not satisfactory. We review below the two models generally considered to include this discontinuity.

6.1.1.1 Thermionic emission

The first possibility is to consider that a charge carrier in a band cannot travel through a barrier, and thus can be transmitted only if states are available at the carrier energy on both sides of the interface. In this case, nothing hinder the flow of carriers and their transmission coefficient is equal to one. This is illustrated in Figure 6.2a, and corresponds to the phenomenon of thermionic

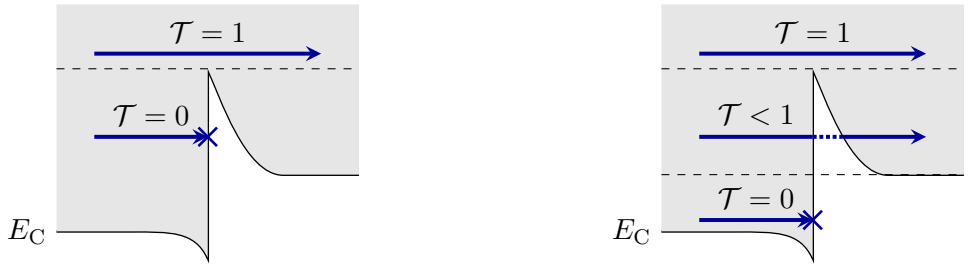

(a) Thermionic emission (b) Thermionic-field emission

Figure 6.2: Transmission coefficient of charge carriers (here, electrons) through a heterojunction.

emission. To implement such an effect in a drift-diffusion solver, the current flowing through the interface shall be expressed from the quasi Fermi levels at both sides starting from the general expression $\mathbf{J} = e \cdot n\mathbf{v}$ (n and $\mathbf{v}$ being the density and velocity of the charge carriers under consideration). Following the developments of [Wu & Yang 1979, Grinberg & Luryi 1998], the general expression of the current of charges from layer i to layer j flowing in the z-direction is:

$$J_{i\to j} = \frac{2e}{(2\pi)^3}\int \frac{1}{\hbar}\frac{\partial E}{\partial k_z}(E(\mathbf{k}))\mathcal{T}(E(\mathbf{k}))f_i(E(\mathbf{k}))(1-f_j(E(\mathbf{k})))d\mathbf{k}, \tag{6.1}$$

$\mathcal{T}$ being here the transmission coefficient of charge carriers, $\mathbf{k}$ their angular wavevector and f their distribution function. One can similarly express the current flowing from j to i, allowing to compute the net flow from i to j as the difference between these two currents. Taking the example of electrons in the conduction band, their energy can be decomposed as $E = (E_\rho + E_z) + E_C$, E_ρ and E_z representing respectively the kinetic energy in the direction parallel and perpendicular to the interface and being equal to $\hbar^2k_\rho^2/2m_n^*$ and $\hbar^2k_z^2/2m_n^*$. Expressing the net current flow through the interface in terms of the normalised electronic energy $\tilde{E} = E/k_BT$ on the i-layer side of the interface gives

$$J_{n,ij} = A_i^*T^2\iint \mathcal{T}(\tilde{E})\Big(f_j(\tilde{E}) - f_i(\tilde{E})\Big)d\tilde{E}_{\rho,i}d\tilde{E}_{z,i}, \tag{6.2}$$

where A_i^* represents the effective Richardson constant, equal to $em_n^*k_B^2/2\pi^2\hbar^3$. $\tilde{E}$ is given without subscript as conservation of energy gives us $\tilde{E}_i = \tilde{E}_j = \tilde{E}$. Considering only thermionic emission, the transmission coefficient is equal to one only if the electron energy is larger than $\tilde{E}_{C,max}$; else, it equals zero. The main difficulty here is therefore to determine the domain of integration for $\tilde{E}_{\rho,i}$ and $\tilde{E}_{z,i}$. In the following, we only consider what happens at the interface, as in [Wu & Yang 1979] and contrarily to [Grinberg & Luryi 1998] in which the maximum of the conduction band is not forced to be at the interface. We can then make use of several equations:

- the conservation of momentum parallel to the interface $m_{n,i}^*\tilde{E}_{\rho,i} = m_{n,j}^*\tilde{E}_{\rho,j}$;
- the conservation of energy $\tilde{E}_i = \tilde{E}_j$;
- the condition that every kinetic term should be positive.

From these, we can obtain

$$\tilde{E}_{z,i} \geq \left(\frac{1}{\theta} - 1\right)\tilde{E}_{\rho,i} + E_B, \tag{6.3}$$

where $\theta = m_{n,j}^*/m_{n,i}^*$ and $E_B = E_{C,j} - E_{C,i}$ represents the variation of energy through the barrier. This equation gives different domains of integration depending on the value of θ and E_B as kinetic

terms must be positive:

- $\theta \geq 1$: $\tilde{E}_{z,i} \geq \max(E_\mathrm{B}, 0) = \alpha$, $0 \leq \tilde{E}_{\rho,i} < \infty = \beta$;
- $\theta < 1$: $\tilde{E}_{z,i} \geq \max(E_\mathrm{B}, 0) = \alpha$, $0 \leq \tilde{E}_{\rho,i} \leq (\tilde{E}_{z,i} - E_\mathrm{B})/(1/\theta - 1) = \beta(\tilde{E}_{z,i})$.

Regarding the distribution function, we use Boltzmann's approximation to simplify the Fermi-Dirac distribution. The net electron current is then expressed as

$$J_{n,ij} = A_i^* T^2 e^{-\tilde{E}_{\mathrm{C},i}} (e^{\tilde{E}_{\mathrm{F}n,j}} - e^{\tilde{E}_{\mathrm{F}n,i}}) \int_\alpha^\infty e^{-\tilde{E}_{z,i}} d\tilde{E}_{z,i} \int_0^{\beta(\tilde{E}_{z,i})} e^{-\tilde{E}_{\rho,i}} d\tilde{E}_{\rho,i}. \tag{6.4}$$

The integration is straightforward and gives the general expression

$$J_{n,ij} = \eta A_i^* T^2 \cdot e^{-\tilde{E}_{\mathrm{C,max}}} (e^{\tilde{E}_{\mathrm{F}n,j}} - e^{\tilde{E}_{\mathrm{F}n,i}}), \tag{6.5}$$

where η is a term including the effects related to effective mass asymmetry and expressed as[1]:

$$\eta = \begin{cases} \theta - (\theta - 1) \exp\Big(-|\tilde{E}_\mathrm{B}|/(\theta - 1)\Big) & \text{if } E_\mathrm{B} \geq 0 \text{ and } \theta > 1, \\ \theta & \text{if } E_\mathrm{B} \geq 0 \text{ and } \theta \leq 1, \\ 1 & \text{if } E_\mathrm{B} < 0 \text{ and } \theta \geq 1, \\ 1 - (1 - \theta) \exp\Big(-|\tilde{E}_\mathrm{B}|/(1/\theta - 1)\Big) & \text{if } E_\mathrm{B} < 0 \text{ and } \theta < 1. \end{cases} \tag{6.6}$$

As long as θ is close to one or $|E_\mathrm{B}|$ is large, η remains respectively close to θ and 1 in the first and the last case. Since $\theta A_i^* = A_j^*$, the effective Richardson constant ηA_i^* is driven by the effective mass of the material where the conduction band maximum is located, as stated in [Grinberg & Luryi 1998]. While the term η is not particularly complicated to take into account in simulations, note that it is not systematically implemented; in SCAPS for instance, the effective Richardson constant is simply taken equal to the Richardson constant of the material with the lowest effective mass.

Coming back to Eq. (6.5), the electron current at the interface depends on the difference in electron Slotboom variable $\Phi_j - \Phi_i$: a current flowing through a heterojunction thus causes a discontinuity in the quasi Fermi level, which grows with the current amplitude. The result is similar if looking at the flow of holes in the valence band:

$$J_{p,ij} = \eta A_i^* T^2 \cdot e^{\tilde{E}_{\mathrm{V,min}}} (e^{-\tilde{E}_{\mathrm{F}p,j}} - e^{-\tilde{E}_{\mathrm{F}p,i}}), \tag{6.7}$$

A_i^* and η being obviously expressed from the hole effective mass.

6.1.1.2 Charge tunnelling and thermionic-field emission

The physical phenomena taken into account in the thermionic emission model are purely classical. However, quantum effects can also modify the transport of charges through the interface. Regarding heterojunctions, the main quantum effect is charge carrier tunnelling, which is the phenomenon whereby charges with normally insufficient energy to cross the interface can pass through a potential barrier if it is thin enough, and thus be transmitted to the next layer. This is similar to the concept of photon tunnelling, photons being able to travel through a usually

[1] Note that the two last expressions can be directly derived from the first two by transposing indices i and j, as explained in [Grinberg & Luryi 1998].

forbidden intermediate region. To be precise, we only consider here intraband tunnelling, meaning that charges which are tunnelling remain in the same band. As displayed in Figure 6.2b, this opens a new channel of charge carrier transmission across the interface, modifying the relation between current and quasi Fermi level. The current at the heterojunction can be once more obtained from Eq. (6.2), however with different integration bounds. Integration can be done separately for classical and quantum transmission, so that the current can be expressed as

$$J = J_{\text{thermionic}} + J_{\text{tunnel}}, \tag{6.8}$$

$J_{\text{thermionic}}$ corresponding to the expressions derived in the previous section. The combination of these two effects is generally called thermionic-field emission. In the following, we take once more the example of electrons in the conduction band, the development being similar for holes in the valence band. In order to compute J_{tunnel}, the integral over energy should only be performed below $E_{\text{C,max}}$, as larger energies are already taken into account in $J_{\text{thermionic}}$. The value of the lower bound E_{min} depends on the shape of the spike. It corresponds to the largest energy between

- the lower value of the conduction band at the interface $E_{\text{C,min}}$ (as electrons must be in the conduction band);
- the value of E_{C} far from the interface on the side of the spike $E_{\text{C},\infty}$ (as electrons with lower energy face a barrier with infinite thickness and thus cannot tunnel through it).

The transmission coefficient of charge carriers crossing a potential barrier is expressed using the one-dimensional WKB approximation, following [Yang *et al.* 1993]:

$$\mathcal{T}_{\text{tunnel}}(E) = \exp\left(-\frac{2}{\hbar}\int_0^{z(E)} \sqrt{2m^*_{n,t}(E_{\text{C}}(z') - E)}dz'\right). \tag{6.9}$$

$m^*_{n,t}$ corresponds to the effective mass of electrons in the layer in which they tunnel, and $z(E)$ is the first position in this layer where $E_{\text{C}}(z) = E$, as represented in Figure 6.3. The transmission coefficient at a given energy E logically depends on the shape of the conduction band between 0 and $z(E)$, i.e. above E. If the lower bound of the integral over energy corresponds to $E_{\text{C,min}}$, $z(E_{\text{C,min}})$ is generally few nanometres away from the interface and the integral can be easily calculated. However, if $E_{\text{min}} = E_{\text{C},\infty}$ - as represented in Figure 6.3 - the lower bound corresponds to the asymptotic value of E_{C} and $z(E)$ can become large, making the integral over z time-consuming. Since the transmission coefficient goes to zero as E approaches $E_{\text{C},\infty}$, the integral over depth is cut at an arbitrary distance z_{c} from the interface, which means that integration only starts at $E_{\text{min}} = E_{\text{C}}(z_{\text{c}})$. In the following, this distance is set to 50 nm, which allows including most of the tunnelling as we will show afterwards. Also, if the layer in which carriers tunnel is thinner than $z(E_{\text{min}})$, the integral is cut at the thickness of the layer. Reflection and transmission at this second interface are neglected.

The integration over energy for computing tunnelling current is simpler than in case of thermionic emission. Indeed, the condition of conservation of the momentum parallel to the interface no longer holds as the kinetic energy of tunnelling charges is not properly defined in the barriers. The only condition which must be satisfied is that the total energy E is between $E_{\text{C,min}}$ and $E_{\text{C,max}}$. Therefore, only one integral over energy remains. Using Eq. (6.2) to express the electron current related to tunnelling in a form similar to (6.4) gives

$$J_{n,\text{tunnel}} = \eta_t A^*_i T^2 (e^{\tilde{E}_{\text{F}n,j}} - e^{\tilde{E}_{\text{F}n,i}}) \int_{\tilde{E}_{\text{min}}}^{\tilde{E}_{\text{C,max}}} e^{-\tilde{E}} \mathcal{T}(\tilde{E}) d\tilde{E}. \tag{6.10}$$

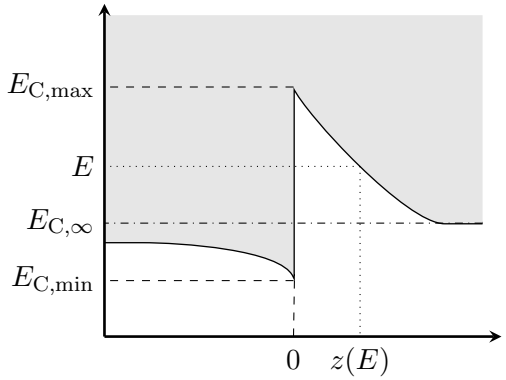

Figure 6.3: Representation of the different quantities useful for thermionic-field emission.

This expression can only be derived in the layer where $E_{\mathrm{C,min}}$ is located, as the way we define the energy of charge carriers does not work in the barrier. Therefore, the effective Richardson constant $\eta_t A_i^*$ must be that of this layer[2], which means that

$$\eta_t = \begin{cases} \theta & \text{if } E_{\mathrm{B}} < 0 \\ 1 & \text{else.} \end{cases} \tag{6.11}$$

The total thermionic-field emission current of electrons can therefore be expressed as

$$J_{n,ij} = A_i^* T^2 (\eta + \varphi) e^{-\tilde{E}_{\mathrm{C,max}}} (e^{\tilde{E}_{\mathrm{F}n,j}} - e^{\tilde{E}_{\mathrm{F}n,i}}) \tag{6.12}$$

where

$$\varphi = \eta_t \int_{\tilde{E}_{\mathrm{min}}}^{\tilde{E}_{\mathrm{C,max}}} e^{\tilde{E}_{\mathrm{C,max}} - \tilde{E}} \mathcal{T}(\tilde{E}) d\tilde{E}. \tag{6.13}$$

Similarly, the current of holes in the valence band can be expressed as

$$J_{p,ij} = A_i^* T^2 (\eta + \varphi) e^{\tilde{E}_{\mathrm{V,min}}} (e^{-\tilde{E}_{\mathrm{F}p,j}} - e^{-\tilde{E}_{\mathrm{F}p,i}}), \tag{6.14}$$

φ being equal to

$$\varphi = \eta_t \int_{\tilde{E}_{\mathrm{V,min}}}^{\tilde{E}_{\mathrm{max}}} e^{\tilde{E} - \tilde{E}_{\mathrm{V,min}}} \mathcal{T}(\tilde{E}) d\tilde{E}. \tag{6.15}$$

In the layer in which the barrier minimum is located, this total current must correspond to drift and diffusion currents. In the opposite layer however, part of the current is due to tunnelling and only a fraction of the carrier current can be related to drift and diffusion. Close to the interface, the drift-diffusion current corresponds to the current induced by charges in the band, i.e. to thermionic emission; for electrons for instance,

$$J_{n,\mathrm{drift-diff}}(0^+) = J_{n,\mathrm{thermionic}}. \tag{6.16}$$

As z increases, more electrons come back to the conduction band and participate to drift-diffusion current. It is then given as [Verschraegen & Burgelman 2007]

$$J_{n,\mathrm{drift-diff}}(z) = J_{n,\mathrm{thermionic}} + \frac{\varphi(z)}{\varphi} J_{n,\mathrm{tunnel}} - e \int_0^z (G(z') - R(z')) dz', \tag{6.17}$$

[2]Note that no reference has been found to support this statement, which only comes from our understanding of the phenomenon.

$\varphi(z)$ being defined as

$$\varphi(z) = \begin{cases} \eta_t \displaystyle\int_{\tilde{E}_{\mathrm{C}}(z)}^{\tilde{E}_{\mathrm{C,max}}} e^{\tilde{E}_{\mathrm{C,max}}-\tilde{E}} \mathcal{T}(\tilde{E}) d\tilde{E} & \text{if } \tilde{E}_{\mathrm{C}}(z) > \tilde{E}_{\mathrm{min}}, \\ \varphi & \text{else.} \end{cases} \tag{6.18}$$

A similar expression applies for holes.

6.1.2 Drift-diffusion solver for heterostructures

The study of heterostructures requires several modifications of the previously-presented drift-diffusion solver. One is the change in the expression of the charge carrier densities. While the expression of the intrinsic energy level provided in Eq. (5.2) could be simplified in the case of homostructures, it cannot for heterostructures and an additional term shall be present to account for the variations of material properties. Following the developments from [Lundstrom & Schuelke 1982], we have:

$$n = n_{\mathrm{i}}(0) e^{\xi_n} e^{+\Psi} \Phi_n, \tag{6.19a}$$

$$p = n_{\mathrm{i}}(0) e^{\xi_p} e^{-\Psi} \Phi_p, \tag{6.19b}$$

where

$$k_{\mathrm{B}}T \cdot \xi_n = \quad (\chi(z) - \chi(0)) \qquad + \frac{k_{\mathrm{B}}T}{2} \ln\left(\frac{N_{\mathrm{C}}(z)}{N_{\mathrm{C}}(0)}\right), \tag{6.20a}$$

$$k_{\mathrm{B}}T \cdot \xi_p = -(\chi(z) - \chi(0)) - \frac{E_g(z) - E_g(0)}{2} + \frac{k_{\mathrm{B}}T}{2} \ln\left(\frac{N_{\mathrm{V}}(z)}{N_{\mathrm{V}}(0)}\right). \tag{6.20b}$$

Even if Ψ, Φ_n and Φ_p are continuous, charge carrier densities are thus discontinuous at heterointerfaces.

Then, specific equations are required at the interfaces to relate the different quantities from one layer to another. Using the equations developed above for thermionic emission or thermionic-field emission, we get the variations of Φ_n and Φ_p from the related current, since $J \propto \Delta\Phi$. The total current related to a kind of charge carrier is supposed to be continuous at a heterointerface. The drift-diffusion current can however be discontinuous at the interface due to tunnelling, as discussed in the previous section: if tunnelling is considered, only a fraction $\eta/(\eta+\varphi)$ of the current coming onto a barrier is related to drift and diffusion after crossing the barrier, the remaining part of the current being reinjected further away from the interface. Last, the component perpendicular to the interface of the electric displacement field $\mathbf{D} = \varepsilon\mathbf{E}$ is considered to be continuous through interfaces since they are considered to be electrically neutral, so that

$$\varepsilon_{\mathrm{s}}(z^-) \frac{\mathrm{d}\Psi}{\mathrm{d}z}(z^-) = \varepsilon_{\mathrm{s}}(z^+) \frac{\mathrm{d}\Psi}{\mathrm{d}z}(z^+). \tag{6.21}$$

In the following, we consider exclusively the thermionic-field emission model as it is the most complete, unless otherwise specified. Details on the numerical model can be found in Appendix E.

6.1.3 Numerical stability issues

In the previous chapter, the resolution of the different equations was performed iteratively to obtain the spatial variations of various quantities. However, nothing guarantees that this iterative

process will converge; and while everything went well in the case of homostructures, convergence issues were observed when trying to solve the set of equations for heterostructures, particularly for high voltages. The first improvement that can be performed to help convergence is to smoothen the iterative process by effectively slowing the variations of the different quantities from one iteration to the next. Taking the example of the normalised electrostatic potential, let $\tilde{\Psi}$ be the result obtained from Poisson equation and Ψ the result after damping, which is the end result of the iteration. We express Ψ_k at iteration k as

$$\Psi^k = w \cdot \tilde{\Psi}^k + (1 - w) \cdot \Psi^{k-1}, \tag{6.22}$$

where w is the weighting factor associated to the current iteration and must be between 0 and 1 (0 excluded), $w = 1$ meaning that the process is not damped. A similar treatment is made on Φ_n and Φ_p, but not for current densities as they will be the first to be computed in the next iteration and will not change the calculations if damped. Since the relative variations of the different quantities are proportional to the weighting factor, the tolerance is reduced by a factor w to maintain the precision requirements similar. We initially take w equal to 1 for both components as it allows attaining convergence faster. If for a given couple of voltages, the solver does not converge, lower values of w are used: in our solver, $w = 0.8$ is tried first, then $w = 0.1$. If it still does not converge, the iterative process is stopped. Considering that the calculation was performed at $(U_{\mathrm{LED}}, U_{\mathrm{PV}}) = (U_i, U_j)$, the solver moves directly to the resolution at $(U_{i+1}, 0)$, since calculations at (U_i, U_{j+1}) require the solution at (U_i, U_j). The weighting factor w is then set back to 1 to increase convergence speed.

One challenging issue that could arise during the iterative procedure is that one of the Slotboom variables becomes locally negative, which is forbidden as they represent exponential term. This occurs especially in the case of heterostructures because of the potentially large discontinuities in Φ at heterointerfaces. While limited to large voltages in the case of a hot LED or an illuminated PV cell, it even arises at low voltages for LED at ambient temperature, making the issue important to consider. To reach convergence in such a case, w needs to be very low because of the quick variations of Φ between iterations: values as low as $w = 10^{-5}$ may be required to obtain a physically valid solution. In terms of computational time, such a low value of the damping factor is excessive. However, when trying to damp the variations of the Slotboom variables, we noticed that the maximum difference between two iterations $\varepsilon_{\mathrm{n/p}}$ seemed to converge towards an almost constant value after a certain number of iterations. Once this is reached, this means that the weighting factor could be increased. To make this clear, let k be the iteration index, p a positive number and w_n the weighting factor associated to Φ_n. If $\varepsilon_{\mathrm{n/p}}$ is perfectly constant, then $\Phi_n^{k+p} - \Phi_n^k = p(\Phi_n^{k+1} - \Phi_n^k)$, therefore $\Phi_n^{k+p} = pw_n\tilde{\Phi}_n^{k+1} + (1 - pw_n)\Phi_n^k$. By multiplying the weighting factor by p, Φ_n^{k+p} could thus be obtained in 1 instead of p iterations. To prevent getting negative Slotboom variables, we therefore adopt the following procedure:

- in any case, the use of a global damping factor w - as described above - is conserved, being a simple solution to help convergence.

- if at a given iteration, one of the Slotboom variables obtained from the drift-diffusion equations reaches a negative value, a secondary iterative process is started, in which only drift-diffusion and continuity equations are solved to reduce computational time and help convergence. Initially, the Slotboom weighting factors - which can be different for electrons and holes - are very low to prevent divergence. Negative values of Φ are accepted during this process to help convergence, but should become permanently positive at some point.

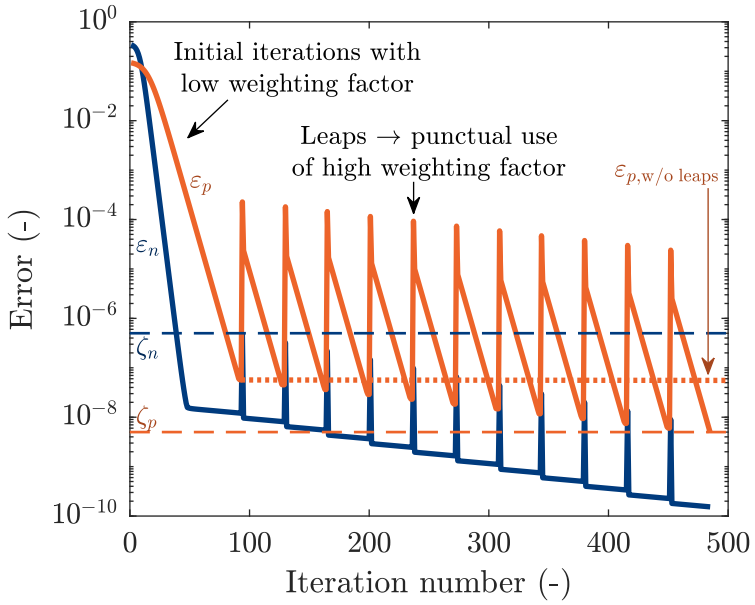

Figure 6.4: Typical variation of the error ε obtained at each iteration, defined as the relative variation of the Slotboom variables. ζ denotes the tolerance.

When Φ is locally negative, the calculation is performed as usual except for the diffusion coefficient which is not updated - we assume its variation with carrier concentration to be sufficiently low to have no dramatic impact on the convergence.

- after some iterations in the secondary process, both ε_n and ε_p should get either below the associated tolerance or close to constant, i.e. show relative variation between two iterations smaller than a given threshold ζ_Δ. If any of the two ε is in the latter case, both Slotboom weighting factors are largely increased, up to a value of the order of 0.1. This allows the solver to quickly approach the solution.

- the new solution being far from the previous one, $\varepsilon_{n/p}$ can become large and the low values of the weighting factors should be used once more to prevent divergence, up until ε becomes almost constant again - this constant value should be lower than the previous one thanks to the quick approach.

- the secondary process is stopped once the error, defined as the maximum relative variation of each of the Slotboom variables, is lower than a given tolerance. As for the global weighting factor, the tolerance is corrected with the Slotboom weighting factors, and is therefore different for electrons and holes. If convergence is not reached, lower values of the weighting factors are tried. If this still not helps, the calculation is stopped and the solver moves to the resolution at $(U_{i+1}, 0)$.

We show in Figure 6.4 how the errors ε_n and ε_p typically vary following this procedure. This was obtained considering an GaAs/InGaP LED at room temperature, for which the secondary iterative process is required to obtain the full characteristic. After roughly 90 iterations performed using low weighting factors, ε_n has got below the related tolerance ζ_n, but not ε_p. Continuing the iterative procedure with these weighting factors does not allow reaching convergence since ε_p remains almost constant, as denoted by the orange dotted line. Instead, the weighting factors are punctually increased, which allow to further decrease the error - although more slowly than initially. The complete flowchart of the drift-diffusion solver is provided in Figure 6.5.

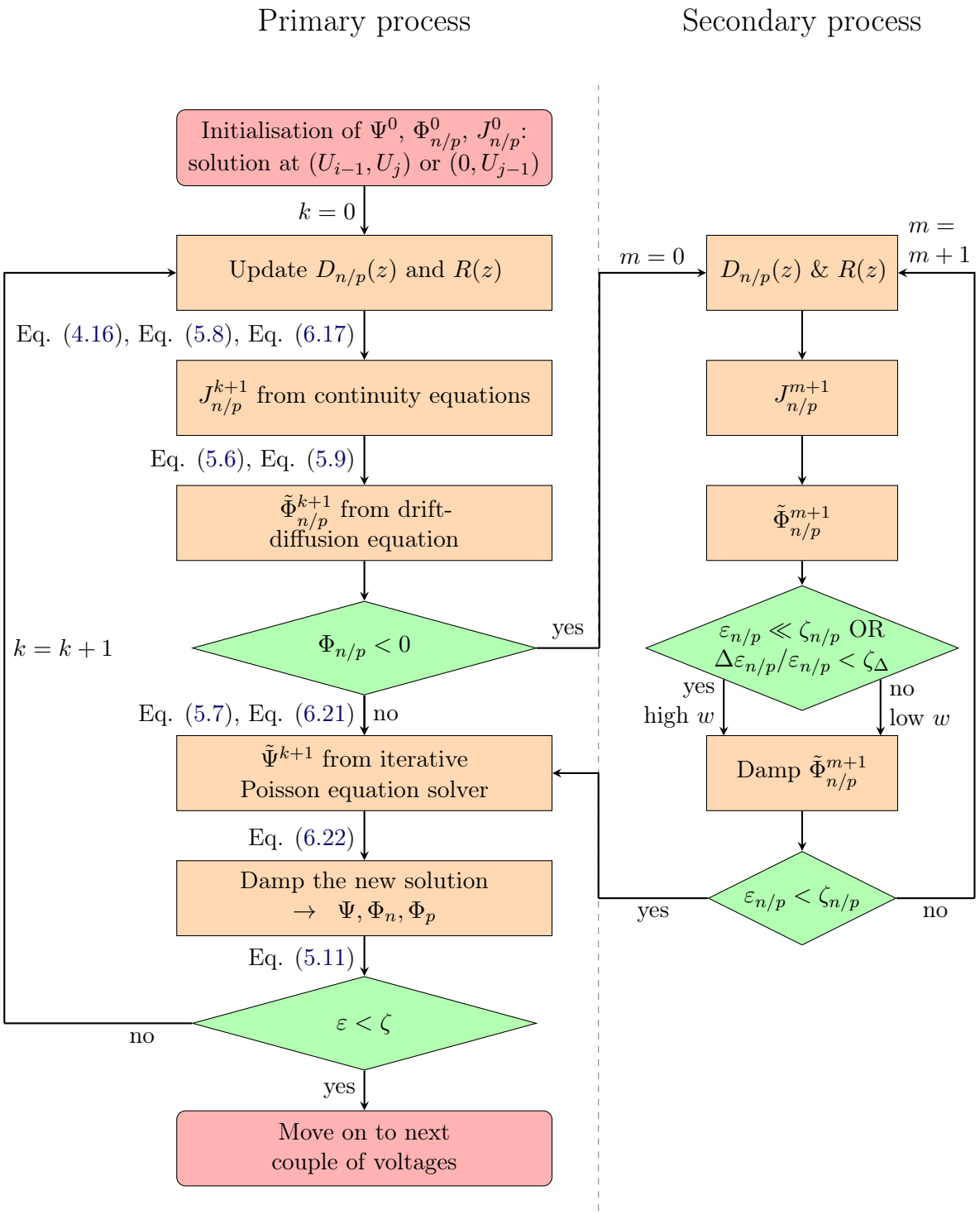

Figure 6.5: Flowchart of the drift-diffusion solver for heterostructures at $(U_{\text{LED}}, U_{\text{PV}}) = (U_i, U_j)$.

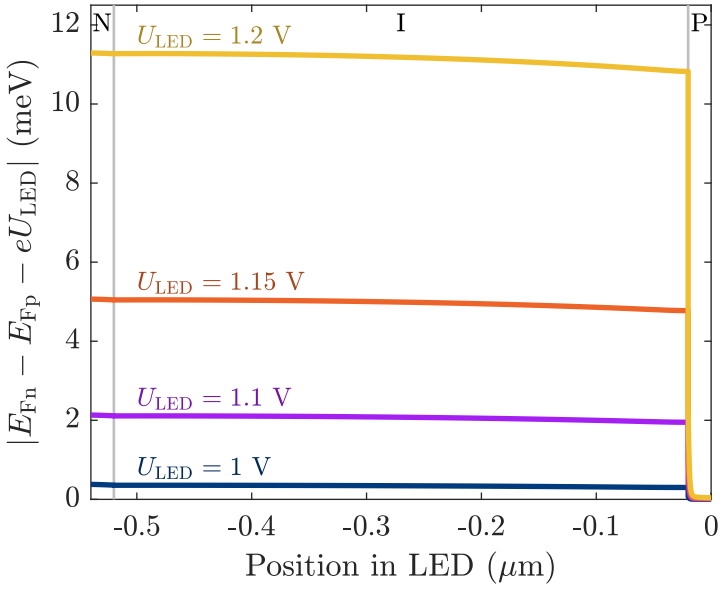

Figure 6.6: Typical deviation of the quasi Fermi level difference with respect to eU in a 600 K LED. It is obtained considering the TPX device shown in Figure 6.8 with an unbiased PV cell.

6.1.4 Back to the chemical potential

Previously, we have shown that any current flowing through a heterointerface causes a discontinuity in the related quasi Fermi level. Because there is no reason that the variation of quasi Fermi level at the interface is the same for electrons and holes, the chemical radiation of photons $\mu = E_{\mathrm{F}n} - E_{\mathrm{F}p}$ shall also vary. This can be observed in Figure 6.6, in which the spatial variation of the quasi Fermi level difference in an LED is given for several biases. This LED comes from the TPX device later considered for verifying the algorithm (see Figure 6.8), the PV cell being unbiased. For any of the voltages, $E_{\mathrm{F}n} - E_{\mathrm{F}p}$ varies abruptly at the P-I interface, being lower than eU_{LED} in the I and N regions. At moderate voltages, electron and hole current densities are relatively low, and so is the associated change in $E_{\mathrm{F}n} - E_{\mathrm{F}p}$: for $U_{\mathrm{LED}} = 1$ V, it deviates at most by 0.35 meV from eU_{LED}. But for larger voltages, it becomes significant in comparison to the thermal energy $k_{\mathrm{B}}T_{\mathrm{LED}} = 52$ meV. Consequently, it impacts significantly the emission of the intermediate layer: compared to the case $\mu = eU$, the reduction of the chemical potential of photons by 11 meV for $U_{\mathrm{LED}} = 1.2$ V roughly reduces the photon and heat flux density emitted by 20%, assuming Boltzmann's approximation.

Since this deviation becomes significant in the LED voltage range in which the MPP typically lies, it is important to take it into account to ensure precise calculation of the maximum power output. Therefore, we implement in this section the iterative procedure presented in [Callahan *et al.* 2021] and discussed in Section 4.1.4. For each couple of voltages, the difference of quasi Fermi levels obtained with the drift-diffusion solver is used to update the electroluminescent radiative terms, which are fed back to the solver in the next iteration if convergence is not reached. To simplify the procedure, we consider only one effective photon chemical potential $\tilde{\mu}$ per layer, which is an acceptable hypothesis as most of the variations of $E_{\mathrm{F}n} - E_{\mathrm{F}p}$ in the LED occur at interfaces. This effective quantity is computed such that in layer i, $\exp(\tilde{\mu}_i/k_{\mathrm{B}}T) = t_i^{-1} \int \exp(\mu/k_{\mathrm{B}}T)dz$, t_i being the layer thickness. This allows to roughly have the correct electroluminescent emission rate for the whole layer. Since the LED and PV cell operation are coupled through radiation, the drift-diffusion solver should be used for both components at each iteration. The iterative procedure

stops once the maximum absolute variation ε_μ of the photon chemical potential associated to each layer of both components becomes lower than a set tolerance ζ_μ.

6.1.5 Photon recycling and thoughts on the locality approximation

Since we now consider the chemical potential to be variable from one layer to another, the difference of modified Bose-Einstein distributions $f_{\mathrm{BE}}(\mu, T)$ between two layers of the same components can be non-zero: a net photon flux therefore arises between them, which leads to photon recycling. However, the transmission function of photons returned by the near-field radiative solver when considering adjacent layers diverges. To ensure such a divergence does not come from numerical instabilities but rather from the model itself, we develop analytically the transmission coefficient obtained in the case of a simpler structure, composed of three adjacent layers placed between two semi-infinite media. More precisely, the two extreme layers (numbered respectively 0 and 2) are assumed to be made of the same material as the adjacent semi-infinite layer. Following [Mulet 2004], the transmission coefficient between layer 0 and layer 2 can be expressed as

$$\mathcal{T}_{02}^{\mathrm{TM}}(\omega, k_\rho) = \frac{1}{|k_{z0}|^2} \frac{\mathrm{Re}(\varepsilon_0 k_{z0}^*)}{|\varepsilon_1|} \frac{\mathrm{Re}(\varepsilon_2 k_{z2}^*)}{|\varepsilon_2|} \left|t_{02}^{TM}\right| \vartheta_0 \vartheta_2, \tag{6.23a}$$

$$\mathcal{T}_{02}^{\mathrm{TE}}(\omega, k_\rho) = \frac{k'_{z0} k'_{z2}}{|k_{z0}|^2} \left|t_{02}^{TE}\right| \vartheta_0 \vartheta_2. \tag{6.23b}$$

In these expressions, whose derivation is provided in Appendix A.2, t_{02}^γ is defined as

$$t_{02}^\gamma = \frac{t_{01}^\gamma t_{12}^\gamma e^{ik_{z1}d}}{1 + r_{01}^\gamma r_{12}^\gamma e^{2ik_{z2}d}}, \tag{6.24}$$

d being the distance between layers 0 and 2. ϑ_i, defined as $1 - e^{-2k''_{zi}t_i}$, corresponds to the exponential variation of the transmission coefficient related to the finite thickness of layer i. If the intermediate layer is a lossless medium, these expressions can be further simplified to give those provided in [Francoeur *et al.* 2010]. Here, we instead consider all layers (along with the semi-infinite media) to be made of the same lossy material. The transmission coefficient obtained at a photon energy of 1.42 eV and for a dielectric function $\varepsilon = 10 + i$ is depicted in Figure 6.7. Several similarities can be found between TM and TE polarisations. Of course, radiation transmitted in the far field is exclusively propagative and thus exchanged within the light cone, i.e. for $k_\rho < n\omega/c$. Decreasing the gap distance leads to an increase in the transmission coefficient for propagative modes - especially close to $k_\rho = n\omega/c$ - and give rise to the transmission of energy through evanescent modes. But while the TE transmission coefficient goes to zero as $k_\rho \to \infty$ for d approaching 0, it goes to a constant non-zero value in the case of TM modes. Consequently, the transmission function $\mathcal{F}$ obtained through integration over k_ρ converges for TE modes as $d \to 0$, but not for TM modes - corresponding to the divergence observed in the more complex systems when considering adjacent layers.

Such a divergence is expected to be caused by non-local effects [Chapuis *et al.* 2008]. In the present work, as in most of the literature on near-field radiation, we have assumed optical properties to be local, i.e. that the movement of dipoles at a given position has no impact at any other position at the same time. While correct in most cases, this hypothesis definitely breaks down when the gap distance goes below the nanometre, and may have a significant impact at larger distances. To take non-local effects into account, the dielectric function must be modified to include dependency on k_ρ [Chapuis *et al.* 2008]. [Joulain 2008] also proposed to replace the Dirac

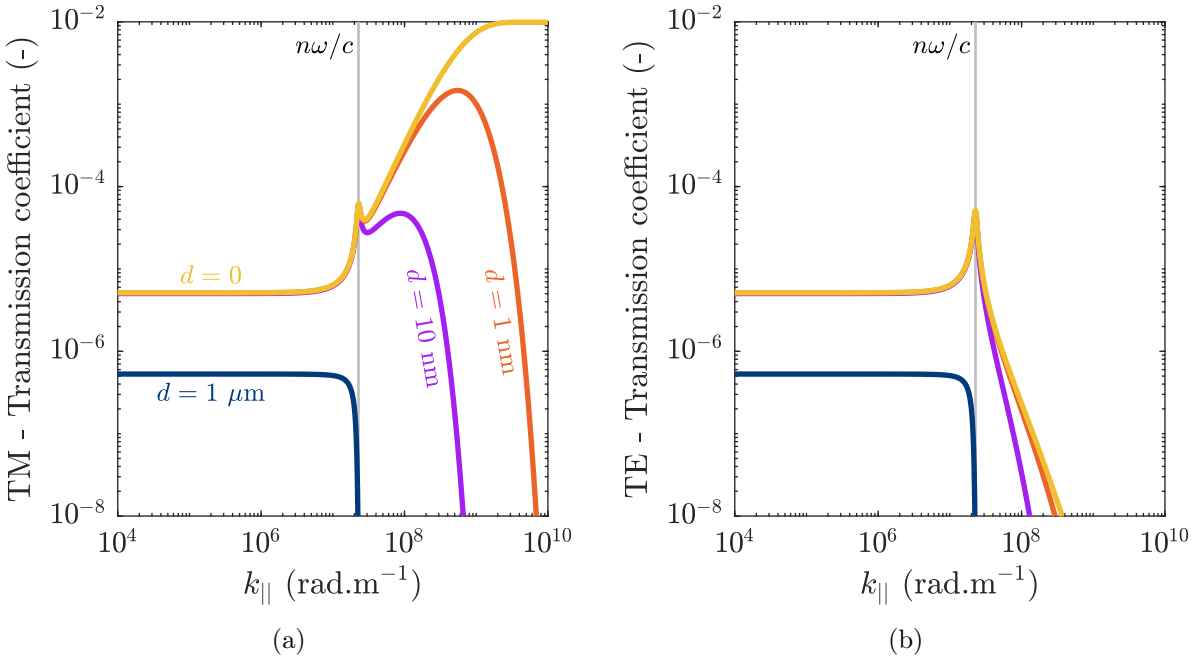

Figure 6.7: Transmission coefficient between two layers separated by a distance d obtained for $\hbar\omega = 1.42$ eV, in an infinite medium with dielectric function $\varepsilon = 10 + i$.

function $\delta(\mathbf{r}' - \mathbf{r}'')$ in the fluctuation-dissipation theorem (see Eq. (1.10)) by a Gaussian function depending on a local distance l. While being a promising solution due to its simplicity, some discrepancies where found in the article, some expressions leading for instance to non-zero heat flux between two media at the same temperature. Additional work would thus be required.

In the studies performed on photon recycling in near-field radiative heat engines, such non-local effects were not taken into account[3]. In the TPV device analysed in [DeSutter *et al.* 2017] for instance, only the emission of the cell towards the emitter is computed from fluctuational electrodynamics, being compared to the internal emission of an isolated cell. In [Callahan *et al.* 2021], only photons which are propagating in the semiconductor (i.e. with $k_\rho < n\omega/c$) are included in the calculations of photon recycling, as they are assumed to gather most of the energy transfer. The paper closest to the aforementioned issues is probably [Aeberhard *et al.* 2021]; however, if they observe the divergence as $k_\rho \to \infty$ and discuss the need for non-local optical properties at large k_ρ, the methodology used to prevent divergence - based on the modification of the Green function and seemingly not related to non-local effects - is to be further analysed.

Unfortunately, we could not further explore the impact of non-local effects on photon recycling; preventing divergence in the transmission function therefore requires setting evanescent modes aside, similarly to [Callahan *et al.* 2021]. Since in the following, we consider only PIN heterostructures in which the two highly-doped barriers are almost transparent to the radiation emitted by the intermediate layer, the net photon flux density occurring inside a component due to the difference of photon chemical potential is weak and therefore has a negligible influence on the performance, as demonstrated in Appendix F.2. Consequently, we still consider the net photon flux density inside a component to be zero in the remaining of the chapter. Nonetheless, the inclusion of non-local effects appears as an interesting development of photon-recycling analyses

[3] In fact, while non-local mechanisms have been dealt with below the bandgap, they do not seem to have been addressed yet for interband transitions.

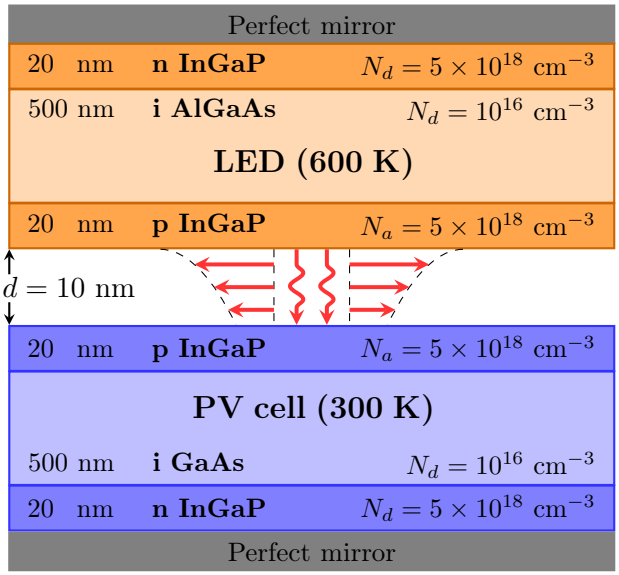

Figure 6.8: Non-optimised heterostructure-based TPX device used to compare the in-house solver with SCAPS.

in near-field radiative heat engines. Also, the exact physical cause of the significant amount of heat transferred through evanescent modes above the bandgap which are observed for TM modes, and which happen in a large bandwidth above the bandgap energy, should be investigated.

6.1.6 Comparison to SCAPS

To conclude this section, we compare results obtained with our in-house algorithm with those from SCAPS for heterostructures. The structure under consideration is shown in Figure 6.8. The LED and the PV cell are supposed to have the same composition for simplicity, the device being not optimised for TPX operation. Since SCAPS cannot take a negative generation rate as an input, we cannot compare results relative to the LED, but studying the PV cell is sufficient to ensure the solver works as expected. In this section, the iterative process on the chemical potential presented in Section 6.1.4 is not applied to make the analysis easier. The radiative quantities must be fed to SCAPS to allow comparison, and are computed from our radiative solver. The generation rate can directly be used in SCAPS; to take the near-field electroluminescent emission of the PV cell into account, the radiative recombination coefficient B is directly computed from the photon emission rate as $B = \dot{N}_{\mathrm{em}}(U = 0)/(n_{\mathrm{i}}^2 t_{\mathrm{PV}})$. The coefficients η and η_t - relative to the change in effective mass at heterointerfaces - are defined as in SCAPS in this section to help comparison. After verification, using our own definition of these parameters does not change significantly the obtained results.

The PV cell I-V characteristic is first presented in Figure 6.9a for different LED voltages. The results from our solver and from SCAPS match well for any of the LED voltage considered, even for $U_{\mathrm{LED}} = 1.15$ V where J_{PV} slowly decreases before reaching U_{oc}. Due to the large current flowing through the device under such illumination, thermionic emission and charge carrier tunnelling have a considerable impact on the charge transport (see Appendix F.3), and the match of I-V characteristics can therefore give confidence in the implementation of these phenomena. For $U_{\mathrm{LED}} = 1.15$ V however, our solver was not capable of converging close to U_{oc} precisely because of the large currents and of the different phenomena occurring. Nevertheless, this is not a significant issue for TPX devices as the PV cell performance is already too low at

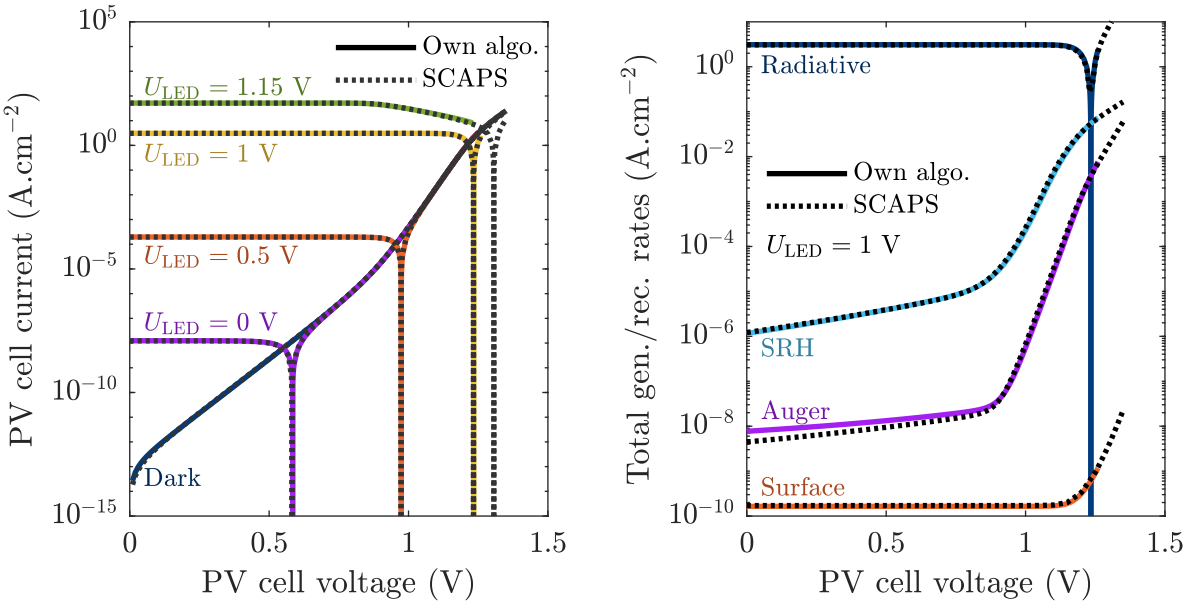

Figure 6.9: Comparison of the PV cell (a) I-V characteristic, (b) total generation-recombination rates obtained with the in-house algorithm and SCAPS considering the structure shown in Figure 6.8.

such voltages to allow efficient TPX operation.

For a more detailed comparison, the variation of the different PV cell generation and recombination rates with PV cell voltage are represented in Figure 6.9b, considering an illumination obtained for $U_{\mathrm{LED}} = 1$ V. The match with SCAPS results is almost perfect for all voltages and all phenomena except for Auger recombinations at low voltage, whose rate obtained by our solver is slightly larger than the one returned by SCAPS - the ratio being almost equal to 2 for $U_{PV} = 0$ V. Under such low biases, Auger recombinations are mostly present in the intermediate layer and close to the interface. Since the charge carrier densities and currents vary rapidly there, the Auger recombination rate is highly sensitive to small differences present between solvers (spatial grid, numerical scheme, etc.), which can cause the observed difference.

6.2 Analysis of TPX devices based on AlGaAs/InGaP heterostructures

We now work on the optimisation and analysis of heterostructure-based TPX devices. As explained previously, the use of heterostructures shall allow for a better separation of charge carriers and therefore reduce the significant impact of surface recombinations. As denoted in Figure 5.21, considering surface recombination velocity of the order of 10^4 cm.s^{-1} - in the range of values found in the literature [Saint-Cast *et al.* 2010, Forcade *et al.* 2022] - completely shatters the performance of the AlGaAs-GaAs TPX device. In this section, we investigate how having InGaP confinement layers - called this way as they are able to confine carriers to specific regions - as highly-doped layers modifies the performance and the charge transport in both components.

6.2.1 Structure optimisation of AlGaAs/InGaP devices

Similarly to the previous chapter, the structure is optimised to obtain a promising architecture. However, we have seen that a device optimised at a 10 nm gap distance may perform very poorly at larger gap distance. On the contrary, since decreasing the gap distance allows to improve the LED QE, we may expect that a device with good performance at 100 nm gap distance will also perform well at lower distances. Therefore, the optimisation is performed at both 10 and 100 nm gap distance, allowing to compare the structures obtained along with the difference of performance at various gap distances.

The device under consideration is illustrated in Figure 6.10a. Each component is supposed to be a PIN heterostructure, the two highly-doped layers being made of InGaP. This material has been chosen as it is the most common ternary III-V semiconductor considered for heterojunction with GaAs. It is lattice-matched with GaAs for a Ga fraction of $x_{\mathrm{Ga}} = 0.51$, at which its bandgap equals approximately 1.9 eV. Since the lattice constant of AlGaAs is constant with the Al fraction, the same Ga fraction is used for the InGaP layers in the LED and the PV cell. Its properties can be found in Appendix B. In the following, we use the term "AlGaAs/InGaP device" to refer to such a device for the sake of brevity, instead of the longer form AlGaAs/InGaP-GaAs/InGaP.

The optimisation is limited to the thickness of the intermediate layers - later named *active layers* since this is where photons get emitted or absorbed - because it was found to have the most critical role on the power output. The thickness of the highly-doped layers is set to 20 nm in both components, which is the value found to be the optimum for the LED in the previous chapter. In fact, these layers only need to be thicker than the depletion region to prevent the semiconductor from being depleted at the metallic contact. Once this is ensured - which is the case for a 20 nm thickness - there is nothing to gain by further increasing these layers, as it would just increase parasitic absorption or non-radiative losses. Their doping level was increased to 10^{19} cm^{-3} as it was found to improve the device performance. While such a high value would have caused Auger recombinations to reduce the power output in the homostructure, it is no longer the case for heterostructures thanks to the low value of n_{i} and rather improves the carrier selectivity of the confinement layers. In fact, larger doping levels could be beneficial, but 10^{19} cm^{-3} could already be difficult to reach and we therefore prefer not further increasing it. In addition, the active layer doping level is set to 10^{18} cm^{-3} in both components to limit SRH recombinations, as discussed at the end of the previous chapter. Because these layers are now significantly doped, we refer to the components as $\mathrm{P^+NN^+}$ heterostructures rather than PIN for clarity, superscript + referring to highly-doped layers.

The active layer thicknesses obtained from the optimisation process are provided in the table of Figure 6.10b. While for an optimisation at a 10 nm gap distance, both thicknesses remain somewhat close to those found with homostructures, we notice a clear decrease in the optimal thicknesses for a 100 nm gap distance. Regarding the LED especially, the active layer is thinned down by factor 4, becoming as narrow as 40 nm. To understand why an LED that small makes the power output optimum, we show in Figure 6.11 the power output obtained for different couples of active layer thicknesses at 10 and 100 nm, which correspond to the different nodes tested during optimisation[4]. Since the optimisation is performed with rough meshes, the values provided in this figure should only be regarded as estimates. Still, two distinct trends appear

[4]One may notice the different couples considered during optimisation are placed on straight lines in Figure 6.11. This is because we forced these thickness couples to be chosen in a provided grid to prevent unnecessary refinement of the optimal thicknesses and improve the coverage of the thickness space. This allows to significantly reduce the optimisation computational time.

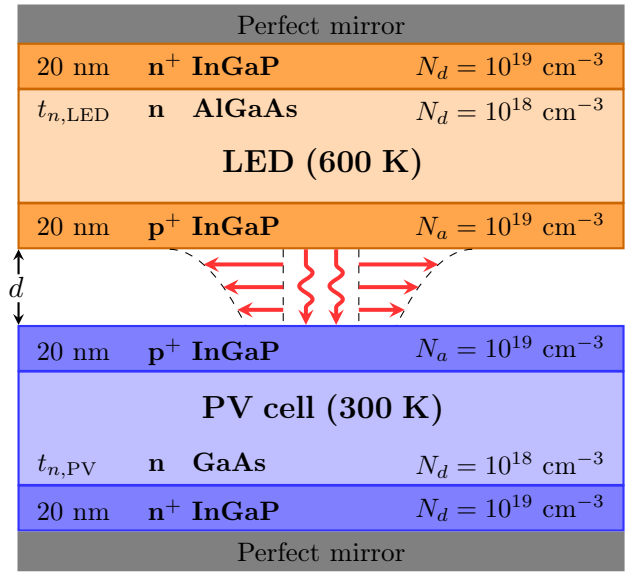

(a)

	Opt. at 10 nm	Opt. at 100 nm
$t_{n,\mathrm{LED}}$	180 nm	40 nm
$t_{n,\mathrm{PV}}$	750 nm	360 nm

(b)

Figure 6.10: (a) Heterostructure-based AlGaAs/InGaP TPX device considered for optimisation. (b) Result of the active layer thickness optimisation.

for the gap distances. At 10 nm (Figure 6.11a), the power output mainly depends on the LED thickness, being maximum at 180 nm. Looking at the variation of power output with LED active layer thickness around the optimum in Figure 6.11c, we can observe some oscillations with a period of the order of 100 nm, which are related to coherence effects. However, these effects only impact moderately the power output, the global trend being that the maximum power output increases up to an optimum LED active layer thickness, before starting to decrease. At this active layer thickness, the LED quantum efficiency is maximised: this optimum thus comes from a trade-off between radiative and non-radiative recombinations. In contrast, P_{max} is almost constant with $t_{i,\mathrm{PV}}$, showing for instance only 10% variations for $t_{i,\mathrm{PV}}$ between 0.3 and 1 μm considering $t_{i,\mathrm{LED}} = 180$ nm. In fact, both $(t_{i,\mathrm{LED}}, t_{i,\mathrm{PV}})$=(180 nm, 360 nm) and (180 nm, 750 nm) can be regarded as global maxima as the maximum power output is almost similar. We have chosen the latter as it led to the best performance at 100 nm.

In comparison, the region of maximised power is very localised for a 100 nm gap distance (Figure 6.11b), power being decreased by a factor 2 or 3 as thicknesses deviate from the optimum. Such a precise requirement on the thicknesses is typically the sign of a radiative resonance caused by coherence effects, a change in thickness of a few nanometres greatly modifying the heat transferred between the LED and the PV cell. To verify this, we show in Figure 6.12 how the radiative transmission coefficient between the LED and the PV cell in normal incidence varies with the photon energy. For a 100 nm gap distance (Figure 6.12b), we can indeed observe a resonance close to the bandgap energy of the active layers for the 100-nm-optimised device, while resonances occur at larger photon energies for the 10-nm-optimised device. Because of this difference of transmission, and although the LED of the latter device is much thicker, the thermal above-bandgap radiation exchanged between the components is in fact similar in both devices. In the previous chapter, we have highlighted the importance of near-field effects for reaching QEs enabling the performant operation of TPX devices. Here, we also notice that coherence effects have a strong impact on the TPX performance in the moderate near field. While these coherence effects allow for a significant increase in power output at 100 nm gap distance, we shall

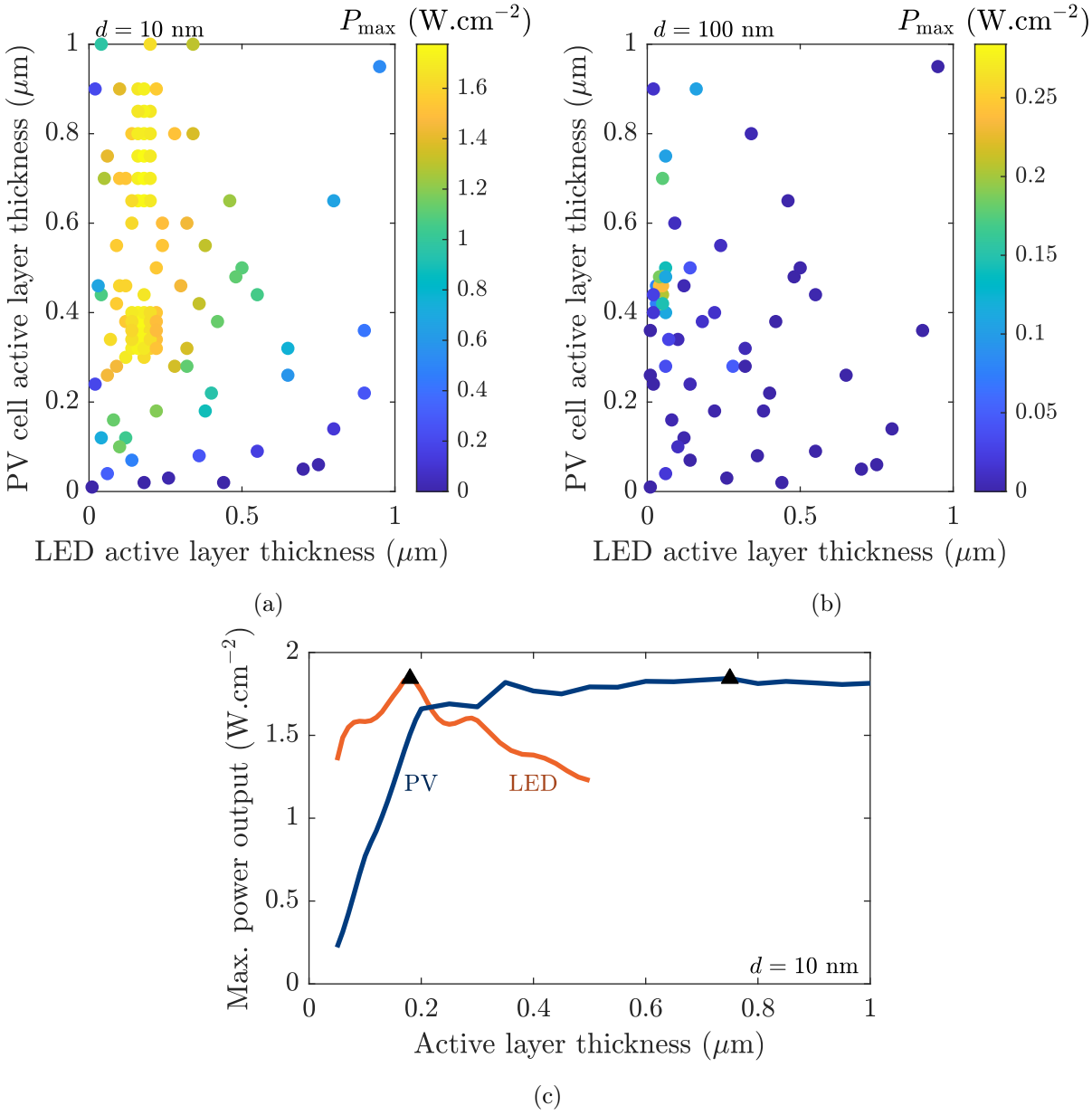

Figure 6.11: Power output estimate for different couples of active layer thicknesses, given by the optimisation process (a) at 10 nm, (b) at 100 nm. In (c) is given the variations of power output with active layer thicknesses at a 10 nm gap distance, around the optimum denoted by the markers.

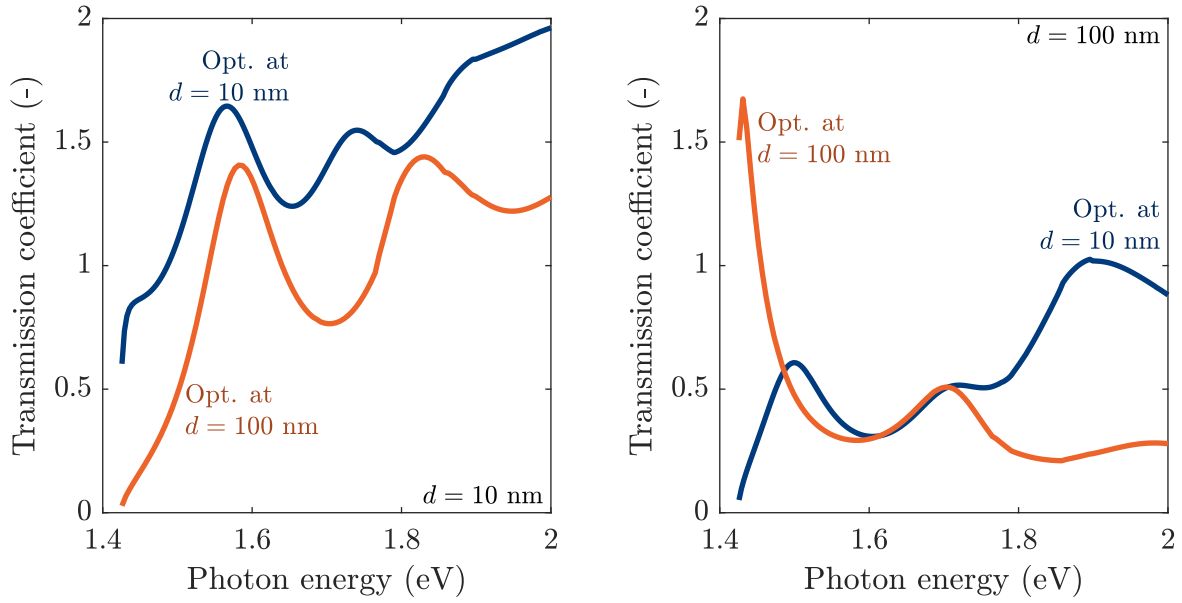

Figure 6.12: Transmission coefficient of radiation between the LED and the PV cell at normal incidence and for a gap distance of (a) 10 nm, (b) 100 nm. Since we consider unpolarised light, the transmission coefficient is equal to the sum of TM and TE transmission coefficients and is therefore bounded by 2.

however mention that the high thickness dependency along with the thinness of the LED may make the 100-nm-optimised device difficult to develop experimentally - at least, more than the 10-nm-optimised device.

6.2.2 Performance of optimised AlGaAs/InGaP heterostructures

We show in Figure 6.13 the P-V_{LED} characteristic of the two optimised devices, which are mostly similar to one another. For a 10 nm gap distance, both are capable of generating electrical power for the whole range of LED voltage - although a local minimum is reached in the low-voltage range for the 100-nm-optimised device. Even if this device can operate as a TPX engine for larger LED voltages than the 10-nm-optimised device, the energy transferred through radiation between the LED and the PV cell remains limited due to the low LED thickness and the power output is therefore lower than that of the other device for most voltages. Its maximum power output equals 1.1 W.cm^{-2} (reached for $U_{LED} = 1.16$ V and $U_{PV} = 1.26$ V), against 1.8 W.cm^{-2} for the 10-nm-optimised device ($U_{LED} = 1.14$ V, $U_{PV} = 1.24$ V). We can also observe that the change in characteristic from 10 to 100 nm is quite different for both devices. While the LED voltage at maximum power remains almost the same for the 100-nm-optimised device, it is reduced by almost 0.1 V for the 10-nm-optimised device. Consequently, the decrease in power output observed in the latter device at 100 nm, caused by the combined reduction of the thermal above-bandgap heat flux density and of the LED voltage at maximum power, is much more important, dropping by a factor 35 down to $P_{max} = 4.7 \times 10^{-2}$ W.cm^{-2}. In comparison, P_{max} only decreases by a factor 3.5 for the 100-nm-optimised device, being equal to 0.32 W.cm^{-2}. However, neither of the two devices are capable of generating power in the low-voltage range for $d = 100$ nm, once more because of SRH recombinations. As in the case of homostructures, they become eventually unable to operate as a TPX engine as we move towards far-field conditions.

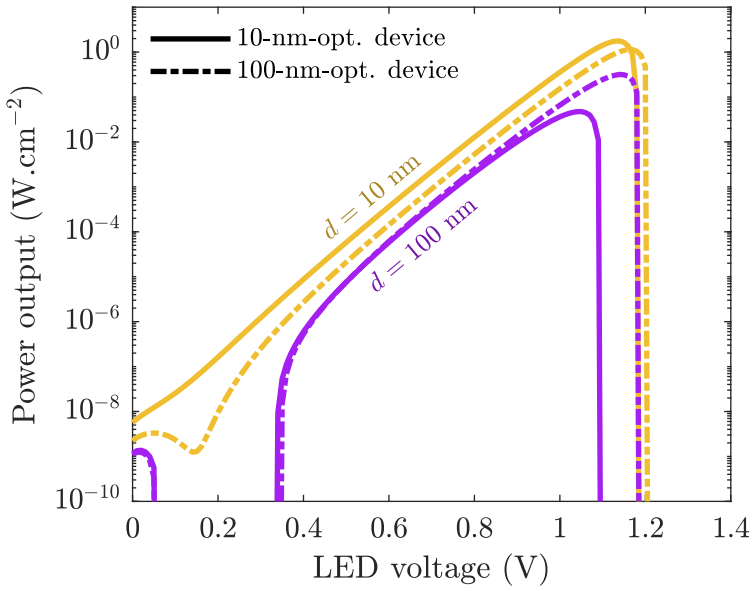

Figure 6.13: P-V_{LED} characteristic of the two optimised TPX devices, at 10 and 100 nm gap distance.

The maximum power output obtained for these two devices at 10 nm are of the same order of those from Chapter 5. However, these new results were obtained with surface recombination velocity 100 times larger, for which the optimum device of Chapter 5 was not working. This highlights the performant charge separation operated by the two confinement layers, which limits the surface recombination rate. Of course, such layers only reduce the effect of surface recombinations, but do not cancel it. For surface recombination velocities of 10^5 cm.s^{-1} for instance, the maximum power output of the 10-nm-optimised device at 10 nm decreases to 1 W.cm^{-2} - the reduction being therefore significant, but reasonable.

6.2.3 Impact of the heterojunction model on TPX performance

To obtain the different results mentioned above, the thermionic-field emission model was considered, and an iterative procedure was implemented for the chemical potential of each layer. We analyse in Figure 6.14a how the P-V_{LED} characteristic of the 10-nm-optimised device changes if, instead of considering a thermionic-field emission model (hence both thermionic emission and charge carrier tunnelling), we only include thermionic emission (TE) or even assume that quasi Fermi levels are continuous at heterointerfaces. For low or even moderate LED voltages, we have seen in Figure 6.6 that the variations of the difference of quasi Fermi levels at interfaces remains limited; therefore, all three models are mostly identical and provide similar power output. But around $U_{LED} = 0.9$ V, the curve relative to thermionic emission suddenly stops, caused by a lack of convergence for larger LED voltages. In fact, this occurs also with the continuity approximation, this time for $U_{LED} = 1.13$ V. While the thermionic-field emission model is the most complex of all three, it is in fact the one achieving the best convergence. We suspect the convergence issues in the two other models to come from the following reason:

- the use of the continuity approximation forces the variation of quasi Fermi levels at the interface to be zero, and therefore locks a degree of freedom, making the convergence more difficult to reach;
- if the current flowing at a heterointerface is written as $J_i = G_i \Delta\Phi_i$, the term G_i is much

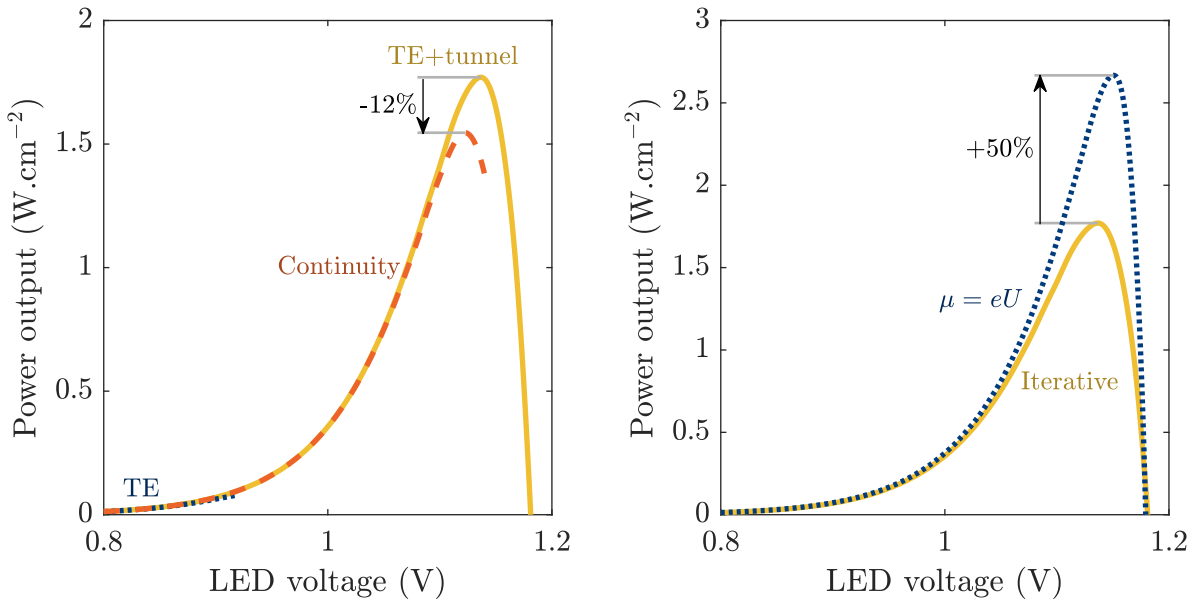

Figure 6.14: Influence of (a) the heterojunction model, (b) the iterative resolution of the photon chemical potential on the P-V_{LED} characteristic of the 10-nm-optimised TPX device.

lower in the case of thermionic emission than for thermionic-field emission (see Eq. (6.12)); therefore, a similar current will give rise to a larger change in Φ_i, which can eventually make it negative and cause a divergence which sometimes cannot be solved by the secondary iterative process introduced in Section 6.1.3.

With the continuity approximation, a maximum is reached before divergence and can therefore be compared to the one obtained with the complete resolution. We observe a reduction of 12% of the maximum power output when considering the continuity approximation. Therefore, such an approximation can be used to get qualitative results, but deviates too much from the full model to be considered quantitative.

We also provide in Figure 6.14b the influence of the chemical potential iterative process on the TPX characteristic. As for the previous study, the change of power output at moderate voltage is negligible at low voltage, the spatial variation of $E_{Fn} - E_{Fp}$ being mostly negligible. But for large voltages, the discontinuities at interfaces become significant and cause a large diminution of the power output when included in the radiative calculations. Indeed, we find out that using the $\mu = eU$ approximation causes the maximum power output to be overestimated by 50%. As for the continuity approximation, assuming $\mu = eU$ may allow to obtain an idea of the order of magnitude of the maximum power output, but is not quantitative.

6.2.4 Charge transport at maximum power point

We end this section by investigating how the use of heterostructures changes various spatially-resolved quantities in the LED in the PV cell. In Figure 6.15 is provided the band diagrams obtained at MPP for both components. They appear to be mostly similar to those obtained in the previous chapter for homostructures. However, by looking in detail, we can notice the slight changes of the quasi Fermi levels in the PV cell confinement layers, which are not as constant as for homostructures. The discontinuities at heterointerfaces are only faintly distinguishable, being

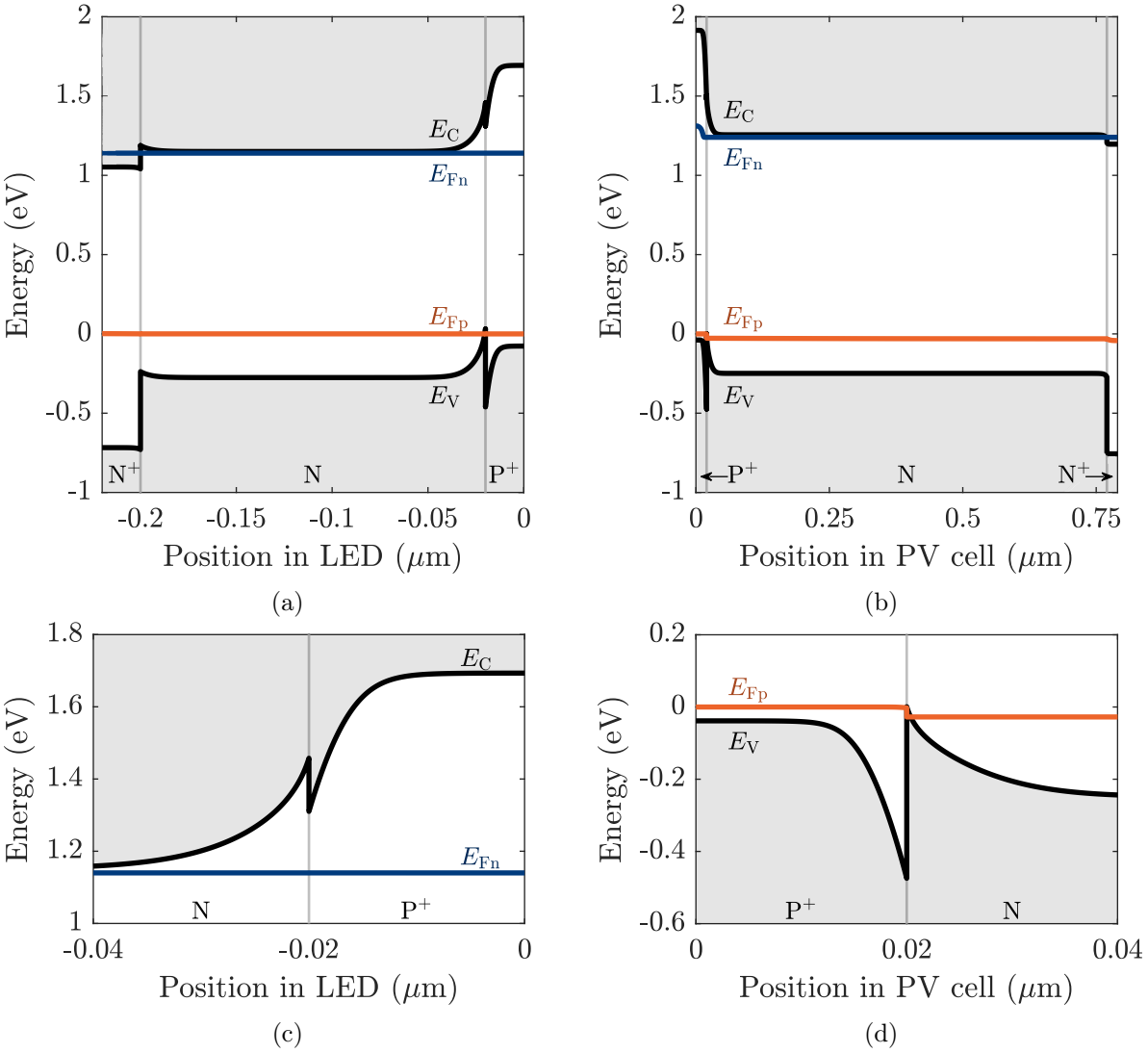

Figure 6.15: Band diagrams at maximum power point (a) in the LED, (b) in the PV cell. Panels (c) and (d) display a zoom of the band diagrams around the $P^+ - N$ interface, respectively in the LED (for electrons) and the PV cell (for holes).

at most of the order of a few tens of meV.

We also show in Figure 6.16 the variation of electron and hole current densities in both components at MPP. At the electrical contact at which carriers are in minority, the related current density are directly related to the surface recombination rate, and are therefore close to 0 for this device thanks to the efficient carrier separation. As we get away from the contact, current densities increase in absolute value, either because of the cumulated generation or recombination of charge carriers. In any device, the total current must remain spatially constant. Here, the total drift-diffusion current varies close to interfaces, where it is even discontinuous. In these regions, a fraction of the charges tunnels through the potential barriers caused by the heterointerface, and the corresponding part of the drift-diffusion current becomes a tunnelling current - up until the charges emerge from the barrier. Summing drift-diffusion and tunnelling current gives as expected a constant total current density.

Looking specifically to the tunnelling current, we can notice several differences between electron

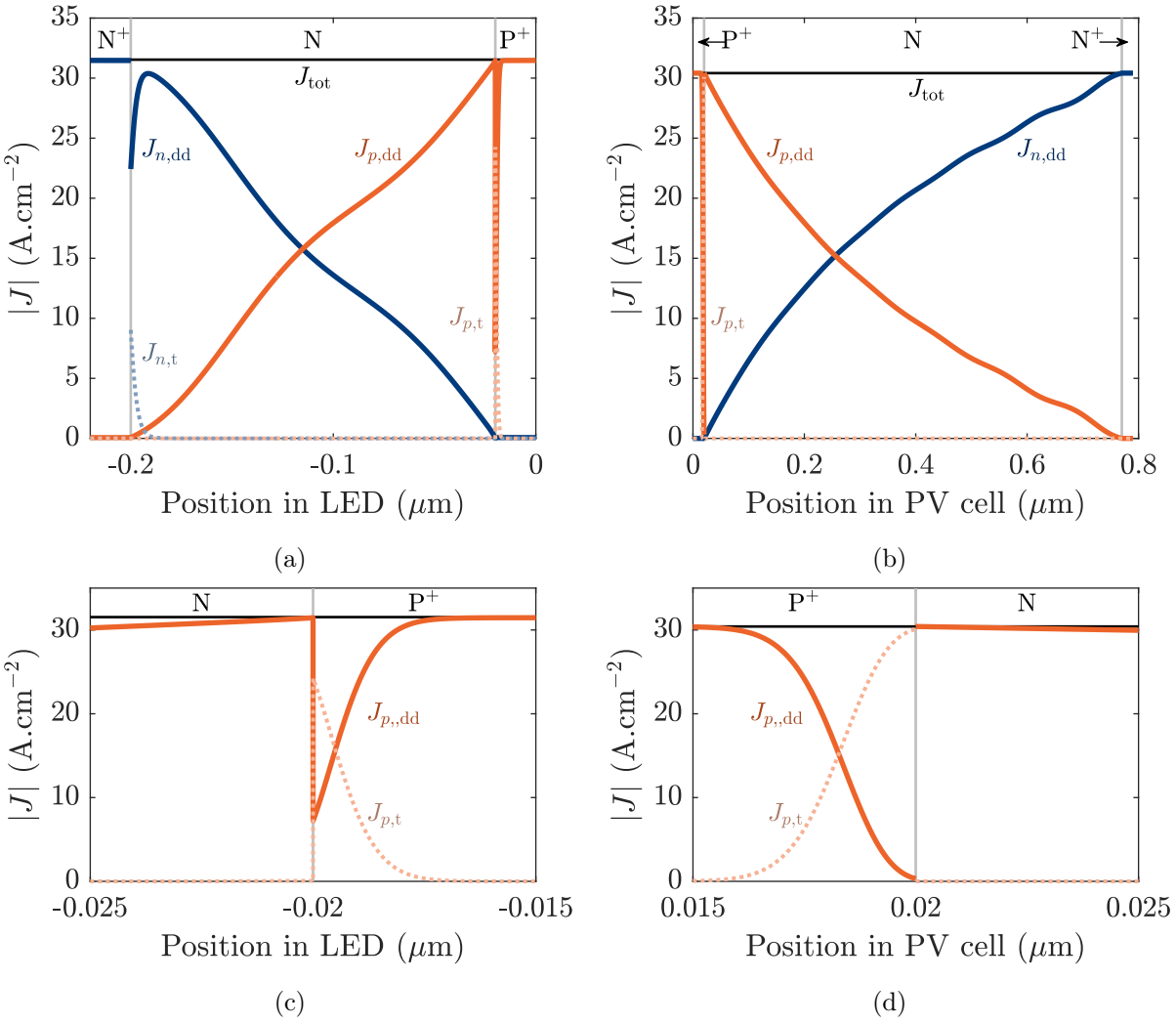

Figure 6.16: Spatially-resolved electron and hole current densities related to drift and diffusion (subscript dd) or to tunnelling (subscript t) at maximum power point (a) in the LED, (b) in the PV cell. Panels (c) and (d) correspond to a zoom of panels (a) and (b) around the interface where hole tunnelling occurs.

and holes. The first difference is related to the influence of tunnelling in the charge flow, which is much more important for holes as most of the charges tunnel through the P-I interface: this is visible by the preponderant share of the tunnelling current in the total hole current. In comparison, tunnelling plays a lesser role for electrons, especially in the PV cell in which it cannot be observed. This is a consequence of the potential barrier height. As this quantity increases (in absolute value), the classical flow of charges in the bands is more and more disturbed, and the transmission of charges through the interface must therefore increasingly rely on tunnelling effects. For electrons, the barrier height equals $\Delta\chi$, which is around 15 meV for the GaAs/InGaP interface and around 0.15 eV for the AlGaAs/InGaP interfaces. In comparison, it is equal to $\Delta\chi + \Delta E_g$ for holes, corresponding to an almost 0.5 eV barrier height at GaAs/InGaP and AlGaAs/InGaP interfaces, therefore greatly impacting the hole flow.

The second difference is related to the penetration depth of charges in potential barriers. Indeed, we can observe that the hole tunnelling current decays much more quickly than the electron tunnelling current as we move away from the interface: most of the hole tunnelling occurs within

a few nanometres, against 10 to 20 nm for electrons[5]. This is related to the effective mass of the carriers: holes being much heavier than electrons, their transmission coefficient (given in Eq. (6.9)) decreases faster with the distance. This makes tunnelling less effective for holes than for electrons.

6.3 Towards more realistic and performant TPX devices

6.3.1 Temperature and alloy fraction dependency of non-radiative recombination coefficients

As we have seen, the use of InGaP for confinement layers allows improving carrier separation and therefore enables to relax the assumption of low surface recombination velocity made with homostructures. However, this is not the sole idealising assumption made in the previous chapter regarding non-radiative recombinations. Indeed, we assumed up until now the SRH and Auger recombination coefficients of AlGaAs to be independent of the temperature and the Al fraction, thus equal to those of GaAs at room temperature - as in the existing literature on thermophotonics (see e.g. [Zhao *et al.* 2018]). This was done for several reasons. As with the assumption of low surface recombination velocity, it limits non-radiative recombinations and make it easier to obtain a performant device for preliminary studies. But it is also very difficult to find precise and trustworthy data which include these different dependencies. LEDs and PV cells have been almost exclusively studied at room temperature, and the few studies at high temperature made for PV cells [Vaillon *et al.* 2020] have focused on their performance rather than on the material properties of the semiconductors. Regarding composition dependency, it is already difficult to obtain data for common alloys at room temperature (e.g. InGaP lattice-matched to GaAs), and becomes almost impossible for alloys with unusual composition (such as AlGaAs with 12.1% Al). Nonetheless, these dependencies are mostly detrimental to the performance, and we shall therefore try to implement a simple model to include them. Since we expect the non-radiative recombinations in the confinement layers to be limited, we suppose for simplicity that the non-radiative coefficients in InGaP remain independent of the temperature and the Ga fraction.

By mixing aluminium and gallium to obtain AlGaAs, the density of traps inside the bandgap increases in comparison to pure GaAs, as it makes the lattice more imperfect. Therefore, SRH recombination lifetime should be largely impacted by semiconductor alloying. Taking the data provided in [Quay 2001] for instance, we found the SRH lifetime for electrons to be equal to few μs for GaAs but only to few tenths of ns for AlGaAs - no dependency on the aluminium fraction being given. In comparison, we expect the Auger recombination coefficient to be relatively unaffected by these new traps, hence by alloying; we assume in the following that they are perfectly independent of the aluminium fraction[6]. Since the data given in [Quay 2001] is not precise, we prefer in the following to manually try out different values for the SRH recombination lifetime in AlGaAs.

We show in Figure 6.17a how the TPX power output and the LED QE changes when the SRH recombination lifetime in AlGaAs is set to 100 ns instead of the value in GaAs ($\sim$ 3 μs). As expected, the LED QE drops mainly in the low-voltage range, in which SRH recombinations are expected to significantly impact the charge flow. Consequently, no electrical power can be extracted there. But while the effect on the LED QE is less pronounced at higher voltage, it is

[5] With these penetration depths in mind, the use of a distance cut-off of 50 nm in integration is more than enough to include almost all the carriers tunnelling.

[6] In fact, looking at the data given in [Levinshtein *et al.* 1999] for AlGaAs, the Auger recombination coefficients may slightly decrease for increasing Al fraction, changing favourably the component performance.

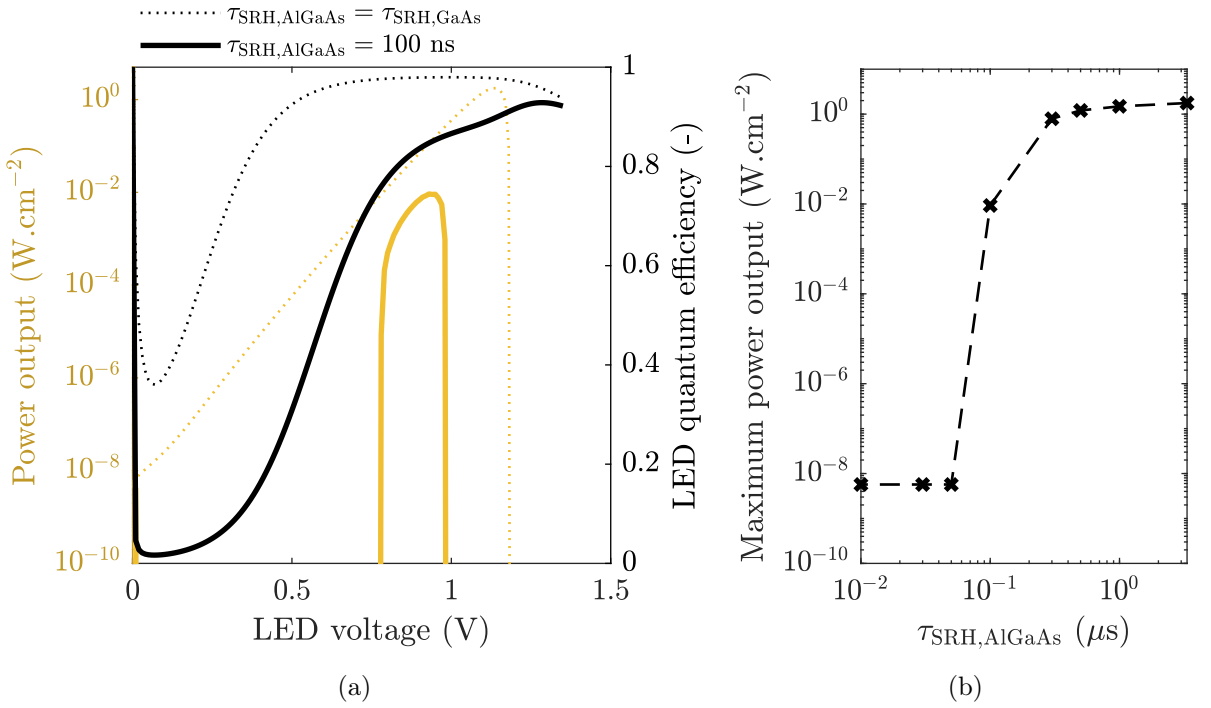

Figure 6.17: Influence of the SRH lifetime in AlGaAs (a) on the P-V_{LED} TPX characteristic, (b) on the maximum power output.

enough to significantly reduce the TPX device power output. Consequently, the maximum power output drops by a factor 180 down to 9×10^{-2} W.cm^{-2}, the LED voltage at maximum power having decreased by 0.2 V. Of course, this reduction becomes larger and larger as the AlGaAs lifetime gets lower, up to the point were the device cannot operate as a TPX heat engine any more and works instead as a TPV device. This can be observed in Figure 6.17b: for $\tau_{SRH,AlGaAs}$ between 50 and 100 ns, the power output drops and becomes constant as the lifetime is further decreased, $\tau_{SRH,AlGaAs}$ having no longer any impact since the LED is now passive. Even if the data given in [Quay 2001] are rough and could lead to an underestimated value of AlGaAs SRH lifetime, the value of $\tau_{SRH,AlGaAs}$ it provides is orders of magnitude lower than the threshold value of Figure 6.17b, and this low value of the SRH lifetime in the LED active layer may very well prevent the device to operate properly.

We now study the influence of temperature dependency. Regarding SRH recombinations, two different models can be found in the literature. The SRH lifetime related to carrier i can be expressed as $\tau_{SRH,i} = [N_t \sigma_i v_i]^{-1}$, where N_t is the trap density, σ_i is the capture cross-section associated to carrier i and v_i its thermal velocity. Since $v_i = \sqrt{3k_B T/m_i^*}$, one possibility is to assume that $\tau_{SRH,i} \propto T^{-1/2}$. This is for instance what is done in SCAPS or in [Gonzalez-Cuevas *et al.* 2006]. It is also possible to find that $\tau_{SRH,i} \propto T^{-3/2}$ in the literature [Schenk 1992, Quay 2001]. In the following, we use the latter model to maximise the potential effect of temperature. For Auger recombinations, we have not found any promising model for the dependency. In [Quay 2001], it is mentioned that the temperature dependency of the Auger recombination coefficient of silicon can be fitted with a simple power law, typically as $C_{n/p} \propto T^{0.5}$. As a first guess, we will therefore use a similar power law for the GaAs alloys considered in this section, however with a different exponent as it varies from one material to another. Using the estimates provided in [Levinshtein *et al.* 1996] for GaAs ($C_{n/p} \sim 10^{-30}$ cm^{-6} and $\sim 10^{-29}$ cm^{-6} for $T = 300$ K and 500 K respectively), we obtain a variation close to T^5 assuming monomial dependency. In contrast,

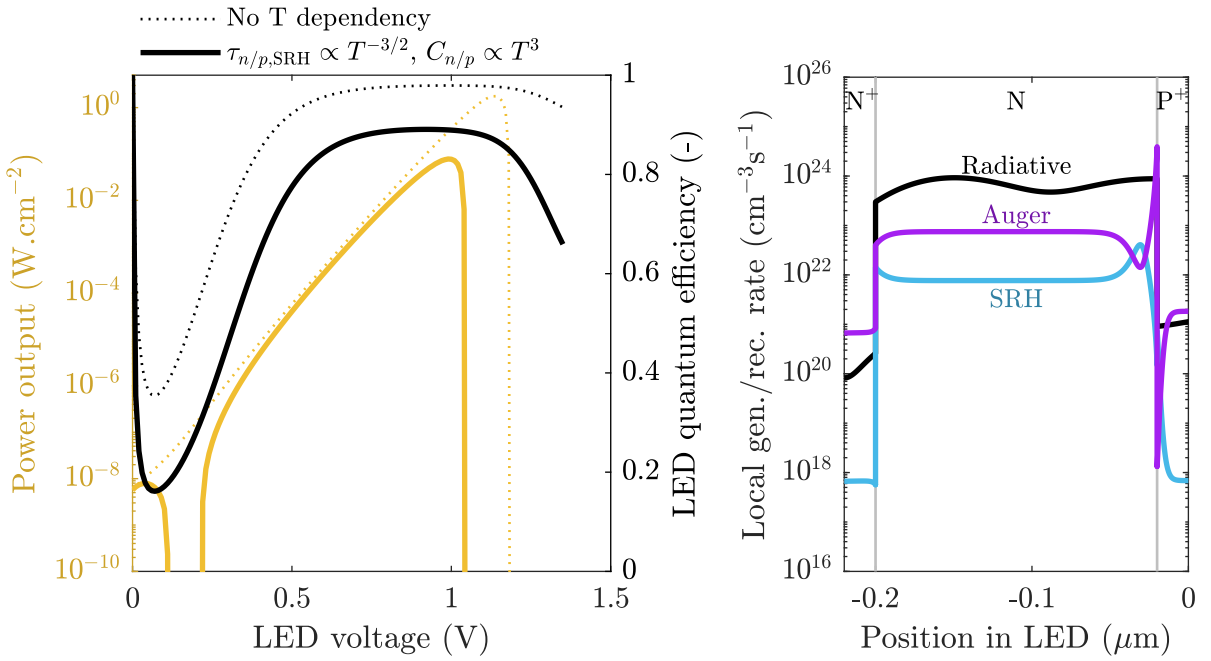

Figure 6.18: Impact of the inclusion of temperature dependency for non-radiative recombination coefficients on (a) the P-V_{LED} TPX characteristic, (b) the local generation and recombination rate in the PV cell at MPP.

data presented on AlGaAs in [Takeshima 1985][7] lead to $C_n \propto T^{2.5}$ and $C_p \propto T^{1.5}$. Therefore, there is a significant variability of the data found in the literature. In the following, we assume that both C_n and C_p vary as T^3, the exponent being an estimate chosen as a compromise between the various values mentioned above. It would be instructive to analyse the sensitivity of the TPX figures of merit to this exponent in future work.

The effect of the temperature dependency of non-radiative recombination coefficients on the TPX device performance is illustrated in Figure 6.18a. Clearly, the change of $\tau_{n/p,\mathrm{SRH}}$ and of $C_{n/p}$ with temperature causes a sizeable drop of the LED QE, which is of the order of 0.1 for most voltage but increases up to almost 0.3 for largest voltages. This decrease is mostly due to Auger recombinations, whose rate becomes of the order of the radiative recombination rate for any LED voltage. This can for instance be observed at MPP: as illustrated in Figure 6.18b, the Auger recombination rate, which is already globally high in the active region, peaks at the P$^+$-N interface on the active layer side. It is caused by the large hole barrier present at the interface, which causes the hole concentration there to be orders of magnitude larger than in the P$^+$ confinement layer. Eventually, this leads to a decrease of the maximum power output by a factor 20, down to 8×10^{-2} W.cm^{-2}.

6.3.2 InGaAs/InGaP heterostructures for robust TPX devices

Taken individually, both temperature and composition dependencies impact drastically the power output. When coupled, we can therefore expect the AlGaAs/InGaP device to be hardly capable of operating as a TPX engine: a more robust device shall therefore be developed. To mitigate

[7] In [Takeshima 1985], the Auger recombination coefficients are fitted with $C \propto \exp(\alpha T + \beta T^2)$. However, the origin of such a model was not found.

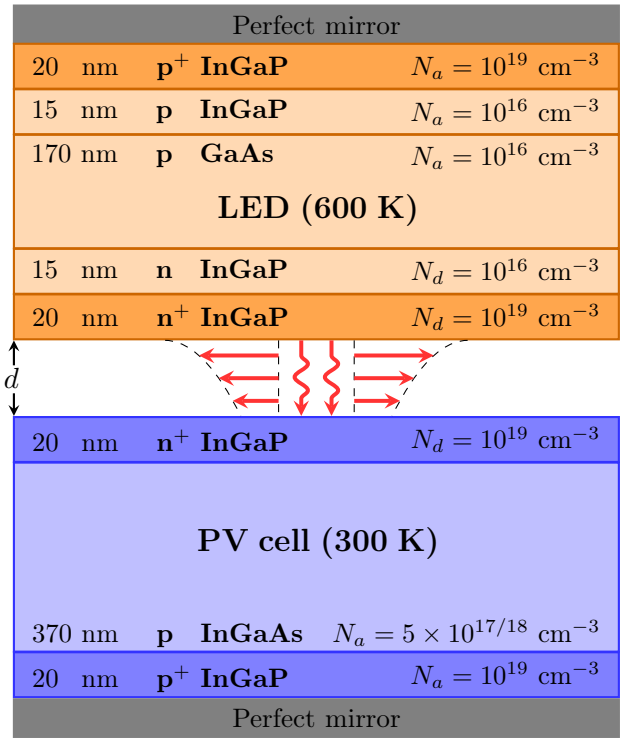

Figure 6.19: Proposed InGaAs/InGaP TPX structure for the reduction of non-radiative recombinations.

the effect of non-radiative recombinations, we propose a new structure which is shown in Figure 6.19. Two main adjustments are made.

- To prevent excessive SRH recombinations in the LED due to the low SRH lifetime in AlGaAs, the active layer is now made of GaAs. To ensure bandgap matching, the PV cell is consequently made of InGaAs. While this will cause a decrease of the PV cell quantum efficiency, we have seen that the influence of the PV cell QE on the power output is less dramatic than that of the LED QE. This change should thus improve the overall TPX performance. Regarding the active layer bandgap energy, it is no longer equal to 1.42 eV and even becomes dependent on the heat source temperature. For $T_{\mathrm{LED}} = 600$ K, it is equal to 1.28 eV, the fraction of In in the PV cell active layer being close to 9%.
- Two thin low-doped InGaP layers were added in the LED between the active layer and the highly-doped layers. These layers allow decreasing the rate of Auger recombinations by greatly reducing the majority carrier concentration in the active layer at the interface with InGaP. Figure 6.18b clearly points out that this is especially important at the interface with p-doped InGaP, and the low-p-doped InGaP is indeed the most beneficial of the two. Still, adding the low-n-doped layer slightly improves the overall performance, and is therefore conserved in the structure. Their thickness is set to 15 nm, which allows covering most of the depletion region around MPP. The addition of such layers in the PV cell was however found to be detrimental to the performance, and the PV cell thus remains a three-layer structure.

In the LED, the doping level of the active layer and of the low-doped InGaP layers is set to 10^{16} cm^{-3}, these layers being thus almost intrinsic: for this component, doping them do not improve the performance of the device as SRH recombinations are not the main limiting factor.

On the contrary, the InGaAs active layer of the PV cell is significantly doped to limit SRH recombinations: the doping level is equal to 5×10^{17} cm^{-3}, except if the decrease of τ_{SRH} related to the non-zero In fraction is included, in which case it is further increased to 5×10^{18} cm^{-3}. In the latter case, τ_{SRH} is supposed to be equal to 10 ns which is of the order of the values obtained for InGaAs using the data from [Quay 2001]. Since a peak of local SRH recombination rate is observed in the active layer close to the $N^+ - P$ interface, the solution proposed in [Santhanam *et al.* 2020] and briefly discussed in the end of Chapter 5 - based on the control of the dopant profile close to the heterointerface - could help to further improve the PV cell performance. However, this peak only represents a minor share of the total SRH rate, and the QE improvement would therefore be limited. Consequently, this solution will not be included here for the sake of simplicity. One can also notice that the n-doped layer is now in front of both components. While this change does not significantly improve the maximum power output, it is done preventively as having the n-doped layer in front shall allow limiting resistive losses related to the lateral flow of charges towards the electrical contact (which must be a thin grid at the front to prevent excessive shadowing).

To choose the thickness of the active layers, an optimisation process similar to the one used previously for the AlGaAs/InGaP device is used. However, to ensure the reliability of the device, the optimisation is performed both at 10 and 50 nm gap distances, and both with and without the temperature and composition dependencies of the non-radiative recombination coefficients. The active layer thicknesses are then set arbitrarily to the values which lead to the best compromise in terms of maximum power output in these different operating conditions. This resulted in an active layer thickness of 170 nm in the LED and 370 nm in the PV cell. The LED active layer thickness is close to the one found for the AlGaAs/InGaP device. While a 70 nm thick active layer leads to quite similar performance, we expect an LED that thin to be more sensitive to losses that are not included here (e.g. parasitic absorption) and therefore stand to the 170 nm thick layer. The PV cell active layer is however twice thinner than in the previous case, as a consequence of the excessive rate of SRH recombinations occurring for thicker layer when $\tau_{\mathrm{SRH,InGaAs}} = 10$ ns is considered.

The characteristic of the InGaAs/InGaP device is displayed in Figure 6.20, along with the LED quantum efficiency at zero PV cell voltage. When none of the dependencies mentioned above are included, the characteristic is mostly similar to that of the AlGaAs/InGaP device, the maximum power output being equal to 1.7 W.cm^{-2}. Because of the smaller active layer bandgap energy in the InGaAs/InGaP device, voltages at MPP are lower than in the case of the AlGaAs layer, with $U_{\mathrm{LED,MPP}} = 1.01$ V and $U_{\mathrm{PV,MPP}} = 1.11$ V. However, $E_g - eU_{\mathrm{LED,MPP}}$ and $E_g - eU_{\mathrm{PV,MPP}}$ are almost the same in the AlGaAs/InGaP and InGaAs/InGaP devices, and are respectively close to 0.28 eV and 0.18 eV. This was partly expected, as the power output is directly related to the electroluminescent radiation exchanged between the LED and the PV cell, which itself depends on $\exp((E_g - eU_{\mathrm{LED}})/k_{\mathrm{B}}T_{\mathrm{LED}})$ and $\exp((E_g - eU_{\mathrm{PV}})/k_{\mathrm{B}}T_{\mathrm{PV}})$ under Boltzmann's approximation. Since maximum power output is similar in both devices, it is not a surprise that the terms $E_g - eU_{\mathrm{MPP}}$ also are.

As in the case of the AlGaAs/InGaP device, including the temperature dependency of the non-radiative recombination coefficients causes a significant decrease of the LED QE at low LED voltage. However, the drop at larger voltage - especially close to the maximum QE - is mitigated thanks to the intermediate InGaP layers, QE dropping only by few percent points around MPP. Consequently, the maximum power output is only reduced by half - instead of 95% for the AlGaAs/InGaP device - and equals 0.77 W.cm^{-2}. The further addition of composition

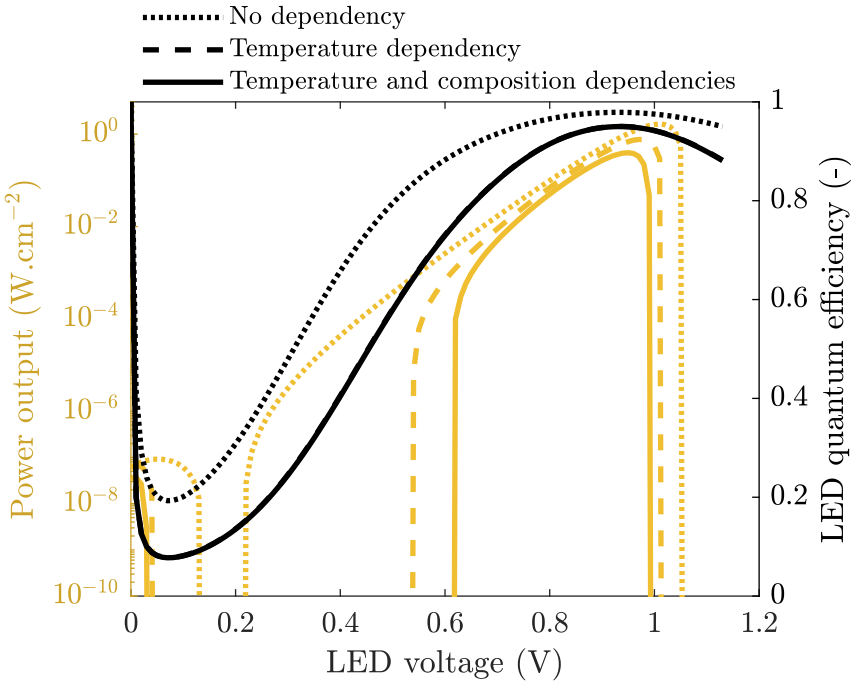

Figure 6.20: P-V_{LED} characteristic of the structure illustrated in Figure 6.19 for different scenarios, along with the LED QE at zero PV cell voltage.

dependency does not change the LED QE, since it only modifies the SRH recombination lifetime in InGaAs. While such a low value of τ_{SRH} caused the AlGaAs/InGaP device to be inoperable - even without temperature dependency - the InGaAs/InGaP device is still able to reach a maximum power output of 0.4 W.cm^{-2}, representing approximately 25% of the maximum power obtained when no dependencies are included.

To complete the analysis of the device, the variations of maximum power output with the gap distance and the heat source temperature are presented in Figure 6.21. Looking first at the influence of the gap distance (Figure 6.21a), the trends obtained with the different scenarios are mostly similar. The lower QEs obtained when including temperature and/or composition dependencies, which cause a decrease in maximum power output at a given gap distance, also lower the gap distance at which power output drops due to the disappearance of the true-TPX PPR: initially close to $d = 180$ nm, it goes down to 70 nm with both dependencies included. Incidentally, we can notice that thanks to the different modifications made in the device, it remains quite performant even in the moderate near field ($d = 100$ nm) when no dependency is included, with a maximum power output of 0.2 W.cm^{-2}.

The variations of maximum power output with heat source temperature are however quite different between the scenarios. When no dependencies are included, the maximum power output increases smoothly, although the increase rate becomes lower as the heat source temperature increases. In fact, it reaches an inflection point for T_{LED} close to 525 K. This happens also when temperature dependency is considered, but at an LED temperature of 500 K only. Roughly speaking, it means that it becomes more interesting to increase the surface than the heat source temperature above these temperatures: to make the most out of the temperature difference in these two scenarios, the device should probably operate with a heat source temperature between 500 and 550 K. While the influence of temperature dependency is reduced in this range of temperatures, the effect of considering a low SRH recombination lifetime in InGaAs however becomes dramatic: at

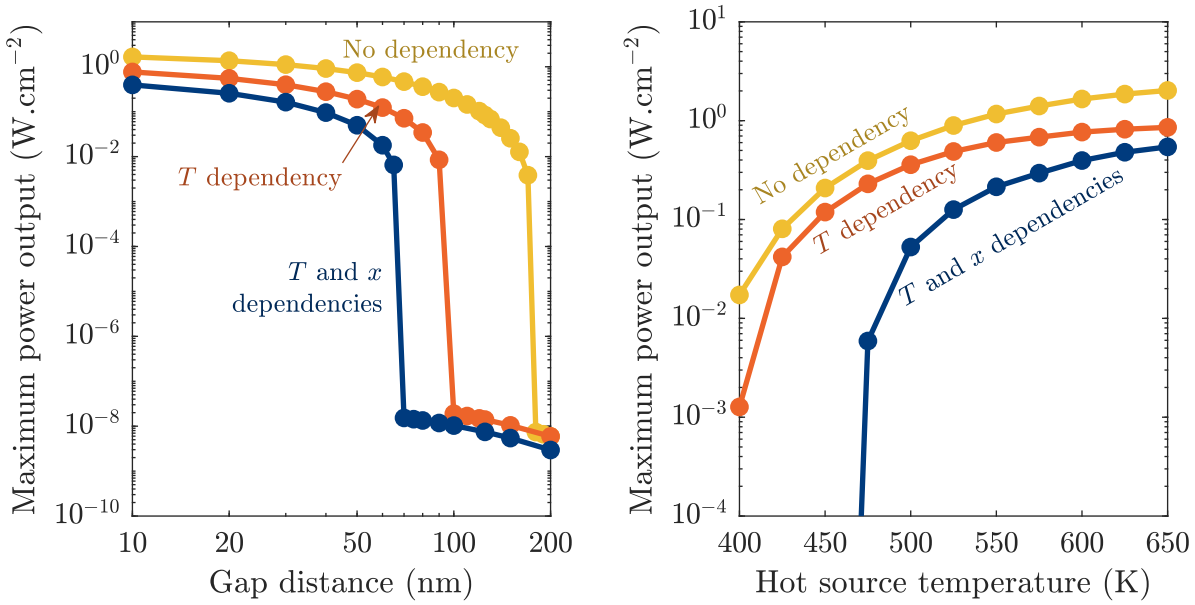

Figure 6.21: Influence of (a) the gap distance, (b) the heat source temperature on the maximum power output of the InGaAs/InGaP device. In the figures, x represent the indium fraction.

$T_{\mathrm{LED}} = 500$ K, maximum power output decreases by a factor 12 in comparison to the best-case scenario, while at 450 K and below the device cannot operate as a TPX heat engine any more. In fact, this also happens in the intermediate scenario for temperatures slightly below 400 K, and we can already notice that the maximum power output starts to drop slightly above 400 K. This is partly due to the reduction of the region of the voltage space in which the device can operate as a heat engine, as discussed in Section 3.3.1.1. Of course, the thicknesses and doping levels of the device may no longer be optimised at these temperatures. Still, this highlights the need for developing efficient devices for moderate-temperature operation. The temperature and composition dependencies considered here being only rough estimates, experimental studies will also be required to make them more precise and allow models to identify more accurately the limiting factors.

6.4 To sum up

To improve carrier separation and therefore the quantum efficiencies of the two components, we focused in the chapter on the operation of TPX devices based on heterostructures. Specific physical phenomena occur at heterointerfaces due to the potential barrier placed on the path of charge carriers. If some approximations are available to make the model simpler, the high voltages and related current densities in the LED and the PV cell around MPP makes them somewhat inaccurate, and the full thermionic-field emission model should be implemented along with an iterative process for handling the spatial variation of photon chemical potential.

Thanks to the improved efficiency of heterostructures, idealising assumptions - which were previously mandatory to make the device able to operate properly - can now be relaxed, allowing to come closer to the operation of realistic devices. This is for instance the case for surface recombinations: while the surface recombination velocity is one hundred times larger in this chapter, the use of InGaP confinement layers allow the TPX device to reach a maximum power

output of the order of the one obtained by the homostructure of Chapter 5. The dependency of non-radiative recombination coefficients on temperature and composition could also be included. Their impact has been mitigated in the improved device based on GaAs and InGaAs active layers (resp. in the LED and the PV cell), although such studies are hampered by the lack of precise data regarding these dependencies. By doing these analyses, we aimed to pinpoint the significant effect that common approximations can have, and to provide guidelines to adapt the device to various losses. The InGaAs/InGaP device, which is the most performant device proposed in this manuscript, remains however somewhat idealistic, several idealising assumptions being still used. Among those, we can notably cite:

- resistive losses, related to the heat released by current flow[8];
- shading of the LED and PV cell front surfaces by metallic grid, which reduces the radiative transfer between the components;
- parasitic absorption of radiation in the back mirrors;
- increase of non-radiative recombination rate due to 2D (or even 3D) transport of charge (which increase the distance travelled by charge carriers), either in the bulk or on the perimeter[9].

Some of these losses are coupled to one another: for instance, decreasing the grid coverage on the front surface reduces shading but increases resistive losses in the grid, and a trade-off shall thus be found. While all these losses are directly related to the physics of the semiconductor device, some other could arise from fabrication imperatives: several etch stop layers are for instance necessary to develop a component, which can further increase radiative and electrical losses. All these different elements shall at some point be implemented for the precise modelling of TPX devices.

To conclude, we compare in Figure 6.22 the variation of maximum power output with heat source temperature obtained in this chapter with those derived for thermoelectrics and NF-TPX in Chapter 3. Even with the dependencies included, the maximum power output of the InGaAs/InGaP device remains between the two limiting cases obtained from detailed-balance - at least between 475 and 650 K. However, its performance remains below that of realistic thermoelectric generators even with some remaining idealising assumptions. While this is not entirely surprising given the difference in maturity between these two technologies - our work being the first to focus on the performance of TPX structures - it does highlight the need for further study and optimisation of complete devices to determine whether TPX can become competitive with TE; and doing so will require to deepen our knowledge on the material properties of promising materials and on their dependency on temperature.

[8] A simple way to model resistive losses in 1D is to use the model considered in [Milovich *et al.* 2020] for NF-TPV.

[9] Current spreading layers are often used in real thin-film devices to prevent excessive losses due to lateral transport.

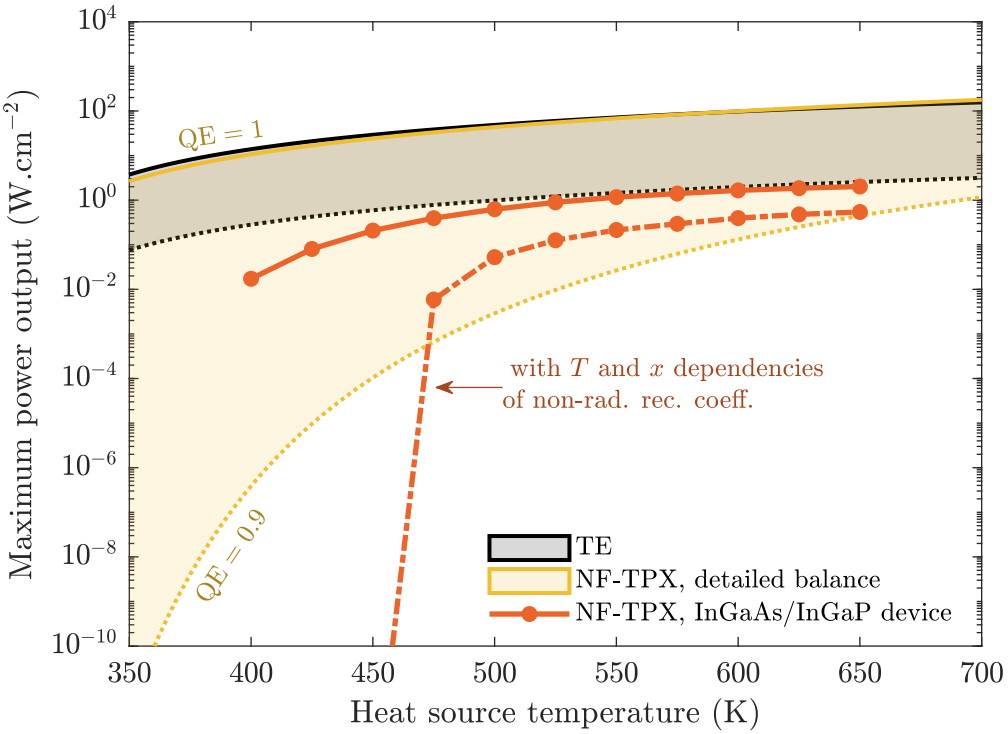

Figure 6.22: Performance of NF-TPX devices obtained from detailed balance (Chapter 3) and from the drift-diffusion modelling of charge transport in the InGaAs/InGaP device (Chapter 6), compared to thermoelectrics.

Conclusion

In this thesis, we have analysed thermophotonic energy harvesters operating in the near field by theoretical and numerical means. As revealed by the literature review, thermophotonics is a fairly young topic in comparison to other solid-state heat engines, with only few detailed-balance analyses performed to estimate their potential as energy harvesters or to study the influence of key parameters [Harder & Green 2003, Zhao *et al.* 2018], and with no thorough physical and thermodynamical description of their operation. Therefore, we have started by providing one, and have discussed the electricity-to-light and light-to-electricity conversion occurring in the LED and the PV cell. This has highlighted that TPX devices rely on the operation of LEDs as heat pumps, since above-unity LED wall-plug efficiencies are required to produce electrical power. Because of the limited temperature an LED can withstand, the use of TPX engines shall be limited to low-grade heat recovery, and a heat source temperature of 600 K has been selected for this study.

We started by developing efficiency bounds for thermophotonic heat engines operating at the radiative limit. In reversible operation, we have highlighted that the active electrical control of the emitter makes it possible to ensure that no entropy is created in the whole device. Reversible thermophotonics can thus reach the Carnot efficiency, which is a fundamental difference to thermophotovoltaics. In irreversible operation, we have found that the efficiency at maximum power is maximised in the limit of monochromatic radiation, where it equals the classical Curzon-Ahlborn efficiency. For a 600 K LED and a 300 K PV cell, this means that while the maximum efficiency theoretically achievable is equal to 50%, the optimal efficiency at maximum power is only 29%. It further decreases as the radiation bandwidth increases, down to around 17% for a bandgap energy of 1 eV when considering a bandwidth of few tenths of eV (which is typical for electroluminescent spectrum). Therefore, thermalisation losses have a significant impact on the overall performance. In the limit of infinite bandgap energy, we have derived a closed-form expression of the efficiency at maximum power that depends only on the heat source and heat sink temperatures: it represents an upper bound of the achievable efficiency at maximum power for broadband radiation.

In Chapter 3, we have studied numerically the performance of thermophotonic energy harvesters in the near field. The quantum efficiency has been found to be a key parameter, which needs to exceed 0.95 to make TPX competitive with thermoelectrics. For this reason, we have chosen to work with GaAs-based devices, more precisely with an AlGaAs LED and a GaAs PV cell, different materials being used for the two components to ensure bandgap matching. We have then investigated in detail how both voltages impact the overall performance of the device. In the voltage space, we have delimited the region in which the TPX device operates as a heat engine or a heat pump, in the form of an equivalent Raveau diagram. We have also underlined that increasing the LED voltage allows enhancing the power output by orders of magnitude, reaching 100 $W.cm^{-2}$ at the radiative limit for a 300 K temperature difference. Such a high power output could only be reached because of near-field enhancements, which increases the maximum power output by a factor of 15. However, we have also shined a light on the possible drawbacks of near-field operation. Indeed, the intensity of below-bandgap radiation - which is a loss - increases quickly in the extreme near field due to polaritonic resonances. This causes the overall efficiency to drop in comparison to the above-bandgap efficiency. Worse, if the losses occurring during the heat transfer with the reservoirs are taken into account, going to the near field can even be detrimental to the power output. It will therefore be necessary to find ways to

limit below-bandgap radiative heat transfer.

In the second part of the manuscript, the charge transport in the semiconductors has been modelled in one-dimension, based on the drift-diffusion equations. This model has been first used to study PIN homostructures, which display better performance than simpler PN junctions [Legendre & Chapuis 2022a]. By optimising the thickness and doping level of the various layers, a maximum power output of 1.9 W.cm^{-2} has been achieved with a 600 K LED and for a moderate recombination velocity of 100 cm.s^{-1}. The LED has been found to be the driving component of the TPX device, the power output being closely related to the LED QE. The lack of power production observed in the low LED voltage region could therefore be associated to the significant SRH recombination rate in the LED at such voltage. In parallel, we have underlined the significant QE improvement obtained in the near field, which is another benefit of operating with nanogaps. However, this means that the power output rapidly drops as the gap distance increases. We have observed that the TPX device was no longer able to operate properly above 80 nm. This is a fundamental difference with TPV: in TPX devices, QE enhancements obtained in the near field can be mandatory to reach proper operation. Along with the performance analysis of this device, we have also investigated the influence of accounting for Urbach tails on the maximum power output. If its value does not change significantly when including such tails, we have however underlined that it relaxes the bandgap matching condition, the maximum power output being almost constant for $E_{g,\mathrm{LED}} - E_{g,\mathrm{PV}}$ between 0 and 50 meV. This shall help for experimental developments.

Last, we have studied heterostructures composed of InGaP confinement layers to improve charge separation in the components. Simulating such components has however required to further develop our model. Both thermionic emission and charge carrier tunnelling have been included to model accurately the charge transport through heterointerfaces. We have also implemented an iterative process between radiative and electrical solvers in order to associate the correct photon chemical potential to radiation. With this complete model, we have optimised the PIN heterostructures and have obtained a device displaying a maximum power output of 1.8 W.cm^{-2} for a more realistic surface recombination velocity of 10^4 cm.s^{-1}. Finally, we have investigated the influence of the dependency of non-radiative recombination coefficients on temperature and composition, which has been previously neglected. After demonstrating that such dependency had a dramatic effect on the performance of the AlGaAs/InGaP device, we have proposed a more robust device with an LED active layer made of GaAs to maximise LED QE, using an InGaAs PV cell active layer to ensure bandgap matching. Intermediate low-doped InGaP layers have also been added in the PV cell to limit Auger recombinations. If the maximum power output obtained without any of the dependencies is similar to that of the previous device, this has allowed largely mitigating the power drop caused by them, down to a reduction factor of 4.

Throughout this manuscript, we have identified several key elements that shall be addressed to refine the device modelling. First, some inherent electrical losses, such as resistive losses, shading losses or parasitic absorption in the back mirrors shall for instance be included. In addition, extending the simulations to 2D or even 3D systems will at some point be necessary. Indeed, some specific phenomena such as current crowding close to the front electrical contact - which takes the form of a metallic grid - cannot be observed in 1D simulations. Regarding electrical contacts, they were supposed to be almost ohmic in Chapter 6 but could also be modelled as Schottky junctions with few modifications of our model. Investigating the impact of using either of these models would be an interesting development of the current work. Moreover, the use of Boltzmann's approximation for the Fermi-Dirac distribution, which is incorrect for degenerate

semiconductors, could have a significant impact on the results we have obtained since our devices are composed of highly-doped layers. Therefore, it seems important to perform a fine study of the influence of using Boltzmann's approximation in future work.

Regarding radiation, the transition from 1D to 2D will also be important: only 2D or 3D modelling can allow including the front electrical contact, whose radiative properties are definitely different from those of the semiconductors considered. Because the front contact is on top of the semiconductor, the gap distance between the front layers of the LED and the PV cell is limited by the front contact thickness, which is an issue to reach near-field operation. To prevent this, an aperture layer can be placed on the front layer of each component. To ensure good near-field radiative heat transfer between the LED and the PV cell, the aperture layers must be transparent for photons with energy close to the bandgap energy of the active layers, and their refractive index must match that of the two components. High-bandgap III-V semiconductors such as InGaP or AlGaAs fit this description. However, transfer of energy through surfaces modes will be driven by these layers. Since III-V semiconductors are polar, they will cause large below-bandgap transfer of energy because of the phonon-polariton resonance. To avoid this, it would be worth looking for non-polar materials which fit the above definition. More generally, because of the harm below-bandgap radiation causes to the performance, it seems important to look for ways to mitigate this heat transfer as much as possible.

Some interesting phenomena which were mentioned in the current work could also be further investigated. One example is photon recycling, whose impact becomes significant as thick layers, such as current spreading layers or aperture layers, are added to the component. This is particularly true when Urbach tails are considered, as they increase the absorption coefficient of normally transparent layers. In addition, we have seen that photon recycling is always calculated considering only the propagating radiation. Therefore, it would be instructive to study the impact of evanescent radiation on this phenomenon. Since the distance between emission and absorption can be infinitely small, this will require a non-local treatment of the radiative transfer, thus a better understanding of the non-local mechanisms related to interband transitions. Another example is related to the study performed in Chapter 3 about the influence of the thermal conductance with the thermal reservoirs. When considering the complete spectrum, we have found that for a given reservoir conductance, there was a gap distance maximising the power output. Because this shares many similarities with the condition of impedance matching discussed for thermoelectrics in [Apertet *et al.* 2012a], further analyses shall be performed on the matter to understand if a similar condition exists for TPX, which may be possible to extend to other radiative heat engines. We shall finally mention that throughout this thesis, we have limited our studies to TPX operation, thus to positive LED and PV cell voltages. However, it has been demonstrated that the device efficiency increases when moving towards negative voltages [Tervo *et al.* 2022]. Therefore, exploring how performance varies in the entire voltage space could complete the analysis and form an interesting extension of our work.

Appendices

Appendix A

Methodology for near-field radiative heat transfer simulations

A.1 Complete expression of the near-field radiative heat transfer

In Chapter 1, we have obtained the expression of the near-field radiative heat transfer under the form (Eq. 1.12)

$$q_\omega(z) = \frac{2\varepsilon''(\omega)}{\pi} k_v^2 \hbar\omega f_{\mathrm{BE}}(\omega,\mu,T) \cdot \mathrm{Re}\left\{ i \int_V \left[G^{\mathcal{E}}_{x\alpha}(z,\boldsymbol{r'},\omega) G^{\mathcal{H}^*}_{y\alpha}(z,\boldsymbol{r'},\omega) - G^{\mathcal{E}}_{y\alpha}(z,\boldsymbol{r'},\omega) G^{\mathcal{H}^*}_{x\alpha}(z,\boldsymbol{r'},\omega) \right] d^3\mathbf{r}' \right\}, \tag{A.1}$$

and we have expressed Green's tensors using two-dimensional Fourier transform as (Eq. 1.13)

$$\bar{\bar{\boldsymbol{G}}}(z,\boldsymbol{r}',\omega) = \frac{1}{(2\pi)^2} \int_{-\infty}^{+\infty} \bar{\bar{\boldsymbol{g}}}(\boldsymbol{k}_\rho, z, z', \omega) e^{i\boldsymbol{k}_\rho(\boldsymbol{R}-\boldsymbol{R}')} d\boldsymbol{k}_\rho, \tag{A.2}$$

$\bar{\bar{\boldsymbol{g}}}$ being the Weyl representation of Green's tensor. This section aims to give the complete development of the near-field radiative heat transfer, following the methodology provided in [Francoeur *et al.* 2009].

A.1.1 Switch to polar coordinates

The first thing to do is to simplify the integral on $d\boldsymbol{k}_\rho$ by switching to polar coordinates. Then,

$$\int_{-\infty}^{+\infty} d\boldsymbol{k}_\rho = 2\pi \int_0^{\infty} k_\rho dk_\rho. \tag{A.3}$$

Using the fact that $\boldsymbol{k}_\rho(\boldsymbol{R}-\boldsymbol{R}') = k_\rho(R-R')$ is real, then $\exp(ik_\rho(R-R'))(\exp(ik_\rho(R-R')))^* = 1$ and

$$\int_V G^{\mathcal{E}}_{\rho\alpha}(z,\boldsymbol{r}',\omega) G^{\mathcal{H}^*}_{\theta\alpha}(z,\boldsymbol{r}',\omega) d^3\mathbf{r}' = \frac{1}{2\pi} \int_0^{\infty} \int_z g^{\mathcal{E}}_{\rho\alpha}(k_\rho,z,z',\omega) g^{\mathcal{H}^*}_{\theta\alpha}(k_\rho,z,z',\omega) dz' \cdot k_\rho dk_\rho, \tag{A.4}$$

and similarly for $\int G^{\mathcal{E}}_{\theta\alpha}(z,\boldsymbol{r}',\omega) G^{\mathcal{H}^*}_{\rho\alpha}(z,\boldsymbol{r}',\omega) d^3\mathbf{r}'$.

A.1.2 Decomposition in terms of forward and backward travelling waves

The different Weyl components can then be expressed using the Sipe formalism [Sipe 1987]. The main idea is to decompose each component into forward- and backward-travelling waves for each

polarisation. Defining the TE and TM polarisation unit vectors as

$$\hat{\mathbf{s}} = \hat{\mathbf{k}}_\rho \times \hat{\mathbf{z}} = \begin{pmatrix} 0 \\ -1 \\ 0 \end{pmatrix}, \tag{A.5a}$$

$$\hat{\mathbf{p}}_i^{\pm} = \frac{1}{k_\mathrm{v}\sqrt{\varepsilon_i}}\left(k_\rho \hat{\mathbf{z}} \mp k_{zi}\hat{\mathbf{k}}_\rho\right) = \frac{1}{k_\mathrm{v}\sqrt{\varepsilon_i}}\begin{pmatrix} \mp k_{zi} \\ 0 \\ k_\rho \end{pmatrix}, \tag{A.5b}$$

the electric Weyl representation of Green's tensor considering an emitting layer m and receiving layer n is for instance

$$\bar{\bar{\mathbf{g}}}^{\mathcal{E}}_{mn}(k_\rho, z, z', \omega) = \frac{i}{2k_{zm}}\begin{bmatrix} (A_n^{\mathrm{TE}}\hat{\mathbf{s}}\hat{\mathbf{s}} + A_n^{\mathrm{TM}}\hat{\mathbf{p}}_n^{+}\hat{\mathbf{p}}_m^{+})e^{i(+k_{zn}(z-z_n)-k_{zm}(z'-z_m))} \\ +(B_n^{\mathrm{TE}}\hat{\mathbf{s}}\hat{\mathbf{s}} + B_n^{\mathrm{TM}}\hat{\mathbf{p}}_n^{-}\hat{\mathbf{p}}_m^{+})e^{i(-k_{zn}(z-z_n)-k_{zm}(z'-z_m))} \\ +(C_n^{\mathrm{TE}}\hat{\mathbf{s}}\hat{\mathbf{s}} + C_n^{\mathrm{TM}}\hat{\mathbf{p}}_n^{+}\hat{\mathbf{p}}_m^{-})e^{i(+k_{zn}(z-z_n)+k_{zm}(z'-z_m))} \\ +(D_n^{\mathrm{TE}}\hat{\mathbf{s}}\hat{\mathbf{s}} + D_n^{\mathrm{TM}}\hat{\mathbf{p}}_n^{-}\hat{\mathbf{p}}_m^{-})e^{i(-k_{zn}(z-z_n)+k_{zm}(z'-z_m))} \end{bmatrix}. \tag{A.6}$$

Four different contributions are obtained as radiation must be segregated according to the travelling direction in both the emitting and receiving layers: for instance, the first line corresponds to waves which are travelling forward in both layers. Coefficients A, B, C and D correspond to the amplitude of the corresponding wave at the entrance of layer j (position z_n) considering an emission with unit amplitude at the entrance of layer i (position z_m). The exponential terms therefore allow to correct the emitting and receiving positions to z and z' exactly. Note that in [Francoeur *et al.* 2009], z_m is not present in the equation, which we suspect is a misprint.

Because some of the Weyl components equal zero, the heat flux density emitted by layer i can be reduced to

$$q_\omega(z) = \hbar\omega\frac{k_\mathrm{v}^2}{4\pi^2}f_{\mathrm{BE}}(\omega, \mu, T)\cdot\int_0^\infty \mathcal{T}(\omega, k_\rho, z)k_\rho dk_\rho, \tag{A.7}$$

$\mathcal{T}(\omega, k_\rho, z)$ being the transmission coefficient written as

$$\mathcal{T}(\omega, k_\rho, z) = 4\varepsilon''(\omega)\mathrm{Re}\left\{ i\int_{z_m}^{z_{m+1}}\begin{bmatrix} g^{\mathcal{E}}_{mn\rho\rho}(k_\rho, z, z', \omega)g^{\mathcal{H}^*}_{mn\theta\rho}(k_\rho, z, z', \omega) \\ +g^{\mathcal{E}}_{mn\rho z}(k_\rho, z, z', \omega)g^{\mathcal{H}^*}_{mn\theta z}(k_\rho, z, z', \omega) \\ -g^{\mathcal{E}}_{mn\theta\theta}(k_\rho, z, z', \omega)g^{\mathcal{H}^*}_{mn\theta\rho}(k_\rho, z, z', \omega) \end{bmatrix} dz' \right\}. \tag{A.8}$$

In this expression, the two first lines are related to TM modes while the last corresponds to TE modes.

A.1.3 S-matrix method

The last step is to express the coefficients A to D. This is done by means of the scattering-matrix method - more commonly called S-matrix method. This matrix allows relating the value of coefficients at different interfaces, for instance

$$\begin{bmatrix} A_n \\ B_m \end{bmatrix} = S(m, n)\begin{bmatrix} A_m \\ B_n \end{bmatrix}, \tag{A.9}$$

$S(m, n)$ being the scattering matrix between layers m and n. A similar expression can be found for C and D. In comparison to the transfer-matrix method, it allows reducing numerical instabilities. However, obtaining the coefficients at a given interface is less straightforward as they are on both

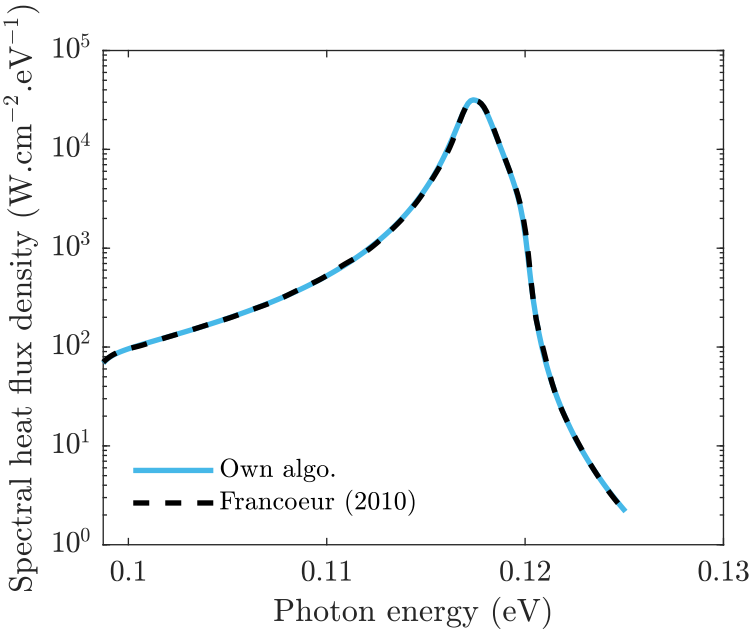

Figure A.1: Reproduction of the results provided in [Francoeur *et al.* 2010], obtained for slabs of thickness 10 nm and for a 10 nm gap distance.

sides of the equation. Each component of S must therefore be computed individually, and depends on the reflection and transmission coefficients at interfaces along with the attenuation factor $e^{ik_z\Delta z}$ obtained in the different layers. The detailed expression of S will not be shown here and can be found in [Francoeur *et al.* 2009]. We would however like to highlight that we performed some corrections regarding the source term $S^{\pm}$ in comparison to [Francoeur *et al.* 2009]. More precisely, we took them equal to 1 instead of $e^{\mp ik_{zm}(z'-z_m)}$. Indeed, based on our understanding, such an exponential term would account for the attenuation between the point of emission z' and the entrance of the emitting layer z_m. Since this is already included with the exponential in Eq. (A.6), the coefficients should only be related to the exchange of radiation from one interface to another, and S should be equal to 1. By doing these corrections, we are able to reproduce the data given in [Francoeur *et al.* 2010], as shown in Figure A.1.

A.2 Transmission coefficient for an arbitrary stack of three media

In the literature, it is possible to find an analytical expression of the transmission coefficient between two semi-infinite layers separated by an arbitrary medium [Mulet 2004, Francoeur *et al.* 2009]. In the following, we aim at demonstrating this expression, and at extending it to the study of the transmission between two thin slabs of the semi-infinite bodies. A schematic of the system is shown in Figure A.2.

To derive the transmission coefficient, we mostly follow the method provided in [Mulet 2004] (in French). Using the polarisation unit vectors introduced in the previous section, the analytical expression of Green's tensors between media 0 and 2 is

$$\bar{\bar{\mathbf{g}}}_{02}^{\mathcal{E}}(k_\rho, z, z') = \frac{i}{2k_{z0}}\left(\hat{\mathbf{s}}t_{02}^{\mathrm{TE}}\hat{\mathbf{s}} + \hat{\mathbf{p}}_2^+ t_{02}^{\mathrm{TM}}\hat{\mathbf{p}}_1^+\right)\exp\left[i\left(k_{z2}(z-d) - k_{z0}z'\right)\right], \tag{A.10a}$$

$$\bar{\bar{\mathbf{g}}}_{02}^{\mathcal{H}}(k_\rho, z, z') = \frac{k_{\mathrm{v}}\sqrt{\varepsilon_1}}{2k_{z0}}\left(\hat{\mathbf{p}}_2^+ t_{02}^{\mathrm{TE}}\hat{\mathbf{s}} + \hat{\mathbf{s}}t_{02}^{\mathrm{TM}}\hat{\mathbf{p}}_1^+\right)\exp\left[i\left(k_{z2}(z-d) - k_{z0}z'\right)\right], \tag{A.10b}$$

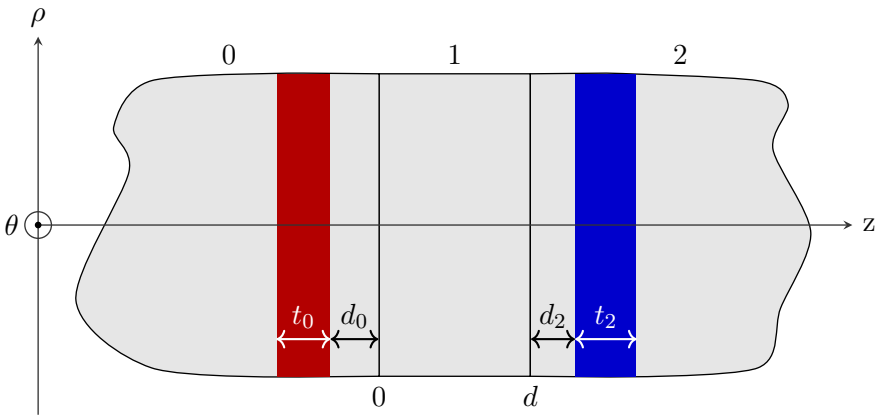

Figure A.2: Schematic of the system considered, the transmission coefficient being derived between the two coloured layers.

z' being the point of emission and z the point of reception. The transmission factor between layers 0 and 2 is

$$t_{02}^{\gamma} = \frac{t_{01}^{\gamma} t_{12}^{\gamma} e^{ik_{z2}d}}{1 + r_{01}^{\gamma} r_{12}^{\gamma} e^{2ik_{z1}d}}. \tag{A.11}$$

Using Eq. (A.8), the transmission coefficient between the emitting layer and a point z in the absorber is expressed as

$$\mathcal{T}^{\gamma}(\omega, k_\rho, z) = \int_{-t_0-d_0}^{-d_0} \tau^{\gamma}(\omega, k_\rho, z, z')dz', \tag{A.12}$$

where τ^{γ} is the equivalent point-point transmission coefficient which, for TM and TE polarisations respectively, equals

$$\tau^{\mathrm{TM}}(\omega, k_\rho, z, z') = \frac{2k''_{z0}}{|k_{z0}|^2} \frac{\mathrm{Re}(\varepsilon_0 k^*_{z0})\mathrm{Re}(\varepsilon_2 k^*_{z2})}{|\varepsilon_0||\varepsilon_2|} \left|t_{02}^{\mathrm{TM}}\right|^2 \exp\left(-2k''_{z2}(z-d) + 2k''_{z0}z'\right) \tag{A.13a}$$

$$\tau^{\mathrm{TE}}(\omega, k_\rho, z, z') = \frac{2k''_{z0}}{|k_{z0}|^2} k'_{z0}k'_{z2} \left|t_{02}^{\mathrm{TE}}\right|^2 \exp\left(-2k''_{z2}(z-d) + 2k''_{z0}z'\right) \tag{A.13b}$$

The slab-slab transmission coefficient is obtained as $\mathcal{T}^{\gamma}(\omega, k_\rho) = \mathcal{T}^{\gamma}(\omega, k_\rho, d+d_2) - \mathcal{T}^{\gamma}(\omega, k_\rho, d+d_2+t_2)$. After integration, we therefore get

$$\mathcal{T}^{\mathrm{TM}}(\omega, k_\rho) = \frac{1}{|k_{z0}|^2} \frac{\mathrm{Re}(\varepsilon_0 k^*_{z0})\mathrm{Re}(\varepsilon_2 k^*_{z2})}{|\varepsilon_0||\varepsilon_2|} \left|t_{02}^{\mathrm{TM}}\right|^2 \vartheta_0\vartheta_2, \tag{A.14a}$$

$$\mathcal{T}^{\mathrm{TE}}(\omega, k_\rho) = \frac{1}{|k_{z0}|^2} k'_{z0}k'_{z2} \left|t_{02}^{\mathrm{TE}}\right|^2 \vartheta_0\vartheta_2, \tag{A.14b}$$

where $\vartheta_i = \exp(-2k''_{zi}d_i)[1-\exp(-2k''_{zi}t_i)]$ accounts for the fact that the emitter and absorber represent only a fraction of the semi-infinite media. In the limit of media 0 and 2 being respectively the emitter and the absorber, $\vartheta = 1$ and we find back the expressions from [Mulet 2004, Francoeur *et al.* 2009]. The analytical transmission coefficient is often expressed as a function of Fresnel coefficients instead of k_z and ε, but this requires the intermediate medium to be lossless and therefore cannot be applied here.

Appendix B

Material properties

We show below the material properties used in this manuscript. The data used for near-field radiative heat transfer and for drift-diffusion modelling have been separated to help the reading. For each property, we indicate if it was obtained at room temperature (written RT in the tables) and provide other information when necessary. To give a better idea of the value taken by each, we also specify the value obtained for a specific composition, indicated in parentheses.

B.1 Properties for near-field radiative heat transfer simulations

For all materials, the effective mass is obtained from [Levinshtein *et al.* 1999]. The electron effective mass is directly provided in it, while the hole effective mass (also called density-of-states hole effective mass) is obtained from the effective masses of light holes m^*_{lh} and heavy holes m^*_{hh} [Rosencher 2002]:

$$m^*_p = \left(m^{*3/2}_{\mathrm{lh}} + m^{*3/2}_{\mathrm{hh}}\right)^{2/3}. \tag{B.1}$$

Since the charge carrier mobilities μ and the dielectric function related to interband transitions $\varepsilon_{\mathrm{IB}}$ vary (respectively with the charge carrier densities and the frequency), we don't provide any value for these parameters.

B.1.1 AlGaAs

Table B.1: Material properties used to obtain the dielectric function of $\mathrm{Al}_x\mathrm{Ga}_{1-x}\mathrm{As}$ alloys.

Parameter	Symbol	Value (GaAs)	Reference	Comments
High freq. dielectric cst	ε_∞	10.9	[Adachi 1994]	RT
Electron effective mass	m^*_n	0.063 m_0	[Levinshtein *et al.* 1999]	RT
Hole effective mass	m^*_p	0.53 m_0	[Levinshtein *et al.* 1999]	RT
Electron/hole mobility	μ		[Sotoodeh *et al.* 2000]	
TO phonon frequency	ω_{TO}	36.2 meV	[Adachi 1994]	RT
LO phonon frequency	ω_{LO}	34.4 meV	[Adachi 1994]	RT,1
Lorentz damping coeff.	γ	0.41 meV	[Adachi 1994]	RT
Interband contribution	$\varepsilon_{\mathrm{IB}}$		[Gonzalez-Cuevas *et al.* 2007]	2

1. There is a mistake in the expression given in [Adachi 1994] for the LO phonon frequency of the AlAs mode, which should be $\omega_{\mathrm{LO}}(\mathrm{AlAs}) = 358.2 + 79.7x - 40.3x^2$ cm^{-1} [Lukeš *et al.* 1989].

2. Even if there is no mention of ε_∞ in [Gonzalez-Cuevas *et al.* 2007], we assume that it is included in the expression $\varepsilon_{\mathrm{IB}}$ given in this article (since it fits experimental data which *has* to be the total dielectric function, thus including ε_∞). The complete dielectric function is thus $\varepsilon = \varepsilon_{\mathrm{IB}} + (\varepsilon_{\mathrm{plasmon}} - \varepsilon_\infty) + (\varepsilon_{\mathrm{phonon}} - \varepsilon_\infty)$.

B.1.2 InGaP

Table B.2: Material properties used to obtain the dielectric function of $In_{1-x}Ga_xP$ alloys.

Parameter	Symbol	Value ($In_{0.49}Ga_{0.51}P$)	Reference	Comments
High freq. dielectric cst	ε_∞	9.35	[Levinshtein *et al.* 1999]	RT
Electron effective mass	m_n^*	0.088 m_0	[Levinshtein *et al.* 1999]	RT
Hole effective mass	m_p^*	0.73 m_0	[Levinshtein *et al.* 1999]	RT
Electron/hole mobility	μ		[Sotoodeh *et al.* 2000]	
TO phonon frequency	ω_{TO}	41.3 meV (InP-like)	[Ferrini *et al.* 2002]	RT,1
		45.9 meV (GaP-like)	[Ferrini *et al.* 2002]	RT,1
LO phonon frequency	ω_{LO}	48.3 meV (InP-like)	[Ferrini *et al.* 2002]	RT,1
		47.4 meV (GaP-like)	[Ferrini *et al.* 2002]	RT,1
Lorentz damping coeff.	γ	1.1 meV (InP-like)	[Ferrini *et al.* 2002]	RT,1
		1.3 meV (GaP-like)	[Ferrini *et al.* 2002]	RT,1
Interband contribution	ε_{IB}		[Schubert *et al.* 1999]	2

1. Several values are given in [Ferrini *et al.* 2002] for the different parameters of the phononic contribution. The values provided in the table are obtained by averaging the published data. Note that the phononic contribution is only given for $x_{Ga} = 0.51$, and is assumed to remain similar if the composition is changed, data lacking for $x_{Ga} \neq 0.51$.

2. The interband contribution given in [Schubert *et al.* 1999] lacks composition and temperature dependency. These are included by gathering the variations of E_g with x and T from the literature; we then assume that each transition energy $E_0 = E_g$, E_1 and E_2 varies as E_g. For the temperature dependency, we consider the linear variation given in [Steiner *et al.* 2011]. The composition-dependent bandgap is obtained from a second-order polynomial fit from the data at $x_{Ga} = 0$ ($E_g = 1.34$ eV [Levinshtein *et al.* 1999]), $x_{Ga} = 0.51$ ($E_g = 1.89$ eV [Schubert *et al.* 1999]) and $x_{Ga} = 0.71$ ($E_g = 2.2$ eV [Alberi *et al.* 2011]).

B.1.3 InGaAs

Table B.3: Material properties used to obtain the dielectric function of $In_xGa_{1-x}As$ alloys.

Parameter	Symbol	Value (GaAs)	Reference	Comments
High freq. dielectric cst	ε_∞	10.9	[Adachi 1994, Adachi 1999a]	RT
Electron effective mass	m_n^*	0.063 m_0	[Levinshtein *et al.* 1999]	RT
Hole effective mass	m_p^*	0.53 m_0	[Levinshtein *et al.* 1999]	RT
Electron/hole mobility	μ		[Sotoodeh *et al.* 2000]	
TO phonon frequency	ω_{TO}	36.2 meV	[Adachi 1994, Adachi 1999a]	RT,1
LO phonon frequency	ω_{LO}	34.4 meV	[Adachi 1994, Adachi 1999a]	RT,1
Lorentz damping coeff.	γ	0.41 meV	[Adachi 1994, Adachi 1999b]	RT,1
Interband contribution	ε_{IB}		[Gonzalez-Cuevas *et al.* 2007]	2

1. Less information are available for InGaAs in comparison to AlGaAs. In order to have a composition-dependent phononic contribution, we simply write it in a simple additive form

$$\varepsilon_{\text{phonon,InGaAs}} = (1 - x_{In})\varepsilon_{\text{phonon,GaAs}} + x_{In}\varepsilon_{\text{phonon,InAs}}, \tag{B.2}$$

$\varepsilon_{\text{phonon,GaAs}}$ and $\varepsilon_{\text{phonon,InAs}}$ coming respectively from [Adachi 1994] and [Adachi 1999a].

2. Even if there is no mention of ε_∞ in [Gonzalez-Cuevas *et al.* 2007], we assume that it is included in the expression ε_{IB} given in this article (since it fits experimental data which *has* to be the total dielectric function, thus including ε_∞). The complete dielectric function is thus $\varepsilon = \varepsilon_{\text{IB}} + (\varepsilon_{\text{plasmon}} - \varepsilon_\infty) + (\varepsilon_{\text{phonon}} - \varepsilon_\infty)$.

B.2 Properties for drift-diffusion simulations

Many of the properties required for charge transport simulations, such as effective masses or bandgap, are already provided in the section above and will therefore not be repeated. The remaining properties, which are gathered below, were only found at room temperature (indicated with RT in the comments). No composition dependency was found for non-radiative recombination coefficients, which are consequently supposed to remain constant around a given composition; we give in the comment the corresponding alloy fraction x.

B.2.1 AlGaAs & InGaAs

Table B.4: Charge transport properties of $Al_xGa_{1-x}As$ and $In_xGa_{1-x}As$ alloys.

Parameter	Symbol	Value (GaAs)	Reference	Comments
Static dielectric cst	ε_s	12.9	[Levinshtein *et al.* 1999]	RT
Electron affinity	χ	4.07 eV	[Levinshtein *et al.* 1999]	RT
Auger rec. coefficient	$C_{n/p}$	10^{-30} cm^{-6}.s^{-1}	[Sadi *et al.* 2019b]	RT,$x = 0$
SRH lifetime	$\tau_{n/p,\text{SRH}}$	3.3 μs	[Sadi *et al.* 2019b]	RT,$x = 0$

B.2.2 InGaP

Table B.5: Charge transport properties of $In_{1-x}Ga_xP$ alloys.

Parameter	Symbol	Value ($In_{0.49}Ga_{0.51}P$)	Reference	Comments
Static dielectric cst	ε_s	11.8	[Levinshtein *et al.* 1999]	RT
Electron affinity	χ	4.1 eV	[Levinshtein *et al.* 1999]	RT
Auger rec. coefficient	$C_{n/p}$	3×10^{-30} cm^{-6}.s^{-1}	[Levinshtein *et al.* 1999]	RT,$x = 0.51$
SRH lifetime	$\tau_{n/p,\text{SRH}}$	3.3 μs	[Sadi *et al.* 2019b]	RT,1

1. This SRH lifetime corresponds in fact to that of GaAs. We have kept this as we did not find proper data for InGaP. Anyway, this parameter does not play a significant role in our devices - especially since InGaP is highly doped. For instance, a decrease in maximum power output of the order of tens of percents can be observed when reducing τ_{SRH} by three orders of magnitude. While significant, it is much less impactful than non-radiative recombination coefficients in the active layer - which can change P_{max} by orders of magnitude - and we can expect to further reduce the effect of $\tau_{\text{SRH,InGaP}}$ by optimising the device with such properties.

Appendix C

Modelling the performance of different solid-state heat engines

C.1 Thermoelectrics

We use the expression of the maximum power given by Apertet et al. [Apertet *et al.* 2012a]:

$$P_{\max} = \frac{(G_{\text{th,contact}}\Delta T)^2}{4(G_{\text{th},\Sigma} + G_{\text{th,contact}})\bar{T}} \frac{Z\bar{T}}{1 + Z\bar{T} + G_{\text{th,contact}}/G_{\text{th},\Sigma}} \tag{C.1}$$

For the lower (resp. higher) limit, we choose $Z\bar{T} = 0.5$ (resp. 3), corresponding to available and ambitious cases. The thermal contact conductance $G_{\text{th,contact}}$ is respectively equal to 1 and 10 W.cm^{-2}.K^{-1}, and the device conductance $G_{\text{th},\Sigma}$ to 0.1 and 1 W.cm^{-2}.K^{-1}.

C.2 Thermophotovoltaics and near-field thermophotovoltaics

We consider that the PV cell is kept at constant temperature to be consistent with NF-TPX calculations. We assume blackbody radiation between the emitter and the PV cell in the case of far-field TPV. Without any non-radiative losses (upper limit) we have:

$$\begin{aligned} P = U_{\text{PV}} \cdot J_{\text{PV}}(U_{\text{PV}}) &= eU_{\text{PV}} \cdot \dot{N}_{\text{net}} \\ &= eU_{\text{PV}} \cdot \frac{\hbar}{4\pi^2 c^2} \int_{\omega_g}^{\infty} \Delta f_{\text{BE}}(\omega) \cdot \omega^3 d\omega \end{aligned} \tag{C.2}$$

If non-radiative losses are added through a flat QE (as in Chapter 3), this becomes:

$$P = U \cdot J_{\text{PV}}(U_{\text{PV}}) = eU_{\text{PV}} \cdot \left(\dot{N} - \frac{1 - \text{QE}}{\text{QE}} (\dot{N}_{\text{em}}(U_{\text{PV}}) - \dot{N}_{\text{em}}(0)) \right) \tag{C.3a}$$

$$\dot{N}_{\text{em}}(U_{\text{PV}}) = \frac{\hbar}{4\pi^2 c^2} \int_{\omega_g}^{\infty} f_{\text{BE,PV}}(\omega, eU_{\text{PV}}, T_{\text{PV}}) \cdot \omega^3 d\omega \tag{C.3b}$$

In this case, we have used $E_g = 0.354$ eV, corresponding to the bandgap of InAs. This low bandgap allows to obtain good capabilities at moderate emitter temperature. For the lower bound, we use a QE of 6×10^{-5}, which allows to obtain a power output similar to that of Milovich et al. [Milovich *et al.* 2020] in the far field at 800 K.

For the near-field effects, we assume a simple enhancement factor equal to 50 compared to the far-field value. This factor corresponds to a rough extrapolation of the power enhancement factor given in [Milovich *et al.* 2020], which is equal to 30 for a 100 nm gap distance.

Appendix D

Additional derivations of the efficiency at maximum power

D.1 Efficiency at maximum power of a monochromatic TPX device derived with Boltzmann's approximation

As a reminder, $P = (\mu_c - \mu_h)\dot{N}$ and $\eta = (\mu_c - \mu_h)/(E_g - \mu_h)$. To obtain the maximum power point, we search for the couple of chemical potentials which cancels the different partial derivatives of the power output. With the Boltzmann approximation, the Bose-Einstein distribution $f_{BE}(x) = 1/(\exp(x) - 1)$ can be approximated by $\exp(-x)$ - this holds if $x \gg 0$. Using this approximation, we obtain

$$\frac{\partial \dot{N}_i}{\partial \mu_i}(\mu_i) = \frac{1}{k_B T_i}\dot{N}_i, \tag{D.1}$$

and therefore

$$\frac{\partial P}{\partial \mu_h}(\mu_h, \mu_c) = -(\dot{N}_h - \dot{N}_c) + \frac{\mu_c - \mu_h}{k_B T_h}\dot{N}_h, \tag{D.2a}$$

$$\frac{\partial P}{\partial \mu_c}(\mu_h, \mu_c) = (\dot{N}_h - \dot{N}_c) - \frac{\mu_c - \mu_h}{k_B T_c}\dot{N}_c. \tag{D.2b}$$

Hence, we obtain at the maximum power point

$$\begin{aligned} &\frac{\partial P}{\partial \mu_h}(\mu_{h,MPP}, \mu_{c,MPP}) = \frac{\partial P}{\partial \mu_c}(\mu_{h,MPP}, \mu_{c,MPP}) = 0 \\ \Leftrightarrow &\dot{N}_h - \dot{N}_c = \frac{\mu_{c,MPP} - \mu_{h,MPP}}{k_B T_h}\dot{N}_h = \frac{\mu_{c,MPP} - \mu_{h,MPP}}{k_B T_c}\dot{N}_c. \end{aligned} \tag{D.3}$$

We can then obtain a relation between μ_c and μ_h at MPP:

$$\begin{aligned} &\dot{N}_c = \left(1 - \frac{\mu_{c,MPP} - \mu_{h,MPP}}{k_B T_h}\right)\dot{N}_h = \left(1 - \frac{\mu_{c,MPP} - \mu_{h,MPP}}{k_B T_h}\right)\left(1 + \frac{\mu_{c,MPP} - \mu_{h,MPP}}{k_B T_c}\right)\dot{N}_c \\ &\Leftrightarrow \left(1 + \frac{\mu_{c,MPP} - \mu_{h,MPP}}{k_B T_c}\right)\left(1 - \frac{\mu_{c,MPP} - \mu_{h,MPP}}{k_B T_h}\right) = 1 \\ &\Leftrightarrow (\mu_{c,MPP} - \mu_{h,MPP})(k_B T_h - k_B T_c - \mu_{c,MPP} + \mu_{h,MPP}) = 0 \\ &\Leftrightarrow \mu_{c,MPP} - \mu_{h,MPP} = k_B(T_h - T_c), \end{aligned} \tag{D.4}$$

since $\mu_{\mathrm{c,MPP}} \neq \mu_{\mathrm{h,MPP}}$ to generate any power. This simple expression obtained for the difference of chemical potentials allows to simplify the first expression provided in Eq. (D.4):

$$\begin{aligned}
&\dot{N}_{\mathrm{c}} = \left(1 - \frac{\mu_{\mathrm{c,MPP}} - \mu_{\mathrm{h,MPP}}}{k_{\mathrm{B}} T_{\mathrm{h}}}\right) \dot{N}_{\mathrm{h}} \\
\Leftrightarrow &\dot{N}_{\mathrm{c}} = (1 - \eta_{\mathrm{C}}) \dot{N}_{\mathrm{h}} \\
\Leftrightarrow &\exp\left(\frac{\mu_{\mathrm{c,MPP}} - E_g}{k_{\mathrm{B}} T_{\mathrm{c}}}\right) = (1 - \eta_{\mathrm{C}}) \exp\left(\frac{\mu_{\mathrm{h,MPP}} - E_g}{k_{\mathrm{B}} T_{\mathrm{h}}}\right) \\
\Leftrightarrow &\exp\left(\frac{k_{\mathrm{B}}(T_{\mathrm{h}} - T_{\mathrm{c}}) + \mu_{\mathrm{h,MPP}} - E_g}{k_{\mathrm{B}} T_{\mathrm{c}}}\right) = (1 - \eta_{\mathrm{C}}) \exp\left(\frac{\mu_{\mathrm{h,MPP}} - E_g}{k_{\mathrm{B}} T_{\mathrm{h}}}\right) \\
\Leftrightarrow &\frac{\mu_{\mathrm{h,MPP}} - E_g}{k_{\mathrm{B}} T_{\mathrm{h}}} \left(1 - \frac{T_{\mathrm{h}}}{T_{\mathrm{c}}}\right) = \frac{T_{\mathrm{h}}}{T_{\mathrm{c}}} - 1 - \ln(1 - \eta_{\mathrm{C}}) \\
\Leftrightarrow &\frac{\mu_{\mathrm{h,MPP}} - E_g}{k_{\mathrm{B}} T_{\mathrm{h}}} = 1 - \frac{1 - \eta_{\mathrm{C}}}{\eta_{\mathrm{C}}} \ln(1 - \eta_{\mathrm{C}}).
\end{aligned} \tag{D.5}$$

The efficiency at maximum power is therefore expressed as

$$\begin{aligned}
\eta_{\mathrm{MPP}} &= \frac{\mu_{\mathrm{c,MPP}} - \mu_{\mathrm{h,MPP}}}{E_g - \mu_{\mathrm{h,MPP}}} \\
&= \frac{k_{\mathrm{B}}(T_{\mathrm{h}} - T_{\mathrm{c}})}{k_{\mathrm{B}} T_{\mathrm{h}} \left(1 - \frac{1 - \eta_{\mathrm{C}}}{\eta_{\mathrm{C}}} \ln(1 - \eta_{\mathrm{C}})\right)} \\
&= \frac{\eta_{\mathrm{C}}^2}{\eta_{\mathrm{C}} - (1 - \eta_{\mathrm{C}} \ln(1 - \eta_{\mathrm{C}}))},
\end{aligned} \tag{D.6}$$

which corresponds to the efficiency derived in [Tu 2008] for a Feynmann ratchet heat engine. As a side note, we can show using Eqs. (D.4) and (D.5) that $E_g - \mu_{opt}$ is of the order of several $k_{\mathrm{B}}T$ ($2k_{\mathrm{B}}T$ being the minimum reached for $T_{\mathrm{c}}/T_{\mathrm{h}} = 1$): while this is quite different from the result obtained with Taylor's expansion in Section 2.1, the maximum efficiency remains very close (at least for moderate heat source temperature).

D.2 Maximum power point for complete above-bandgap radiation

As a reminder, setting $X_i = \exp((\mu_i - E_g)/k_{\mathrm{B}}T_i)$, the expression of the electrical power generation is

$$P = \frac{E_g^2 k_{\mathrm{B}}^2 T_{\mathrm{h}}^2}{4\pi^2 c^2 \hbar^3} \left(\ln(X_{\mathrm{h}}) - \ln(X_{\mathrm{c}}) \frac{T_{\mathrm{c}}}{T_{\mathrm{h}}}\right) \left(\ln(1 - X_{\mathrm{h}}) - \ln(1 - X_{\mathrm{c}}) \frac{T_{\mathrm{c}}}{T_{\mathrm{h}}}\right). \tag{D.7}$$

Our goal is to determine the couple $(X_{\mathrm{h}}, X_{\mathrm{c}})$ which allows maximising P. The first thing to verify is whether the maximum power is reached inside the domain (i.e. for $0 < X_i < 1$) or at the boundary. For instance, if X_{h} goes to 0, it gives

$$P \sim -\frac{E_g^2 k_{\mathrm{B}}^2 T_{\mathrm{h}}^2}{4\pi^2 c^2 \hbar^3} \ln(X_{\mathrm{h}}) \ln(1 - X_{\mathrm{c}}) \frac{T_{\mathrm{c}}}{T_{\mathrm{h}}} \to -\infty, \tag{D.8}$$

and the maximum power is therefore not reached at this boundary (the power being negative). A similar treatment can be done at the three other boundaries to ensure that the maximum power point is indeed located inside the domain. We should then find the couple $(X_{\mathrm{h}}, X_{\mathrm{c}})$ which makes both partial derivatives equal to zero. If the couple found is unique, it is the maximum power

point since P goes to $-\infty$ at the boundaries (which means that a maximum power point must exist).

The partial derivatives of P with respect to X_i are

$$\frac{\partial P}{\partial X_\mathrm{h}}(X_\mathrm{h}, X_\mathrm{c}) = \frac{\ln(1-X_\mathrm{h}) - \ln(1-X_\mathrm{c})\frac{T_\mathrm{c}}{T_\mathrm{h}}}{X_\mathrm{h}} - \frac{\ln(X_\mathrm{h}) - \ln(X_\mathrm{c})\frac{T_\mathrm{c}}{T_\mathrm{h}}}{1-X_\mathrm{h}}, \tag{D.9a}$$

$$\frac{\partial P}{\partial X_\mathrm{c}}(X_\mathrm{h}, X_\mathrm{c}) = -\frac{T_\mathrm{c}}{T_\mathrm{h}}\left(\frac{\ln(1-X_\mathrm{h}) - \ln(1-X_\mathrm{c})\frac{T_\mathrm{c}}{T_\mathrm{h}}}{X_\mathrm{c}} - \frac{\ln(X_\mathrm{h}) - \ln(X_\mathrm{c})\frac{T_\mathrm{c}}{T_\mathrm{h}}}{1-X_\mathrm{c}}\right). \tag{D.9b}$$

Then

$$\frac{\partial P}{\partial X_\mathrm{h}}(X_\mathrm{h}, X_\mathrm{c}) = 0 \Leftrightarrow \frac{\ln(1-X_\mathrm{h}) - \ln(1-X_\mathrm{c})\frac{T_\mathrm{c}}{T_\mathrm{h}}}{\ln(X_\mathrm{h}) - \ln(X_\mathrm{c})\frac{T_\mathrm{c}}{T_\mathrm{h}}} = \frac{X_\mathrm{h}}{1-X_\mathrm{h}}, \tag{D.10a}$$

$$\frac{\partial P}{\partial X_\mathrm{c}}(X_\mathrm{h}, X_\mathrm{c}) = 0 \Leftrightarrow \frac{\ln(1-X_\mathrm{h}) - \ln(1-X_\mathrm{c})\frac{T_\mathrm{c}}{T_\mathrm{h}}}{\ln(X_\mathrm{h}) - \ln(X_\mathrm{c})\frac{T_\mathrm{c}}{T_\mathrm{h}}} = \frac{X_\mathrm{c}}{1-X_\mathrm{c}}. \tag{D.10b}$$

Note that this holds only if $\ln(X_\mathrm{h}) - \ln(X_\mathrm{c})\frac{T_\mathrm{c}}{T_\mathrm{h}}$ is non-zero at the maximum power point. If the former term was equal to zero, then $\ln(1-X_\mathrm{h}) - \ln(1-X_\mathrm{c})\frac{T_\mathrm{c}}{T_\mathrm{h}}$ should also be zero to satisfy that partial derivatives are equal to zero, which would give the condition $1 - X_\mathrm{c}^{T_\mathrm{c}/T_\mathrm{h}} = (1-X_\mathrm{c})^{T_\mathrm{c}/T_\mathrm{h}}$. This equation being satisfied only for X_c equal to 0 or 1 (which are not inside the domain), $\ln(X_\mathrm{h}) - \ln(X_\mathrm{c})\frac{T_\mathrm{c}}{T_\mathrm{h}}$ is therefore non-zero at the maximum power point.

Combining the two expressions given in Eq. (D.10), we have

$$\frac{\partial P}{\partial X_\mathrm{h}}(X_\mathrm{h}, X_\mathrm{c}) = \frac{\partial P}{\partial X_\mathrm{c}}(X_\mathrm{h}, X_\mathrm{c}) = 0 \Rightarrow X_\mathrm{h} = X_\mathrm{c}. \tag{D.11}$$

We can now write $X = X_\mathrm{h} = X_\mathrm{c}$ and $x = x_\mathrm{h} = x_\mathrm{c}$, which gives

$$P = \frac{E_g^2 k_\mathrm{B}^2 T_\mathrm{h}^2}{4\pi^2 c^2 \hbar^3}\eta_\mathrm{C}^2 \ln(X)\ln(1-X). \tag{D.12}$$

Notice how P is symmetric around the axis $X = 1/2$ (since $P(X) = P(1-X)$): the couple $(X_\mathrm{h} = 1/2, X_\mathrm{c} = 1/2)$ is therefore the only couple which allows making partial derivatives equal to zero, and corresponds consequently to the maximum power point of P. Since $X = \exp(-x)$, the maximum power point is reached for $(x_\mathrm{h} = \ln(2), x_\mathrm{c} = \ln(2))$.

Appendix E

Detailed numerical methods for 1D drift-diffusion resolution

This appendix aims to detail different equations and numerical schemes considered for the resolution of the drift-diffusion equations. The different equations given correspond to those obtained in non-equilibrium conditions and for heterostructures. They are given in the order of resolution during an iteration.

The first element to mention is the spatial mesh implemented for the different electrical quantities. In our case, we consider an almost uniform grid in each layer. More precisely, two nodes are placed on each side of every interface, at a distance $\delta z = 1$ pm to help convergence in the case of heterojunctions. The grid is uniform between these two nodes in a layer, the spatial step being indirectly set by the user through the grid size in each layer[1]. The grid is represented in Figure E.1.

E.1 Current densities and continuity equations

E.1.1 Total current

We start by computing the total electron and hole current densities in a component. Partially following the Scharfetter-Gummel implementation [Scharfetter & Gummel 1969], current densities are not resolved at the grid nodes, but in-between each grid nodes. In the following, we take the example of the electron current, the resolution being similar for holes. Assuming that the leftmost layer is p-doped, the electron current density at the interface (node 1) equals $J_{n,1} = e \cdot R_{\text{surf}}$.

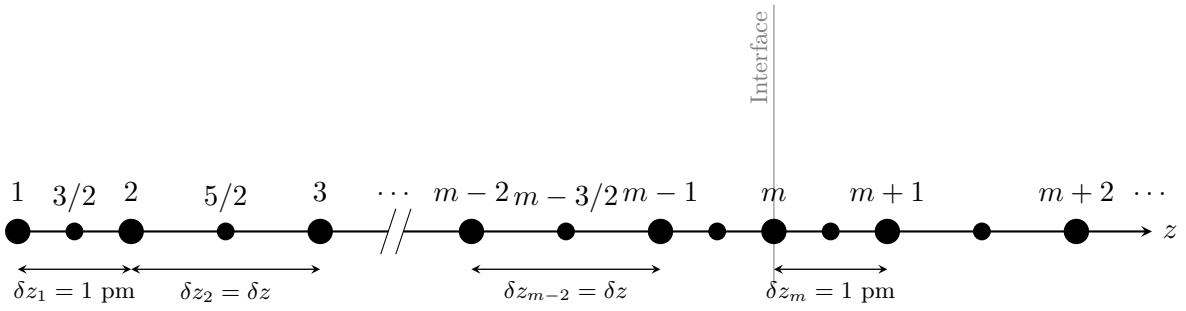

Figure E.1: Schematic of the spatial grid.

[1]Since large variations occur around interfaces, the implementation of adaptative mesh could help increase the precision of the results and potentially reduce the computational time. It would be a useful improvement of the current solver.

Using a trapezoidal rule, the electron current at node 3/2 is then expressed as

$$\begin{aligned} J_{n,3/2} &= J_{n,1} + e\frac{\delta z_1}{4}\left(R_1 - G_1 + \frac{1}{2}[R_1 - G_1 + R_2 - G_2]\right) \\ &= J_{n,1} + e\frac{\delta z_1}{2}\left(\frac{3}{4}(R_1 - G_1) + \frac{1}{4}(R_2 - G_2)\right). \end{aligned} \tag{E.1}$$

Inside a layer, the current at node $i + 1/2$ is then

$$J_{n,\mathrm{i}+1/2} = J_{n,\mathrm{i}-1/2} + e\frac{\delta z_{i-1} + \delta z_i}{2}\left(\frac{1}{4}(R_{i-1} - G_{i-1}) + \frac{1}{2}(R_i - G_i) + \frac{1}{4}(R_{i+1} - G_{i+1})\right). \tag{E.2}$$

In the next steps of the calculations, the current must be known at each interface. Therefore, the current at the interface (at node m) is calculated in a similar fashion to Eq. (E.1) from the current at node $m - 1/2$.

The equations provided above allow obtaining J_n if its value is originally known at node 1 (i.e. if the leftmost layer is p-doped). On the contrary, if the leftmost layer is n-doped, then the calculation of J_n shall be done in the opposite direction, from node N (where J_n is known) towards node 1. In this case, the resolution is relatively similar, except that we shall take $J_{n,N} = -e \cdot R_{\mathrm{surf}}$. This comes from the fact that we perform the resolution backwards. Indeed, we have

$$J_n(z) = J_n(t) - e\int_z^t (R(z') - G(z'))dz', \tag{E.3}$$

and the only way to add the bulk recombination rate $R(z)$ to the surface recombination rate R_{surf} (instead of subtract it) is to take $J_n(t) = -e \cdot R_{\mathrm{surf}}$. Doing the resolution in this manner however has the undesired consequence that the total current has opposite sign whether the front layer is n- or p-doped. To correct this, the total current density returned by the solver at the end of the calculation is taken as the opposite of $J_n + J_p$ in the case of a front p-doped layer, which allows to have $J > 0$ for PV cells and $J < 0$ for LEDs.

E.1.2 Tunnelling and drift-diffusion current

The current expressed above corresponds to the total electron current. To obtain the drift-diffusion current, one should subtract the tunnelling current from the total quantity. Eq. (6.16) can be transformed into

$$\begin{aligned} J_{n,\mathrm{drift-diff}}(z) &= \frac{\eta + \varphi(z)}{\eta + \varphi} J_n(z_0) + e\int_{z_0}^{z} (R(z') - G(z'))dz' \\ &= J_n(z) - \frac{\varphi - \varphi(z)}{\eta + \varphi} J_n(z_0), \end{aligned} \tag{E.4}$$

where z_0 corresponds to the position of the interface. The only unknown is $\varphi(z)$ (along with its limit φ), whose expression is provided in Eq. (6.18). Two successive trapezoidal rules are applied to compute it: one first to obtain the electron transmission coefficient $\mathcal{T}(E)$ after integrating on position, and a second to obtain $\varphi(z)$ after integrating on energy. In the following J_n will correspond to the drift-diffusion electron current to simplify the notation.

E.2 Slotboom variables and drift-diffusion equations

Next, the Slotboom variables shall be expressed from the drift-diffusion current. To do so, we use the drift-diffusion equations, and more precisely the discretisation method proposed in [Scharfetter & Gummel 1969] and discussed in [Vasileska *et al.* 2017]. For electrons, it gives

$$J_{n,i+1/2} = \frac{eD_{n\,i+1/2}}{\delta z_i}(n_{i+1}B(\Psi_{i+1}-\Psi_i) - n_i B(\Psi_i - \Psi_{i+1})), \tag{E.5}$$

where B is the Bernoulli function defined as $B(x) = x/(\exp(x)-1)$; if x is too close to 0, $B(x)$ shall rather be computed from its Taylor expansion around 0 to prevent numerical errors: $B(x) \approx 1 - x/2 + x^2/12$. The equation above however relates the current to the charge carrier density, not to the Slotboom variable. In a homogeneous material, it can be translated into

$$\begin{aligned} J_{n,i+1/2} &= \frac{eD_{n,i+1/2}}{\delta z_i} n_\mathrm{i}(0) e^{\xi_{n,i+1/2}+\Psi_{i+1}} B(\Psi_{i+1}-\Psi_i)(\Phi_{n,i+1}-\Phi_{n,i}) \\ &= \mathcal{G}_{n,i+1/2}(\Phi_{n,i+1}-\Phi_{n,i}), \end{aligned} \tag{E.6}$$

$\mathcal{G}$ being a parameter relating J and Φ and being independent of these two quantities. At the electrical contact where electrons are in majority, Φ_n is known and equal to $\exp(eU/k_\mathrm{B}T)$. We must last relate the current at an interface between two semiconductors to the drop of Φ_n at this interface. This is done by using the expression of the total thermionic-field current of electrons at the interface provided in Eq. (6.12), which gives

$$J_{n,m} = \mathcal{G}_{n,m}(\Phi_{n,m,\mathrm{right}} - \Phi_{n,m,\mathrm{left}}), \tag{E.7}$$

where $\mathcal{G}_{n,m} = A^*_\mathrm{left} T^2(\eta+\varphi)e^{-\tilde{E}_{\mathrm{C,max}}}$. In the equations above, $J_{n,m}$ is the drift-diffusion current but equals the total current if taken on the right side of the interface (i.e. not on the barrier side). With these different equations, Φ_n can be computed from the contact where electrons are in majority towards the opposite contact.

E.3 Electrostatic potential and Poisson equation

Last, the Poisson equation must be solved to obtain the normalised electrostatic potential Ψ. However, this equation is non-linear; we therefore linearise it and solve it iteratively. Let Ψ^j be the value of Ψ at iteration j. Assuming the variation between two iterations steps is small enough ($\delta\Psi = \Psi^{j+1} - \Psi^j \ll 1$), we can use Taylor's expansion $\exp(\pm\delta\Psi) = 1 \pm \delta\Psi$. The Poisson equation for heterostructure then becomes

$$\begin{aligned} \frac{\mathrm{d}^2\delta\Psi}{\mathrm{d}\tilde{z}^2}(z) &= -\frac{\mathrm{d}^2\Psi^j}{\mathrm{d}\tilde{z}^2}(z) + e^{\xi_n}e^{\Psi^j(z)}(1+\delta\Psi(z))\Phi_n(z) - e^{\xi_p}e^{-\Psi^j(z)}(1-\delta\Psi(z))\Phi_p(z) + \tilde{N}_\mathrm{dop}(z) \\ &= -\frac{\mathrm{d}^2\Psi^j}{\mathrm{d}\tilde{z}^2}(z) + \delta\Psi(z)\Big(e^{\xi_n}e^{\Psi^j(z)}\Phi_n(z) + e^{\xi_p}e^{-\Psi^j(z)}\Phi_p(z)\Big) \\ &\qquad + \Big(e^{\xi_n}e^{\Psi^j(z)}\Phi_n(z) - e^{\xi_p}e^{-\Psi^j(z)}\Phi_p(z)\Big) + \tilde{N}_\mathrm{dop}(z), \end{aligned} \tag{E.8}$$

where $\tilde{z}$ and $\tilde{N}_\mathrm{dop}$ must be defined relatively to the intrinsic carrier concentration in the first layer $n_\mathrm{i}(0)$, not to its value in the current layer n_i.

Since the distance between two nodes is different close to the interfaces than in most of the layers, we need to use a finite difference scheme that works with an irregular grid. The second-order

central finite difference of the second derivative of Ψ can be written on an irregular mesh as

$$\frac{\mathrm{d}^2\Psi}{\mathrm{d}z^2}(z_i) \approx \frac{K_i(1)\Psi_{i-1} + K_i(2)\Psi_i + K_i(3)\Psi_{i+1}}{\delta z_{i-1}^2}, \tag{E.9}$$

where

$$K_i = 2\left[\frac{1}{a_i+1} \quad -\frac{1}{a_i} \quad \frac{1}{a_i(a_i+1)}\right], a_i = \frac{\delta z_i}{\delta z_{i-1}}. \tag{E.10}$$

At the boundaries, we suppose that charge neutrality holds, which implies that at any iteration j

$$e^{\xi_n} e^{\Psi^j(z)} \Phi_n(z) - e^{\xi_p} e^{-\Psi^j(z)} \Phi_p(z) + \tilde{N}_{\mathrm{dop}}(z) = 0. \tag{E.11}$$

Following [Blandre 2016], replacing e^{Ψ} by X allows to obtain a quadratic equation and thus to derive the value of Ψ at the boundaries:

$$\begin{aligned}\Psi(z_n) = &-\xi_n(z_n) - \ln(\Phi_n(z_n)) \\ &+ \ln\left(\sqrt{\left(\frac{\tilde{N}_{\mathrm{dop}}(z_n)}{2}\right)^2 + e^{\xi_n(z_n)+\xi_p(z_n)}\Phi_n(z_n)\Phi_p(z_n)} - \frac{\tilde{N}_{\mathrm{dop}}(z_n)}{2}\right),\end{aligned} \tag{E.12a}$$

$$\begin{aligned}\Psi(z_p) = &\quad \xi_p(z_p) + \ln(\Phi_p(z_p)) \\ &- \ln\left(\sqrt{\left(\frac{\tilde{N}_{\mathrm{dop}}(z_p)}{2}\right)^2 + e^{\xi_n(z_p)+\xi_p(z_p)}\Phi_n(z_p)\Phi_p(z_p)} + \frac{\tilde{N}_{\mathrm{dop}}(z_p)}{2}\right),\end{aligned} \tag{E.12b}$$

where z_n and z_p represent respectively the position of the n and p contacts. Since these expressions do not depend on the value of Ψ in adjacent nodes, Ψ is perfectly known at the boundaries and therefore $\delta\Psi = 0$. Note that both of the equations above should theoretically work for any of the two contacts. However, numerical errors become significant if the term inside the last logarithm is close to zero, which depends on the sign of $\tilde{N}_{\mathrm{dop}} = (N_{\mathrm{a}} - N_{\mathrm{d}})/n_{\mathrm{i}}(0)$: in Eq. (E.12a) for instance, this term becomes small if $\tilde{N}_{\mathrm{dop}} \gg 1$, hence if the layer is p-doped. This is why two different expressions are used for the boundary conditions. These expressions are also used to obtain a first guess of Ψ in equilibrium equations. In subsequent calculations, the first guess corresponds to the value of Ψ used in the previous equations (see the flowchart in Figure 6.5 for more details).

At the interfaces between semiconductors, the electric displacement field is supposed to be continuous. This gives a condition on the electrostatic potential first derivative, as expressed in Eq. (6.21):

$$\varepsilon_s(z^-)\frac{\mathrm{d}\Psi}{\mathrm{d}z}(z^-) = \varepsilon_s(z^+)\frac{\mathrm{d}\Psi}{\mathrm{d}z}(z^+). \tag{E.13}$$

These two derivatives are expressed using respectively a backward and a forward finite difference. The related second-order finite difference schemes on an irregular mesh are respectively

$$\frac{\mathrm{d}\Psi}{\mathrm{d}z}(z_m) \approx \frac{K_m^B(1)\Psi_{m-2} + K_m^B(2)\Psi_{m-1} + K_m^B(3)\Psi_m}{\delta z_{m-1}^2}, \tag{E.14a}$$

$$\frac{\mathrm{d}\Psi}{\mathrm{d}z}(z_m) \approx \frac{K_m^F(1)\Psi_m + K_m^F(2)\Psi_{m+1} + K_m^F(3)\Psi_{m+2}}{\delta z_m^2}, \tag{E.14b}$$

where

$$K_m^B = \begin{bmatrix} \frac{a_m^2}{a_m+1} & -(a_m+1) & \frac{2a_m+1}{a_m+1} \end{bmatrix}, K_m^F = \begin{bmatrix} -\frac{a_m+2}{a_m+1} & \frac{a_m+1}{a_m} & -\frac{1}{a_m(a_m+1)} \end{bmatrix}. \tag{E.15}$$

To solve the Poisson equation, we use a tridiagonal matrix algorithm. This requires that the equation at node i depends only on the value of $\delta\Psi$ at this node or at the adjacent ones. While it is the case in the layers and at the boundaries, it is not at the interfaces between semiconductors, where we also have a dependency on Ψ_{m-2} and Ψ_{m+2}. To correct this, the equation at the interface is combined with the Poisson equation obtained at node $m-1$ and $m+1$ to cancel the terms related to Ψ_{m-2} and Ψ_{m+2}.

Appendix F

Supplementary data on 1D charge transport

F.1 Low-field vs. field-dependent mobility

In all Part II, the mobility was expressed using a low-field expression, making it independent of the electric field. But the average drift velocity, equal to μE, saturates under a strong electric field: therefore, mobility must decrease accordingly. To quantify the impact of the low-field approximation, we analyse how using a field-dependent expression modifies the performance of the optimised device composed of AlGaAs homostructures from Chapter 5. To do so, we use the expression from [Xu & Shur 1987] for GaAs, and assume it to be valid for AlGaAs. The change of mobility obtained in the PV cell at equilibrium is first displayed in Figure F.1a. Clearly, mobility can drop significantly close to the junctions, with a decrease of more than an order of magnitude for electron mobility. However, as voltage increases, the built-in field decreases in amplitude, damping the mobility reduction. Eventually, mobility remains sufficiently high to prevent significant change of power output, as revealed by Figure F.1b.

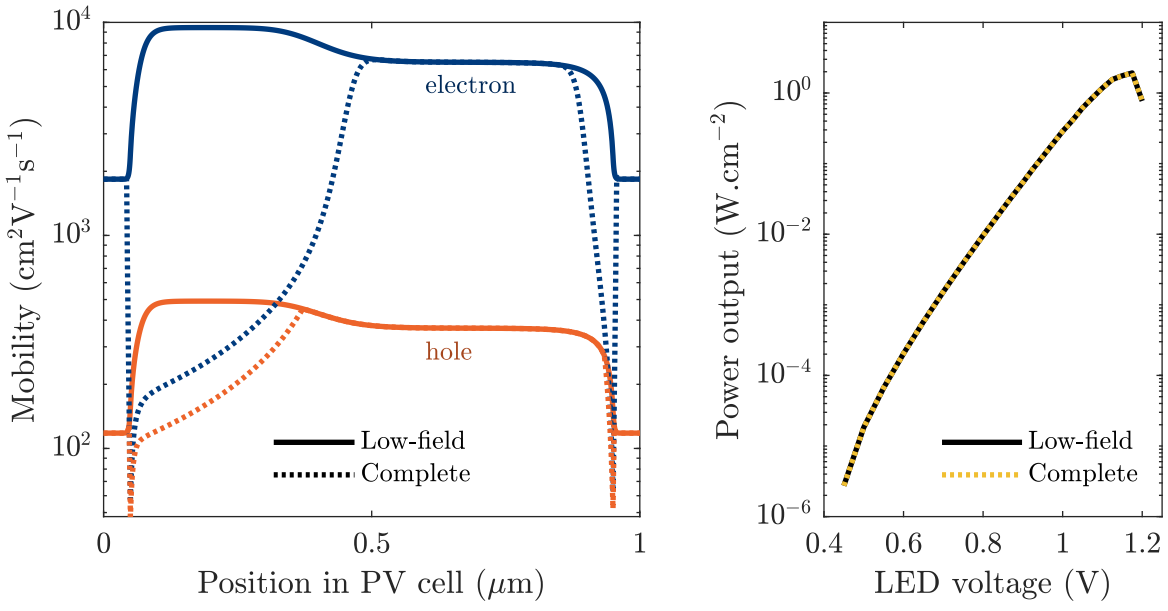

Figure F.1: Impact of using low-field or field-dependent mobility (a) on the value of mobility in the PV cell at equilibrium, (b) on the overall TPX performance. The device considered is provided in Figure 5.4.

F.2 Effect of net internal photon flux on performance of AlGaAs/InGaP device

The results gathered in Chapter 6 were obtained by assuming that the contribution of the net photon transfer occurring inside a component to the overall photon flux density was negligible. Such as assumption is made valid by the low thickness of the confinement layers and by their transparency for photon energy close to the bandgap of the active layers. To ensure the validity of the assumption, we show in Figure F.2 how the P-V_{LED} characteristic of the AlGaAs/InGaP device represented in Figure 6.10a is impacted by including this contribution[1]. Quantitatively, no change can be observed. The power output actually decreases slightly due to this new contribution, but is indeed negligible: the maximum power output, which is originally close to 1.8 W.cm^{-2}, decreases only by 20 mW.cm^{-2}. This low impact can be attributed to the low transmission of photons from active layers to adjacent confinement layers: the transmission function at the active layer bandgap $\mathcal{F}(E_g)$, defined as

$$\frac{1}{4\pi^2}\int_0^\infty \mathcal{T}(E_g,k_\rho)k_\rho dk_\rho = \frac{\dot{N}_{E_g,\text{net}}}{\Delta f_{\text{BE}}}, \tag{F.1}$$

equals 5×10^8 cm^{-2} between the two active layers, but only 3×10^5 cm^{-2} between an active layer and the adjacent confinement layers (in the absence of evanescent contribution in the latter case).

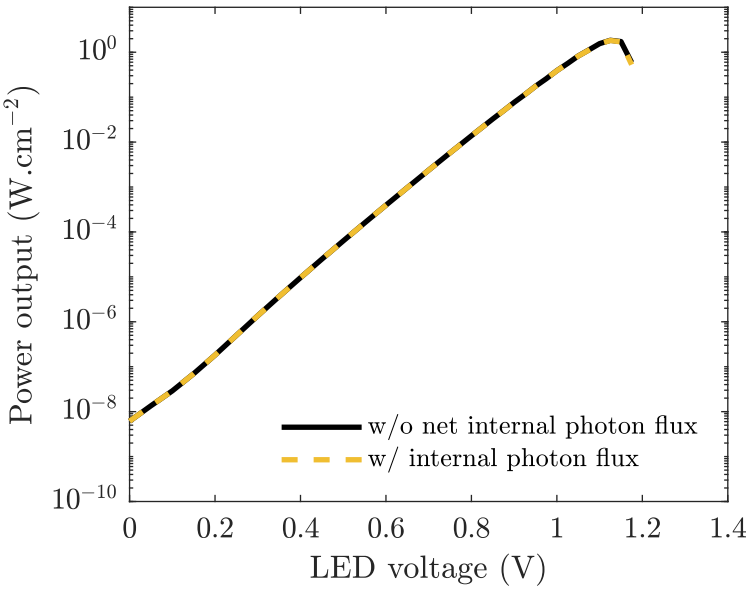

Figure F.2: P-V_{LED} characteristic of the AlGaAs/InGaP device represented in Figure 6.10a, either with or without the contribution of the photon flux internal to a component.

[1]Note that these results were obtained with a relatively rough mesh for simplicity.

F.3 Impact of tunnelling under high illumination

In Chapter 6, we showed that our in-house solver returned results similar to SCAPS for the charge transport occurring in heterostructures. For these simulations, both thermionic emission and charge carrier tunnelling were included. To quantify how much tunnelling impacts charge transport, we show in Figure F.3 the I-V characteristic of the PV cell voltage obtained with SCAPS with or without tunnelling, considering a 1.15 V LED voltage. The comparison is not done with our solver as it does not converge for such a strong illumination when tunnelling is ignored. The effect of ignoring tunnelling is large, with more than an order of magnitude of difference in current for a given voltage: this highlights the importance of including it in calculations under high illumination. Current being highly sensitive to tunnelling, the good match of the results obtained with our solver and with SCAPS confirms that our implementation of charge carrier tunnelling is correct - or at least, similar to SCAPS.

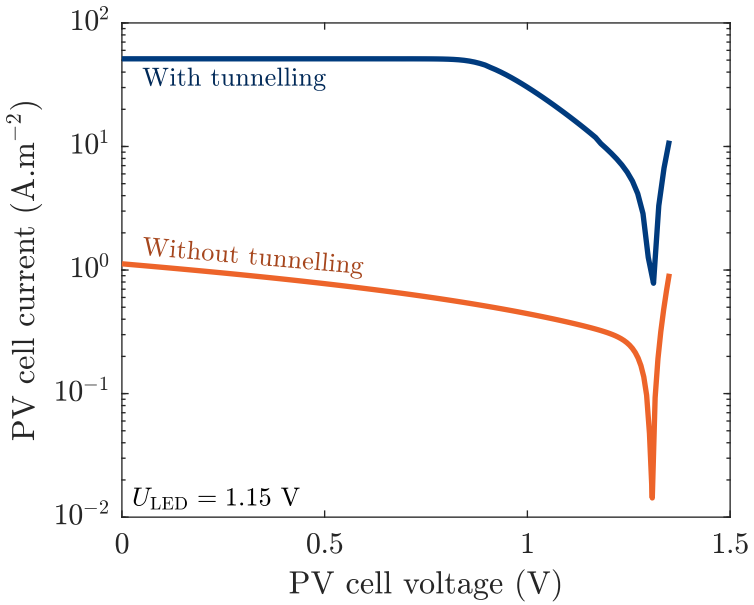

Figure F.3: I-V characteristic of the PV cell from Figure 5.2 with an LED voltage of 1.15 V.

Bibliography

[Adachi 1987] Sadao Adachi. *Model dielectric constants of GaP, GaAs, GaSb, InP, InAs, and InSb.* Physical Review B, vol. 35, no. 14, pages 7454–7463, 1987. (Cited on page 24.)

[Adachi 1988] Sadao Adachi. *Optical properties of $Al_xGa_{1-x}As$ alloys.* Physical Review B, vol. 38, no. 17, pages 12345–12352, dec 1988. (Cited on page 126.)

[Adachi 1989] Sadao Adachi. *Optical dispersion relations for GaP, GaAs, GaSb, InP, InAs, InSb, $Al_xGa_{1-x}As$, and $In_{1-x}Ga_xAs_yP_{1-y}$.* Journal of Applied Physics, vol. 66, no. 12, pages 6030–6040, dec 1989. (Cited on pages 25 and 26.)

[Adachi 1994] Sadao Adachi. GaAs and Related Materials. WORLD SCIENTIFIC, oct 1994. (Cited on pages 22, 71, 177 and 178.)

[Adachi 1999a] Sadao Adachi. Optical Constants of Crystalline and Amorphous Semiconductors. Springer US, Boston, MA, 1999. (Cited on page 178.)

[Adachi 1999b] Sadao Adachi. Optical Properties of Crystalline and Amorphous Semiconductors. Springer US, Boston, MA, 1999. (Cited on page 178.)

[ADEME 2017] ADEME. *La chaleur fatale.* Technical report, ADEME, 2017. (Cited on pages 1 and 16.)

[Aeberhard *et al.* 2021] Urs Aeberhard, Simon Zeder and Beat Ruhstaller. *Reconciliation of dipole emission with detailed balance rates for the simulation of luminescence and photon recycling in perovskite solar cells.* Optics Express, vol. 29, no. 10, page 14773, may 2021. (Cited on page 145.)

[Alberi *et al.* 2011] Kirstin Alberi, Brian Fluegel, Myles A. Steiner, Ryan M. France, Waldo J. Olavarria and Angelo Mascarenhas. *Direct-indirect crossover in $Ga_xIn_{1-x}P$ alloys.* Journal of Applied Physics, vol. 110, no. 11, pages 1–6, 2011. (Cited on page 178.)

[Antora Energy 2023] Antora Energy. https://antoraenergy.com/, 2023. (Cited on pages 15 and 30.)

[Apertet *et al.* 2012a] Y. Apertet, H. Ouerdane, O. Glavatskaya, C. Goupil and P. Lecoeur. *Optimal working conditions for thermoelectric generators with realistic thermal coupling.* EPL (Europhysics Letters), vol. 97, no. 2, page 28001, jan 2012. (Cited on pages 85, 169 and 181.)

[Apertet *et al.* 2012b] Y. Apertet, H. Ouerdane, C. Goupil and P. Lecoeur. *Irreversibilities and efficiency at maximum power of heat engines: The illustrative case of a thermoelectric generator.* Physical Review E, vol. 85, no. 3, page 031116, mar 2012. (Cited on page 42.)

[Apertet *et al.* 2017] Y. Apertet, H. Ouerdane, C. Goupil and P. Lecoeur. *True nature of the Curzon-Ahlborn efficiency.* Physical Review E, vol. 96, no. 2, pages 1–6, 2017. (Cited on page 42.)

[Apertet 2014] Y. Apertet. *Réflexions sur l'optimisation thermodynamique des générateurs thermoélectriques.* PhD thesis, Université Paris-Sud, 2014. (Cited on page 42.)

[Basore 1990] P.A. Basore. *Numerical modeling of textured silicon solar cells using PC-1D.* IEEE Transactions on Electron Devices, vol. 37, no. 2, pages 337–343, 1990. (Cited on page 99.)

[Bender *et al.* 2013] Daniel A. Bender, Jeffrey G. Cederberg, Chengao Wang and Mansoor Sheik-Bahae. *Development of high quantum efficiency GaAs/GaInP double heterostructures for laser cooling.* Applied Physics Letters, vol. 102, no. 25, page 252102, jun 2013. (Cited on page 62.)

[Berdahl 1985] Paul Berdahl. *Radiant refrigeration by semiconductor diodes.* Journal of Applied Physics, vol. 58, no. 3, pages 1369–1374, aug 1985. (Cited on page 31.)

[Bernardi *et al.* 2015] Michael P. Bernardi, Olivier Dupré, Etienne Blandre, Pierre-Olivier Chapuis, Rodolphe Vaillon and Mathieu Francoeur. *Impacts of propagating, frustrated and surface modes on radiative, electrical and thermal losses in nanoscale-gap thermophotovoltaic power generators.* Scientific Reports, vol. 5, no. 1, page 11626, dec 2015. (Cited on page 69.)

[Bhatt *et al.* 2020] Gaurang R. Bhatt, Bo Zhao, Samantha Roberts, Ipshita Datta, Aseema Mohanty, Tong Lin, Jean-Michel Hartmann, Raphael St-Gelais, Shanhui Fan and Michal Lipson. *Integrated near-field thermo-photovoltaics for heat recycling.* Nature Communications, vol. 11, no. 1, page 2545, dec 2020. (Cited on page 30.)

[Blandre *et al.* 2017] Etienne Blandre, Pierre-Olivier Chapuis and Rodolphe Vaillon. *High-injection effects in near-field thermophotovoltaic devices.* Scientific Reports, vol. 7, no. 1, page 15860, dec 2017. (Cited on pages 26, 30, 32, 93, 94, 100, 105, 109 and 115.)

[Blandre 2016] Etienne Blandre. *Thermal radiation at the nanoscale: near-field and interference effects in few-layer structures and on the electrical performances.* PhD thesis, Université de Lyon, 2016. (Cited on pages 19, 104, 105, 106, 107, 108 and 190.)

[Boltzmann 1884] Ludwig Boltzmann. *Ableitung des Stefan'schen Gesetzes, betreffend die Abhängigkeit der Wärmestrahlung von der Temperatur aus der electromagnetischen Lichttheorie.* Annalen der Physik, vol. 258, no. 6, pages 291–294, 1884. (Cited on page 8.)

[Broyden 1965] C. G. Broyden. *A Class of Methods for Solving Nonlinear Simultaneous Equations.* Mathematics of Computation, vol. 19, no. 92, page 577, oct 1965. (Cited on page 78.)

[Buddhiraju *et al.* 2018] Siddharth Buddhiraju, Parthiban Santhanam and Shanhui Fan. *Thermodynamic limits of energy harvesting from outgoing thermal radiation.* Proceedings of the National Academy of Sciences, vol. 115, no. 16, pages E3609–E3615, apr 2018. (Cited on page 35.)

[Burgelman *et al.* 2000] M. Burgelman, P. Nollet and S. Degrave. *Modelling polycrystalline semiconductor solar cells.* Thin Solid Films, vol. 361-362, pages 527–532, feb 2000. (Cited on page 99.)

[Burger *et al.* 2020] Tobias Burger, Caroline Sempere, Bosun Roy-Layinde and Andrej Lenert. *Present Efficiencies and Future Opportunities in Thermophotovoltaics.* Joule, vol. 4, no. 8, pages 1660–1680, 2020. (Cited on page 30.)

[Callahan *et al.* 2021] William A. Callahan, Dudong Feng, Zhuomin M. Zhang, Eric S. Toberer, Andrew J. Ferguson and Eric J. Tervo. *Coupled Charge and Radiation Transport Processes in Thermophotovoltaic and Thermoradiative Cells.* Physical Review Applied, vol. 15, no. 5, page 054035, may 2021. (Cited on pages xvii, 26, 30, 33, 94, 95, 143 and 145.)

[Chapuis *et al.* 2008] Pierre-Olivier Chapuis, Sebastian Volz, Carsten Henkel, Karl Joulain and Jean Jacques Greffet. *Effects of spatial dispersion in near-field radiative heat transfer*

between two parallel metallic surfaces. Physical Review B - Condensed Matter and Materials Physics, vol. 77, no. 3, pages 1–9, 2008. (Cited on page 144.)

[Chen *et al.* 2015] Kaifeng Chen, Parthiban Santhanam, Sunil Sandhu, Linxiao Zhu and Shanhui Fan. *Heat-flux control and solid-state cooling by regulating chemical potential of photons in near-field electromagnetic heat transfer*. Physical Review B, vol. 91, no. 13, page 134301, apr 2015. (Cited on pages 31 and 124.)

[Chen *et al.* 2016] Kaifeng Chen, Parthiban Santhanam and Shanhui Fan. *Near-Field Enhanced Negative Luminescent Refrigeration*. Physical Review Applied, vol. 6, no. 2, page 024014, aug 2016. (Cited on page 31.)

[Chen *et al.* 2017] Kaifeng Chen, Tianyao P. Xiao, Parthiban Santhanam, Eli Yablonovitch and Shanhui Fan. *High-performance near-field electroluminescent refrigeration device consisting of a GaAs light emitting diode and a Si photovoltaic cell*. Journal of Applied Physics, vol. 122, no. 14, 2017. (Cited on pages 31 and 63.)

[Chen *et al.* 2021] Hung Ling Chen, Andrea Scaccabarozzi, Romaric De Lépinau, Fabrice Oehler, Aristide Lemaître, Jean Christophe Harmand, Andrea Cattoni and Stéphane Collin. *Quantitative Assessment of Carrier Density by Cathodoluminescence. I. GaAs Thin Films and Modeling*. Physical Review Applied, vol. 15, no. 2, page 1, 2021. (Cited on page 128.)

[Choi *et al.* 2023] Minwoo Choi, Jaeman Song and Bong Jae Lee. *Bifacial near-field thermophotovoltaic converter with transparent intermediate substrate*. arXiv, pages 1–32, jun 2023. (Cited on page 30.)

[Curzon & Ahlborn 1975] F. L. Curzon and B. Ahlborn. *Efficiency of a Carnot engine at maximum power output*. American Journal of Physics, vol. 43, no. 1, pages 22–24, jan 1975. (Cited on pages 48 and 76.)

[Datas & Vaillon 2019] Alejandro Datas and Rodolphe Vaillon. *Thermionic-enhanced near-field thermophotovoltaics*. Nano Energy, vol. 61, no. March, pages 10–17, jul 2019. (Cited on page 30.)

[Datas 2016] Alejandro Datas. *Hybrid thermionic-photovoltaic converter*. Applied Physics Letters, vol. 108, no. 14, page 143503, apr 2016. (Cited on page 30.)

[Datas 2023] Alejandro Datas. *Bifacial Thermophotovoltaic Energy Conversion*. ACS Photonics, vol. 10, no. 3, pages 683–690, mar 2023. (Cited on page 30.)

[De Vos 1992] Alexis De Vos. Endoreversible Thermodynamics of Solar Energy Conversion. Oxford University Press, 1992. (Cited on pages 17 and 35.)

[Delgado-Bonal 2017] Alfonso Delgado-Bonal. *Entropy of radiation: the unseen side of light*. Scientific Reports, vol. 7, no. 1, page 1642, dec 2017. (Cited on page 42.)

[DeSutter *et al.* 2017] John DeSutter, Rodolphe Vaillon and Mathieu Francoeur. *External Luminescence and Photon Recycling in Near-Field Thermophotovoltaics*. Physical Review Applied, vol. 8, no. 1, page 014030, jul 2017. (Cited on pages 30, 44, 94, 124 and 145.)

[Dousmanis *et al.* 1964] G. C. Dousmanis, C. W. Mueller, H. Nelson and K. G. Petzinger. *Evidence of Refrigerating Action by Means of Photon Emission in Semiconductor Diodes*. Physical Review, vol. 133, no. 1A, pages A316–A318, jan 1964. (Cited on page 31.)

[Dyachenko *et al.* 2016] P. N. Dyachenko, S. Molesky, A. Yu Petrov, M. Störmer, T. Krekeler, S. Lang, M. Ritter, Z. Jacob and M. Eich. *Controlling thermal emission with refractory epsilon-near-zero metamaterials via topological transitions.* Nature Communications, vol. 7, no. May, 2016. (Cited on page 30.)

[European Commission *et al.* 2023] European Commission, Directorate-General for Internal Market, Industry, Entrepreneurship and SMEs, Milan Grohol and Constanze Veeh. *Study on the critical raw materials for the EU.* Technical report, Publications Office of the European Union, 2023. (Cited on pages xv, 28 and 29.)

[Fan *et al.* 2020] Dejiu Fan, Tobias Burger, Sean McSherry, Byungjun Lee, Andrej Lenert and Stephen R. Forrest. *Near-perfect photon utilization in an air-bridge thermophotovoltaic cell.* Nature, vol. 586, no. 7828, pages 237–241, oct 2020. (Cited on page 29.)

[Feng *et al.* 2021] Dudong Feng, Eric J. Tervo, Dragica Vasileska, Shannon K. Yee, Ajeet Rohatgi and Zhuomin M. Zhang. *Spatial profiles of photon chemical potential in near-field thermophotovoltaic cells.* Journal of Applied Physics, vol. 129, no. 21, page 213101, jun 2021. (Cited on page 30.)

[Feng *et al.* 2022] Dudong Feng, Shannon K. Yee and Zhuomin M. Zhang. *Geometric and doping effects on radiative recombination in thin-film near-field energy converters.* AIP Advances, vol. 12, no. 9, page 095006, sep 2022. (Cited on pages 30 and 94.)

[Ferrini *et al.* 2002] R. Ferrini, G. Guizzetti, M. Patrini, A. Parisini, L. Tarricone and B. Valenti. *Optical functions of InGaP/GaAs epitaxial layers from 0.01 to 5.5 eV.* The European Physical Journal B - Condensed Matter, vol. 27, no. 4, pages 449–458, jun 2002. (Cited on page 178.)

[Fiorino *et al.* 2018] Anthony Fiorino, Linxiao Zhu, Dakotah Thompson, Rohith Mittapally, Pramod Reddy and Edgar Meyhofer. *Nanogap near-field thermophotovoltaics.* Nature Nanotechnology, vol. 13, no. 9, pages 806–811, sep 2018. (Cited on page 30.)

[Forcade *et al.* 2022] Gavin P. Forcade, Christopher E. Valdivia, Sean Molesky, Shengyuan Lu, Alejandro W. Rodriguez, Jacob J. Krich, Raphael St-Gelais and Karin Hinzer. *Efficiency-optimized near-field thermophotovoltaics using InAs and InAsSbP.* Applied Physics Letters, vol. 121, no. 19, page 193903, nov 2022. (Cited on pages 30, 32, 94, 96, 109, 112 and 147.)

[Forman *et al.* 2016] Clemens Forman, Ibrahim Kolawole Muritala, Robert Pardemann and Bernd Meyer. *Estimating the global waste heat potential.* Renewable and Sustainable Energy Reviews, vol. 57, pages 1568–1579, 2016. (Cited on pages 1 and 16.)

[France *et al.* 2022] Ryan M. France, John F. Geisz, Tao Song, Waldo Olavarria, Michelle Young, Alan Kibbler and Myles A. Steiner. *Triple-junction solar cells with 39.5% terrestrial and 34.2% space efficiency enabled by thick quantum well superlattices.* Joule, vol. 6, no. 5, pages 1121–1135, may 2022. (Cited on page 62.)

[Francoeur *et al.* 2009] Mathieu Francoeur, M. Pinar Mengüç and Rodolphe Vaillon. *Solution of near-field thermal radiation in one-dimensional layered media using dyadic Green's functions and the scattering matrix method.* Journal of Quantitative Spectroscopy and Radiative Transfer, vol. 110, no. 18, pages 2002–2018, dec 2009. (Cited on pages 19, 21, 173, 174, 175 and 176.)

[Francoeur *et al.* 2010] Mathieu Francoeur, M Pinar Mengüç and Rodolphe Vaillon. *Spectral tuning of near-field radiative heat flux between two thin silicon carbide films.* Journal of Physics D: Applied Physics, vol. 43, no. 7, page 075501, feb 2010. (Cited on pages xviii, 130, 144 and 175.)

[Gaury *et al.* 2019] Benoit Gaury, Yubo Sun, Peter Bermel and Paul M Haney. *Sesame: A 2-dimensional solar cell modeling tool.* Solar Energy Materials and Solar Cells, vol. 198, no. May 2018, pages 53–62, aug 2019. (Cited on page 99.)

[Giteau *et al.* 2023] Maxime Giteau, Michela F. Picardi and Georgia T. Papadakis. *Thermodynamic performance bounds for radiative heat engines.* arXiv, no. 2, apr 2023. (Cited on pages 30, 32, 35 and 42.)

[Gonzalez-Cuevas *et al.* 2006] Juan A. Gonzalez-Cuevas, Tamer F. Refaat, M. Nurul Abedin and Hani E. Elsayed-Ali. *Modeling of the temperature-dependent spectral response of InGaSb infrared photodetectors.* Optical Engineering, vol. 45, no. 4, page 044001, apr 2006. (Cited on pages 62 and 157.)

[Gonzalez-Cuevas *et al.* 2007] Juan A. Gonzalez-Cuevas, Tamer F. Refaat, M. Nurul Abedin and Hani E. Elsayed-Ali. *Calculations of the temperature and alloy composition effects on the optical properties of $Al_xGa_{1-x}As_ySb_{1-y}$ and $Ga_xIn_{1-x}As_ySb1-y$ in the spectral range 0.5–6 eV.* Journal of Applied Physics, vol. 102, no. 1, page 014504, jul 2007. (Cited on pages xv, 24, 25, 26, 126, 177, 178 and 179.)

[Greeff & Glyde 1995] C. W. Greeff and H. R. Glyde. *Anomalous Urbach tail in GaAs.* Physical Review B, vol. 51, no. 3, pages 1778–1783, jan 1995. (Cited on page 128.)

[Green *et al.* 2023] Martin A. Green, Ewan D. Dunlop, Gerald Siefer, Masahiro Yoshita, Nikos Kopidakis, Karsten Bothe and Xiaojing Hao. *Solar cell efficiency tables (Version 61).* Progress in Photovoltaics: Research and Applications, vol. 31, no. 1, pages 3–16, 2023. (Cited on page 28.)

[Green 2006] Martin A. Green. Third Generation Photovoltaics, volume 12 of *Springer series in photonics.* Springer Berlin Heidelberg, 2006. (Cited on pages 35, 54 and 96.)

[Green 2012a] Martin A. Green. *Analytical treatment of Trivich-Flinn and Shockley-Queisser photovoltaic efficiency limits using polylogarithms.* Progress in Photovoltaics: Research and Applications, vol. 20, no. 2, pages 127–134, mar 2012. (Cited on pages 38 and 55.)

[Green 2012b] Martin A. Green. *Radiative efficiency of state-of-the-art photovoltaic cells.* Ieee Trans Fuzzy Syst, vol. 20, no. 6, pages 1114–1129, 2012. (Cited on page 59.)

[Grinberg & Luryi 1998] Anatoly A. Grinberg and Serge Luryi. *On electron transport across interfaces connecting materials with different effective masses.* IEEE Transactions on Electron Devices, vol. 45, no. 7, pages 1561–1568, jul 1998. (Cited on pages 135 and 136.)

[Grundmann 2016] Marius Grundmann. The Physics of Semiconductors. Springer-Verlag Berlin Heildelberg, 2016. (Cited on pages 93 and 116.)

[Harder & Green 2003] Nils-Peter Harder and Martin A. Green. *Thermophotonics.* Semiconductor Science and Technology, vol. 18, no. 5, pages S270–S278, may 2003. (Cited on pages 31, 43, 58, 59, 63, 64 and 167.)

[Harder *et al.* 2001] Nils-Peter Harder, Dirk H. Neuhaus, Peter Würfel, Armin G. Aberle and Martin A. Green. *Thermophotonics and its application to solar thermophotovoltaics.* In 17th European Photovoltaic Solar Energy Conference, 2001. (Cited on page 31.)

[Heikkilä *et al.* 2009] Oskari Heikkilä, Jani Oksanen and Jukka Tulkki. *Ultimate limit and temperature dependency of light-emitting diode efficiency.* Journal of Applied Physics, vol. 105, no. 9, page 093119, may 2009. (Cited on page 31.)

[Hirst & Ekins-Daukes 2011] Louise C. Hirst and Nicholas J. Ekins-Daukes. *Fundamental losses in solar cells.* Progress in Photovoltaics: Research and Applications, vol. 19, no. 3, pages 286–293, may 2011. (Cited on page 14.)

[Horowitz *et al.* 2018] Kelsey A. Horowitz, Timothy W. Remo, Brittany Smith and Aaron J. Ptak. *A Techno-Economic Analysis and Cost Reduction Roadmap for III-V Solar Cells.* Technical report November, National Renewable Energy Laboratory, 2018. (Cited on page 28.)

[IEA 2022] IEA. *Solar PV.* https://www.iea.org/reports/solar-pv, 2022. (Cited on page 28.)

[IEA 2023] IEA. *IEA energy statistics data browser.* https://www.iea.org/data-and-statistics/data-tools/energy-statistics-data-browser, 2023. (Cited on page 1.)

[Inoue *et al.* 2019] Takuya Inoue, Takaaki Koyama, Dongyeon Daniel Kang, Keisuke Ikeda, Takashi Asano and Susumu Noda. *One-Chip Near-Field Thermophotovoltaic Device Integrating a Thin-Film Thermal Emitter and Photovoltaic Cell.* Nano Letters, vol. 19, no. 6, pages 3948–3952, jun 2019. (Cited on page 30.)

[Inoue *et al.* 2021] Takuya Inoue, Keisuke Ikeda, Bongshik Song, Taiju Suzuki, Koya Ishino, Takashi Asano and Susumu Noda. *Integrated Near-Field Thermophotovoltaic Device Overcoming Blackbody Limit.* ACS Photonics, vol. 8, no. 8, pages 2466–2472, aug 2021. (Cited on pages 30 and 76.)

[Jouhara *et al.* 2018] Hussam Jouhara, Navid Khordehgah, Sulaiman Almahmoud, Bertrand Delpech, Amisha Chauhan and Savvas A. Tassou. *Waste heat recovery technologies and applications.* Thermal Science and Engineering Progress, vol. 6, no. April, pages 268–289, 2018. (Cited on page 1.)

[Joulain 2008] Karl Joulain. *Near-field heat transfer: A radiative interpretation of thermal conduction.* Journal of Quantitative Spectroscopy and Radiative Transfer, vol. 109, no. 2, pages 294–304, jan 2008. (Cited on page 144.)

[Kantner 2020] Markus Kantner. *Generalized Scharfetter–Gummel schemes for electro-thermal transport in degenerate semiconductors using the Kelvin formula for the Seebeck coefficient.* Journal of Computational Physics, vol. 402, page 109091, feb 2020. (Cited on page 116.)

[Katahara & Hillhouse 2014] John K. Katahara and Hugh W. Hillhouse. *Quasi-Fermi level splitting and sub-bandgap absorptivity from semiconductor photoluminescence.* Journal of Applied Physics, vol. 116, no. 17, page 173504, nov 2014. (Cited on pages 126, 127 and 128.)

[Kayes *et al.* 2011] Brendan M. Kayes, Hui Nie, Rose Twist, Sylvia G. Spruytte, Frank Reinhardt, Isik C. Kizilyalli and Gregg S. Higashi. *27.6% Conversion efficiency, a new record for single-junction solar cells under 1 sun illumination.* Conference Record of the IEEE Photovoltaic Specialists Conference, pages 000004–000008, 2011. (Cited on page 62.)

[Kitai 2018] Adrian Kitai. Principles of Solar Cells , LEDs and Related Devices. Wiley, 2018. (Cited on pages 22 and 95.)

[Kivisaari *et al.* 2015] Pyry Kivisaari, Jani Oksanen, Jukka Tulkki and Toufik Sadi. *Monte Carlo simulation of hot carrier transport in III-N LEDs.* Journal of Computational Electronics, vol. 14, no. 2, pages 382–397, 2015. (Cited on page 98.)

[Kukharskii 1973] A.A. Kukharskii. *Plasmon-phonon coupling in GaAs.* Solid State Communications, vol. 13, no. 11, pages 1761–1765, dec 1973. (Cited on page 22.)

[Landsberg & Evans 1968] P. T. Landsberg and D. A. Evans. *Thermodynamic Limits for Some Light-Producing Devices.* Physical Review, vol. 166, no. 2, pages 242–246, feb 1968. (Cited on page 31.)

[Landsberg & Tonge 1980] P. T. Landsberg and G. Tonge. *Thermodynamic energy conversion efficiencies.* Journal of Applied Physics, vol. 51, no. 7, pages R1–R20, jul 1980. (Cited on pages 10, 31, 32, 35 and 37.)

[LaPotin *et al.* 2022] Alina LaPotin, Kevin L. Schulte, Myles A. Steiner, Kyle Buznitsky, Colin C. Kelsall, Daniel J. Friedman, Eric J. Tervo, Ryan M. France, Michelle R. Young, Andrew Rohskopf, Shomik Verma, Evelyn N. Wang and Asegun Henry. *Thermophotovoltaic efficiency of 40%.* Nature, vol. 604, no. 7905, pages 287–291, apr 2022. (Cited on pages 29 and 96.)

[Legendre & Chapuis 2022a] Julien Legendre and Pierre-Olivier Chapuis. *GaAs-based near-field thermophotonic devices: Approaching the idealized case with one-dimensional PN junctions.* Solar Energy Materials and Solar Cells, vol. 238, page 111594, may 2022. (Cited on pages 59, 64, 103 and 168.)

[Legendre & Chapuis 2022b] Julien Legendre and Pierre-Olivier Chapuis. *Overcoming non-radiative losses with AlGaAs PIN junctions for near-field thermophotonic energy harvesting.* Applied Physics Letters, vol. 121, no. 19, page 193902, nov 2022. (Cited on pages 59, 64 and 108.)

[Lehovec *et al.* 1953] K. Lehovec, C. A. Accardo and E. Jamgochian. *Light Emission Produced by Current Injected into a Green Silicon-Carbide Crystal.* Physical Review, vol. 89, no. 1, pages 20–25, jan 1953. (Cited on page 30.)

[Levinshtein *et al.* 1996] M. Levinshtein, S. Rumyantsev and M. Shur. Handbook series on semiconductor parameters: Volume 1. World Scientific, 1996. (Cited on page 157.)

[Levinshtein *et al.* 1999] M. Levinshtein, S. Rumyantsev and M. Shur. Handbook Series on Semiconductor Parameters, Vol. 2—Ternary and Quaternary III-V Compounds. World Scientific, nov 1999. (Cited on pages 156, 177, 178 and 179.)

[Li *et al.* 2021a] Bowen Li, Qiang Cheng, Jinlin Song, Kun Zhou, Lu Lu and Zixue Luo. *Thermodynamic performance of near-field electroluminescence and negative electroluminescent refrigeration systems.* AIMS Energy, vol. 9, no. 3, pages 465–482, 2021. (Cited on page 31.)

[Li *et al.* 2021b] Bowen Li, Qiang Cheng, Jinlin Song, Kun Zhou, Lu Lu, Zixue Luo and Xusheng Zhuo. *Thermodynamic bounds of work and efficiency in near-field thermoradiative systems.* International Journal of Heat and Mass Transfer, vol. 180, page 121807, dec 2021. (Cited on page 30.)

[Lin *et al.* 2004] Kuolong L. Lin, Kylie R. Catchpole, Patrick Campbell and Martin A. Green. *High external quantum efficiency from double heterostructure InGaP/GaAs layers as selective emitters for thermophotonic systems.* Semiconductor Science and Technology, vol. 19, no. 11, pages 1268–1272, nov 2004. (Cited on page 31.)

[Lin *et al.* 2018] Chungwei Lin, Bingnan Wang, Koon Hoo Teo and Zhuomin M. Zhang. *A coherent description of thermal radiative devices and its application on the near-field negative electroluminescent cooling.* Energy, vol. 147, pages 177–186, mar 2018. (Cited on pages 24 and 61.)

[Liu & Zhang 2016] Xianglei Liu and Zhuomin M. Zhang. *High-performance electroluminescent refrigeration enabled by photon tunneling.* Nano Energy, vol. 26, pages 353–359, aug 2016. (Cited on page 31.)

[Loomis & Maris 1994] Jackson J. Loomis and Humphrey J. Maris. *Theory of heat transfer by evanescent electromagnetic waves.* Physical Review B, vol. 50, no. 24, pages 18517–18524, dec 1994. (Cited on page 70.)

[Losego *et al.* 2009] Mark D. Losego, Alina Y. Efremenko, Crissy L. Rhodes, Marta G. Cerruti, Stefan Franzen and Jon-Paul Maria. *Conductive oxide thin films: Model systems for understanding and controlling surface plasmon resonance.* Journal of Applied Physics, vol. 106, no. 2, page 024903, jul 2009. (Cited on page 22.)

[Lucchesi *et al.* 2021a] Christophe Lucchesi, Dilek Cakiroglu, Jean-Philippe Perez, Thierry Taliercio, Eric Tournié, Pierre-Olivier Chapuis and Rodolphe Vaillon. *Near-Field Thermophotovoltaic Conversion with High Electrical Power Density and Cell Efficiency above 14%.* Nano Letters, vol. 21, no. 11, pages 4524–4529, jun 2021. (Cited on pages 30 and 33.)

[Lucchesi *et al.* 2021b] Christophe Lucchesi, Rodolphe Vaillon and Pierre-Olivier Chapuis. *Radiative heat transfer at the nanoscale: experimental trends and challenges.* Nanoscale Horizons, vol. 6, no. 3, pages 201–208, 2021. (Cited on page 26.)

[Lucchesi 2020] Christophe Lucchesi. *Design and development of a near-field thermophotovoltaic conversion device.* PhD thesis, Université de Lyon, 2020. (Cited on pages 26 and 30.)

[Lukeš *et al.* 1989] I. Lukeš, J. Humlíček, V. Vorlíček and M. Závětová. *Infrared Reflectance of the GaAlAs/GaAs System.* Physica Status Solidi (a), vol. 111, no. 2, pages 655–665, feb 1989. (Cited on page 177.)

[Lundstrom & Schuelke 1982] Mark S. Lundstrom and Robert J. Schuelke. *Modeling semiconductor heterojunctions in equilibrium.* Solid-State Electronics, vol. 25, no. 8, pages 683–691, aug 1982. (Cited on page 139.)

[Luque & Martí 1997] Antonio Luque and Antonio Martí. *Entropy production in photovoltaic conversion.* Physical Review B - Condensed Matter and Materials Physics, vol. 55, no. 11, pages 6994–6999, 1997. (Cited on page 36.)

[Maros *et al.* 2015] Aymeric Maros, Srikanth Gangam, Yi Fang, Justin Smith, Dragica Vasileska, Stephen Goodnick, Mariana I. Bertoni and Christiana B. Honsberg. *High temperature characterization of GaAs single junction solar cells.* In 2015 IEEE 42nd Photovoltaic Specialist Conference (PVSC), pages 1–5. IEEE, jun 2015. (Cited on page 100.)

[Matsuno *et al.* 2022] Yuki Matsuno, Nobuhiro Nagumo, Masaya Araki, Kyohei Yada, Kazuki Yamaga and Atsushi Sakurai. *Non-equilibrium mid-infrared black phosphorus light emitter*

and absorber for thermophotonic applications. Journal of Quantitative Spectroscopy and Radiative Transfer, vol. 288, page 108271, sep 2022. (Cited on pages 32, 63 and 68.)

[McSherry *et al.* 2019] Sean McSherry, Tobias Burger and Andrej Lenert. *Effects of narrowband transport on near-field and far-field thermophotonic conversion*. Journal of Photonics for Energy, vol. 9, no. 03, page 1, mar 2019. (Cited on pages 17, 32, 53 and 57.)

[Melnick & Kaviany 2019] Corey Melnick and Massoud Kaviany. *From thermoelectricity to phonoelectricity*. Applied Physics Reviews, vol. 6, no. 2, page 021305, jun 2019. (Cited on page 1.)

[Mesodyne 2023] Mesodyne. https://mesodyne.com/, 2023. (Cited on pages 15 and 30.)

[Milovich *et al.* 2020] Daniel Milovich, Juan Villa, Elisa Antolin, Alejandro Datas, Antonio Marti, Rodolphe Vaillon and Mathieu Francoeur. *Design of an indium arsenide cell for near-field thermophotovoltaic devices*. Journal of Photonics for Energy, vol. 10, no. 02, page 1, jun 2020. (Cited on pages 30, 94, 112, 163 and 181.)

[Mittapally *et al.* 2021] Rohith Mittapally, Byungjun Lee, Linxiao Zhu, Amin Reihani, Ju Won Lim, Dejiu Fan, Stephen R. Forrest, Pramod Reddy and Edgar Meyhofer. *Near-field thermophotovoltaics for efficient heat to electricity conversion at high power density*. Nature Communications, vol. 12, no. 1, page 4364, dec 2021. (Cited on page 30.)

[Mittapally *et al.* 2023] Rohith Mittapally, Ayan Majumder, Pramod Reddy and Edgar Meyhofer. *Near-Field Thermophotovoltaic Energy Conversion: Progress and Opportunities*. Physical Review Applied, vol. 19, no. 3, page 1, 2023. (Cited on page 30.)

[Mulet *et al.* 2002] Jean Philippe Mulet, Karl Joulain, Rémi Carminati and Jean Jacques Greffet. *Enhanced radiative heat transfer at nanometric distances*. Microscale Thermophysical Engineering, vol. 6, no. 3, pages 209–222, 2002. (Cited on page 21.)

[Mulet 2004] Jean-Philippe Mulet. *Modélisation du rayonnement thermique par une approche électromagnétique*. PhD thesis, Université Paris XI, 2004. (Cited on pages 20, 144, 175 and 176.)

[Nelson 2003] Jenny Nelson. The Physics of Solar Cells. Imperial College Press, may 2003. (Cited on pages 22 and 95.)

[Nemova & Kashyap 2010] Galina Nemova and Raman Kashyap. *Laser cooling of solids*. Reports on Progress in Physics, vol. 73, no. 8, page 086501, aug 2010. (Cited on page 31.)

[NREL 2023] NREL. *Best Research-Cell Efficiency Chart*. https://www.nrel.gov/pv/cell-efficiency.html, 2023. (Cited on pages xv and 28.)

[Oehler 2022] Jakob Oehler. Characterization of (In)GaAs photodiodes for thermophotonic applications using high intensity flash illumination. Master's thesis, Radboud University, 2022. (Cited on pages 128 and 129.)

[Okanimba Tedah *et al.* 2019] Irene Ambo Okanimba Tedah, Franziska Maculewicz, Dietrich E. Wolf and Roland Schmechel. *Thermoelectrics versus thermophotovoltaics: two approaches to convert heat fluxes into electricity*. Journal of Physics D: Applied Physics, vol. 52, no. 27, page 275501, jul 2019. (Cited on page 34.)

[Oksanen & Tulkki 2010] Jani Oksanen and Jukka Tulkki. *Thermophotonic heat pump—a theoretical model and numerical simulations.* Journal of Applied Physics, vol. 107, no. 9, page 093106, may 2010. (Cited on page 31.)

[Omair *et al.* 2019] Zunaid Omair, Gregg Scranton, Luis M. Pazos-Outón, T. Patrick Xiao, Myles A. Steiner, Vidya Ganapati, Per F. Peterson, John Holzrichter, Harry Atwater and Eli Yablonovitch. *Ultraefficient thermophotovoltaic power conversion by band-edge spectral filtering.* Proceedings of the National Academy of Sciences of the United States of America, vol. 116, no. 31, pages 15356–15361, 2019. (Cited on page 29.)

[Oublon 2023] Paul Oublon. *Physique des cellules solaires fonctionnant sous stress thermique.* PhD thesis, Université de Montpellier, 2023. (Cited on page 100.)

[Papadakis *et al.* 2021] Georgia T. Papadakis, Meir Orenstein, Eli Yablonovitch and Shanhui Fan. *Thermodynamics of Light Management in Near-Field Thermophotovoltaics.* Physical Review Applied, vol. 16, no. 6, page 064063, dec 2021. (Cited on pages 26, 30, 58 and 124.)

[Park *et al.* 2022] Yubin Park, Zunaid Omair and Shanhui Fan. *Nonreciprocal Thermophotovoltaic Systems.* ACS Photonics, vol. 9, no. 12, pages 3943–3949, dec 2022. (Cited on page 35.)

[Pascale *et al.* 2023] Mariano Pascale, Maxime Giteau and Georgia T. Papadakis. *Perspective on near-field radiative heat transfer.* Applied Physics Letters, vol. 122, no. 10, page 100501, mar 2023. (Cited on page 70.)

[Perl *et al.* 2017] Emmett E. Perl, Darius Kuciauskas, John Simon, Daniel J. Friedman and Myles A. Steiner. *Identification of the limiting factors for high-temperature GaAs, GaInP, and AlGaInP solar cells from device and carrier lifetime analysis.* Journal of Applied Physics, vol. 122, no. 23, dec 2017. (Cited on page 100.)

[Planck 1901] Max Planck. *Ueber das Gesetz der Energieverteilung im Normalspectrum.* Annalen der Physik, vol. 309, no. 3, pages 553–563, 1901. (Cited on page 8.)

[Planck 1914] Max Planck. The Theory of Heat Radiation. P. Blakiston's Son & Co, 1914. (Cited on page 9.)

[Polder & Van Hove 1971] D. Polder and M. Van Hove. *Theory of Radiative Heat Transfer between Closely Spaced Bodies.* Physical Review B, vol. 4, no. 10, pages 3303–3314, nov 1971. (Cited on page 19.)

[Pusch *et al.* 2019] Andreas Pusch, Jeffrey M. Gordon, Alex Mellor, Jacob J. Krich and Nicholas J. Ekins-Daukes. *Fundamental Efficiency Bounds for the Conversion of a Radiative Heat Engine's Own Emission into Work.* Physical Review Applied, vol. 12, no. 6, page 064018, dec 2019. (Cited on pages 30, 35 and 38.)

[Quay 2001] Rüdiger Quay. *Analysis and Simulation of High Electron Mobility Transistors.* PhD thesis, Technischen Universität Wien, 2001. (Cited on pages 156, 157 and 160.)

[Radevici *et al.* 2019] Ivan Radevici, Jonna Tiira, Toufik Sadi, Sanna Ranta, Antti Tukiainen, Mircea Guina and Jani Oksanen. *Thermophotonic cooling in GaAs based light emitters.* Applied Physics Letters, vol. 114, no. 5, page 051101, feb 2019. (Cited on pages 31 and 62.)

[Rosencher 2002] Emmanuel Rosencher. Optoelectronics. Cambridge University Press, 2002. (Cited on page 177.)

[Rytov 1959] S. M. Rytov. *Theory of electric fluctuations and thermal radiation*. Technical report, Armed Services Technical Information Agency, Rep. AFCRC-TR-59-162 (Air Force. Cambridge Research Center, Bedford, Mass.), Arlington, VA, 1959. (Cited on page 19.)

[Sadi *et al.* 2019a] Toufik Sadi, Alberto Casado, Ivan Radevici, Pyry Kivisaari and Jani Oksanen. *Efficient Fully-Coupled Electro-Optical Simulation Framework for Large-Area Planar Devices*. In 2019 International Conference on Numerical Simulation of Optoelectronic Devices (NUSOD), pages 9–10. IEEE, jul 2019. (Cited on page 100.)

[Sadi *et al.* 2019b] Toufik Sadi, Ivan Radevici, Pyry Kivisaari and Jani Oksanen. *Electroluminescent Cooling in III–V Intracavity Diodes: Efficiency Bottlenecks*. IEEE Transactions on Electron Devices, vol. 66, no. 6, pages 2651–2656, jun 2019. (Cited on pages 131 and 179.)

[Sadi *et al.* 2020] Toufik Sadi, Ivan Radevici and Jani Oksanen. *Thermophotonic cooling with light-emitting diodes*. Nature Photonics, vol. 14, no. 4, pages 205–214, apr 2020. (Cited on pages 31 and 44.)

[Sadi *et al.* 2022] Toufik Sadi, Ivan Radevici, Benoît Behaghel and Jani Oksanen. *Prospects and requirements for thermophotonic waste heat energy harvesting*. Solar Energy Materials and Solar Cells, vol. 239, no. February, page 111635, jun 2022. (Cited on pages 32 and 61.)

[Saint-Cast *et al.* 2010] Pierre Saint-Cast, Marc Rüdiger, Andreas Wolf, Marc Hofmann, Jochen Rentsch and Ralf Preu. *Advanced analytical model for the effective recombination velocity of locally contacted surfaces*. Journal of Applied Physics, vol. 108, no. 1, page 013705, jul 2010. (Cited on pages 109 and 147.)

[Sakakibara *et al.* 2019] Reyu Sakakibara, Veronika Stelmakh, Walker R. Chan, Michael Ghebrebrhan, John D. Joannopoulos, Marin Soljačić and Ivan Čelanović. *Practical emitters for thermophotovoltaics: a review*. Journal of Photonics for Energy, vol. 9, no. 03, page 1, feb 2019. (Cited on page 30.)

[Santhanam *et al.* 2012] Parthiban Santhanam, Dodd Joseph Gray and Rajeev J. Ram. *Thermoelectrically Pumped Light-Emitting Diodes Operating above Unity Efficiency*. Physical Review Letters, vol. 108, no. 9, page 097403, feb 2012. (Cited on page 31.)

[Santhanam *et al.* 2013] Parthiban Santhanam, Duanni Huang, Rajeev J. Ram, Maxim A. Remennyi and Boris A. Matveev. *Room temperature thermo-electric pumping in mid-infrared light-emitting diodes*. Applied Physics Letters, vol. 103, no. 18, page 183513, oct 2013. (Cited on page 31.)

[Santhanam *et al.* 2020] Parthiban Santhanam, Wei Li, Bo Zhao, Chris Rogers, Dodd Joseph Gray, Phillip Jahelka, Harry A. Atwater and Shanhui Fan. *Controlling the dopant profile for SRH suppression at low current densities in $\lambda \approx$ 1330 nm GaInAsP light-emitting diodes*. Applied Physics Letters, vol. 116, no. 20, page 203503, may 2020. (Cited on pages 132 and 160.)

[Scharfetter & Gummel 1969] D.L. Scharfetter and H.K. Gummel. *Large-signal analysis of a silicon Read diode oscillator*. IEEE Transactions on Electron Devices, vol. 16, no. 1, pages 64–77, jan 1969. (Cited on pages 187 and 189.)

[Schenk 1992] A. Schenk. *A model for the field and temperature dependence of Shockley-Read-Hall lifetimes in silicon*. Solid-State Electronics, vol. 35, no. 11, pages 1585–1596, nov 1992. (Cited on page 157.)

[Schmiedl & Seifert 2008] T. Schmiedl and U. Seifert. *Efficiency at maximum power: An analytically solvable model for stochastic heat engines.* EPL (Europhysics Letters), vol. 81, no. 2, page 20003, jan 2008. (Cited on page 42.)

[Schubert *et al.* 1999] M. Schubert, J. A. Woollam, G. Leibiger, B. Rheinländer, I. Pietzonka, T. Saß and V. Gottschalch. *Isotropic dielectric functions of highly disordered AlxGa1-xInP ($0 \leq x \leq 1$) lattice matched to GaAs.* Journal of Applied Physics, vol. 86, no. 4, pages 2025–2033, aug 1999. (Cited on page 178.)

[Seletskiy *et al.* 2016] Denis V. Seletskiy, Richard Epstein and Mansoor Sheik-Bahae. *Laser cooling in solids: advances and prospects.* Reports on Progress in Physics, vol. 79, no. 9, page 096401, sep 2016. (Cited on page 31.)

[Shimizu *et al.* 2018] Makoto Shimizu, Asaka Kohiyama and Hiroo Yugami. *Evaluation of thermal stability in spectrally selective few-layer metallo-dielectric structures for solar thermophotovoltaics.* Journal of Quantitative Spectroscopy and Radiative Transfer, vol. 212, pages 45–49, 2018. (Cited on page 30.)

[Shockley & Queisser 1961] William Shockley and Hans J. Queisser. *Detailed Balance Limit of Efficiency of p-n Junction Solar Cells.* Journal of Applied Physics, vol. 32, no. 3, pages 510–519, mar 1961. (Cited on pages 15, 35, 55 and 61.)

[Sipe 1987] J. E. Sipe. *New Green-function formalism for surface optics.* Journal of the Optical Society of America B, vol. 4, no. 4, page 481, apr 1987. (Cited on pages 20 and 173.)

[Slotboom 1973] J.W. Slotboom. *Computer-aided two-dimensional analysis of bipolar transistors.* IEEE Transactions on Electron Devices, vol. 20, no. 8, pages 669–679, aug 1973. (Cited on page 104.)

[Song *et al.* 2020] Jaeman Song, Junho Jang, Mikyung Lim, Jungchul Lee, Seung S. Lee and Bong Jae Lee. *Near-Field Electroluminescent Refrigeration System Consisting of Two Graphene Schottky Diodes.* Journal of Heat Transfer, vol. 142, no. 7, pages 1–8, jul 2020. (Cited on page 31.)

[Song *et al.* 2022] Jaeman Song, Jihye Han, Minwoo Choi and Bong Jae Lee. *Modeling and experiments of near-field thermophotovoltaic conversion: A review.* Solar Energy Materials and Solar Cells, vol. 238, no. January, page 111556, may 2022. (Cited on page 30.)

[Sotoodeh *et al.* 2000] M. Sotoodeh, A. H. Khalid and A. A. Rezazadeh. *Empirical low-field mobility model for III–V compounds applicable in device simulation codes.* Journal of Applied Physics, vol. 87, no. 6, pages 2890–2900, mar 2000. (Cited on pages 106, 177 and 178.)

[Steiner *et al.* 2011] Myles A. Steiner, John F. Geisz, Daniel J. Friedman, Waldo J. Olavarria, Anna Duda and Tom E. Moriarty. *Temperature-dependent measurements of an inverted metamorphic multijunction (IMM) solar cell.* Conference Record of the IEEE Photovoltaic Specialists Conference, no. July, pages 002527–002532, 2011. (Cited on page 178.)

[Sze 2006] S.M. Sze. Physics of semiconductor devices. Wiley, 2006. (Cited on page 116.)

[Takamoto *et al.* 2014] Tatsuya Takamoto, Hidetoshi Washio and Hiroyuki Juso. *Application of InGaP/GaAs/InGaAs triple junction solar cells to space use and concentrator photovoltaic.* In 2014 IEEE 40th Photovoltaic Specialist Conference (PVSC), pages 0001–0005. IEEE, jun 2014. (Cited on page 62.)

[Takeshima 1985] Masumi Takeshima. *Effect of Auger recombination on laser operation in Ga1-x Al x As.* Journal of Applied Physics, vol. 58, no. 10, pages 3846–3850, nov 1985. (Cited on page 158.)

[Tervo *et al.* 2018] Eric J. Tervo, Elham Bagherisereshki and Zhuomin M. Zhang. *Near-field radiative thermoelectric energy converters: a review.* Frontiers in Energy, vol. 12, no. 1, pages 5–21, mar 2018. (Cited on pages 18 and 30.)

[Tervo *et al.* 2020] Eric J. Tervo, William A. Callahan, Eric S. Toberer, Myles A. Steiner and Andrew J. Ferguson. *Solar Thermoradiative-Photovoltaic Energy Conversion.* Cell Reports Physical Science, vol. 1, no. 12, page 100258, dec 2020. (Cited on page 30.)

[Tervo *et al.* 2022] Eric J. Tervo, Ryan M. France, Daniel J. Friedman, Madhan K. Arulanandam, Richard R. King, Tarun C. Narayan, Cecilia Luciano, Dustin P. Nizamian, Benjamin A. Johnson, Alexandra R. Young, Leah Y. Kuritzky, Emmett E. Perl, Moritz Limpinsel, Brendan M. Kayes, Andrew J. Ponec, David M. Bierman, Justin A. Briggs and Myles A. Steiner. *Efficient and scalable GaInAs thermophotovoltaic devices.* Joule, pages 1–27, 2022. (Cited on pages 29, 67 and 169.)

[Thermophoton 2023] Thermophoton. https://www.thermophoton.com/index.php, 2023. (Cited on pages 15 and 30.)

[Tobias & Luque 2002] Ignacio Tobias and Antonio Luque. *Ideal efficiency and potential of solar thermophotonic converters under optically and thermally concentrated power flux.* IEEE Transactions on Electron Devices, vol. 49, no. 11, pages 2024–2030, nov 2002. (Cited on page 31.)

[Tsurimaki *et al.* 2017] Yoichiro Tsurimaki, Pierre-Olivier Chapuis, Junnosuke Okajima, Atsuki Komiya, Shigenao Maruyama and Rodolphe Vaillon. *Coherent regime and far-to-near-field transition for radiative heat transfer.* Journal of Quantitative Spectroscopy and Radiative Transfer, vol. 187, pages 310–321, 2017. (Cited on page 70.)

[Tu 2008] Z. C. Tu. *Efficiency at maximum power of Feynman's ratchet as a heat engine.* Journal of Physics A: Mathematical and Theoretical, vol. 41, no. 31, 2008. (Cited on pages 42, 48 and 184.)

[Vaillon *et al.* 2020] Rodolphe Vaillon, Stéphanie Parola, Chrysovalantou Lamnatou and Daniel Chemisana. *Solar Cells Operating under Thermal Stress.* Cell Reports Physical Science, vol. 1, no. 12, page 100267, dec 2020. (Cited on pages 16, 17 and 156.)

[Varshni 1967] Y.P. Varshni. *Temperature dependence of the energy gap in semiconductors.* Physica, vol. 34, no. 1, pages 149–154, jan 1967. (Cited on page 62.)

[Vasileska *et al.* 2017] Dragica Vasileska, Stephen M. Goodnick and Gerhard Klimeck. Computational Electronics. CRC Press, dec 2017. (Cited on pages 104, 105 and 189.)

[Verschraegen & Burgelman 2007] J. Verschraegen and M. Burgelman. *Numerical modeling of intra-band tunneling for heterojunction solar cells in scaps.* Thin Solid Films, vol. 515, no. 15, pages 6276–6279, may 2007. (Cited on page 138.)

[Wang *et al.* 2011] Tianyou Wang, Yajun Zhang, Zhijun Peng and Gequn Shu. *A review of researches on thermal exhaust heat recovery with Rankine cycle.* Renewable and Sustainable Energy Reviews, vol. 15, no. 6, pages 2862–2871, 2011. (Cited on page 1.)

[Wang *et al.* 2023a] Junyi Wang, Youlin Wang, Xiaohang Chen, Jincan Chen and Shanhe Su. *Hot carrier-based near-field thermophotovoltaics with energy selective contacts.* Applied Physics Letters, vol. 122, no. 12, page 122203, mar 2023. (Cited on page 30.)

[Wang *et al.* 2023b] Qixiang Wang, Zhequn Huang, Jiazhou Li, Guan-Yao Huang, Dewen Wang, Heng Zhang, Jiang Guo, Min Ding, Jintao Chen, Zihan Zhang, Zhenhua Rui, Wen Shang, Jia-Yue Xu, Jian Zhang, Junichiro Shiomi, Tairan Fu, Tao Deng, Steven G. Johnson, Hongxing Xu and Kehang Cui. *Module-Level Polaritonic Thermophotovoltaic Emitters via Hierarchical Sequential Learning.* Nano Letters, vol. 23, no. 4, pages 1144–1151, feb 2023. (Cited on page 30.)

[Weinstein 1960] M. A. Weinstein. *Thermodynamic Limitation on the Conversion of Heat into Light.* Journal of the Optical Society of America, vol. 50, no. 6, page 597, jun 1960. (Cited on page 31.)

[Wu & Yang 1979] C.M. Wu and E.S. Yang. *Carrier transport across heterojunction interfaces.* Solid-State Electronics, vol. 22, no. 3, pages 241–248, mar 1979. (Cited on page 135.)

[Würfel & Würfel 2016] Peter Würfel and Uli Würfel. Physics of Solar Cells. Wiley, jan 2016. (Cited on pages 10, 12, 22, 90, 95, 118 and 120.)

[Würfel 1982] Peter Würfel. *The chemical potential of radiation.* Journal of Physics C: Solid State Physics, vol. 15, no. 18, pages 3967–3985, jun 1982. (Cited on pages 12, 31, 36 and 43.)

[Xu & Shur 1987] Jingming Xu and Michael Shur. *Velocity-Field Dependence in GaAs.* IEEE Transactions on Electron Devices, vol. 34, no. 8, pages 1831–1832, 1987. (Cited on page 193.)

[Xue *et al.* 2017] Jin Xue, Zheng Li and Rajeev J. Ram. *Irreversible Thermodynamic Bound for the Efficiency of Light-Emitting Diodes.* Physical Review Applied, vol. 8, no. 1, page 014017, jul 2017. (Cited on page 31.)

[Yang *et al.* 1993] Kyounghoon Yang, Jack R. East and George I. Haddad. *Numerical modeling of abrupt heterojunctions using a thermionic-field emission boundary condition.* Solid-State Electronics, vol. 36, no. 3, pages 321–330, mar 1993. (Cited on page 137.)

[Yang *et al.* 2020] Zhimin Yang, Junyi Wang, Juncheng Guo, Guoxing Lin and Jincan Chen. *Parametric Optimum Design and Performance Improvement of a Thermophotonic Cell.* IEEE Transactions on Electron Devices, vol. 67, no. 6, pages 2376–2380, jun 2020. (Cited on pages 32 and 77.)

[Yang *et al.* 2022] Fan Yang, Kaifeng Chen, Yiting Zhao, Sun-Kyung Kim, Xiaobing Luo and Run Hu. *Near-field thermophotonic system for power generation and electroluminescent refrigeration.* Applied Physics Letters, vol. 120, no. 5, page 053902, jan 2022. (Cited on pages 17, 32, 63, 68, 69 and 89.)

[Zhang 2007] Zhuomin M. Zhang. Nano/Microscale heat transfer. McGraw Hill, 2007. (Cited on pages 19 and 58.)

[Zhao *et al.* 2017] Bo Zhao, Kaifeng Chen, Siddharth Buddhiraju, Gaurang R. Bhatt, Michal Lipson and Shanhui Fan. *High-performance near-field thermophotovoltaics for waste heat recovery.* Nano Energy, vol. 41, no. September, pages 344–350, 2017. (Cited on page 30.)

[Zhao *et al.* 2018] Bo Zhao, Parthiban Santhanam, Kaifeng Chen, Siddharth Buddhiraju and Shanhui Fan. *Near-Field Thermophotonic Systems for Low-Grade Waste-Heat Recovery.* Nano Letters, vol. 18, no. 8, pages 5224–5230, aug 2018. (Cited on pages 17, 26, 32, 33, 44, 63, 68, 69, 89, 100, 156 and 167.)

[Zhao *et al.* 2019] Bo Zhao, Siddharth Buddhiraju, Parthiban Santhanam, Kaifeng Chen and Shanhui Fan. *Self-sustaining thermophotonic circuits.* Proceedings of the National Academy of Sciences, vol. 116, no. 24, pages 11596–11601, jun 2019. (Cited on pages 17, 32 and 60.)

[Zhao *et al.* 2021] Bo Zhao, Sid Assawaworrarit, Parthiban Santhanam, Meir Orenstein and Shanhui Fan. *High-performance photonic transformers for DC voltage conversion.* Nature Communications, vol. 12, no. 1, page 4684, dec 2021. (Cited on page 32.)

[Zhu *et al.* 2019] Linxiao Zhu, Anthony Fiorino, Dakotah Thompson, Rohith Mittapally, Edgar Meyhofer and Pramod Reddy. *Near-field photonic cooling through control of the chemical potential of photons.* Nature, vol. 566, no. 7743, pages 239–244, feb 2019. (Cited on page 31.)

Folio administratif
Thèse de l'INSA Lyon, membre de l'Université de Lyon

NOM :	LEGENDRE	Date de soutenance : 22/11/2023
Prénom :	Julien	
Titre :	Étude théorique et numérique de systèmes thermophotoniques en champ proche appliqués à la récupération d'énergie	
Nature :	Doctorat	Numéro d'ordre : 2023ISAL0094
Ecole doctorale :	ED162 MEGA	
Spécialité :	Thermique et Énergétique	

RÉSUMÉ : Dans un système thermophotonique en champ proche, une diode électroluminescente chaude est placée à faible distance d'une cellule photovoltaïque maintenue à température ambiante. Le rayonnement émis par la diode électroluminescente, qui présente une intensité élevée grâce aux phénomènes d'électroluminescence et d'effet tunnel de photons, permet à la cellule photovoltaïque de produire une quantité importante d'énergie électrique : le système convertit la chaleur fournie au corps chaud en électricité. Dans cette thèse, on analyse le fonctionnement de ce système par des approches théoriques et numériques. La conversion rayonnement-puissance électrique ayant lieu dans les deux composants est d'abord modélisée à l'aide d'équations de conservation. Cela permet de développer une expression analytique de la valeur maximale de l'efficacité au maximum de puissance pour un rayonnement monochromatique ou à large spectre. Des efficacités quantiques élevées doivent être considérées pour rendre la puissance de sortie et l'efficacité compétitives. Le transport de charges dans les semi-conducteurs est ensuite simulé grâce à un code résolvant les équations de dérive-diffusion en une dimension et incluant l'émission thermoïonique et l'effet tunnel aux interfaces, permettant l'étude de structures réalistes. L'optimisation de systèmes composés d'homostructures permet d'introduire un dispositif capable de générer une puissance maximale de l'ordre du $W.cm^{-2}$ pour une diode électroluminescente à 600 K. Son analyse révèle l'importance de la configuration en champ proche, l'augmentation de l'efficacité quantique qu'elle induit étant essentiel au bon fonctionnement du système. On propose finalement un dispositif plus robuste, basé sur des hétérostructures composées de couches actives en InGaAs et de couches de confinement en InGaP. Cette architecture permet de conserver une puissance électrique élevée même lorsque des pertes auparavant négligées sont considérées, la puissance maximale ne diminuant alors que d'un facteur 4. Ces travaux démontrent que cette technologie de récupération d'énergie originale est prometteuse pour des températures de quelques centaines de degrés Celsius.

MOTS-CLÉS : Thermophotonique, Rayonnement en champ proche, Machine thermique optoélectronique, Thermodynamique

Laboratoire de recherche :	CETHIL
Directeur de thèse :	Pierre-Olivier CHAPUIS
Président de jury :	Christophe GOUPIL

Composition du jury :

NOM, Prénom	Grade/Qualité	Établissement	Rôle
GOUPIL, Christophe	Professeur	Univ. Paris-Cité	Président
PAPADAKIS, Georgia	Professeure	ICFO	Rapporteure
VAILLON, Rodolphe	Directeur de recherche	CNRS	Rapporteur
CLERC, Raphaël	Professeur	Univ. Jean-Monnet	Examinateur
REVOL, Inès	Chargée de recherche	CNRS	Examinatrice
CHAPUIS, Pierre-Olivier	Chargé de recherche HDR	CNRS	Directeur de thèse
OKSANEN, Jani	Chercheur	Aalto Univ.	Membre invité